ISSN 0915-6348

NATIONAL INSTITUTE FOR FUSION SCIENCE

Production, Diagnostics and Application of High Energy Density Plasmas

K. Hirano (Ed.)

(Received - Nov. 17, 1998)

NIFS-PROC-39 Dec. 1998

This report was prepared as a preprint of work performed as a collaboration reserch of the National Institute for Fusion Science (NIFS) of Japan. This document is intended for infomation only and for future publication in a journal after some rearrangements of its contents.

Inquiries about copyright and reproduction should be addressed to the Research Information Center, National Institute for Fusion Science, Oroshi-cho, Toki-shi, Gifu-ken 509-5292 Japan.

RESEARCH REPORT
NIFS-PROC Series

NAGOYA, JAPAN

Production, Diagnostics and Application of High Energy Density Plasmas

Edited by K. Hirano

Abstract

This is the proceedings of "Production, Diagnostics and Application of High Energy Density Plasma" held in National Institute for Fusion Science on December 18 - 19, 1997. Recent progress of experimental and theoretical works on dense z-pinches, physics of particle beam-target interaction diagnostics of dense plasmas, technology related pulsed power generator and surface modification by ion beams is presented.

Key words: z-pinch, plasma focus, gas puff pinch, soft x-ray, x-ray laser, pulsed power, high energy density

PREFACE

This publication is a collection of papers presented at the research meeting on "Production, Diagnostics and Application of High Energy Density Plasmas" held at National Institute for Fusion Science in December 18-19 under a collaborating research program of the Institute. The research meeting was attended by forty-three persons from the ten laboratories, and twenty-five lectures were given.

The high energy density plasmas are able to be generated with a lot of facilities such as a gas puff pinches and plasma foci and have many fields of applications because they are able to generate an intense source of soft x rays, neutrons, electron and ion beam. The researchers from different fields gathered to discuss a variety of problems in the high energy density plasmas, namely spectroscopy, diagnostics, pinch dynamics and related engineering aspects, and were stimulated by the researches in this fields.

The editor of these proceedings wish to thank all the authors of papers, the research meeting participants and the Sub-committee on Scientific Research collaborations of the National Institute for Fusion Science who contributed to the success of this research meeting.

Katsumi Hirano
Gunma University
April, 1998

CONTENTS

LIST OF ATTENDEES

H. Akiyama	Kumamoto University
R. Ando	Kanazawa University
A. Baba	Nihon University
S. Furuya	Nagaoka University of Technology
Y. Goshima	Nihon University
D. Hasegawa	Kanazawa University
K. Hirano	Gunma University
K. Hiraoka	Tokyo Institute of Technology
K. Horioka	Tokyo Institute of Technology
M. Horiuchi	Nihon University
T. Igusa	Nihon University
M. Ikarashi	Nagaoka University of technology
S. Ishii	Tokyo Institute of Technology
K. Kamada	Kanazawa University
S. Katsuki	Kumamoto University
Y. S. Liu	Tokyo Institute of Technology
T. Masuda	Himeji Institute of Technology
K. Masugata	Nagaoka University of Technology
M. Masuzaki	Kanazawa University
H. Matsuzawa	Yamanashi University
S. Miki	Himeji Institute of Technology
T. Miyamoto	Nihon University
A. Muravich	Nihon University
M. Nakayama	Nagaoka University of Technology
N. Nishino	Hiroshima University

K. Ogura	Nagaoka University of Technology
M. Ohnishi	Tokyo Institute of Technology
T. Okuda	Tokyo Institute of Technology
M. Sato	Gunma University
N. Sato	Nihon University
B. Shan	Gunma University
T. Shinkai	Kumamoto University
T. Sueda	Kumamoto University
H. Takano	Nagaoka University of Technology
K. Takasugi	Nihon University
M. Tanigawa	Himeji Institute of Technology
T. Tazima	National Institute for Fusion Science
T. Yamamoto	Gunma University
T. Yanagidaira	Gunma University
K. Yasuoka	Tokyo Institute of Technology
K. Yatsui	Nagaoka University of Technology
M. Yatsuzuka	Himeji Institute of Technology
H. Yoshida	Kanazawa University

Light emission from a PTFE insulator in vacuum subjected to ac electrical fields

Yuan-Shing Liu, Takehiko Mizuno, Sadao Matsushima, Masami Okada, Koichi Yasuoka and Shozo Ishii

Department of Electrical and Electronic Engineering, Tokyo Institute of Technology
2-12-1 O-okayama, Meguro-ku, Tokyo 152, Japan

Light emission from the surface of PTFE insulator with metallized electrodes has been investigated under ac electric field application along the polymer surface in order to understand the initiation mechanism of the prebreakdown. Two distinct stages of light emission according to the applied voltage were observed: a low-level stable light emission, so-called electroluminescence (EL), before prebreakdown and an irregular intense light emission during prebreakdown. Before prebreakdown, charge injection from the electrode directly into the polymer surface layer results in EL emission and the formation of long-term electron space charges away from the electrode. The crucial factor of the prebreakdown initiation is the strong modification of the local electric field near the electrode because of the space charge formation in the surface layer before prebreakdown. The prebreakdown with intense light emission is initiated by detrapping the long-term trapped electrons toward the electrode via vacuum and/or the surface layer in the positive half cycle of ac voltage.

1 Introduction

Surface flashover across solid insulators limits the maximum power density transferable in high voltage power systems. Up to now, several models of surface flashover on solid insulators in vacuum have been proposed. [1] However, a generalized mechanism for all the aspects of experimental observations has not been developed yet. It has been shown that the development of the prebreakdown gives rise to the initiation of surface flashover. [2, 3] Therefore, the understanding of prebreakdown phenomena is needed to gain the fundamental insights about the physical mechanism of surface flashover.

It has been reported that the prebreakdown phenomena are similar to partial discharges (PD) under ac voltage application in vacuum. [4, 5] The initiation mechanism of the prebreakdown has been considered to be a field emission of electrons from the cathode into vacuum, giving rise to the secondary electron emission due to the impact of the emitted

electrons on the surface of the insulator. The field emission of electrons is determined by the local electric field at the triple junction, which is formed at the interface of the metal cathode, the insulator and the vacuum. The crucial factor in the local electric field leading to field emission of electrons has been considered to be the microscopic shape of the electrode, and little attention has been paid to the space charge distribution near the electrode. However, electron injection from the electrode directly into the insulator will be possible prior to the field emission of electrons from the cathode into vacuum. Such injected electron gives rise to the formation of space charges and hence the strong modification of the local electric field near the electrode, which greatly influences the field emission of electrons from the cathode and the subsequent prebreakdown.

The charge injection into polymers such as polyethylene has been reported to cause electroluminescence (EL) in the polymers due to the radiative recombination of electrons and holes under ac voltage application. [6] [7] In this paper, we tried to measure the light emission phenomena in the polymer before and during the prebreakdown under ac voltage application in vacuum, using a photon counting method. Based on the optical observations, we discuss the initiation mechanism of the prebreakdown for the metallized polymer, taking into account the effect of space charge formation in the polymer before the prebreakdown.

2 Experimental

PTFE sample, 5 mm in thickness and 50 mm in diameter, was used. Two concentric electrodes of gold were deposited on one side of the sample surface by a sputtering method in a vacuum. The geometry of the metallized sample is shown in Fig. 1. The inner gold

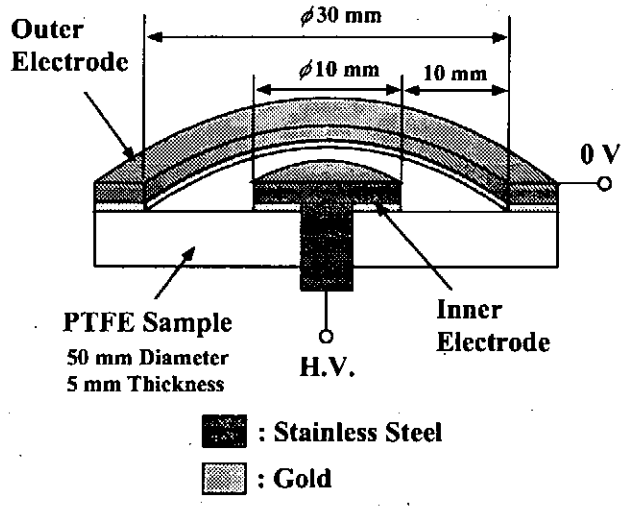

Fig.1. Geometry of the metallized sample.

electrode was connected to a high voltage power supply via a stainless steel electrode, and

the outer gold electrode was mounted to a stainless steel ring electrode held at ground potential. The metallized sample and the stainless steel electrodes were ultrasonically cleaned in a methanol bath for one hour before experiments.

The diagram of the experimental arrangement is shown in Fig. 2. The sample setup was

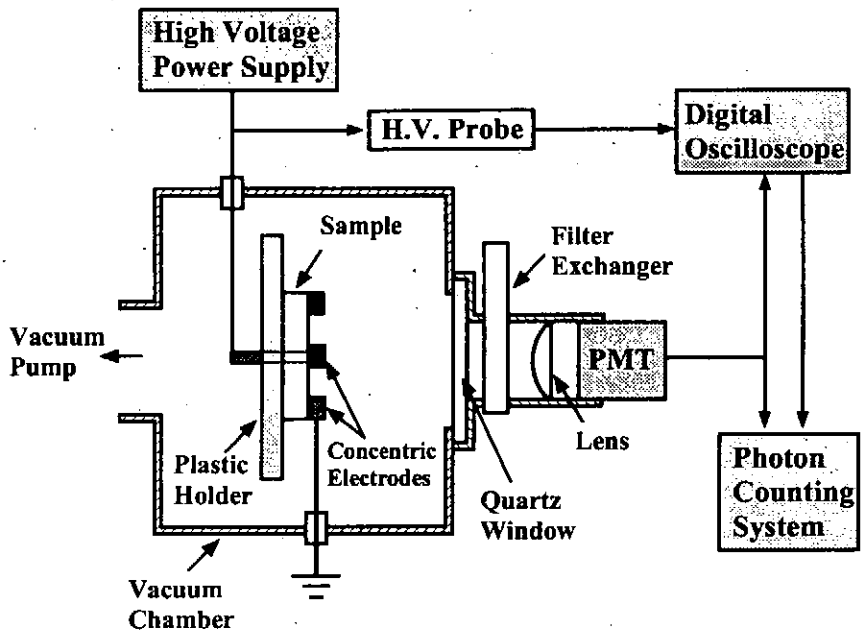

Fig.2. Diagram of the experimental arrangement.

placed in a vacuum chamber. All tests were performed in a vacuum of 10^{-4} Pa. The electric field was applied along the sample surface by the ac voltage application with 50 Hz between inner and outer electrodes. Initially, the voltage was held at 0 V and then increased in steps of 500 V with 5 min at each step. The applied voltage was monitored by a digital oscilloscope (HP 54542A) using a 1000:1 high-voltage probe (Tektronix P6015A).

Emitted light from the sample surface was focussed by a lens onto the photocathode of the photomultiplier tube (PMT, Hamamatsu R943-02) having a spectral range of 160-930 nm. The PMT was operated at $-30°$ C in order to minimize the number of dark pulses to about 2/sec. The output signal from the PMT was directed either to the photon counting system employing a multichannel scaler (MCS) or to the digital storage oscilloscope.

3 Results

A typical plot of light intensity and applied voltage is shown in Fig. 3, measured by the photon counting system. As seen in Fig. 3, two distinct stages of light emission, referred to as stages A and B, according to the applied voltage were observed. Light emission at the stage A was a low-level stable light emission under constant ac voltage and was observed

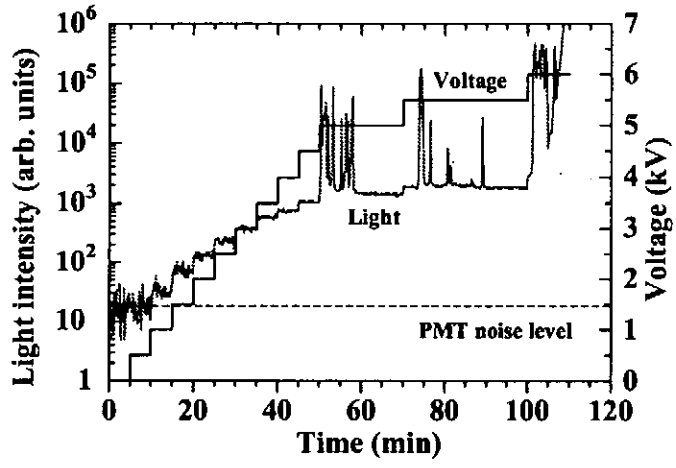

Fig.3. Typical plot of light intensity and applied voltage.

at the voltage as low as 1 kV. The light intensity at the stage A was regularly increased with the applied voltage up to 4.5 kV.

The phase relationship between the light intensity and the applied ac voltage of 4.5 kV at the stage A is shown in Fig. 4(a), measured by the photon counting system. The peak of

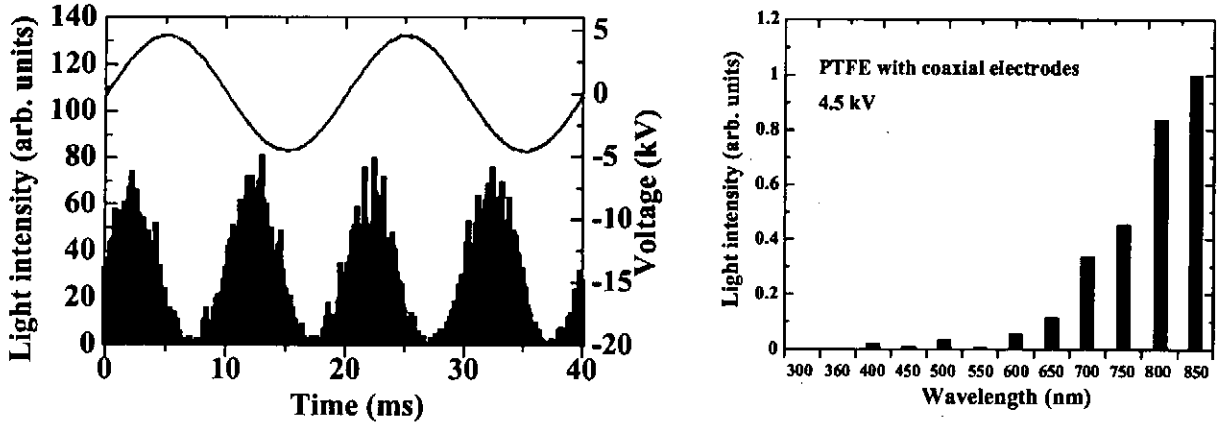

(a) (b)

Fig.4. (a) Phase relationship between the light intensity and the applied ac voltage, and (b) Spectra of the light emission at the stage A.

light intensity appeared in the positive and negative half cycle of ac voltage, respectively,

and preceded the voltage peaks by about 2.5 msec in each half cycle. No significant effect of the voltage polarity was observed in the light emission at the stage A. The light emission spectra during the stable light emission at the stage A under ac voltage of 4.5 kV is shown in Fig. 4(b), measured by the twelve broad optical interference filters (10 nm bandwidth) between 300 and 850 nm. The light emission spectra were corrected for the quantum efficiency of the photocathode of the PMT and the transmittance of the filters. The main spectral component of emitted light at the stage A was in the red and infrared region between 700 and 850 nm or longer. The above spectral features did not depend on the applied voltage below 4.5 kV.

The phase relationship between the light emission and the applied ac voltage of 6 kV at the stage B is shown in Fig. 5(a), measured by the oscilloscope. As seen in Fig. 5(a), the

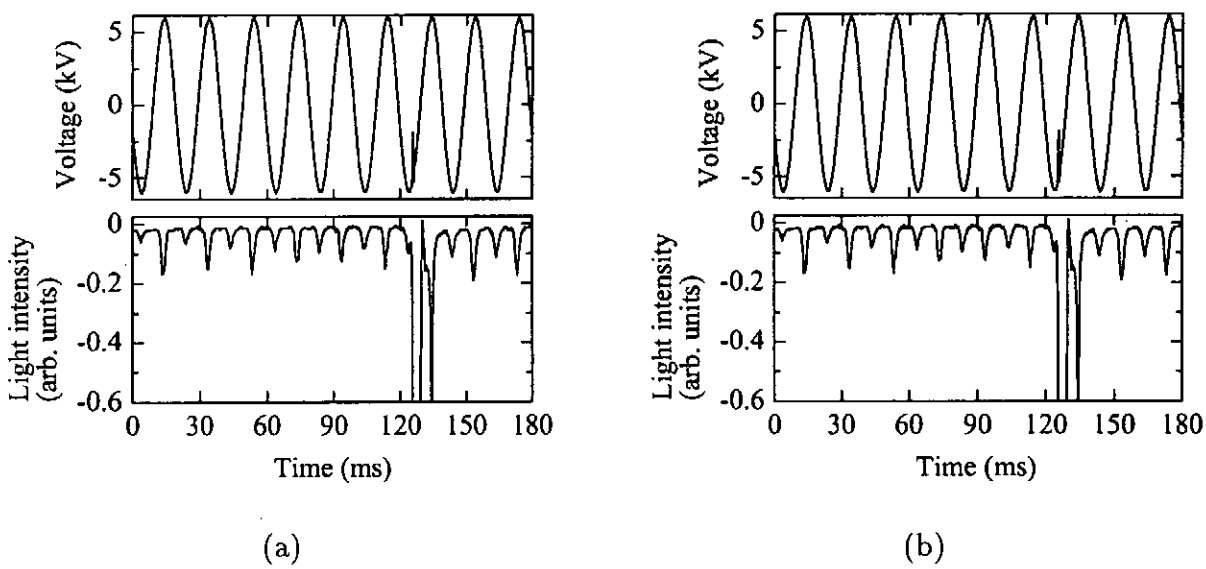

Fig.5. Phase relationship between the light emission and the applied ac voltage (a) at the initiation phase of stage B, and (b) about 5 min after the stage B inception.

intense light pulses appeared near the voltage peaks in the positive and negative half cycle, respectively. Significant effect of the voltage polarity on the light intensity was observed and changed with time. In the initiation phase of the light emission at the stage B, the light intensity in the positive half cycle was larger than that in the negative half cycle. The light intensity in the positive half cycle gradually decreased and the light intensity in the negative half cycle increased. Subsequently, the light intensity in the negative half cycle became larger than that in the positive half cycle, as shown in Fig. 5(b). Occasionally, large light pulses with voltage breakdown appeared, as shown in Figs. 5(a) and (b). Several minutes after the onset of the stage B, the intense light emission as shown in Fig. 3 tended

to be suppressed and then the light emission like stage A was observed.

4 Discussion

Our observation of two distinct stages of light emission according to the applied voltage shows that the mechanisms of light emission strongly depend on the applied ac voltage. The characteristics of light emission at the stages A and B indicate the light emission before and during prebreakdown, respectively.

We discuss the initiation mechanism of the prebreakdown on the polymer surface, based on our optical observation in the following sections.

4.1 Space charge formation due to charge injection before prebreakdown

The characteristics of light emission at the stage A cannot be explained by the light emission caused by the field emission of electrons from the cathode into vacuum which has been considered as the onset of the prebreakdown. First, the spectral features of light emission at the stage A shown in Fig. 4(b) did not have any strong emission bands and did not depend on the applied field. Moreover, the emitted photon energy (1.5-1.8 eV) seems to be very low for the light emission through the processes caused by field emitted electron. Second, the inception voltage of light emission at the stage A was as low as 1 kV, where the electric field at the triple junction was estimated to be about 4 kV/mm for our electrode configuration, calculated by a finite element method. The field emission of electrons from the cathode into vacuum is practically impossible at such low electric field.

We consider that the light emission at the stage A is caused by charge injection from the electrode directly into the polymer surface layer. Such light emission phenomenon in the polymer is known as electroluminescence (EL). [8, 9, 10] The characteristics of light emission at the stage A are similar to those of EL in the metal-deposited polymeric film [7]: the EL inception electric field of 7 kV/mm for PTFE, the phase relationship between the light intensity and the applied ac voltage (Fig. 4(a)) and the light emission spectra (Fig. 4(b)). The light emission at the stage A can be explained by the radiative recombination process of the electrons and holes injected into the polymer surface layer. The detailed light emission process due to the electron-hole recombination process taking into account the surface states of the polymer under ac voltage application is described elsewhere. [7]

Under ac voltage application, electrons and holes are easily injected into the surface states of the polymer which are extensively distributed in the energy band gap. Such injected carriers transfer between the surface states via a hopping mechanism in the metal-polymer interface region and in the polymer surface layer along the polymer surface. The energy levels of the electrons and holes trapped at the surface states will be close to the Fermi level of the metal, so that the photon energy through the radiative recombination of

the electrons and holes will be low, probably in the red and infrared region, as shown in Fig. 4(b).

The phase relationship between the light intensity and the ac voltage shown in Fig. 4(a) is considered to describe the picture of charge flow along the polymer surface according to the temporal variation of the local electric field. It has been reported that the injected carriers located away from the electrode give rise to the formation of long-term space charges [12, 13] and that the necessary condition for EL emission is the formation of such long-term space charges in the metal-polymer interface region [7]. The local electric field near the electrode is strongly modified by the formation of space charges due to the charge injection. The peak of the local electric field in the polymer surface layer near the electrode is expected to precede that of external applied voltage due to the space charge formation in the polymer surface layer.

The characteristics of light emission at the stage A imply that the formation of space charge region due to charge injection occurs in the polymer surface layer near the electrode and causes the strong modification of the local electric field before prebreakdown.

4.2 Initiation mechanism of prebreakdown

During the prebreakdown, the characteristics of light emission at the stage B show the occurrence of intense light pulses near the voltage peaks with the strong depencence of the voltage polarity and the voltage application time, as shown in Figs. 5(a) and (b). We consider that the light emission at the stage B is closely related to the space charges near the electrode, especially long-term space charges, previously formed at the stage A. The light emission at the stage B is considered to occur mainly near the inner electrode because the higher tangential electric field occur at the inner electrode triple junction than at the outer electrode one in our electrodes system. In the following discussion on the initiation mechanism of prebreakdown, we focus our attention mainly on the region of surface layer near the inner electrode.

Figure 6 shows schematics of space charge distribution in the polymer surface layer near the electrode during the positive half cycle of the ac voltage. Near the threshold voltage where the light emission behavior is switched from the stage A to the stage B, the large amount of long-term negative space charges will be probably formed away from the electrode during the negative half cycle, which enhances the local electric field in the polymer surface layer in the following positive half cycle. The local electric field in the polymer surface layer becomes maximum at the voltage peaks in the positive half cycle. When the local electric field exceeds the detrapping threshold of the long-term trapped electrons away from electrode, the trapped electrons are detrapped by tunneling or hopping mechanisms. The detrapped electrons transfer toward the electrode via vacuum and/or the polymer surface layer and give rise to intense light emission through the excitation/ionization processes of the molecules of the polymer and the desorbed gases due to the impact of emitted electrons.

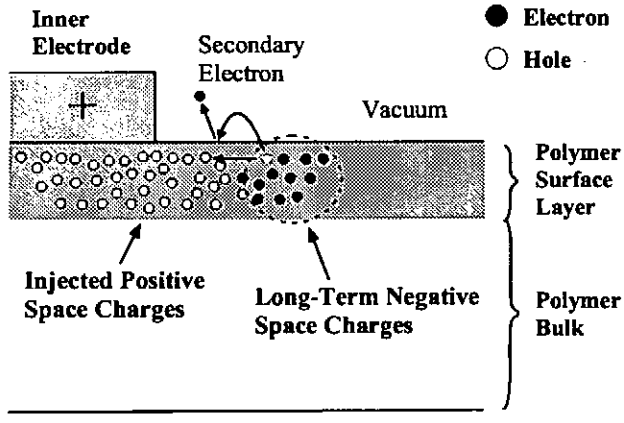

Fig.6. Schematic of space charge distribution in the polymer surface layer near the electrode during the positive half cycle of ac voltage.

Le Gressus *et al.* [14] have stated that when the dielectric surface is charged up, the maximum electric field is close to the end of the space charge distribution and that the electric field created by the space charges induces the abrupt expansion of the trapped charges along the surface, based on the experimental results using the scanning electron microscope (SEM). Our interpretation of the injected charge behavior in the polymer surface, based on our optical observation, is in agreement with their reports. Such electron impact on the polymer surface layer causes a secondary electron emission which makes positive charges left behind. The above transport processes of the detrapped electrons during the positive half cycle result in the positive charging in the polymer surface layer, which gives rise to the enhancement of the local electric field at the electrode and hence the field emission of electrons from the electrode in the following negative half cycle. This interpretation is consistent with our results that at the initiation phase of the stage B, the light intensity in the positive half cycle was larger than that in the negative one and that the intense light pulses appeared near the voltage peaks (Fig. 5(a)).

Similary, the field emission of electrons from the electrode into vacuum in the negative half cycle causes the secondary electron emission from the polymer surface due to the impact of emitted electrons on the polymer surface. Through the secondary electron emission, positive ions remain in the polymer surface layer near the electrode, which decreases the local electric field near the electrode in the following positive cycle. The density of positive charges in the surface layer in the negative half cycles will increase and the density of negative charges in the positive half cycles decrease with the time of ac voltage application. This means that the amount of emitted electrons from the electrode in the negative half cycle will be larger than that of emitted electrons from the polymer surface layer in the positive half cycle with time. That is why the light intensity in the negative half cycle became larger than that in the positive one, several minutes after the voltage application,

as shown in Fig. 5(b). The above positive feedback effect of the field electron emission from the cathode probably induces the breakdown along the polymer surface with large light pulses, as shown in Figs. 5(a) and (b).

The intense light emission tended to be suppressed several minutes after the onset of the stage B, as shown in Fig. 3. The space charges trapped in the polymer surface layer are slowly dissipated along the surface during the above processes with time, causing the redistribution of the space charges and hence the electric field. The most likely interpretation of the suppression of the intense light emission is that the redistribution of the space charges in the surface layer gives rise to lowering the electric field at the electrode and in the surface layer below the emission and detrapping threshold of electrons.

5 Conclusion

The characteristics of light emission from the PTFE surface under ac voltages show two distinct stages according to the applied voltage: a low-level stable light emission at the stage A below 5 kV, so-called electroluminescence (EL), and an irregular intense light emissin at the stage B above 5 kV. The characteristics of light emission at the stages A and B correspond to the light emission before and during prebreakdown, respectively. The initiation mechanism of prebreakdown derived from optical observations is described as follows: Before prebreakdown (stage A), charges are injected directly into the polymer surface layer and accumulated in the surface layer, leading to EL emission. This gives rise to the strong modification of the local electric field near the electrode, causing the following prebreakdown. The prebreakdown (stage B) with the intense light emission is initiated by detrapping the electrons trapped away from the electrode in the surface layer due to the intense electric field. The detrapped electrons are transferred toward the electrode via vacuum and/or the surface layer in the positive half cycle of ac voltage, which causes the secondary electron emission from the the surface layer due to the electron impact, leading to the prebreakdown.

The measurement of light emission is considered to be useful for understanding the initiation mechanism of the prebreakdown and hence the surface flashover.

Acknowledgments

We would like to thank Fujikura Ltd. for supplying the samples. Part of this work was supported by a Grant-in-Aid for Scientific Research from the Ministry of Education, Science, Sports and Culture.

References

[1] H. C. Miller: IEEE Trans. Electr. Insul. **28** (1993) 512.

[2] C. R. Li and T. S. Sudarshan: J. Appl. Phys. **76** (1994) 3313.

[3] N. S. Xu, R. V. Latham, B. Goddard, J. Tan and W. Taylor: J. Phys. D: Appl. Phys. **30** (1997) 666.

[4] J. Lewis, T. S. Sudarshan, J. E. Thompson, D. Lee and R. A. Dougal: IEEE Trans. Electr. Insul. **19** (1984) 512.

[5] H. Mościcka-Grzesiak and W. Ziomek: *17th Int. Symp. on Discharges and Electr. Insul. in Vacuum, Berkeley, 1996,* p. 410.

[6] T. Mizuno, Y. S. Liu, W. Shionoya, K. Yasuoka and S. Ishii: Jpn. J. Appl. Phys. **36** (1997) 754.

[7] T. Mizuno, Y. S. Liu, W. Shionoya, K. Yasuoka, S. Ishii, H. Miyata and A. Yokoyama,: IEEE Trans. Dielectr. Electr. Insul., **4** (1997) 433.

[8] K. Kojima, Y. Takai and M. Ieda: Jpn. J. Appl. Phys. **22** (1983) 1436.

[9] C. Laurent, C. Mayoux and S. Noel: J. Appl. Phys. **58** (1985) 4346.

[10] S. S. Bamji, A. T. Bulinski and R. J. Densley: IEEE Trans. Electr. Insul. **21** (1986) 639.

[11] J. Jonsson, B. Rånby, D. Mary, C. Laurent and C. Mayoux: IEEE Trans. Dielectr. Electr. Insul. **2** (1995) 107.

[12] T. Lebey and C. Laurent: J. Appl. Phys. **68** (1990) 275.

[13] T. Tanaka: IEEE Trans. Electr. Insul. **27** (1992) 424.

[14] C. Le Gressus, F. Valin, M. Henriot, M. Gautier, J. P. Duraud, T. S. Sudarshan and R. G. Bommakanti : J. Appl. Phys. **69** (1991) 6325.

Characteristics of multichannel arc gap

S.Furuya, J.Ohrui, T.Akiyama, S.Takano and J.Irisawa

Department of Electrical Engineering, Nagaoka University of Technology

Abstract

The characteristics of multichannel arc gap are investigated experimentally. The gap is composed of 12 steel needle electrodes and a brass rod. In the first case, the characteristics of self-breakdown mode of multichannel arc gap are tested. It is found that the kinds and the pressure of inter-gap gas influence the number of arc channels. In the second case, UV irradiation to inter-gap is attempted to increase the number of arc channels. As a result, we confirm that UV irradiation is useful for the help of multichannel operation.

1. Introduction

Multichannel arc gap is a switch which has a large number of gaps in parallel. Compared to single gap, multichannel arc gap has lower switching inductance and electrode erosion rate, which is superior in fast rise time and long life time. Multichannel arc gap is frequently used as pulsed power switch, however, its characteristics have hardly been investigated.

Therefore, we have examined the characteristics of multichannel arc gap. The gap is composed of 12 steel needle electrodes and a brass rod. Voltage pulses which have high dV/dt are necessary to generate a large number of arc channels simultaneously[1]. A non-linear coaxial line of ferrite sharpener has been used to produce voltage pulses which have high dV/dt of 12kV/ns and peak voltage of 45kV[2]. In the fast case, we examined the characteristics of self-breakdown mode of multichannel arc gap when the kinds and the pressure of inter-gap gas are changed. In the second case, ultraviolet irradiation to inter-gap is attempted to increase the number of arc channels under the consideration that the number of channels may increase with initial electrons generated by photo-ionization. Ultraviolet light is generated by a preliminary spark discharge near the main gap.

In Sec.2, the experimental setup of multichannel arc gap is described. In Sec.3, the experimental results of self-breakdown mode of multichannel arc gap are presented. In Sec.4, the effect of UV irradiation to inter-gap is described. Finally, the results of this report are summarized in Sec.5.

2. Experimental setup

Voltage pulses which have high dV/dt are produced by a ferrite sharpener. Fig.1 shows the ferrite sharpener which is non-linear coaxial line. A piece of ferrite bead is TDK-HF70BB 2.5×5×0.8 mm. The principle of the sharpener is illustrated in Fig.2. The input voltage pulse which has low dV/dt is steepened at the end of the sharpener. Typical output voltage waveform of open ended ferrite sharpener is shown in Fig.3. The rise time and the peak voltage of the pulse are 2.4ns and 45kV respectively, high dV/dt of 12kV/ns is achieved. Voltages were measured by Tektronix high voltage probe: P6015A and Hewlett Packard digital oscilloscope: HP54510A.

Fig.4 shows the geometry of multichannel arc gap. The gap is composed of 12 steel needle electrodes and a brass rod of 18mm diameter. The rod electrode is grounded and positive or negative high voltage is applied to the needle electrodes. The apparatus allows the gap length to be varied. The gap is contained in the chamber, the kinds and the pressure of inter-gap gas are changeable. In the experiments helium, argon, oxygen and nitrogen were used as inter-gap gas. The number of arc channels are detected by Sony CCD video camera: CCD-TR650. 50 shots at each experimental conditions were performed, the data of the number of arc channels were handled by taking the mean.

3. Experimental results

In this section, the experimental results of self-breakdown mode of multichannel arc gap are presented. The range of experimental parameters are 0.1-3atm in pressure and 1-5mm in gap length. Fig.5 shows the relation between the average number of arc channels and gas pressure. (a) and (b) are the data for helium when positive and negative high voltage are applied to the needle electrodes, respectively. (c)(d), (e)(f), (g)(h) and (i)(j) are the data for argon, oxygen, nitrogen and mixture(1:1) of oxygen and nitrogen, respectively. The principal results are following: The kinds and the pressure of inter-gap gas influence the number of arc channels. The average number of arc channels decreases with increasing gap length. The number of arc channels for argon is larger than that for helium. The number of arc channels decreases with increasing gas pressure for oxygen and nitrogen. The data for mixture of oxygen and nitrogen has the middle properties between ones for oxygen and nitrogen. Physical mechanisms in the results are not clear in present.

4. Effect of UV irradiation

Ultraviolet irradiation to inter-gap is attempted to increase the number of arc channels under the consideration that the number of channels may increase with initial electrons generated by photo-ionization. Ultraviolet light is generated by a preliminary spark discharge near the main gap. The cross-sectional view of main gap and pre-discharge electrode geometries is shown in Fig.6. Fig.7 is an integrated photograph of pre- and main-discharge. As 100Ω resistors are inserted in series to pre-discharge gaps, arc channels are generated in all gaps. Compared to pre-discharge gaps, only 5 channels are generated in main gaps. Fig.8 shows the relation between the average number of arc channels and main gap length. The experiments were carried out in air of 1atm for three different delay time between the onset of pre- and main-discharge. In any case the average number of arc channels increases with UV irradiation, it is found that UV irradiation is useful for the help of multichannel operation.

5. Conclusion

The characteristics of multichannel arc gap are investigated experimentally. The gap is composed of 12 steel needle electrodes and a brass rod. In the first case, the characteristics of self-breakdown mode of multichannel arc gap are tested. It is found that the kinds and the pressure of inter-gap gas influence the number of arc channels. In the second case, UV irradiation to inter-gap is attempted to increase the number of arc channels. As a result, we confirm that UV irradiation is useful for the help of multichannel operation.

Reference

(1) G.R.Neil and R.S.Post, Rev. Sci. Instrum., 49 (1978) 401

(2) S.Takano et. al., NIFS-PROC-26 (1996) 115

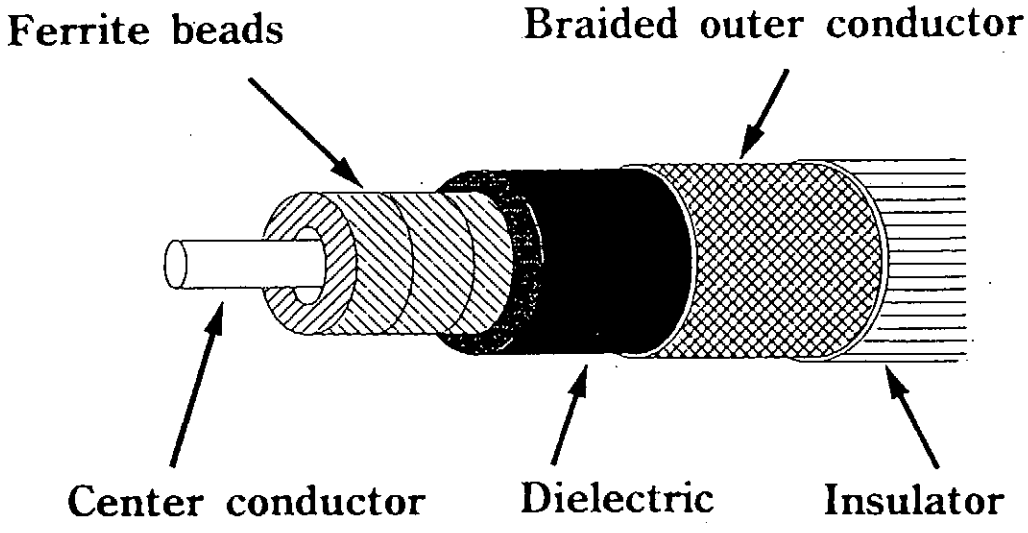

Fig.1 Ferrite sharpener

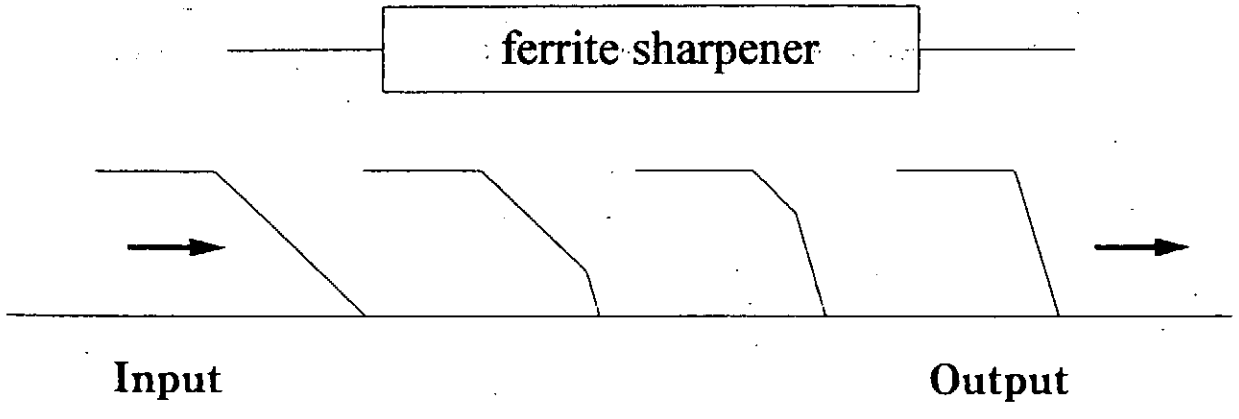

Fig.2 Principle of ferrite sharpener

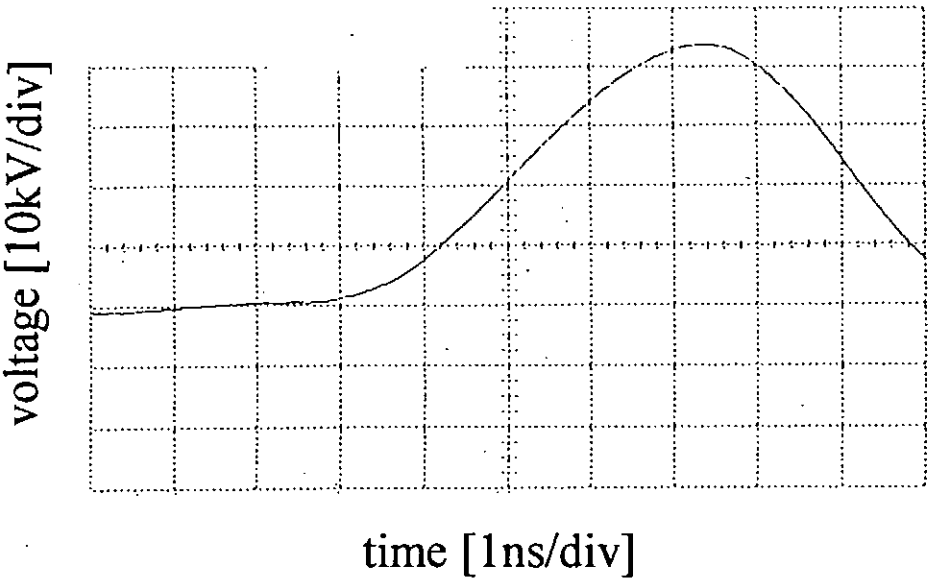

Fig.3 Output voltage of open ended ferrite sharpener

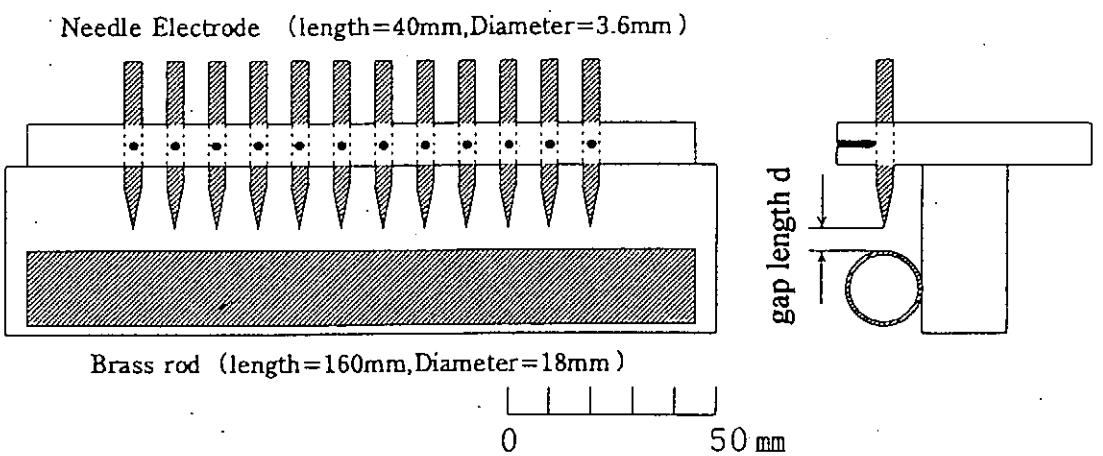

Fig.4 Geometry of multichannel arc gap

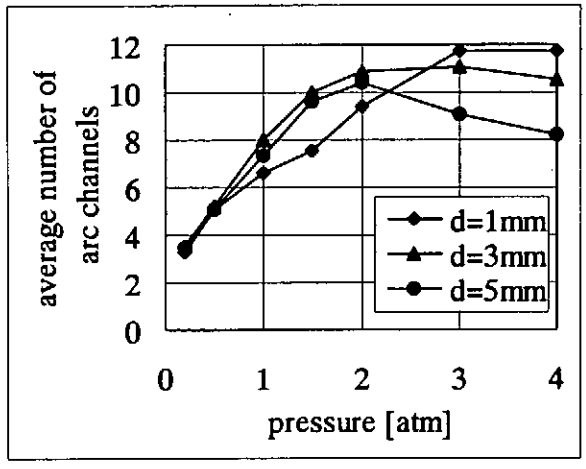

(a) helium
for positive needle

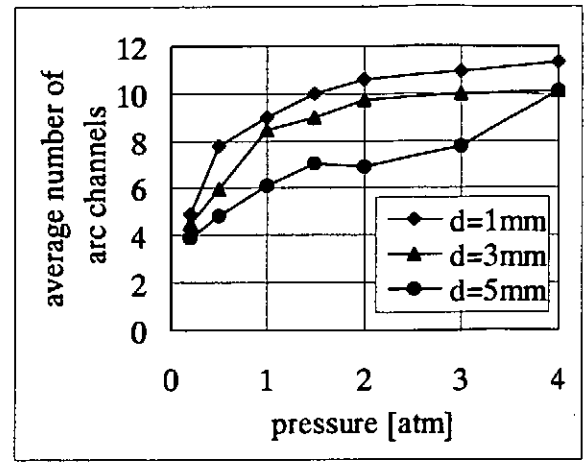

(b) helium
for negative needle

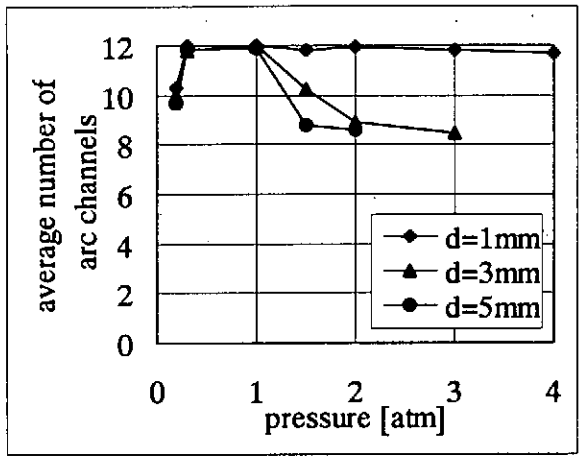

(c) argon
for positive needle

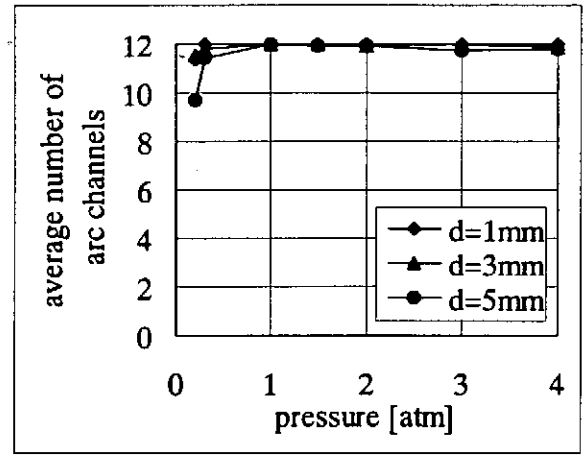

(d) argon
for negative needle

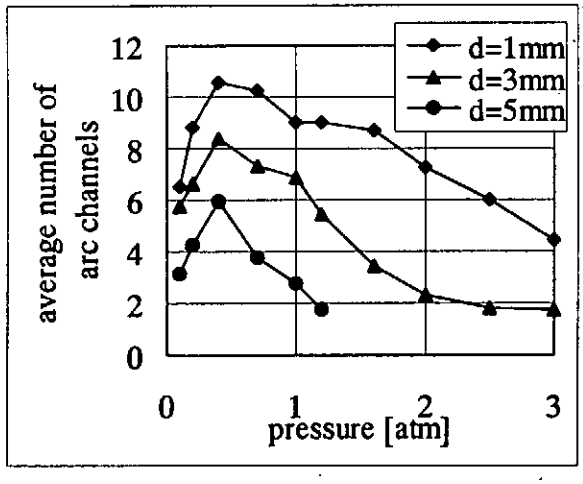

(e) oxygen
for positive needle

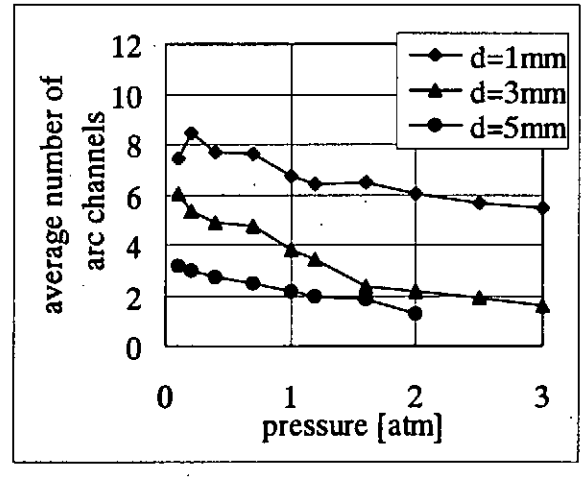

(f) oxygen
for negative needle

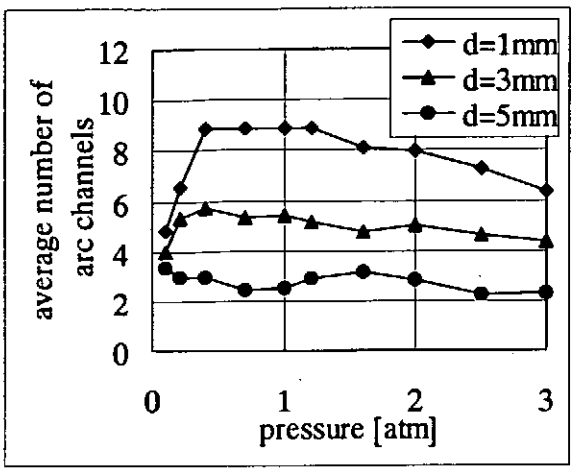

(g)nitrogen
for positive needle

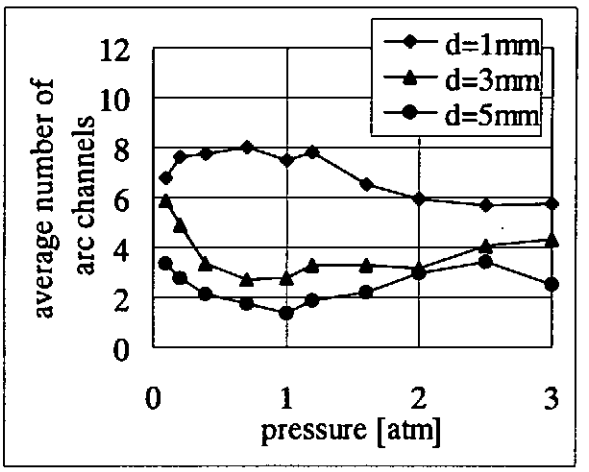

(h)nitrogen
for negative needle

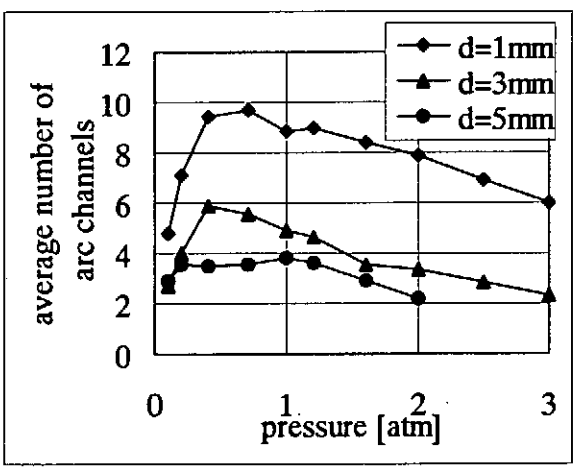

(i) mixture of oxygen
and nitrogen for
positive needle

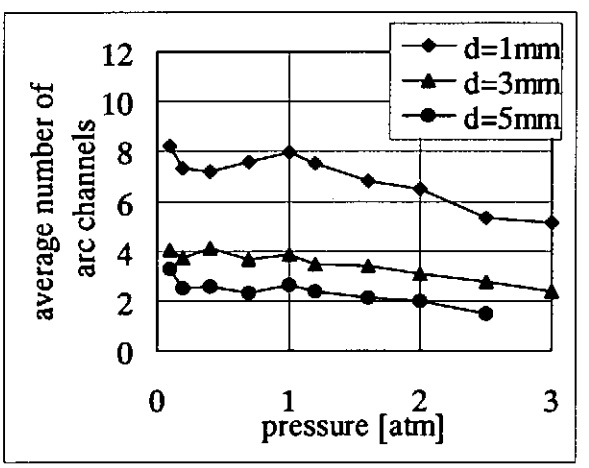

(j) mixture of oxygen
and nitrogen for
negative needle

Fig.5 Relation between
average number of arc channels
and gas pressure

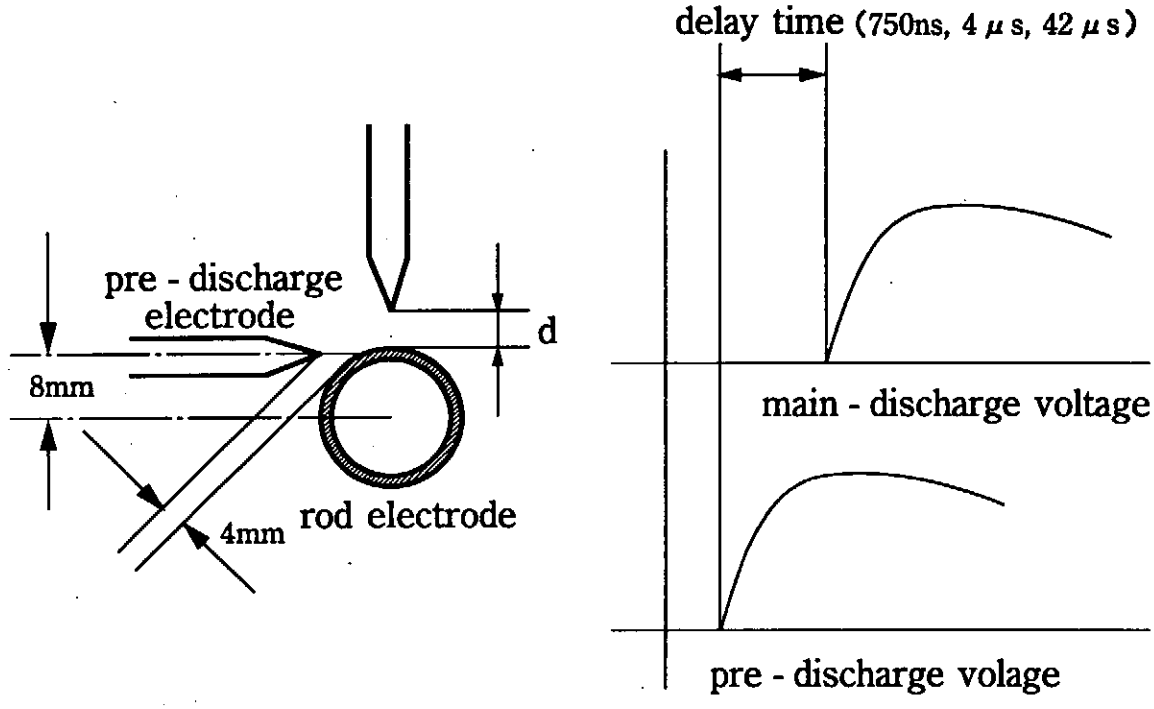

Fig.6 Cross-sectional view of main gap and pre-discharge electrode geometries

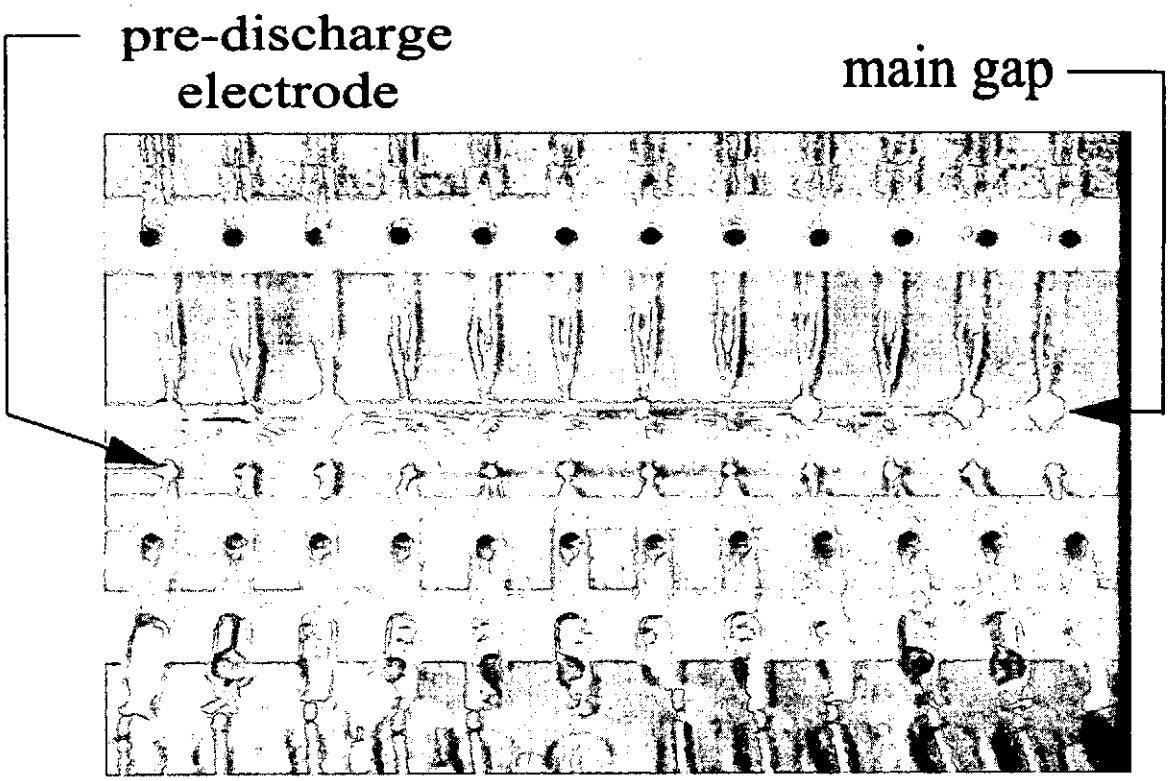

Fig.7 Integrated photograph of
pre- and main-discharge

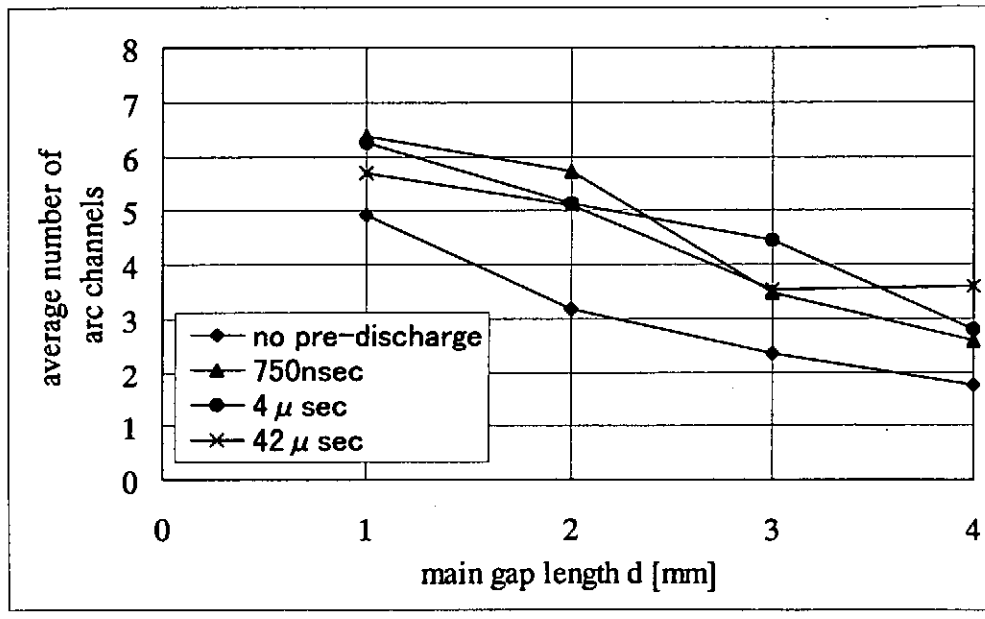

(a) positive needle

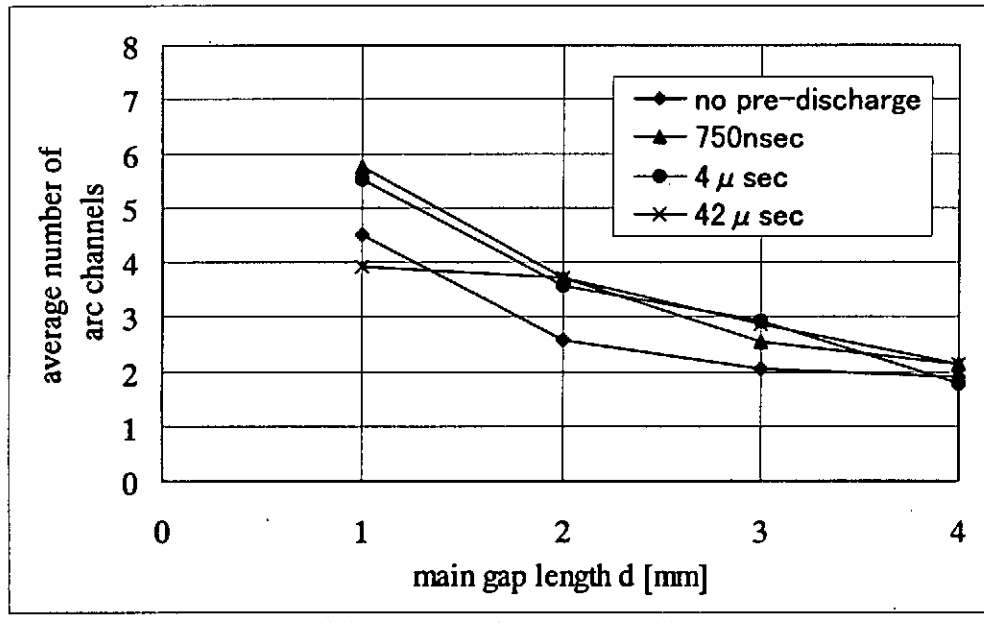

(b) negative needle

Fig.8 Relation between average number of arc channels and main gap length with and without UV irradiation

Characteristics of Repetitively Operated High-Current Discharge Gap Switch

N. Nakayama, N. Hasegawa, K. Masugata and K. Yatsui

Nagaoka University of Technology,

Nagaoka, Niigata 940-21 Japan

Abstract

Characteristics of repetitively operated high-current discharge gap switches were investigated to develop long life, highly-repetitive pulsed power switches. The discharge gap switches of gap length 4 mm were filled with 0.6 atom of SF_6 or 3 atom H_2 to obtain the initial self breakdown voltage ≈ 20 kV. The switch was pulse discharged at peak current ≈ 8 kA, duration ≈ 400 ns with repetition rate ≈ 2 Hz. The breakdown voltages (V_b) were recorded for 10000 shot of discharges. From the experiment we found that V_b and the scattering of V_b increases with increasing the shots when using SF_6. In contrast V_b and the scattering of V_b are almost constant when using H_2. After the shot the discharge gas are analyzed and found that new composites were produced when using SF_6, whereas no new compost was observed when using H_2.

1. Introduction

Pulsed power technology[1,2] has a wide area of applications including the generation of high-power particle beams, X-ray or gas laser excitation , etc. In these applications, it is very important to develop a highly repetitive system to obtain a higher average power. In the pulsed power technology, a number of discharge gap switches filled with pressurized SF_6 or air have been utilized.[1,2] However, since such the switches take a long time for the recovery of breakdown voltage and the energy loss in the switching is relatively large, it has been considered to be difficult to achieve a highly repetitive operation.[3] In the previous works dependence of the characteristics of the switches on

the filling gas were studied and found that the recovery speed and the efficiency are enhanced by using H_2.[3,4]

For highly repetitive operation of the gap swatches it is also very important to obtain a stability of the breakdown voltage. To evaluate the stability, a gap switch using SF_6 and H_2 was repetitively pulse discharged at repetition rate 2 Hz and observed the stability of the breakdown voltage. In addition, to clarify the cause of the scattering of the breakdown voltage, gas composition and the materials deposited were analyzed after the operation. In the paper the results of the experiments are described.

2. Experimental apparatus

Figure 1 shows the circuit used in the experiment. A C-R discharge circuit was used to damp the ringing current and to obtain a single polarity discharge current. For the capacitor (C), fast capacitor bank of capacitance 150 nF was used, which was charged by the high voltage power supply (H. V.) through a chrging resister (R_1). As the dumping resister (R), low inductance type ceramic resister of resistance 1 Ω was utilized. The charging resister and the dumping resister were cooled by circulating oil to keep the resistance be constant. As the gap switch, a pair of hemispherical electrodes (brass, 25 mm diameter) were utilized which were installed inside the acrylic vessel. The gap length (d) was adjusted to be 4.0 mm. Filling gas of SF_6 and H_2 were utilized, the filling pressure were 0.6 atm for SF_6 and 3 atm for H_2 to obtain the initial breakdown voltage around 20 kV. Before filling the gas, the gap switch was evacuated to the pressure 10^{-2} Torr to reduce impurity. The experiment was done on two conditions of filling gas, that is the sealed off condition and the gas flow condition. For the gas flow condition flow rate of the gas was kept to be around 3 *l*/min with keeping the constant gas pressure.

The applied voltage of the high voltage power supply was adjusted to keep the repetition rate of the discharge to be around 2 Hz. For the measurement of the waveforms of charging voltage (V_{ch}) and the discharge current (I_{ch}), a resistive voltage divider and a current transformer were utilized as shown in Fig. 1, the waveforms of which were recorded by a digitizing oscilloscope. In addition, to record the breakdown voltages (V_b) for each shot, maximal values of V_{ch} for each shot were AD converted and recorded on a personal computer. For the analysis of filling gas after the operation, quadrapole mass spectrometer (QMS) was utilized.

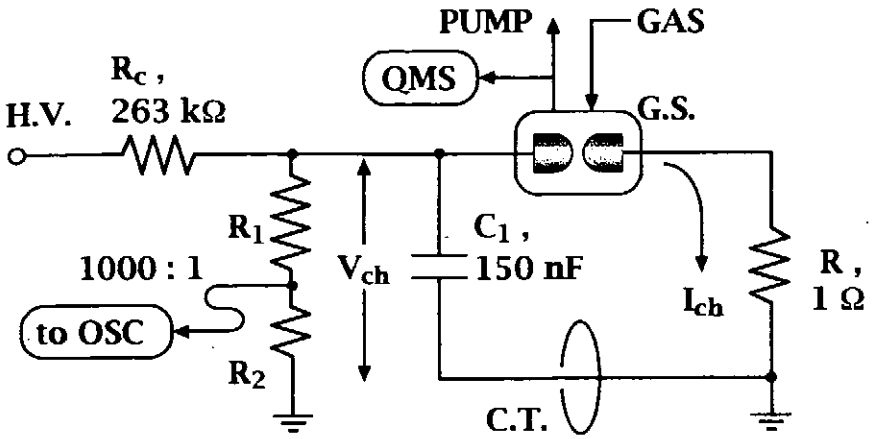

Fig.1. Experimental circuit.

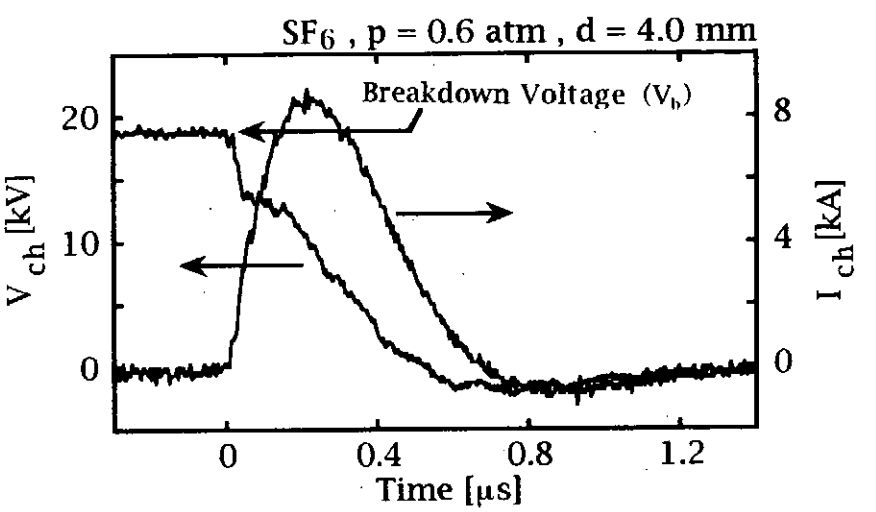

Fig.2. Typical wave forms of V_{ch} and I_{ch}.

3. Experimental results

Figure 2 shows the typical waveforms of V_{ch} and I_{ch} when V_b = 19 kV. Peak current of 9 kA is observed with pulse duration 400 ns (Full Width at Half-Maximum, FWHM). The waveform was almost similar for each condition in the experiment.

Figure 3 shows the dependence of V_b on the shot number with frequency distribution

of V_b when using SF_6. The V_b is normalized by the initial value of V_b (V_{b0}). As seen in the figure, for seal off condition (Fig. 3 (a)) V_b increases with increasing the number of shot. In addition, scattering of V_b also increases with increasing shots. In contrast, in the gas flow condition average value of V_b and the scattering of V_b have no dependence on the shot number. This result suggests the change of gas composition changes in the sealed off condition, which affected the breakdown voltage. In the gas flow condition the scattering of V_b in the initial stage is larger than that of sealed off condition. This may be due to that circulation of the gas flying up the dust in the vessel of the switch. In addition, for very few shots (in the order of 0.1 % of total shots) we see extremely low values of V_b (around 60 % of V_{b0}) in both conditions.

Figure 4 shows the results when using H_2. In contrast to the case of using SF_6, the average value of V_b is almost constant and has no dependence on the shot number. The scattering of V_b tend to decrease with increasing shots in the seal off condition (Fig. 4 (a)). The distribution of V_b has two component, very narrow distribution around V_{b0} and relatively wide distribution around 5-10 % below V_{b0}. For gas flow condition (Fig. 4 (b)) the tendency is almost same as Fig. 4 (a) however, the width of the distribution of V_b is larger and it doesn't decrease with increasing shots.

After the shots we see that the electrodes were heavily covered with white materials in both condition when using SF_6, whereas in the case of using H_2, electrodes were slightly covered with black materials.

To clarify the cause of the increase of the scattering of V_b in the seal off condition of SF_6 shown in Fig. 3 (a), gas was exchanged in every 2000 shot. The result is shown in Fig. 5. In the case, V_b recovers to the initial value (V_{b0}) just after the exchange of the gas, however, the increase of the scattering of V_b becomes rapid when total shot number is larger. This result suggests that the increase of the scattering of V_b is caused both by the change of the quality of the gas and the deposition of the materials on the electrodes.

Same experiment was done for the case of using H_2, the result is shown in Fig. 6. In contrast to the case of using SF_6, the change of the distribution of V_b is not observed when the gas is exchanged. This result suggests that change of the quality of the gas dos not occurs when using H_2.

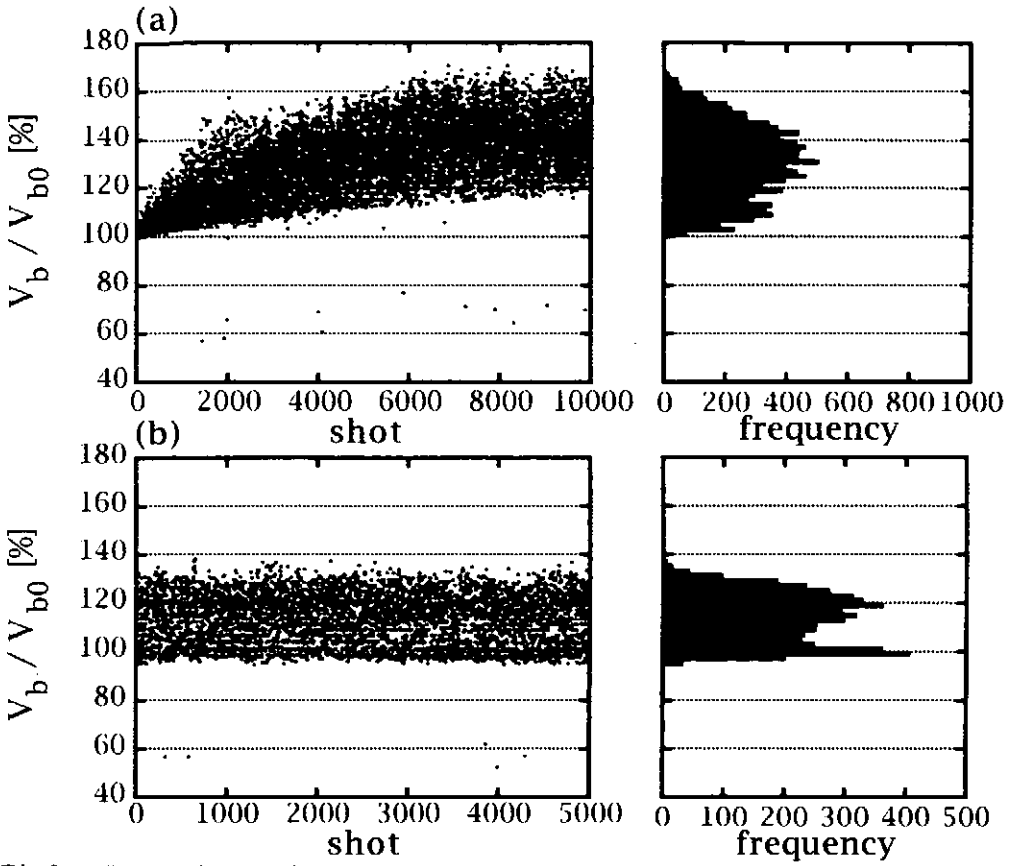

Fig.3. Dependence of V_b on the shot number with frequency profiles when using SF_6.
(a) seal off condition. (b) gas flow conditon.

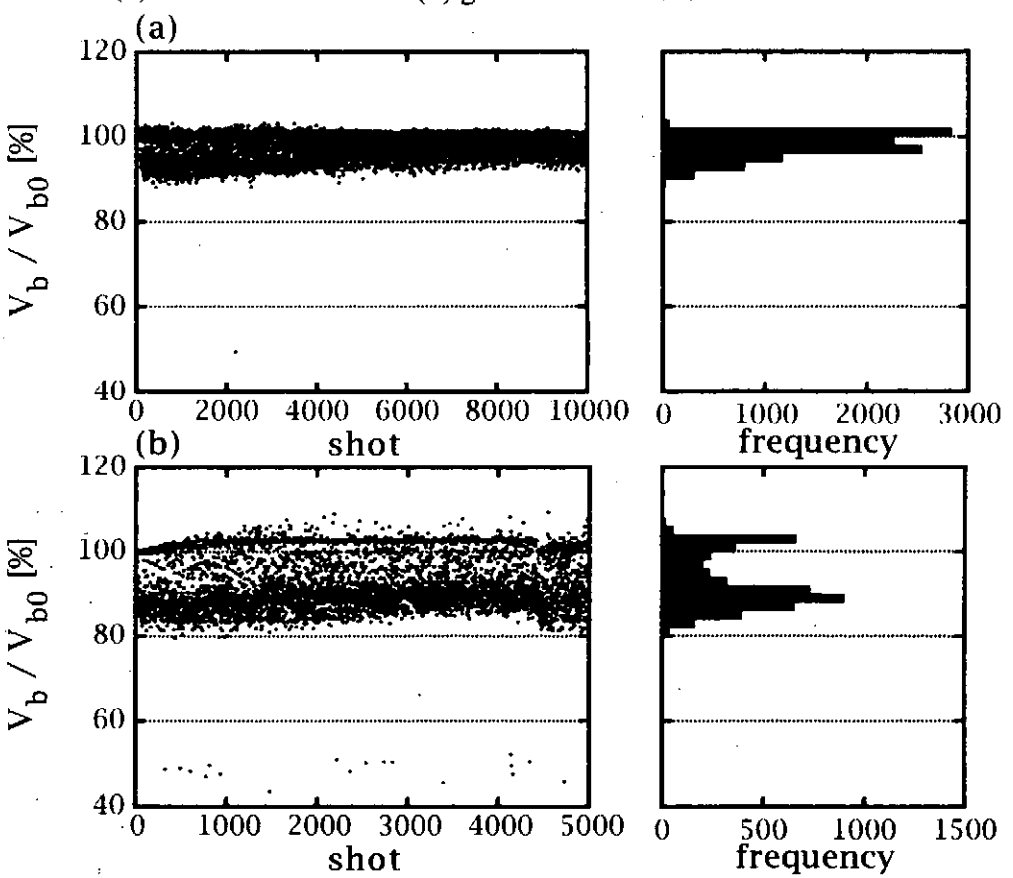

Fig.4. Dependence of V_b on the shot number with frequency profiles when using H_2.
(a) seal off condition. (b) gas flow conditon.

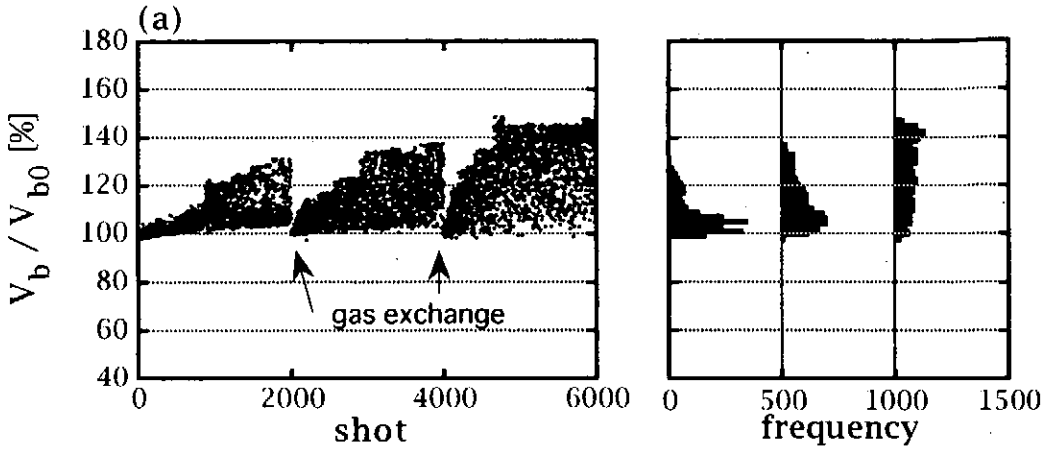

Fig.5. V_b - shot number characteristiscs with frequncy profile.
Filling gas of SF_6 is exchangedevery 2000 shot.

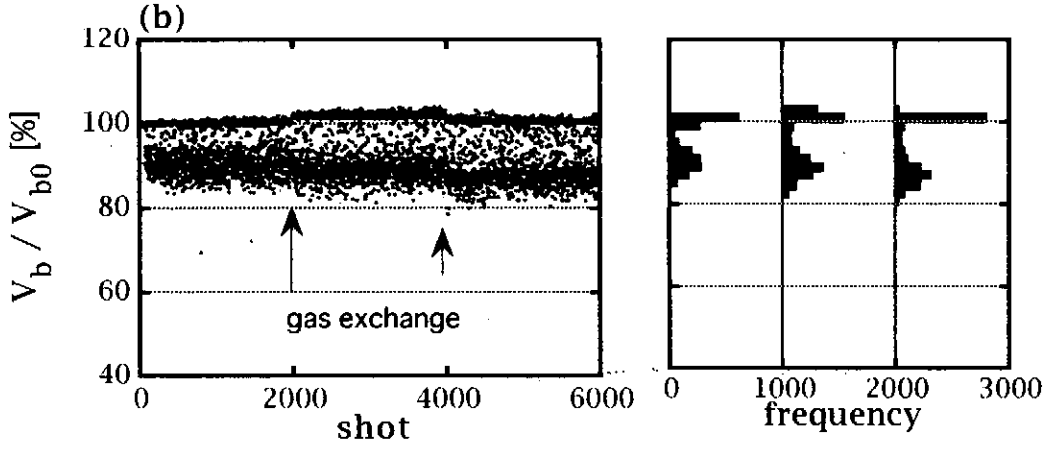

Fig.6. V_b - shot number characteristiscs with frequncy profile.
Filling gas of H_2 is exchangedevery 2000 shot.

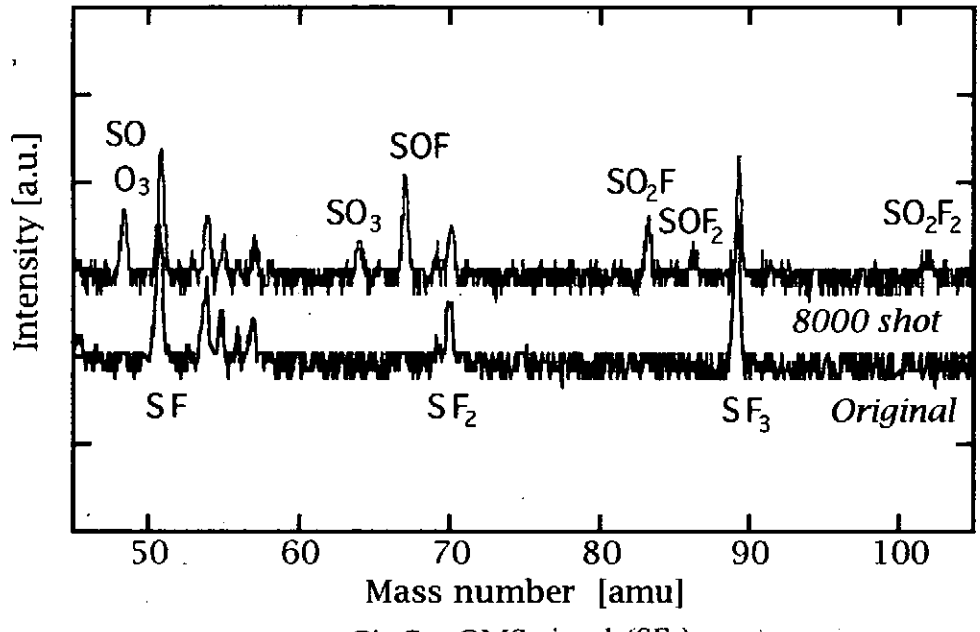

Fig.7. QMS signal. (SF_6)

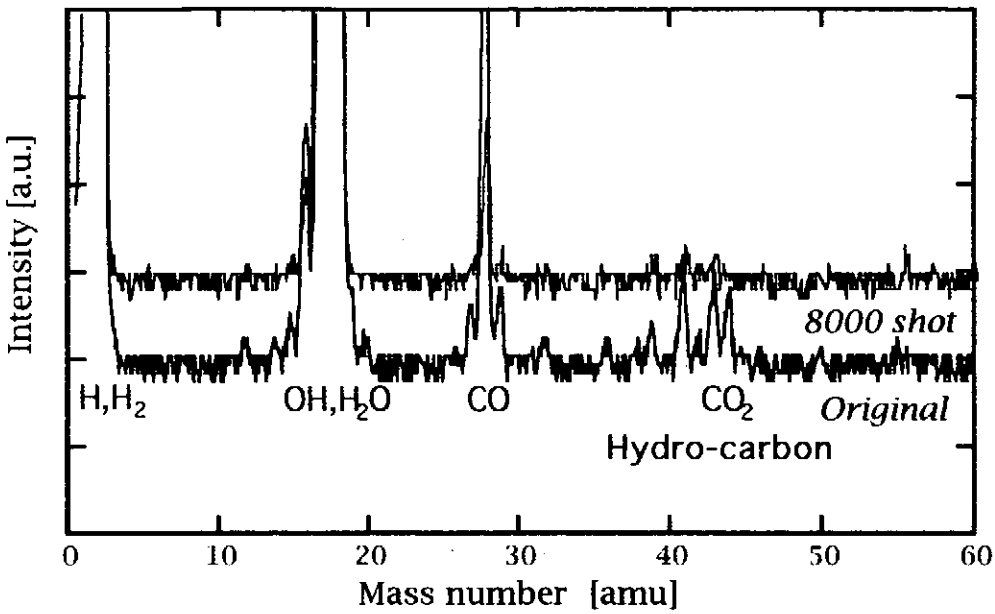

Fig.8. QMS signal. (H_2)

Figure 7 shows the results of QMS analysis of the discharge gas before and after 8000 shots of operation under the seal off condition of SF_6. As seen in the figure, after the shots new molecules of mass numbers 48, 64, 66, 83, 86 and 102 are observed, which correspond to the molecules of O_3, SO_3, SOF, SO_2F, SO_2F_2, respectively. Since oxygen was not introduced into the switch, it seems to be originated from the absorbed gas on the electrode or on the plastic vessel of the gap switch.

Figure 8 show the QMS data when using H_2 gas after 8000 shot of operation in the sealed off condition of H_2. In the case impurities such as OH, H_2O, CO, CO_2 are observed before and after the operation and new molecular was not observed in the data.

To identify the deposited material on the electrode when SF_6 gas is used, we collected it by scrubbing a fine SUS mesh on the electrode. After that the mesh was inspected by an X-ray diffraction meter (XRD). Figure 9 shows the results of the measurement. As seen in the figure number of peaks are observed. Among them, a peak at 29 degree is identified to be CuF_2, which seems to be produced by the reaction between the dissociated florin with electrode material.[5,6] Figure 10 shows the XRD pattern when using H_2. As seen in the figure no peak was observed expect for the small peak of ZnO.

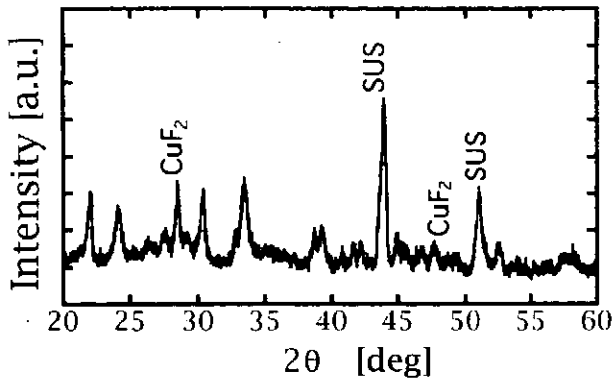

Fig.9. XRD pattern of matelial on the deposited electrodes. (SF_6)

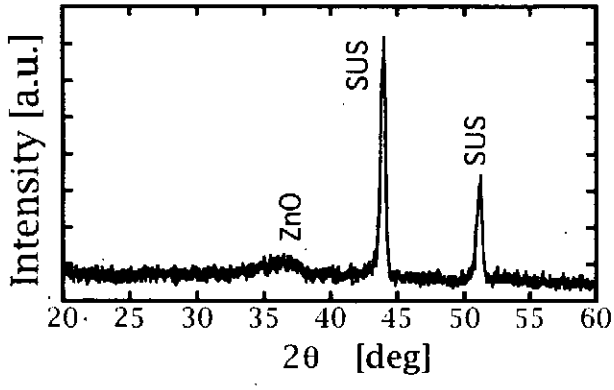

Fig.10. XRD pattern of matelial on the deposited electrodes. (H_2)

4. Conclusion

Characteristics of repetitively operated high-current discharge gap switches are investigated and obtained the following results.

1. When using SF_6 gas in the seal off condition V_b and the scattering of V_b increases with increasing shot number whereas both have no dependence on the shot number in the gas flow condition.
2. When using H_2 gas in the seal off condition the average value of V_b is almost constant and the scattering of V_b decreases with increasing shot number.
3. In the seal off and gas flow condition of H_2 the distribution of V_b has two component, i.e., around the V_{b0} and 5-15 % below V_{b0}, the width of the latter component is larger in the gas flow condition.
4. After the operation new molecules were observed in the SF_6 discharge whereas no new molecule was produced in H_2 discharges.

References

1) A. Nation: Particle accelerators **10** (1979) 1.

2) C. Martin: Proc. IEEE **80** (1992) 934.

3) L. Moran and L. W. Hardesty: IEEE Trans. Electron Devices **38** (1991) 726 .

4) K. Masugata, H. Maekawa, M. Yoshida, T. Ishii, T. Suzuki, K. Yatsui: Jpn. J. of Appl. Phys. **35** (10) (1996) 5487.

5) M. Yumoto, H. Iida, and T. Sakai: "Formation Process of SF_6 gas Decomposition Product and its Effects on Breakdown Voltage", The trans. of IEE of Japan **A105** (8) (1986) 437. (in Japanese)

6) K. Masugata, T. Suzuki, N. Nakayama, K. Takao and K. Yatsui, "Characteristics of high current pulsed discharge" Proc. 1st Asia-Pacific Int'l Symp. on the Basic and Applications of Plasma Technology, (National Yunlin Univ. of Sci. & Tech., Touliu, Taiwan, R.O.C., December 15-16, 1997) pp.71-74 (1997)

MODELING AND PARTICLE SIMULATIONS OF MAGNETICALLY INSULATED TRANSMISSION LINES WITH CROSS SECTIONAL CHANGES

Kazuki HIRAOKA, Mitsuo NAKAJIMA, Kazuhiko HORIOKA and Makoto Shiho*

Department of Energy Sciences, Tokyo Institute of Technology
Nagatsutacho 4259, Midori-ku Yokohama, Japan 226-0026
**Japan Atomic Energy Resaerch Institute*
Tokai-mura, Ibaraki, Japan 319-11

ABSTRACT

In order to discuss the power transportation through the high power MITLs (Magnetically Insulated Transmission Lines), we have modified the equivalent circuit model. Typical results show that our model can describe the pulse front velocity and effective impedance fairly well. The ratio of space charge current versus total current qualitatively agrees well. When the MITL has an abrupt geometrical change, this model is thought not to work well. Validity of the model is estimating by comparing the results with those of the particle-in-cell simulation (PIC). Subsequently, we study the stability of space-charge electron flow in the gaps by the PIC simulation.

1. INTRODUCTION

The Magnetically Insulated Transmission Line (MITL, Fig.1) insulates the field emitted electrons with self magnetic field and can transport multi-terawatt electromagnetic pulse. Thinking of TEM mode in vacuum, the magnitude of Poynting vector (power density) is propotional to the square of electric field, therefore high electric fields are inevitable to high power transportation. Such strong fields over 0.2MV/cm^2 cause field emission of electrons from the cathode and cause large losses of current. Consequently MITLs are necessarily needed for efficient high power EM power transportation[1),2)].

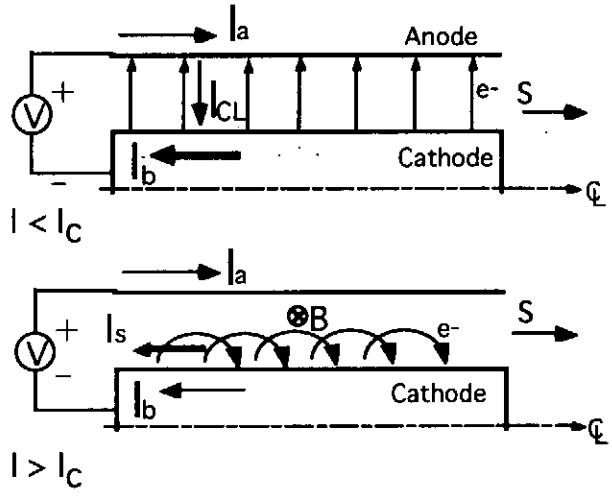

Fig.1 Schematic diagram of MITL. When the current I is smaller than critical value Ic, the Child-Langmuir current flow across the gap, and once I is become larger than Ic, electrons are insulated from reaching the anode.

As a characteristic of the MITLs, presence of space-charge electron current is important. Electrons emitted from cathode move toward output side and carry charges, thus current flows in space-charge electron layer. The ra-

tio of this space-charge current to total current is up to about 50%[3),4)] and varies as a function of local voltage and current level. However, the space-charge electrons in the gap considerably reduce the effective inductance and increase the effective capacitance from the vacuum values. These value should be self-consistently decided from the local electric and magnetic field. So these non-linear effects are essential for analyses of the high power transport in vacuum.

In the design and parametric analysis of MITLs, the equivalent circuit modeling[5)] is widely used. It can describe the generator, MITL and load by a single network consist of liner circuit components, so interaction of these components can be easily discussed. MITL part of this model is expressed by a ladder-shaped circuit. In the conventional circuit, the vacuum inductance and capacitance are used in spite of the presence of space charge fields.

By using PIC (Particle-in-cell) simulation, we can estimate these effects. However, PIC traces individual particles, therefore it is not easy to evaluate the geometrical influences on current, voltage and power flow. In addition, PIC code needs a large amount of memory and computer time, so the survey for optimization of the power transport efficiency over a wide range of parameter is troublesome and very difficult task. Subsequently, flow impedance model is developed, recently[6),7)]. This model obtains a profile function of current density from a series of PIC simulation results. Although this method greatly simplifies the simulation process, it still needs the semi-empirical profile function in advance.

Consequently, we have developed a new equivalent circuit model including space-charge flow[8)]. This model uses space-charge current profile of relativistic Brillouin theory (or laminar flow theory). This theory give very similar results for cases the boudary current is sufficiently large to keep magnetic insulation.[9)] As shown later, validity of this circuit model is confirmed by comparing the results with those of PIC.

However, when the MITL has too rapid geometrical change, the laminar flow approximation is not necessarily valid. The characteristics of space-charge electron flow has been investigated in parallel coaxiall lines or gentle taper. So the behavior of the flow at rapid geometry is not studied well. In order to specify the applicability of this model and reveal the behavior of the flow, we use PIC simulation.

2. EQUIVALENT CIRCUIT MODEL

Fig.2 shows our modified equivalent circuit model of MITL. In our modeling, we assume that once magnetic insulation is established ($I > I_c$), the equivalent circuit (a) is replaced by modified circuit (b) that has space charge current path. Here, I_c is the critical current and G is the conductance of space charge limited current flows across the vacuum gap. The effect of space charge electron is expressed by effective inductance L, mutual inductance M, and capacitance C. To determine these

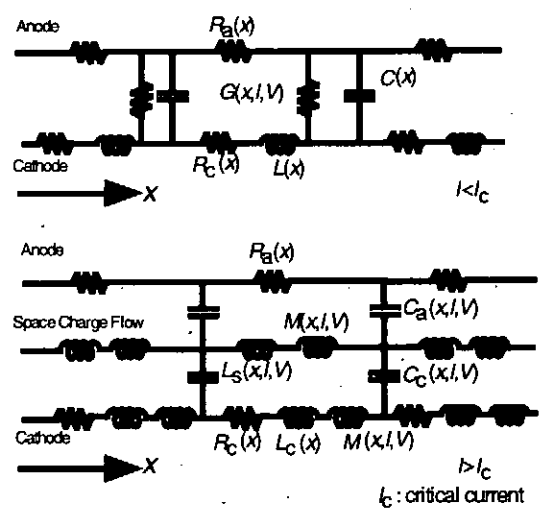

Fig.2 Modified equivalent circuit of MITL.

values analytically, we use laminar flow theory[9),10)]. In this theory, solutions for potential, charge density distribution, fraction of the current carried by the space charge, and radius of the space-charge layer are obtained self-consistently as follows,

$$I = \frac{I_\alpha}{\ln\left(\frac{r_a}{r_c}\right)}\gamma_m \cdot \left[\ln\left(\gamma_m + \sqrt{\gamma_m^2 - 1}\right) + \frac{\gamma_0 - \gamma_m}{\sqrt{\gamma_m^2 - 1}}\right] \quad (1)$$

$$i(r) = \frac{I}{\gamma_m}\cosh\left(\frac{I}{I_\alpha \gamma_m}\ln\frac{r}{r_c}\right) \quad (2)$$

$$I_b = \frac{I}{\gamma_m} \quad (3)$$

$$r_b = \exp\left(\ln r_a - \frac{\gamma_0 - \gamma_m}{\sqrt{\gamma_m^2 - 1}}\frac{I_\alpha \gamma_m}{I}\right). \quad (4)$$

Here, $I\alpha$=8500(A) is Alfven current, I is the total (anode) current, I_b is conduction (boundary) current on the cathode, γ=1+eV/m_0c^2 is relativistic weighting factor and subscripts 0 and m represent at anode and maximum extent of the space-charge layer. r is the radius and subscripts a, b and c represnt at anode, the edge of space-charge flow and cathode(see Fig.3). With these functions, effective value of L, M and C are evaluated.

Validity of the model is confirmed by comparing the results with those of the particle-in-cell simulation and with analytical estimations. As Fig.4 shows, typical results of PIC show that our model can describe the pulse front velocity (about 80% of light speed) and effective impedance (78% of vacuum impedance, before the pulse returns) fairly well. The ratio of space charge current versus total current is as follows: in our model, it is 56% before the pulse returns and 6.3% after the pulse returns, in the PIC, 67% and 7.7% respectively. Here, the MITL is straight 2m long line, line impedance is 24.3Ω, load impedance is 7Ω, and applied voltage is 10MV.

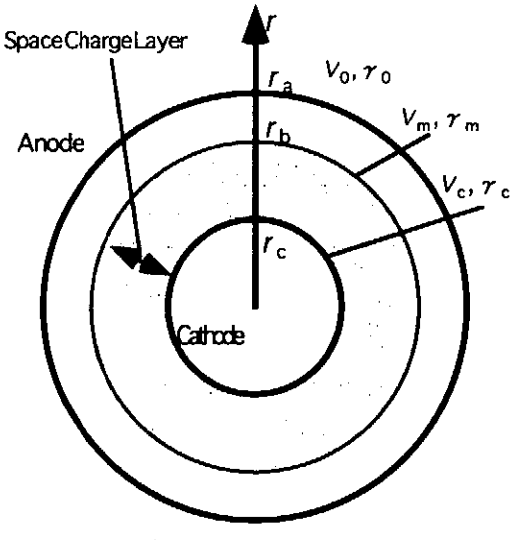

Fig.3 Schematic diagram of cross section of the MITL in magnetical insulation mode.

Fig.5 shows example of a gentle tapered line with the modified model(a) and the normal model(b). The upper graphs represent input side and the bottom output. The characteristic impedance changes from 28.2Ω at imput side to 15.7Ω at output side and load is matching condition. At the input side signal, piled reflected wave is observed in the front triangler region, and as the ratio of voltage to current shrinks, fraction of the space-charge current gets smaller.

In comparing our model with the conventional model, wave forms are similar but effective impedances(V/I) are reduced. These results are all reasonable.

Fig.6 shows the case that MITL has an abrupt geometrical change in the middle of the line, and (a) is the result of of PIC and (b) is our model. In this case, currents at the down-stream side of the slope do not agree between (a) and (b). Especially the value of total current is deffernt. As previously mentioned, this is probably because of laminar flow approximation.

3. PARTICLE SIMULATION

Subsequently, we study the behavior of electron-flow in the gap between the electrodes of MITLs by the PIC simulation. We investigate the condition that how rapid geometry cause disagreement with PIC, and determine the limit of application of our model. Furthermore, we will study the general characteristics of electron flow including flow stability and electron distribution profile, in such steep shaped MITLs or magnetically insulated diodes.

Here we use TS2 module of MAFIA program package. MAFIA is interactive programs for the computation of electromagnetic fields. It is based on theory of discrete Maxwell grid equations, the finite integration technique. TS2 module is a 2-dimentional PIC code which solves fully selfconsistent Maxwell's equations and equations of motion in time domain. A cylindrical symmetric coordinate system (r,z) is used.

Fig.7 shows the example of results from our first calculation. As a test case, 1m long tapered MITL is simulated. The characteristic impedance changes from 10.9Ω to 41.6Ω toward output side. Fig.7(a) shows the case magnetical insulation is achieved(applied voltage is 6000kV) and (b) shows not achieved(600kV). In figure (a) we can see electrons stay in cathode-side region by magnetic insulation although in (b) electrons reach to the anode. Because this calculation has not adjusted yet, the number of particles is few, so farther optimization is needed.

4. CONCLUDING REMARKS

We have developed an equivalent circuit model of MITLs which includes space charge effects. This model can be used for estimating influences of space-charge electrons on power flow and design works of high power MITLs. With PIC simulation, we are investigating the applicability of this model and the general characteristics of electron flow.

REFERENCES

1) K. Horioka, K. Hiraoka, M. Nakajima and T. Aoki: *NIFS-PROC-23* (1994) p.118.

2) M. S. Di Capua: *IEEE TRANSACTIONS ON PLASMA SCIENCE PS-11* (1983) No.3, p.205.

3) J. T. Crow and G. D. Peterson: *IEEE TRANSACTIONS ON PLASMA SCIENCE PS-11* (1983) No.3, p.219.

4) M. S. Di Capua and D. G. Pellinen: J. Appl. Phys. **50** (1979) No.5, 3713.

5) K. D. Bergeron: J. Appl. Phys. **48** (1977) No.7, 3065.
6) C. W. Mendel Jr. and S. E. Rosenthal: *Proc. 10th Int. Conf. High Power Particle Beams* (1994) p.276.
7) C. W. Mendel Jr. and S. E. Rosenthal: Phys. Plasmas **2** (1995) No.4, 1332.
8) K. Hiraoka, M. Nakajima and K. Horioka: *Proc. 11th Int. Conf. High Power Particle Beams* (1996) p.1022.
9) John M. Creedon: J. Appl. Phys. **48** (1977) No.3, 1070.
10) John M. Creedon: J. Appl. Phys. **46** (1975) No.7, 2946.

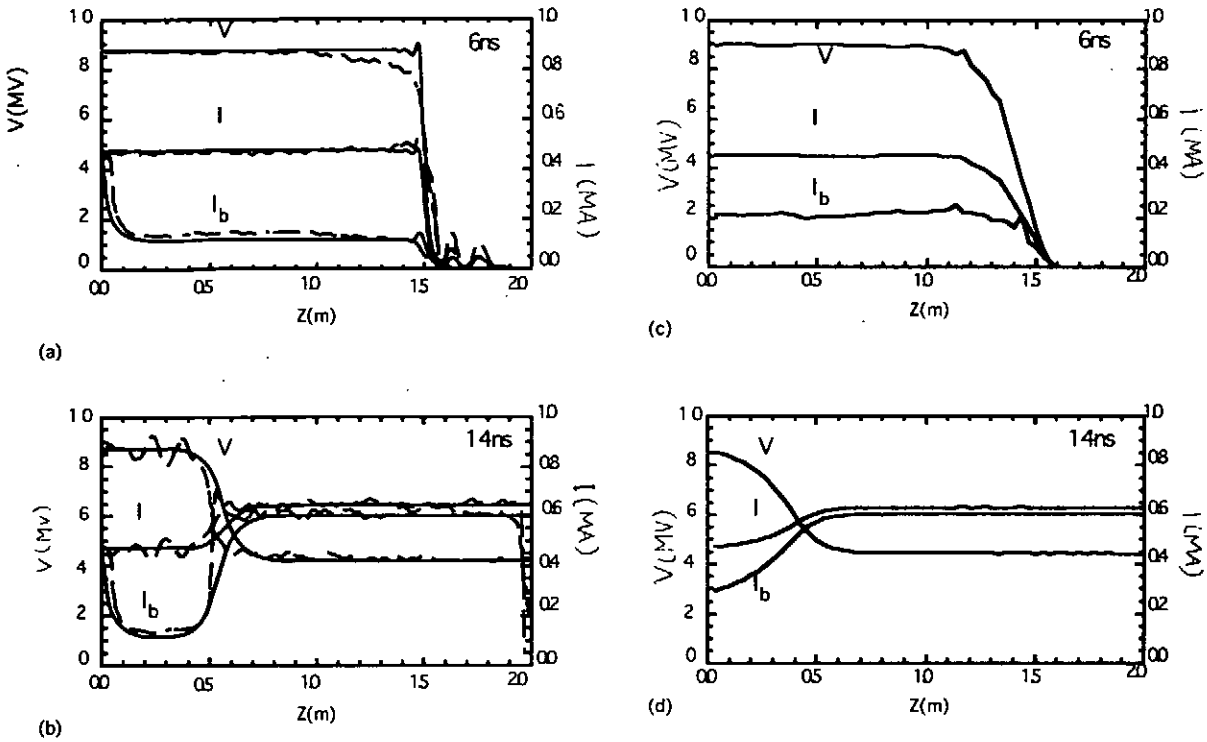

Fig.4 (a),(b) PIC(dashed) and Flow Impedance model(solid) and (c),(d)the model caluculations for a step voltage in a 24.3Ω, 2m long MITL.

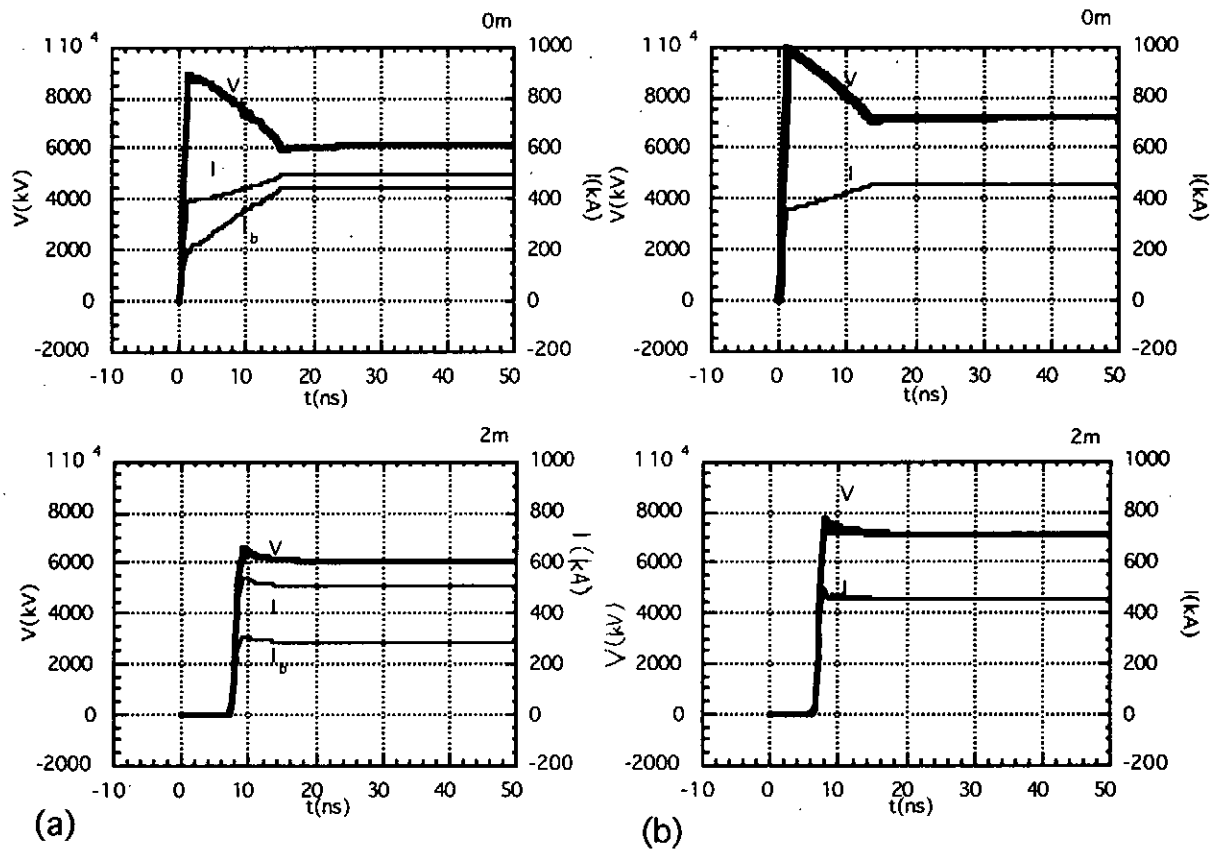

Fig.5 Results of calculation by equivalent circuit of tapered MITL. (a):our model (b):normal model

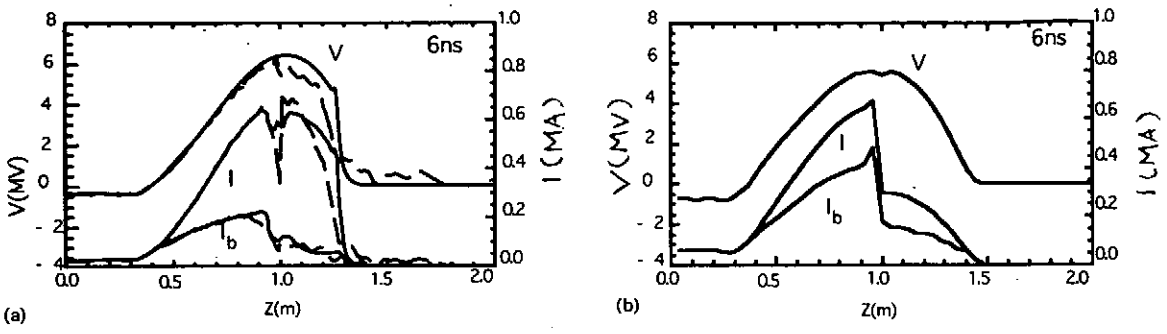

Fig.6 (a)PIC(dashed) and Flow Impedance model(solid) and (b)the model caluculations for a 5ns wide pulse traveling down a MITL that begins at 11.9 Ω and changes abruptly to 24.3 Ω at the middle of the 2m long line.

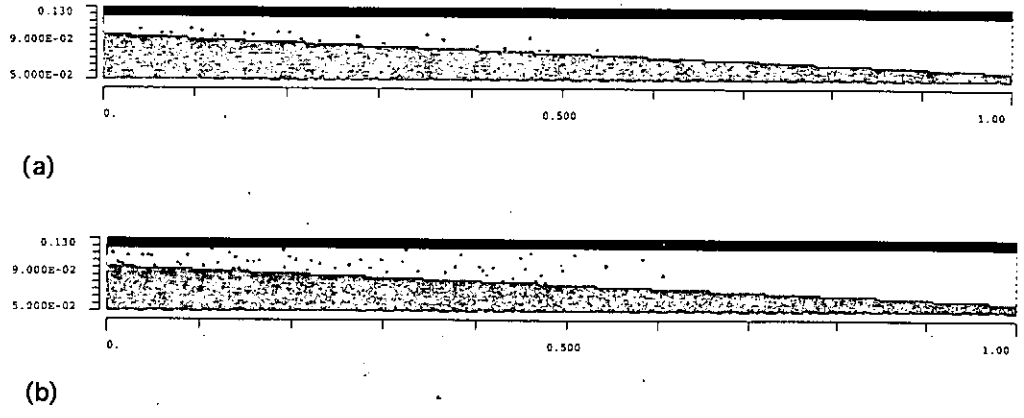

Fig.7 Results of calculations by MAFIA. (a) In magnetic insulation mode (b) Magnetic insulation is not achieved

MEASUREMENT OF STRONG LANGMUIR TURBULENCE FIELDS USING AN ELECTRON BEAM PROBE

Ritoku Ando, Shingo Taniguchi, Haruhisa Koguchi,* Keiichi Kamada, and Masaru Masuzaki

Faculty of Science, Kanazawa University, Kanazawa 920-1192, Japan

Abstract

A study of IREB-driven strong Langmuir turbulence fields in a plasma after the IREB passes through the plasma was carried out by measuring deflection of a weak low-energy electron probe beam injected across the plasma. The result indicates that turbulent electric fields last even ~ 900 ns after the IREB passes through the plasma. Although quantitative result has not been obtained yet, this result agrees with the previous result of spectroscopic measurement that strong fields lasted for much longer time than 300 ns.

1. Introduction

Theories and numerical simulations[1] have shown that the cavitons are formed in a plasma if large amplitude Langmuir waves are excited. Cavitons are defined as spatially localized volumes with density depletion in which large amplitude electrostatic fields are trapped. Such a state, which has been referred to as the strong Langmuir turbulence state, can be driven by injection of an intense relativistic electron beam (IREB) into a plasma. Our previous experiment showed that high frequency strong electric fields with Gaussian distribution existed in the plasma.[2] The fields lasted for much longer time than 300 nsec after the IREB passed through the plasma.

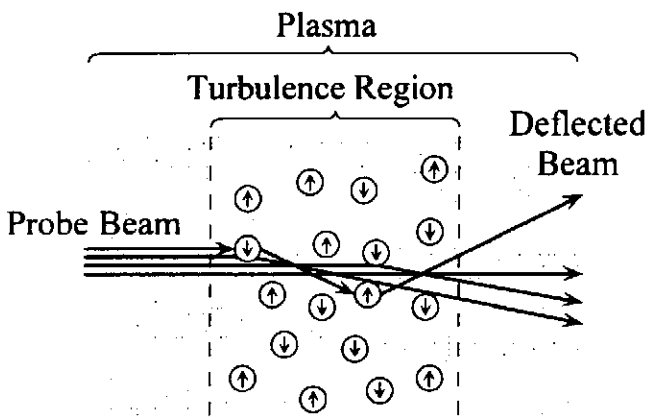

Fig. 1 A model used for an estimation of the deflection of the electron beam probe by turbulent plasma.

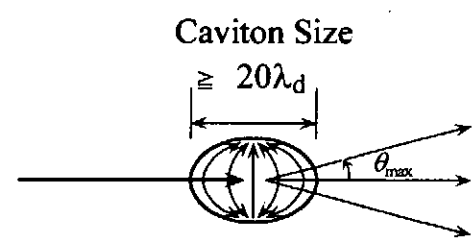

Fig. 2 Caviton size is assumed to be 20 Debye-lengths in the estimation.

* Present address: *Electrotechnical Laboratory, Tsukuba 305-0045, Japan*

The return current vanished out in a shorter time. Other data indicate that the cavitons play an important role for IREB scattering,[3] for background plasma heating,[4] and for generation of broadband microwaves.[5]

Table 1 Estimated scattering angles for various energies of probe-electron.

Probe Electron Energy [keV]	Scattering Angle θ max [deg]
5	29°
10	16°
50	3.3°
100	1.7°

Studies of the high frequency strong fields after the IREB passes through the plasma are being carried out by measuring deflection of a weak low-energy electron beam (probe beam) injected across the plasma. In absence of a longitudinal static magnetic field, the probe beam can pass through the plasma without deflection, if no Langmuir turbulence fields remain in the plasma. Rough estimation was carried out on a deflection angle of the probe beam due to turbulence fields. The model used for the estimation is shown in Fig. 1 and Fig. 2. The estimation was based on the data obtained in a previous experiment [2] that the strong field regions occupied a few percent of the plasma volume and that the typical field strength was 50 kV/cm. By assuming the caviton size to be 0.9 mm, which is 20 Debye-lengths, the number density of cavitons was estimated to be 8.8 cm^{-3}, the probability for a probe beam electron to collide with cavitons to be about 1.1, and the deflection angle to be from -3.3 to 3.3 deg. for probe beam energy of 50 keV. Table 1 shows scattering angles of a probe electron which are estimated for various acceleration energies, assuming that the strong field regions occupy 0.6% of the plasma volume. We determined to employ a 50 keV beam for the probe because its scattering angle was suitable for measurement.

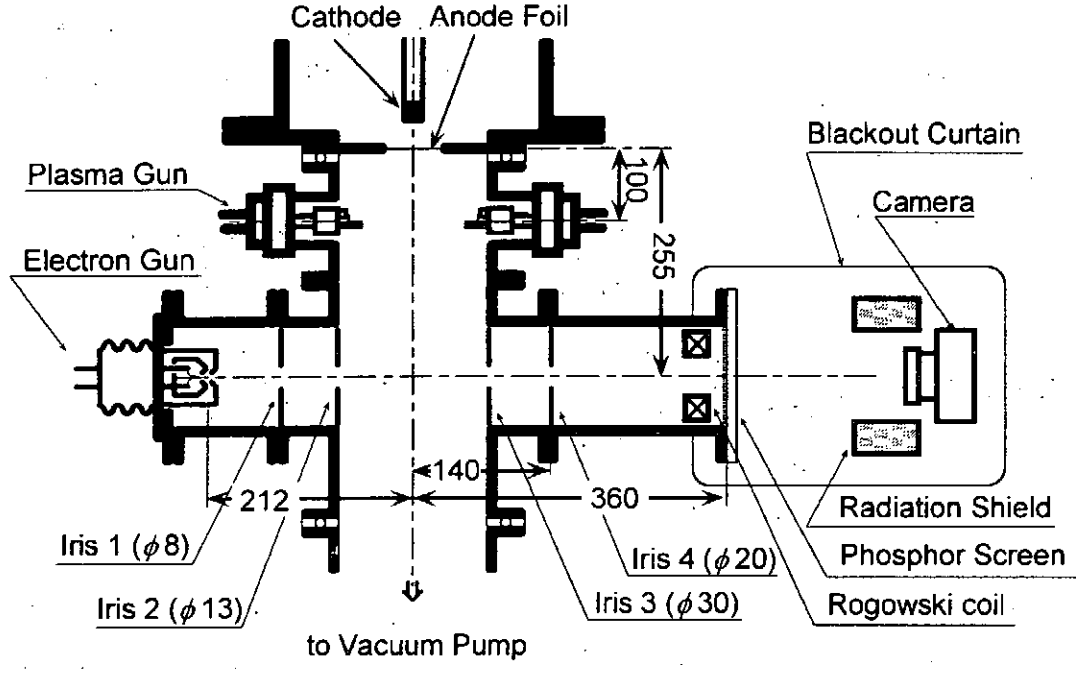

Fig. 3 Experimental apparatus for the IREB-plasma interaction. Probe beam was injected transversely to the aixs of the main chamber at 25.5 cm downstream from the anode foil of the IREB diode.

2. Experimental Setup

The setup of the experimental apparatus is shown in Fig. 3. An IREB source gave a pulse of 1.5 MeV, 30 kA, and 30 nsec into a matched load. A drift chamber of 16 cm in diameter and 60 cm long was served as an interaction space. A plasma was produced with a couple of rail type guns, which were set opposite to each other at 10 cm downstream from the anode foil. The chamber was filled up with the plasma in ~ 12 μsec after the discharge of the plasma guns. The plasma density was changed by changing the delay time, τ, of injection of IREB from the beginning of the discharge of the plasma guns. The plasma density range in the experiment was from 10^{12} to 10^{13} cm^{-3}. The IREB was injected into the plasma through a thin anode foil, titanium foil of 20 μm, which separated the IREB diode from the plasma. The electron density ratio of the IREB to the target plasma, n_b/n_p, was varied from 0.001 to 0.1. The IREB current in the interaction region was about 10 kA, and the beam diameter was about 8 cm.[6]

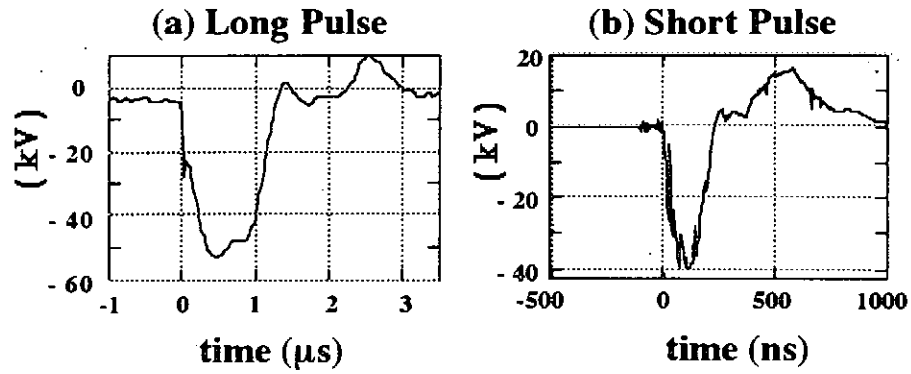

Fig. 4 Voltage pulses applied to the electron gun for the probe beam. (a) long pulse: ~ 1 μs , (b) Short pulse: ~ 200 nsec.

A short-focus electron gun with a conical grid and a hairpin-type cathode was used for the probe beam source. The acceleration pulse voltage for the probe beam was 30 - 50 kV, as seen in Fig. 4 (a) and (b). The probe beam was injected across the plasma at 25.5 cm downstream from the anode foil. The probe beam was detected with a phosphor screen and its luminescence was photographed. The total path length of the probe beam was 57 cm. A Rogowski coil was set just in front of the phosphor screen. Diaphragms were set on the probe beam path at both sides of the plasma column, the detector side and the

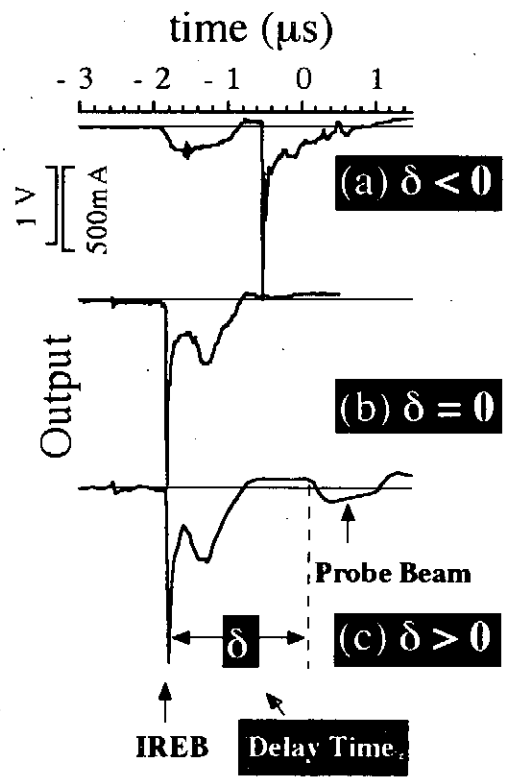

Fig. 5 Output sygnals from a Rogowski coil which was set at just in front of the screen. δ is taken as a parameter. (a) $\delta < 0$, (b) $\delta = 0$, (c) $\delta > 0$.

electron gun side, to prevent influx of plasma and beam electrons from the drift chamber. The diameter of the undeflected probe beam was ~ 2.5 cm at the screen position. The probe beam diverged slightly. The deflection angle that can be detected in this system was limited by size of apertures on diaphragms. The maximum deflection angle was expected to be about 4.1 deg. for this system. The phosphor screen was coated with carbon on the phosphor to obstruct the lights from the filament of the probe beam gun and from the plasma. The coated screen also rejected the electron influx which had energies less than ~ 30 keV.

3. Results

Time interval between the injection of the IREB and that of the beam probe was taken as a parameter, δ. Output signals of the Rogowski coil are shown in Fig. 5 for different δ's, which are sum of the probe beam current and fluxes of the IREB and the plasma electrons. The pulse length of the probe beam was ~ 1 μsec, and the beam current was ~ 100 mA in this case. A square

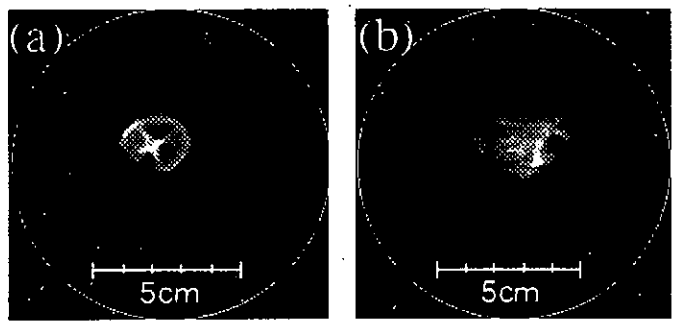

Fig. 6 Samples of the beam pattern without deflection and that with deflection; (a) $\delta = 0.45$ μs, (b) $\delta = -0.12$ μs. Probe pulse length was ~1 μs.

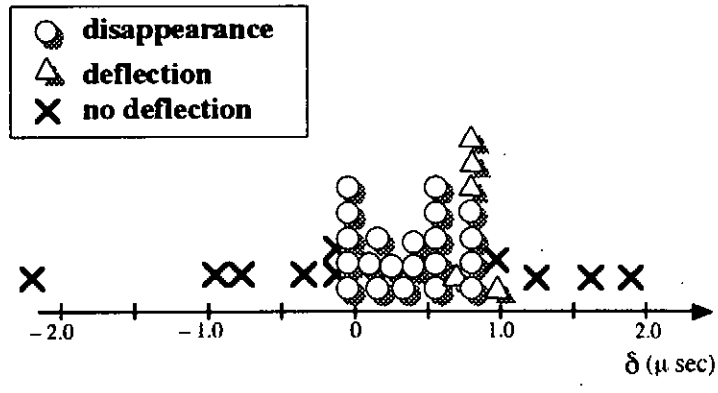

Fig. 7 Appearance of the beam pattern versus δ. A circle indicates the shot with disappearance of the beam pattern. A triangle and a cross indicate the shot with deflection and the shot without deflection of the probe beam, respectively.

pulse on the signals corresponds to the beam probe current. Sudden increase of the current is observed at the injection time of the IREB. The IREB pulse length is very short in this scale. So the increase of the current is thought to be due to increase of the electron flux owing to temperature rise in the plasma caused by heating by the IREB.

The probe beam did not deflect when it was injected into vacuum, into the plasma without the IREB injection, and into the IREB propagating in vacuum. It deflected when $\delta \approx 0$ or $\delta > 0$ for both long and short pulse probe beams. Examples of the beam pattern with deflection and without deflection are shown in Fig. 6 (a) and (b), respectively. In these cases the pulse length of the beam probe was ~ 1 μs. The change of the beam pattern was investigated at the plasma density $n_p = 4.6 \times 10^{12}$ cm^{-3} ($\tau = 30$ μs). The pulse length of the probe beam was ~ 200 nsec, and the beam current was ~ 50 mA in this case. The beam pattern disappeared or broadened when δ was short. This disappearance is thought to be due to larger deflection angle than the maximum deflection angle of 4.1 degrees. Figure 7 shows number of shots in which the probe beam pattern disappeared or broadened versus δ. The beam disappearance or broadening was observed only for -100 nsec < δ < 800 nsec. This result indicates that turbulent electric fields last even ~ 900 ns after the IREB passes through the plasma. Although quantitative result has not been obtained yet, it agrees with the former spectroscopic result that strong fields lasted for much longer time than 300 ns.

4. Discussion and Concluding Remark

The deflection angle estimated under the assumption that the probe beam is deflected by caviton fields was about 3.3 degrees. The observed deflection angles of the probe beam were almost the same as the estimated one, or larger than 4.1 deg. when the beam patterns disappeared. Generally the deflection angle would be in proportion to the electric-field strength and its scale. It would also be affected by phase-coherence of the fields on the path of the probe beam. In the IREB-plasma system large amplitude Langmuir waves are excited and finally the plasma becomes a strong Langmuir turbulence state. A detailed argument has been carried out on a statistical distribution of the high frequency electric fields of Langmuir turbulence.[1] From simulation there are two clearly distinguishable components of the turbulence; (i) localized, coherent wave packets, which have high fields and short scales and (ii) background incoherent waves, which have low fields and longer scales. The knowledge on strength of the latter waves in a system must be important, because these waves may also contribute to the deflection of the probe beam.

A lot of theories and simulations treat steady states today. However, the subject of our study is the behavior of the electric fields after the IREB passes through the plasma. The energy source is terminated under this condition. Naturally the wave distribution in k-space will be change from the steadily driven system. Further experimental study is being carried out to make more clear the fields after IREB passes through the plasma.

References

[1] P. A. Robinson, 'Nonlinear wave collapse and strong turbulence', Rev. Mod. Phys., **69** (1997) pp. 507-573.

[2] Y. Yoshikawa, M. Masuzaki, R. Ando, 'Spectroscopic measurement of intense relativistic electron beam driven turbulence', J. Phys. Soc. Jpn., **63** (1994) pp. 3303-3310.

[3] H. Koguchi, M. Masuzaki, R. Ando, K. Kamada, 'Beam energy distribution and perpendicular velocity scattering', to be published in J. Phys. Soc. Jpn.

[4] M. Yoshikawa, M. Masuzaki, R. Ando, K. Kamada, 'Correlation between high-power broadband microwave radiation an strong Langmuir turbulence in an intense relativistic electron beam-plasma system', J. Phys. Soc. Jpn., **65** (1996) pp. 2081-2086.

[5] M. Masuzaki, H. Yoshida, R. Ando, K. Kamada, A. Ikeda, C. Y. Lee, M. Kawada, 'Broadband mm radiation from beam driven strong turbulence', *Proc. of 11th Intern. Conf. on High-Power Particle Beams* (ISBN 80-902250-3-9, 1996), Vol. 1, pp. 339-342.

[6] R. Ando, M. Masuzaki, H. Morita, K. Kobayashi, M. Yoshikawa, H. Koguchi, K. Kamada, 'Microwave power emission from a beam-plasma system', J. Phys. Soc. Jpn., **65** (1996) pp. 2518-2521.

Relation between Beam Modulation and Millimeter-Wave Radiation from a Strong Beam-Turbulent Plasma

Hiroshi Yoshida, Masaru Masuzaki, Shintaro Ooyama, Kenichi Natsume,
Ritoku Ando, and Keiichi Kamada
Department of Physics, Faculty of Science, Kanazawa University, Kanazawa 920-1192, Japan

Abstract

Broadband millimeter-wave radiation is emitted from a beam-driven strong Langmuir turbulent plasma. We measured directivity of the radiation and its spectrum in an observation window of 18 - 140 GHz. Directivity measurements indicate that the radiation source is the beam electrons accelerated by caviton's electric field. The measured radiation power was rather high, and the spectrum was nearly flat up to about 40 GHz and declined steeply above this frequency. A modulated beam can emit coherently high power radiation and its spectrum may affect the radiation. We devised a waveguide pickup for measurement of the beam modulation. The measured spectrum of the beam modulation is similar to the radiation spectrum. This indicates that the radiation spectrum depends on the beam modulation.

1 Introduction

When an intense relativistic electron beam (IREB) is injected into a plasma, the plasma becomes a strong Langmuir turbulence state. In this state processes of creation, collapse, and burnout of cavitons, which are localized electrostatic fields with density depletion, are repeated [1 - 3]. This plasma emits powerful millimeter-wave radiation during passage of the beam through the plasma. Several investigators reported that the spectrum of this radiation spread widely above the plasma frequency [4 - 10]. We also measured the spectrum in the frequency range of 18 - 140 GHz, and found that the spectrum was of Gaussian type and had a cutoff frequency, which is a point of 3 dB down in power, of around 40 GHz [11].

The source of the radiation is thought to be beam electrons accelerated by the electric fields in the cavitons [12] because the radiation was observed only during the passage of the beam through the plasma. Spectrum of radiation of this type is expected to be broad, like bremsstrahlung, up to submillimeter or far-infrared region for our experimental condition. However, for high power radiation some coherence mechanism such as beam modulation [13, 14] is necessary. Then the beam modulation may influence the radiation spectrum.

To confirm further whether the radiation originated from accelerated beam electrons or not, we measured the directivity of the radiation. The radiation spectrum was also measured. For determination of the k-spectrum of the beam modulation, a waveguide pickup using WR-42 was devised. For these purposes two spectrometers covering 18 - 140 GHz were prepared. The measured ω-spectrum of the beam modulation was compared with the radiation spectrum. Also it was transformed to the k–spectrum using the relation $\omega = kv_0$, where v_0 is the beam velocity, from which we estimated the spatial beam distribution.

2 Apparatus

The setup of the interaction system is sketched in Figure 1. Major components of the system were a modified pulserad 110A electron beam generator produced by Physics International, a plasma gun system, and a drift chamber. The beam generator consisted of a Marx generator, a Blumelein line, and a diode consisting of a carbon cathode of 36 mm in diameter and a titanium foil anode of 20 μm thick. The beam generator could generate a pulse with diode voltage up to 1.4 MV, diode current up to 27 kA, and duration of 30 ns. When the anode-cathode distance of the diode was 30 mm, the beam current, I_b, of about 10 kA was injected into the drift tube. The plasma gun system was composed of a pair of rail-type plasma guns, a capacitor bank, and a trigger set. The guns were installed opposite to each other at 100 mm downstream from the anode. The drift chamber was of stainless steel, and 600 mm long and 160 mm in diameter. It had two observation ports at 175 mm downstream from the anode. An electromagnetic-wave absorber, Eccosorb AN73, which absorbs power over 24 dB, was put on the inner wall of the chamber. The chamber was evacuated to the pressure less than 5×10^{-5} torr. Net current was monitored by two Rogowski coils which were set just behind the anode foil and 260 mm downstream from the anode, respectively. The plasma density, n_p, at 175 mm downstream from the anode was determined with a microwave interferometer and a triple probe. The plasma density changed with the delay time, τ, after the gun firing. The density became maximum at about 12 μs after the gun firing and then decreased. Experimental setup for the observation of radiation spectrum was also shown in Figure 1. Horn antennas were attached in the observation ports.

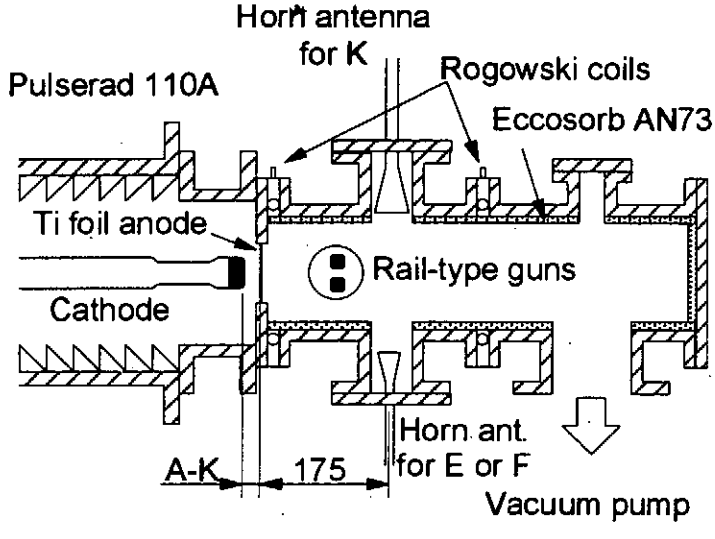

Figure 1: The experimental setup for the observation of radiation spectrum.

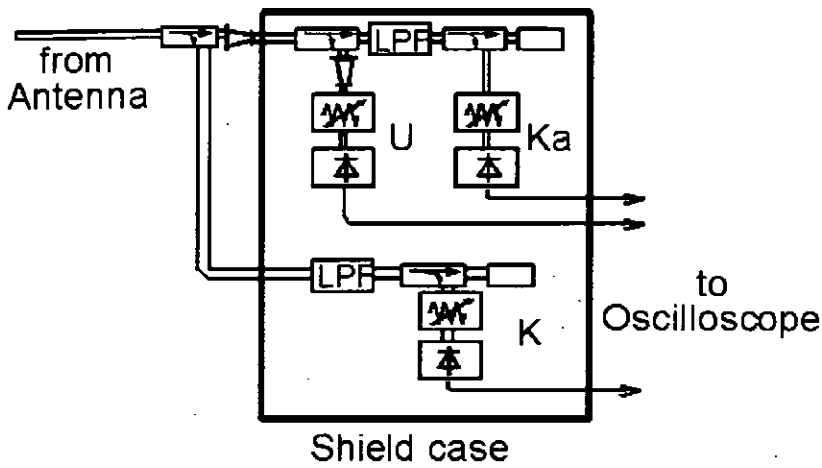

Figure 2: A block diagram of the filter-bank spectrometer.

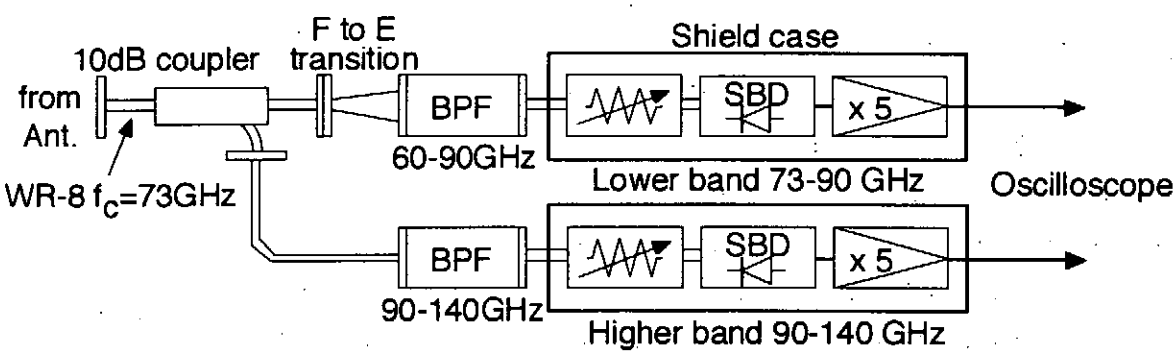

Figure 3: A block diagram of the combination spectrometer.

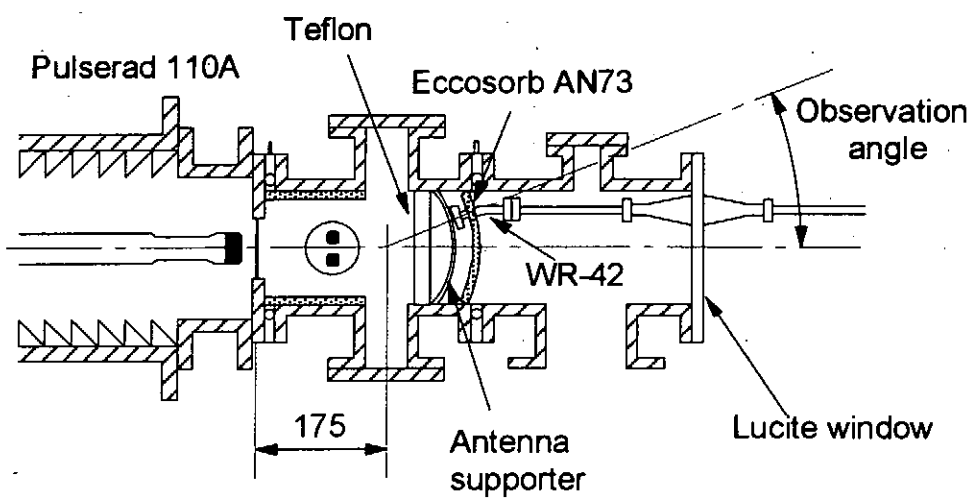

Figure 4: The set up for observation of the directivity. A WR-42 waveguide antenna was movable on an antenna supporter.

We prepared a three-channel filter-bank spectrometer for frequency range of 18 GHz - 60 GHz and a two-channel filter and waveguide combination spectrometer for 73 GHz - 140 GHz. The filter-bank spectrometer consisted of directional couplers, variable attenuators, bandpass filters (BPFs), and detectors. Figure 2 shows its block diagram. The combination spectrometer consisted of BPFs, variable attenuators, detectors, and wideband amplifiers as illustrated in Figure 3. Received signals were distributed by a directional coupler to the lower band (73 - 90 GHz) and the higher band (90 - 140 GHz) legs. Both spectrometers were calibrated utilizing Gunn oscillators.

Figure 4 shows the setup for the directivity measurement. The directivity of the radiation from a region around the point 175 mm downstream from the anode was measured because the transverse measurement had been done mainly for the radiation from this region. A WR-42 waveguide antenna movable on an arc with radius of 90 mm was located downstream side as shown in the Figure. To separate the antenna and the plasma, a 10 mm thick Teflon plate was placed in front of the antenna. The observation angle were 0°, 10°, 20°, and 30° to the beam propagation axis. The directivity measurement was carried out for frequency range of 18 - 26.5 GHz using a part of the three-channel filter bank spectrometer.

For the measurement of the beam modulation the waveguide pickup illustrated in Figure 5 was devised. The pickup was consisted of a WR-42 waveguide, an attachment with a hole of 1 mm in diameter and 12 mm long for beam introduction into the waveguide, a mini-Faraday cup, and an absorbing section. The waveguide had holes of 1 mm and 2 mm in diameter for the beam entrance and the beam exit on the center of the each broad side, respectively. The attachment was set in front of the entrance hole. The Faraday cup was attached behind the exit hole to measure net current coming through the holes. Eccosorb AN73 was set at the end of the waveguide to absorb the wave energy arrived at the end. When the modulated beam passes across the waveguide through the holes, it excites electromagnetic waves which couple with waveguide modes. In this pickup, the main excited modes may be TE_{n0} modes. The excited waves were directed to the spectrometers described above. We calculated the frequency response of this pickup for TE_{n0} modes using Lorentz reciprocity theorem and assuming that a line current changing sinusoidally with time traveled across the pickup. Figure 6 shows the excited power in the TE_{10} mode as a function of the

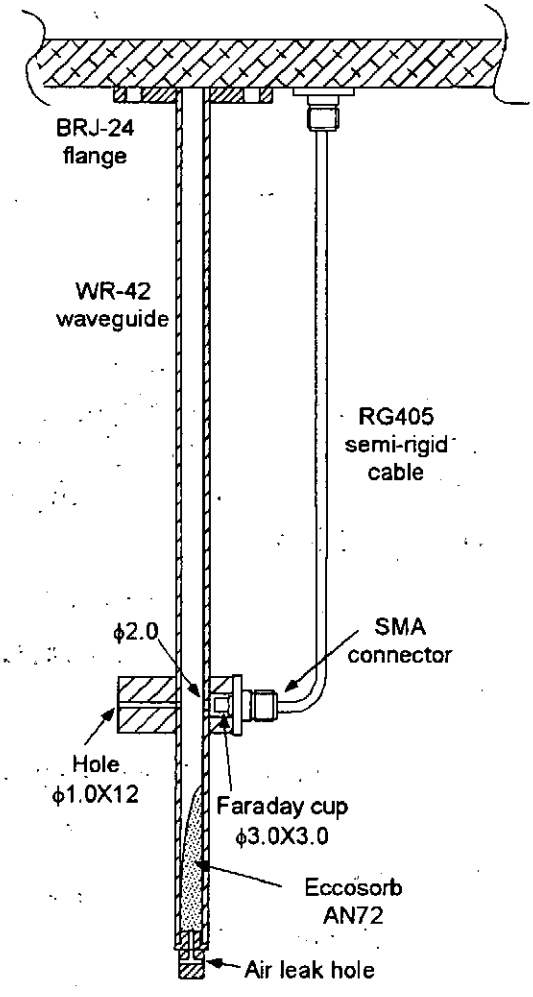

Figure 5: Waveguide pickup

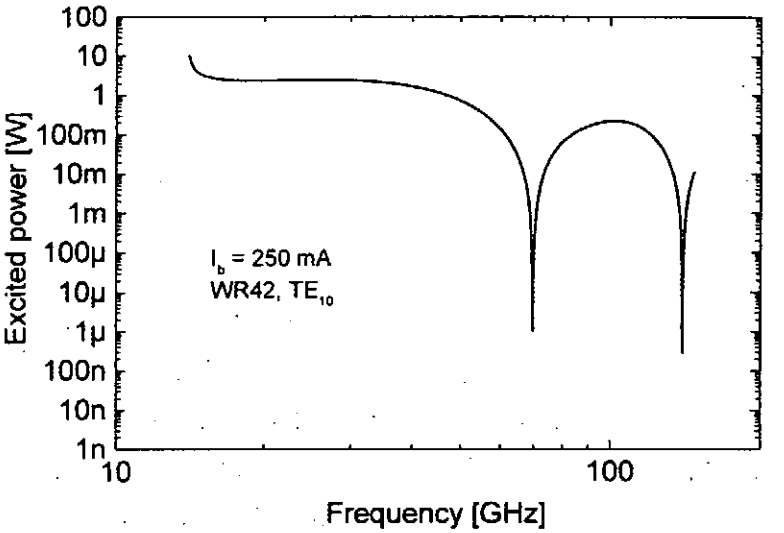

Figure 6: Frequency response of the waveguide pickup.

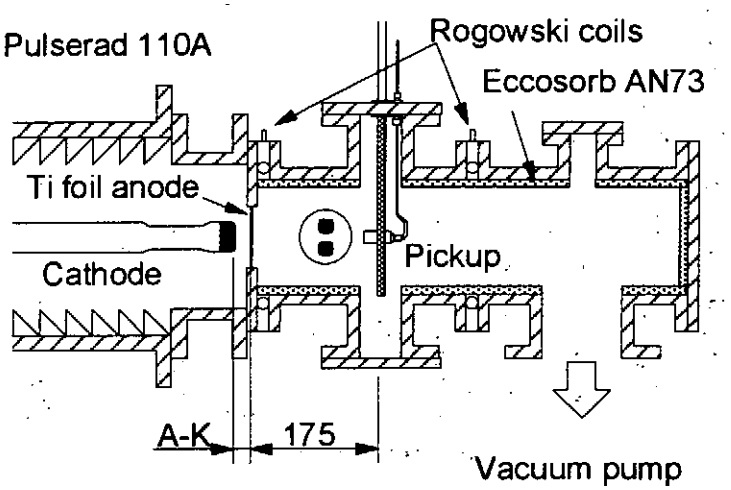

Figure 7: The experimental setup for the beam modulation measurement.

frequency of the current. This characteristic was used to correct the spectra obtained from the modulated beam. Figure 7 shows the setup for the measurement of the beam modulation. The pickup was placed at 175 mm downstream from the anode and the centers of the holes were adjusted to lie on the chamber axis.

3 Experimental results and discussion

The broadband radiation was emitted only during the passage of the electron beam through the plasma, although the Langmuir turbulence state continued after the beam passed through the plasma [2]. If radiation sources are the beam electrons, the radiation should be relativistically beamed with a half of opening angle $1/2\gamma$, which is 7° for our case. The results of the directivity measurement are shown in Figure 8. The plasma frequency was 16 GHz when $\tau = 30$ μs and 9 GHz when $\tau = 40$ μs, respectively. Figure 8 shows that the main radiation beams make an angle 10° - 20° to the axis. This angle roughly agrees with the estimated value. So we think that the radiation sources were the beam electrons. It is to be noted that if the electrons accelerated by the electric fields in the cavitons emit the radiation, the angle of the main radiation beam may be modified by orientation of the dipole moments of the cavitons to the velocity vectors of the electrons. When the dipole moment is oriented perpendicular to the velocity, the radiation is intensified at an angle of 0°. On the other hand, when the dipole moment is parallel to the electron velocity, the angle is $1/2\gamma$ [13, 14].

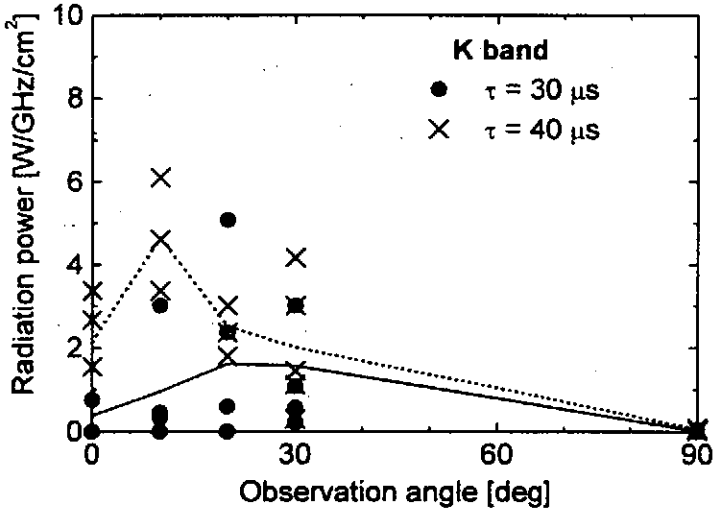

Figure 8: Measured directivity. Solid and dotted lines represent averages of measured values at $\tau = 30$ μs and $\tau = 40$ μs, respectively. Data at angle of 90 ° are those obtained by radial measurements.

Figure 9 (a) shows the radiation spectra at $\tau = 30$ μs and 40 μs, respectively. Solid line in the Figure shows the lowest detection limit of the detectors in the measurement system. The spectra are nearly flat up to 40 GHz and decline with about 40 dB/oct in the higher frequency side.

We tried to use the collective Compton boosting model proposed by Benford and Weatherall in order to explain the observed spectra. In this model they take into account the beam density fluctuation. They assume four spectral density functions: power law, delta function, exponential, and Gaussian. We calculated spectra using each spectral functions with our experimental

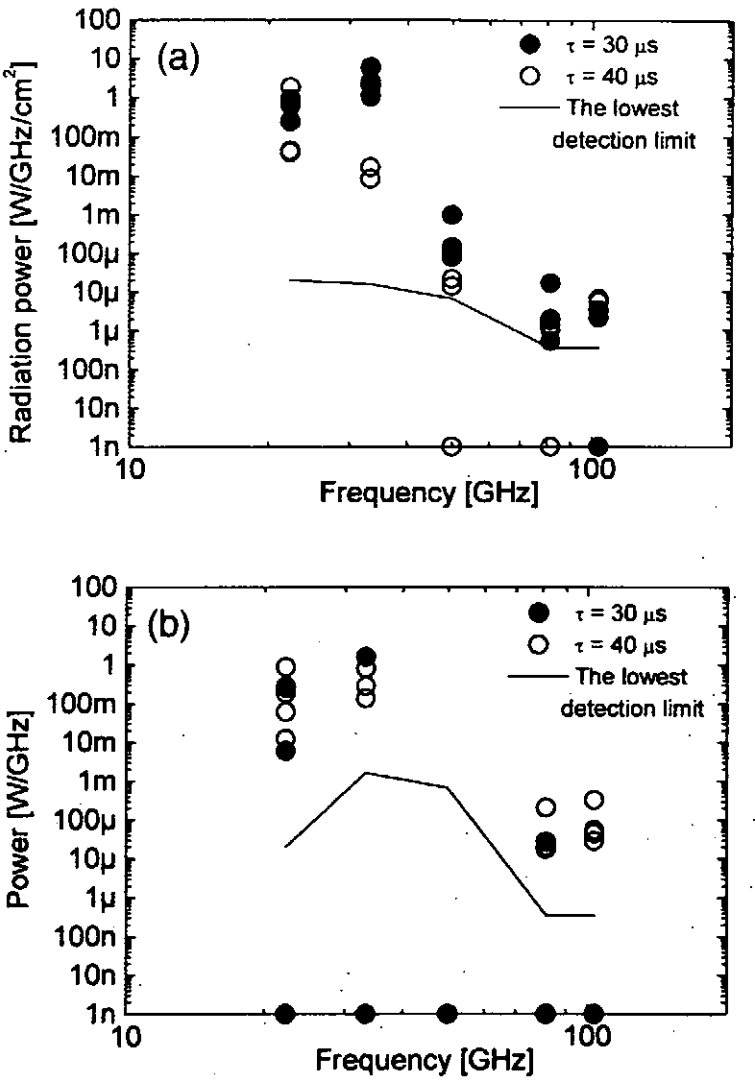

Figure 9: Spectra obtained at $\tau = 30$ μs and 40 μs. Solid lines show the lowest detection limit in the measurement systems. (a) The radiation spectrum observed by the spectrometers with the horn antennas. (b) The frequency spectrum of the beam modulation measured by the spectrometers with the waveguide pickup.

parameters. The calculated spectrum using the Gaussian spectral function was similar to the measured spectrum in shape but the cutoff frequency of the latter was much less than the former. This difference comes from the difference in the spectral bandwidth in the spectral density function. In the model, the Gaussian spectral function is given by [13]

$$V(k) = n_b^2 \left(\frac{\delta n_b}{n_b} \right)^2 \frac{2}{\sqrt{\pi}} \frac{\exp\left(-k^2 / k_m^2\right)}{k_m}, \qquad (1)$$

where n_b denotes the beam density, $\delta n_b/n_b$ is the beam density fluctuation, k is the wave number, and k_m is the spectral bandwidth. The cutoff frequency of the spectrum depends on this spectral bandwidth. They defined the bandwidth as $k_m = \gamma^2/D$ where γ is Lorentz factor, $D = 20\,\lambda_d$, and λ_d is Debye length. From this definition the cutoff frequency of the calculated spectrum becomes approximately several THz. On the other hand, the cutoff frequency of our experimental spectrum was several tens GHz. The spectral bandwidth was estimated from the experimentally obtained spectrum with help of the equation for the coherent radiation from a bunch [15]

$$P = I\,N^2 f(k), \tag{2}$$

where P is the total radiation power, I is the radiation power from single electron, N is the number of electrons in a bunch, and $f(k)$ is the form factor,

$$f(k) = \left| \int S(x) \exp(ikx) dx \right|^2. \tag{3}$$

Here $S(x)$ is the spatial beam distribution and $f(k)$ corresponds to $V(k)$ in the collective Compton boosting model. First, we converted the experimentally obtained ω-spectrum to the k-spectrum by assuming constant beam velocity. Then we fitted the spectrum to Gaussian and calculated the symmetric spatial beam distribution of Gaussian shape using equation (3). The spectral bandwidth was estimated to be 5 mm.

We measured the beam modulation directly using the waveguide pickup. Figure 9 (b) shows measured frequency spectra of the beam modulation at τ = 30 μs and 40 μs. The power in U-band (40 - 60 GHz) disappeared because, in this experiment, the lowest detection limit of the detector for the frequency range of 18 - 60 GHz was rather high as shown in the Figure. The spectra are also nearly flat up to 40 GHz and decline steeply above this frequency. These spectra are similar to the radiation spectra with slight difference that the power ratio of the lower frequency side (18 - 40 GHz) to the higher frequency side (60 - 140 GHz) in the former was about 10^4, while the power ratio in the latter was about 10^6. From this ω-spectrum we obtain directly the k-spectrum of the beam modulation under the assumption of constant beam velocity. On the other hand the radiation spectrum is expressed as the product of the radiation spectrum from single electron and the spectrum of the beam modulation. Since the radiation spectrum from single electron in our observation range is estimated to be flat, we could compare directly both spectra. So we think that the k-spectrum of the beam modulation determines the radiation spectrum.

4 Conclusion

The directivity of the radiation from the beam-turbulent plasma was measured. The directivity was fairly sharp and the main beam angle was about 10° to the direction of the beam propagation. This indicates that the radiation source is the beam electrons accelerated by caviton electric fields. We observed the radiation spectrum with two spectrometers covering 18 - 140 GHz. The measured spectrum was nearly flat up to 40 GHz and declines steeply above this

frequency. Comparison of the experimentally obtained spectrum with spectra calculated using the collective Compton boosting model indicated that, although the experimentally obtained one agreed in shape with the spectrum calculated using the Gaussian spectral function, the cut off frequency of the former was much less than that of the latter. This disagreement was attributed to the disagreement of the spectral bandwidth of the spatial beam distribution between the model and the experiment. The experimentally obtained spectrum was fitted to Gaussian and transformed to the spatial distribution of the beam electrons by the inverse Fourier transform. The width of the distribution was estimated to be 5 mm. We devised a waveguide pickup to measure the spectrum of the beam modulation directly. The ω-spectrum of the beam modulation was similar to the radiation spectrum. The radiation spectrum is expressed as the product of the radiation spectrum from single electron, which is estimated to be flat in our observation window, and the spectrum of the beam modulation. Therefore, the fact that both spectra are almost the same indicates that the beam modulation determines the radiation spectrum. For further confirmation of this conclusion we are now preparing another experimental method for measurement of the beam modulation.

Acknowledgment

Part of this work was supported by a Grant-in Aid for Scientific Research from the Ministry of Education, Science and Culture.

References

[1] P. A. Robinson, and D. L. Newman, Phys. Fluids **B2** (1990) 3120.

[2] M. Yoshikawa, M. Masuzaki, and R. Ando, J. Phys. Soc. Jpn. **64** (1994) 3303.

[3] H. Koguchi, M. Masuzaki, M. Yoshikawa, S. Takahata, K. Toda, R. Ando, and K. Kamada, *Proc. of the 11th International Conference on High Power Particle Beams*, 1996, Prague, Czech., vol. 1, p. 331.

[4] K. G. Kato, G. Benford, and D. Tzach, Phys. Fluids **26**, 12 (1983)

[5] M. S. DiCapua, J. F. Camacho, E. S. Fulkerson, and D. Meeker, IEEE Trans. Plasm **16**, 2 (1988)

[6] M. Masuzaki, R. Ando, A. Yoshimoto, M. Ishikawa, M. Yoshikawa, K. Kitawada, H. Morita, and K. Kamada, *Proc. of the 8th International Conference on High Power Particle Beams*, 1991, Novosibirsk, USSR, vol. 2, p. 683.

[7] M. Masuzaki, M. Yoshikawa, H. Morita, J. Yasuoka, and K. Kamada, *Proc. of the 9th International Conference on High Power Particle Beams*, 1992, Washington, DC., vol. 2, p. 1227.

[8] R. Ando, M. Masuzaki, K. Kobayashi, M. Yoshikawa, H. Morita, H. Koguchi, D. Yamada, and K. Kamada, *Proc. of the 10th International Conference on High Power Particle Beams*, 1994, San Diego, California, vol. 2, p. 933

[9] R. Ando, M. Masuzaki, H. Morita, K. Kobayashi, M. Yoshikawa, H. Koguchi, and K. Kamada, J. Phys. Soc. Jpn. **65** (1996) 2518.

[10] M. Masuzaki, H. Yoshida, R. Ando, K. Kamada, A. Ikeda, C. Y. Lee, and M. Kawada, *Proc. of the 11th International Conference on High Power Particle Beams*, 1996, Prague, Czech., vol. 1, p. 339.
[11] H. Yoshida, M. Masuzaki, S. Oyama, R. Ando, and K. Kamada, NIFS-Proc **36** (1997) 140.
[12] J. C. Weatherall, Phys. Rev. Letters, **60** (1988) 1302.
[13] G. Benford, and J. C. Weatherall, Phys. Fluids, **B4** (1992) 4111.
[14] J. C. Weatherall, and G. Benford, Astrophys. J. **378** (1991) 543.
[15] J. S. Nodvic and D. S. Saxson, Phys. Rev. **96**, (1954) 180..

TWO-STAGE AUTOACCELERATION OF AN INTENSE RELATIVISTIC ELECTRON BEAM

Daisuke Hasegawa, Keiichi Kamada, Kazuhiro Shimizu,
Masaru Miyamoto, Ritoku Ando and Masaru Masuzaki

Department of Physics, Faculty of Science, Kanazawa University,
Kanazawa 920-1192, Japan

Abstract

Experiments of the two-stage autoacceleration are carried out to compress an intense relativistic electron beam (IREB). An annular IREB of 600 keV, 3.5 kA and 10 ns is propagated through a two-stage cavity structure immersed in a uniform axial magnetic field. The lengths of the first and the second cavities are a quarter and one-eighth of the beam length, respectively. The kinetic energy of electrons increases from 600 to 750 and to 850 keV after passing through the first and the second cavities, respectively. The duration of the accelerated part in the beam pulse decreases from 10 to 5 ns after passing through the first cavity and to 2.5 ns after the second. The increase of energy of electrons and the decrease of the duration of the accelerated part in the beam are well explained by the principle of the multi-stage autoacceleration.

1. Introduction

Generation of a short duration intense relativistic electron beam (IREB) is an interesting subject of study for, for example, application to high-power, short pulse millimeter-wave generation [1]. However, it is difficult for conventional pulse-forming-line systems to generate an IREB of short duration on order of 1 ns or less because of their structure. We proposed to compress pulse duration of an IREB after emission from a diode utilizing multi-stage autoacceleration process [2] which uses a series of cavities with decreasing lengths. Multi-stage autoacceleration process is potentially simple approach to produce a sub-ns electron beam with high particle energies. One-stage autoacceleration experiments with various energies of IREB were reported extensively in the 1970's [3-6]. And a collective autoacceleration experiment with the same length cavities was also already reported [7]. In this paper, experiments of the two-stage autoacceleration with different lengths cavities are carried out to investigate the applicability of the multi-stage autoacceleration for compression of an IREB.

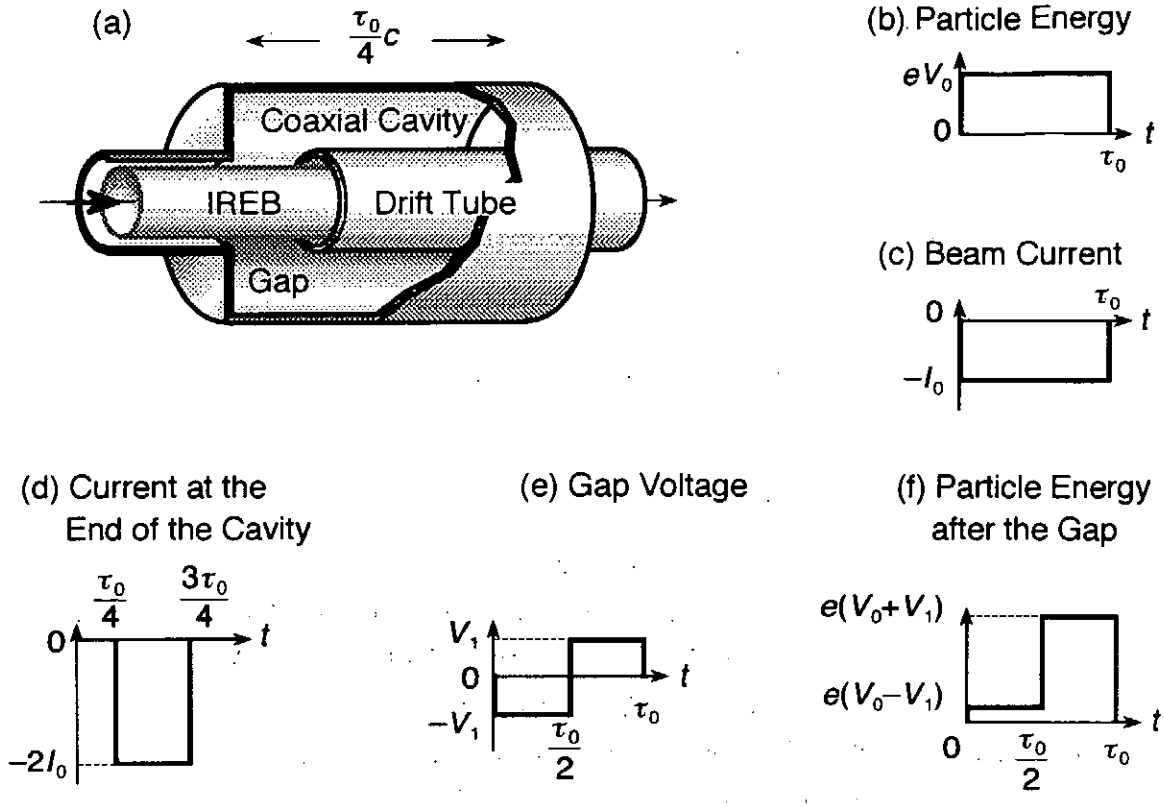

Fig. 1 Simple Model of the Autoacceleration process.

2. Principle of Multi-Stage Autoacceleration

The autoacceleration process occurs during a mutual interaction between an IREB and a passive structure. A simple model of the autoacceleration process are given in Fig. 1 [8]. A coaxial cavity of impedance Z is connected to the drift tube via a gap [Fig. 1(a)]. The length of the cavity is $l = \tau_0 c/4$, where τ_0 is the beam duration and c is the speed of light. An IREB of particle energy $eV_0(t)$ [Fig. 1(b)], current $I_0(t)$ [Fig. 1(c)] and duration τ_0 propagates through a drift tube immersed in a uniform axial magnetic field. When the beam reaches the gap, the voltage $V_1(t)$ appears across the gap. An induced current in the cavity propagates to the right in Fig. 1(a) and is reflected by the shorted end of the wall. The current in the cavity $I_1(z,t)$ and $V_1(t)$ was calculated in ref. 8 using the transmission line theory. The current at the end of the cavity is expressed as

$$I_1(l,t) = 2I_1(0,t) - 2I_1(0,t - \tau_0/2) + \cdots , \qquad (1)$$

where $I_1(0,t)=I_0(t)$, and is shown in Fig. 1(d). The voltage across the gap V_1 is

$$V_1(t) = Z\,[\, I_1(0,t) - 2I_1(0,t - \tau_0/2) + \cdots \,] . \qquad (2)$$

$V_1(t)$ is depicted in Fig. 1(e). A beam electron loses kinetic energy $eV_1(t)$ during the first half portion of the beam duration ($0 < t < \tau_0/2$) and gain the same amount of energy during the second half ($\tau_0/2 < t < \tau_0$) [Fig. 1(f)].

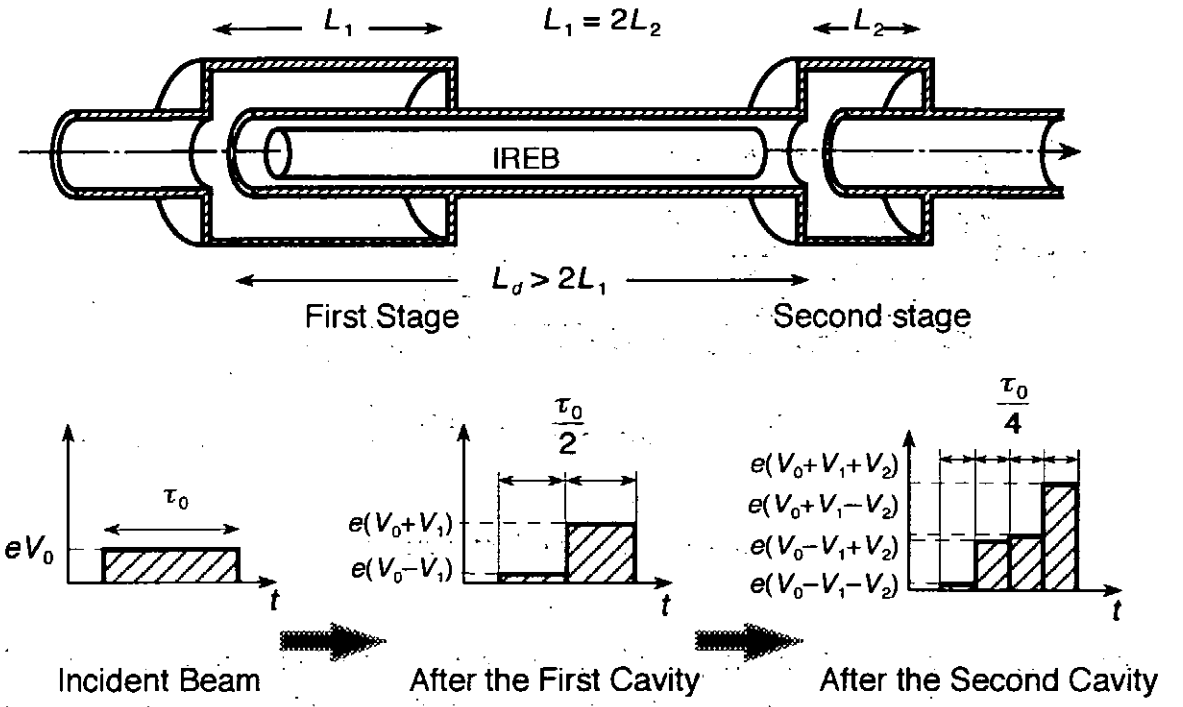

Fig.2 Schematic of the Two-Stage Autoacceleration. V_1 and V_2 are the voltage at the first and second gaps, respectively.

The principle of the multi-stage autoacceleration is to autoaccelerate the accelerated part of the IREB repeatedly. As the duration of the autoaccelerated part of the beam decreases to half of its incident duration, the length of the $n+1$ th cavity is adjusted to the half of that of the n th cavity. Then the IREB is expected to decrease its pulse width to half at each stage with increase of its particle energy (in other words, IREB compression) as shown in Fig. 2.

The multi-stage autoacceleration is a simple and inexpensive approach for generation of a short duration, high energy IREB.

3. Experimental Apparatus

A Pulserad 105A of Physics International which utilizes a conventional Blumlein line is used as a beam source. A 650 kV, 16 kA, 10 ns pulse is available to a matched load. As the velocity of the beam is nearly equal to that of light, the pulse length is calculated to be ~3 m. A schematic diagram of the experiment is shown in Fig. 3. An annular electron beam with a diameter of 2.4 cm and a thickness of 2 mm is injected from a foilless diode into a 3 cm inner diameter, 3.5 m long conducting drift tube. Axial magnetic field of 1 T is applied by solenoid coils of total length of 3 m as shown in Fig. 3. The first cavity with length of 75 cm (= 3/4 m) is connected to the drift tube via a gap at 20 cm downstream from the anode. The length of the second cavity is 37.5 cm (= 75/2 cm). As the beam length is 3 m, the second cavity is located 2

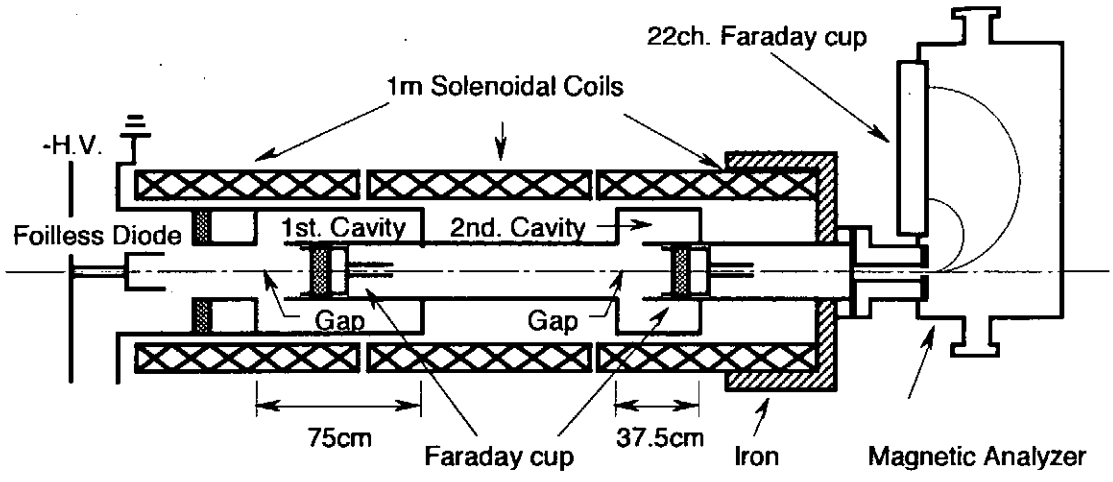

Fig.3 Experimental Configuration.

m, more than 3/2 m, apart from the gap of the first cavity to avoid the mutual interaction between the cavities. The gap length of the first and the second cavities is 3 cm and the impedance of them is 46 ohm.

The beam current is monitored by a movable Faraday cup at various locations along the axis in the drift tube. Aluminum foils of different thickness are placed in front of the Faraday cup in order to estimate the kinetic energy of the beam electrons. A magnetic analyzer located at the end of the drift tube is also utilized to determine the kinetic energy of the beam electrons that emerge outside the axial magnetic field. The electrons which enter the analyzer are deflected 180 degree by a magnetic field and are detected by a 6 mm diameter Faraday cup array. The energy resolution of each Faraday cup is less than 5 %.

4. Experimental Results

Typical waveforms of the diode voltage, the diode current and the beam current are shown in Fig. 4. The peak voltage of the diode is ~ 600 kV with the pulse width of ~ 10 ns. The beam current detected at 50 cm downstream from the anode (z = 50 cm) without cavity is 3.5 kA with the half width of ~10 ns.

The Faraday cup waveforms for different thicknesses of aluminum foils are shown in Fig. 5. The beam current in the control experi-

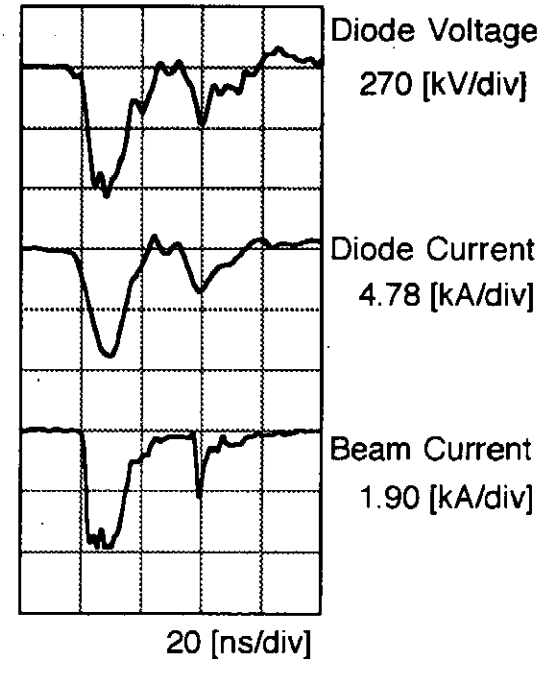

Fig. 4 Typical Waveforms.

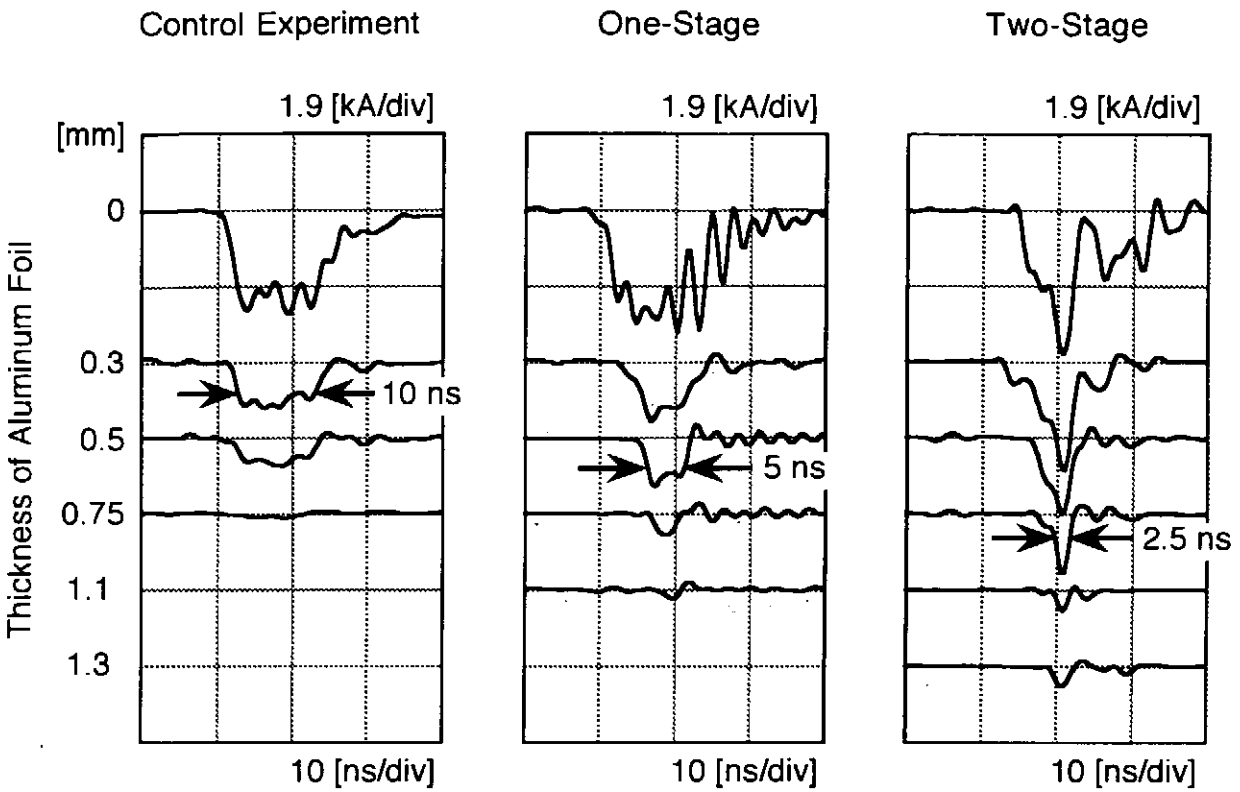

Fig.5 Faraday Cup Waveforms for Different Thicknesses of Aluminum Foils.

ment without foil appears smaller than the current shown in Fig. 4 because of the attachment device of the aluminum foils. In the control experiment, the cavities are not mounted and the beam propagating through the drift tube is detected at z = 50 cm. The center portion of the beam current pulse with the duration of ~10 ns passes through a 0.5 mm thick aluminum foil. But the beam current disappears behind an aluminum foil with thickness of 0.75 mm. In the one-stage experiment, the Faraday cup is located at z = 50 cm between the first and the second gaps. In comparison with the control experiment, only the second half portion of 5 ns duration of the beam current pulse is observed in the waveform with a 0.5 mm thick aluminum foil. And it passes through thicker aluminum foil than the control experiment. In the two-stage experiment, the beam current passing through the first and the second gaps is monitored at z = 250 cm. The last quarter portion of the beam current pulse with 2.5 ns duration survives behind a 0.75 mm thick aluminum foil. The electrons in the last quarter portion pass through thicker aluminum foil than the one-stage experiment.

The kinetic energies of electrons in the control, in the one-stage and in the two-stage experiments are estimated by the range-energy relation for relativistic electrons [9]. The ratio of the transmitted current through an aluminum foil with thickness x , I_x, to the current, I_0, detected without foil is plotted against x in Fig. 6. The energies of beam electrons in the control, in the one-stage and in the two-stage experiments are estimated to be 550 keV, 750 keV and 850 keV,

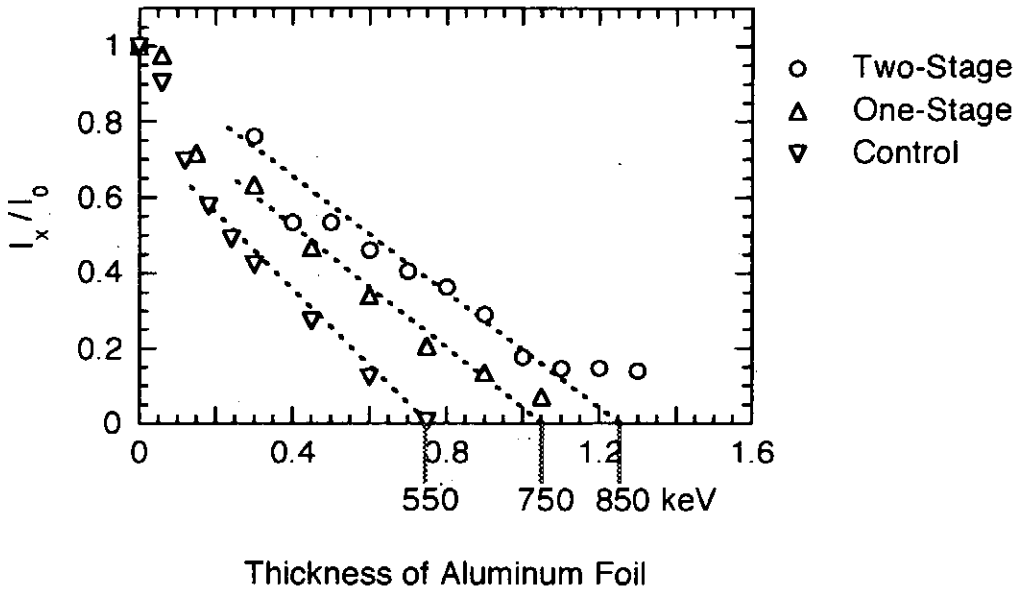

Fig.6 Energy Estimation by the Range-Energy Relation.

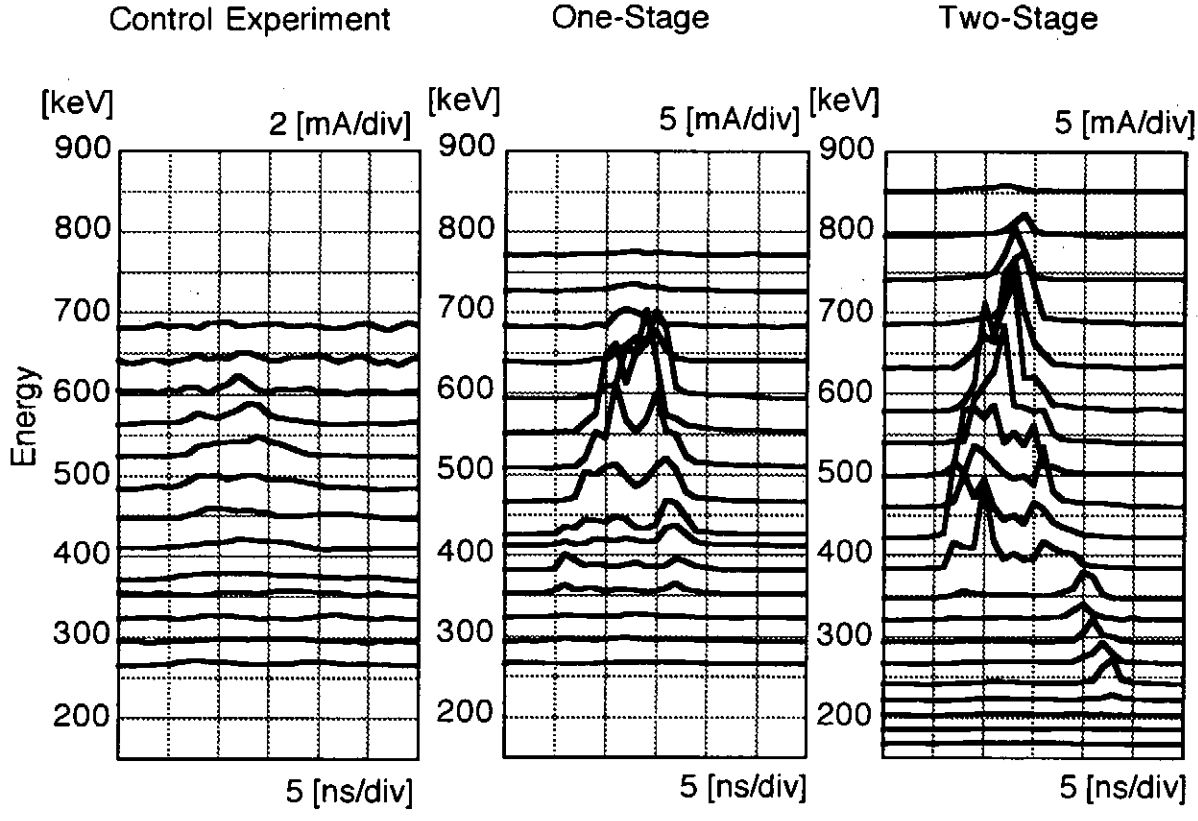

Fig.7 Waveforms of Faraday Cups of the Magnetic Analyzer

respectively.

A magnetic momentum analyzer is utilized to determine the kinetic energy of electrons that emerge outside the axial magnetic field. Throughout all experiments, it is located at the end of the 3.5 m drift tube. The waveforms detected by each Faraday cup are shown in Fig. 7. The maximum particle energies in the control, in the one-stage and in the two-stage experiments are evaluated to be 600 keV, 730 keV and 850 keV, respectively. In the one-stage and the two-stage experiments, the higher energy part of the beam is clearly observed in the later portion of the pulse. These results agree well with results of the Faraday cup measurement with aluminum foils.

To confirm that the energy increase of accelerated electrons by autoacceleration process is related to the cavity impedance, an additional one-stage experiment that employs a cavity with impedance of 76 ohm is carried out. The diode and the radius of the drift tube are the same as the previous apparatus. The outer radius of the cavity is expanded. New solenoid coil with inner radius of 15 cm is utilized. The axial magnetic field strength is 1 T as in the previous experiment. The beam current increases to 4.5 kA probably because of the change of the magnetic field line by new solenoid coil, though the diode voltage and the current waveforms show a little difference from the waveforms shown in Fig. 4,

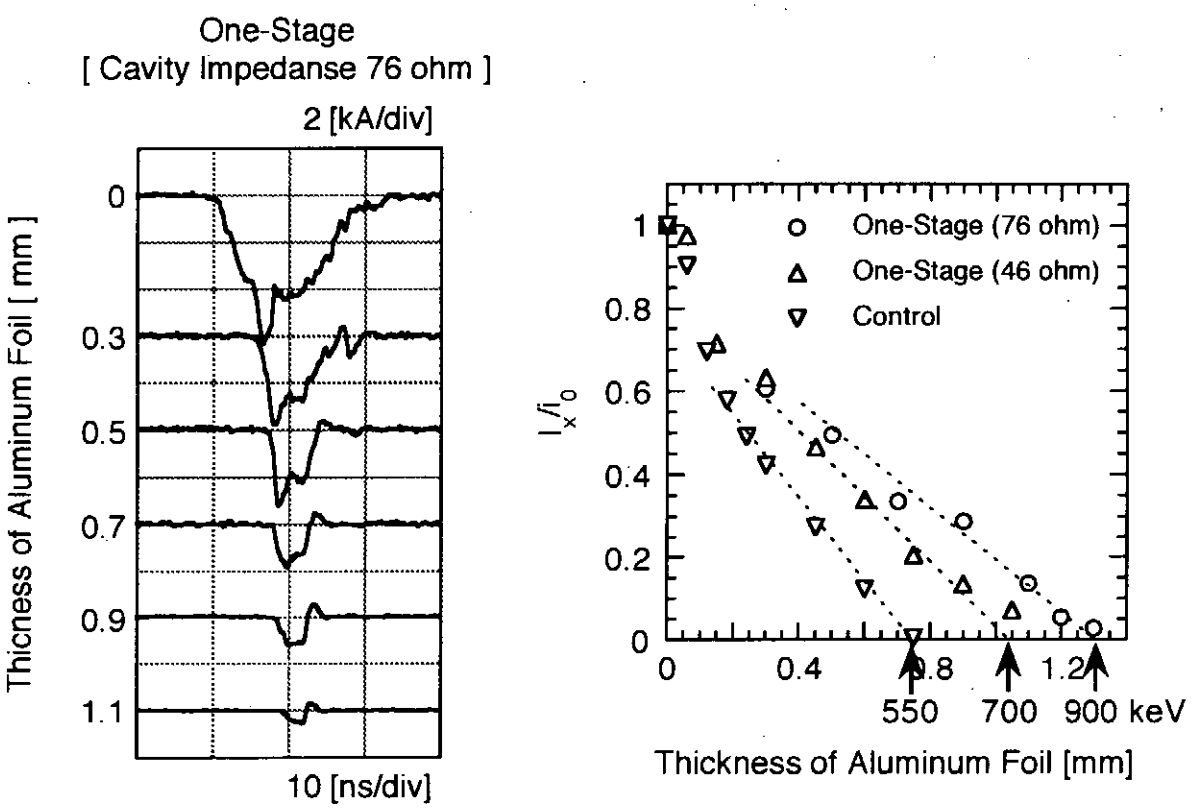

Fig.8 Faraday Cup Waveforms (left) and Energy Estimation (right).

The Faraday cup waveforms with different thicknesses of aluminum foils are shown in Fig. 8. From the range-energy relation, the maximum accelerated energy is estimated to be 900 keV. So the accelerated energy of electrons becomes higher with the higher impedance cavity. The accelerated part of the beam appears in the second half of the beam duration as in the previous experiment.

5. Discussions

The energies of the beam electrons measured by the Faraday cup with aluminum foils and the magnetic analyzer in the one- and the two-stage experiments agree well as described in the previous section. The simple model described in Sect. 2 says that the increase of the energy at each stage is the product of the cavity impedance and the current. As the beam current is measured to be 3.5 kA and the cavity impedance is 46 ohm, the expected increase of the energy at each stage is calculated to be 161 keV. The measured increases of the beam electron energy are 200 keV by the Faraday cup with aluminum foils and 130 keV by the magnetic analyzer in the one-stage experiment. They agree with the calculated value. And those are 300 keV by the former and 250 keV by the latter in the two-stage experiment. They are nearly twice as much as the calculated value. In the experiment with the cavity of 76 ohm, the increase of the energy of 350 keV show good agreement with the calculated value of 342 keV. As a result, the estimation of the increase of the beam electron energy by using the eq. (2) is applicable for the multi-stage autoacceleration.

The energy of the electrons in the first half portion of the beam duration in the one-stage experiment with $Z = 46$ ohm is roughly estimated to be 340 keV from the range-energy relation. Therefore, the beam electrons lose its energy of 210 keV in the first half portion and gain almost the same amount of energy of 200 keV in the second half. This result agrees well with the model in Fig. 1(e).

The observed energies of beam electrons in the accelerated portion of the beam duration extend from about half of the maximum to the maximum value as shown in Fig. 7. The lower energy electrons are not the decelerated electrons, as described below. In the model in Sect. 2, the accelerated electrons run after the decelerated ones after the gap section. However, in our experimental situation, the distance between the gap and the observation point is calculated to be too short for the accelerated electrons to catch up with the decelerated ones. Moreover, the decelerated electrons are observed before the arrival of the accelerated ones. Therefore, the lower energy electrons in the accelerated portion are not the decelerated electrons. Although the model assumes square pulse shapes for the beam parameters, both the energy and the current of our IREB have finite rise times. Then, we can suppose two origins of the lower energy electrons in the accelerated portion. First, the electrons in the earlier rise time portion have the lower energy than those in the following portion, so that they may be caught up with the accelerated

electrons. Second, the voltage across the gap, which is estimated to be the product of the cavity impedance and the current, should increase in the finite rise time of the current. Consequently, electrons in the accelerated portion may have wide spectrum in energy distribution.

The duration of the accelerated part of the beam corresponds with the length of each cavity. As shown in Fig. 2, the energy of the electrons detected after the second stage may change stepwisely with time. The beam electrons in 0-2.5 ns in the beam duration lose their energy twice by the 2 cavities. Those in 2.5-5 ns are decelerated by the first cavity and are accelerated by the second cavity. Those in 5-7.5 ns are accelerated by the first cavity and are decelerated by the second cavity. Those in 7.5-10 ns are accelerated by both cavities. The waveforms of the two-stage experiment in Fig. 5 clearly show the stepwise waveforms. The electrons in 0-2.5 ns disappears. Those in 2.5-5.0 ns are observed behind a 0.3 mm thick aluminum foil but not detected behind a 0.5 mm thick foil. The pulse through a 0.5 mm thick foil is observed in 5-10 ns. The beam with the energy of 850 keV appears in 7.5-10 ns from the current rise of the control waveform.

Comparing with our experimental results, we accept the model of the multi-stage autoacceleration described in Sect. 2 in principle. Our goal is to generate a short duration, high energy IREB, so that the decelerated electrons are useless for the acceleration of electrons in the next stage. Further improvement of the structure of the multi-stage autoacceleration may be necessary to scrape off the decelerated electrons.

6. Conclusion

The principle of the multi-stage autoacceleration is confirmed experimentally by the two-stage autoacceleration experiment. The energy that the electrons gain at each stage agrees with the product of the cavity impedance and the current. While the energy increases in arithmetic progression with the same impedance cavities, the duration of the accelerated part of the beam decreases in geometrical progression with the cavity lengths. As the length of the cavity for 0.5 ns duration is 7.5 cm, which is still within the limits of construction, the multi-stage autoacceleration is applicable for pulse compression of the IREB of short duration less than order of 1 ns. We now start a four-stage autoacceleration experiment with cavities with impedance of 76 ohm.

References

[1] N. S. Ginzburg et al., Phys. Rev. Lett. 78, 2365 (1997).

[2] K. Kamada et al., Proceedings of the 11th International Conference on High-Power Particle Beams, vol. 1, 351 (1996).

[3] M. Friedman, Phys. Rev. Lett. 31, 1107 (1973).

[4] L. N. Kazanski, A. Kiisletsov and A. N. Lebedev, At.Energ. 30, 27 (1971).

[5] M. Friedman, Phys. Rev. Lett. 32, 92 (1974).

[6] I. A. Grishaev, A. N. Debik, V. V. Zakutin, I. I. Magda, Yu. V. Tkach and A. M. Shenderovich, Sov. Phys. Tech. Phys. 19, 1087 (1975).

[7] T. R. Lockner and M. Friedman, J. Appl. Phys. 51, 6068 (1980).

[8] M. Friedman, Appl. Phys. Lett. 41, 419 (1982).

[9] Seligar H H, Phys. Rev. 100, 1029 (1955).

Design rule and performance of nonlinear transmission line with specially fabricated nonlinear capacitors

Mitsuru OHNISHI, Tatsuya OKUDA, Shinji IBUKA, Koichi YASUOKA and Shozo ISHII

Tokyo Institute of Technology

Abstract

A nonlinear transmission line (NLTL) with nonlinear capacitors can sharpen the front edge of voltage pulses generated by semiconductor switches to nano second order. This paper reports the results of numerical calculation for optimizing the sharpening effects of NLTL and experimental data using specially fabricated $BaTiO_3$ ceramic capacitors. The nonlinearity of capacitance defined as $C_0/C(V)$, $C(V)$ is the capacitance under voltage V, strongly affects the sharpening efficiency of high voltage pulses. The calculation result shows that the sharpening efficiency is much more improved by tapering the capacitance of NLTL according to the direction of pulse propagation. We have fabricated $BaTiO_3$ based ceramic disk capacitors that showed strong nonlinear characteristics with voltage and had minimum inductance for reducing a residual inductance in NLTL. The input pulse of 150nsec rise time and of 10kV peak voltage was sharpened to 60nsec rise time without voltage drop.

1. Introduction

High repetitive and long-lived pulsed power generators could be produced by using semiconductor switches. Because of the limitation of switching speed and withstand voltage, semiconductor switches must be used by series-parallel connection and adding special devices such as pulse sharpening circuits or pulse compression circuits. A nonlinear transmission line (NLTL) with nonlinear capacitors is applicable for high voltage generator. In NLTL, a pulsed voltage is sharpened by a formation of electromagnetic shock wave and is compressed by a generation of soliton wave. We have successfully generated a pulsed voltage of 20kV peak and of several MW for exciting a TEA-CO_2 laser [1]. The rise-time was reduced from 1μs to 200ns. However, the design parameters of NLTL, such as nonlinearity of capacitors, residual circuit inductance, are not confirmed up to now. This seems to be a reason why NLTL is not widely used in various pulsed power systems. In this report, we estimate nonlinearity needed for effective sharpening or compression, and show the newly proposed tapered transmission lines and fabrication of $BaTiO_3$ ceramic capacitors used in a NLTL.

2. The pulse sharpening mechanism

A NLTL is a ladder-type transmission line consisting of inductors L and nonlinear capacitors C as shown in Fig.1(a). Each capacitors show nonlinear capacitance with applied voltage as shown in Fig.1(b). The phase velocity of an electromagnetic wave in the NLTL is given by equation (1).

$$v(V) = \frac{1}{\sqrt{LC(V)}} \quad \cdots\cdots (1)$$

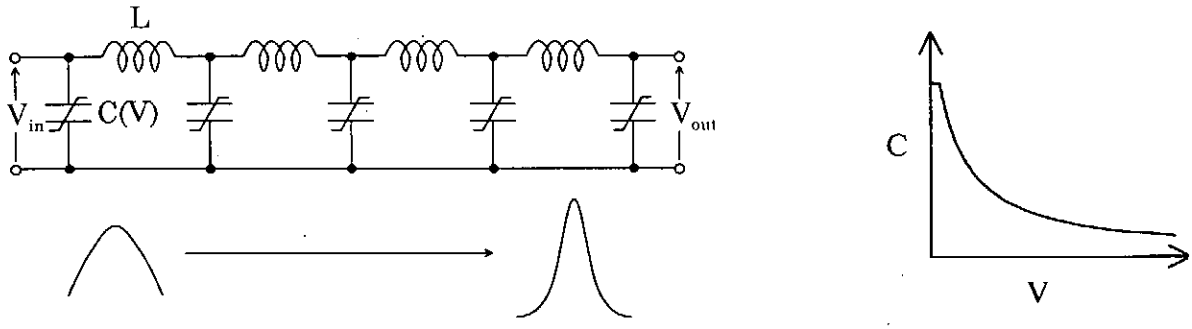

(a) A equivalent circuit (b) C-V characteristic

Fig.1 Schematic diagram of a NLTL

The velocity of the leading edge of a pulse voltage increases faster than that of the other parts during propagating, hereby the pulse front is sharpened. In the case of no dispersion, the pulse sharpening time is given by equation (2) [2].

$$\Delta T = n\left(\sqrt{LC_0} - \sqrt{LC(V_{max})}\right) \quad \cdots\cdots (2)$$

, where n is the number of LC sections, V_{max} is the maximum voltage of propagating pulse. The NLTL acts as a low-pass filter, so the higher frequency components over Bragg cut off frequency can't propagate in the NLTL. Bragg cut off frequency f_r is given by equation (3).

$$f_r = 1/\pi\sqrt{LC(V)} \quad \cdots\cdots (3)$$

The solitons are produced by the balance between the sharpening effect and the dispersion effect. The forming process of solitons has both a pulse compression effect and a voltage amplification effect.

3. Evaluation of pulse compression in NLTL by numerical calculations

An analytical solution of soliton can be deduced only with a simple circuit configuration, so the numerical analysis is very important to understand the phenomenon in NLTL. There are many parameters to be considered, such as nonlinearity of dielectrics, circuit parameters, and the shape of the input pulse to the line and so on.

Figure 2 shows how the nonlinearity α of a dielectric affects on the pulse compressing characteristics. The parameter α is defined as $C_0/C(V_{in})$, where C_0 is the no biased capacitance and $C(V_{in})$ is the capacitance under the voltage V_{in}. The pulse compression ratio is defined by $2\tau/f_r$, where τ is pulse width of a soliton and f_r is Bragg cut off frequency given by equation (3). Figure2 suggests that there is a limitation of the pulse compression and the voltage amplification ratio at larger α values. The number of sections in NLTL can be reduced at a larger α value, but in this case, energy transfer efficiency and impedance matching are not good at the load. From Fig.2, the optimum value of α is from 5 to 8.

Figure 3 shows the number of solitons generated in NLTL according with the input pulse

width where the parameter α is 5. As increasing the input pulse width, more soliton waves are generated to form a soliton array. Consequently the pulse compression effect of soliton is up

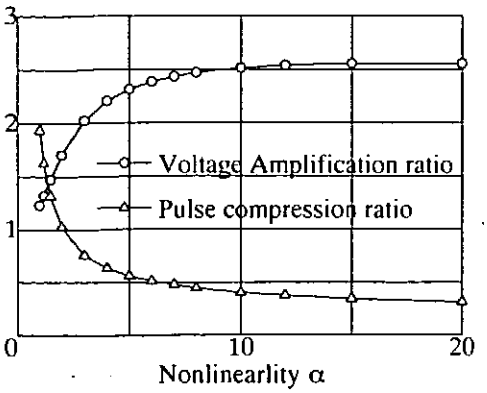

Fig.2 Effect of the nonlinearity α

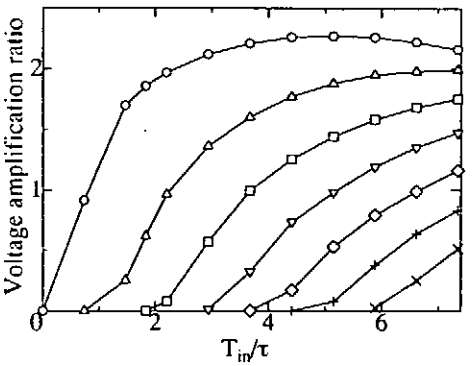

Fig.3 Number of generated soliton pulses

to $T_{in} \lessapprox 1.5\tau$, and the pulse energy is dispersed in the case of exceeding T_{in} . Although the soliton array is applicable to a burst generator, it comes into problem when we make a single highly compressed pulse.

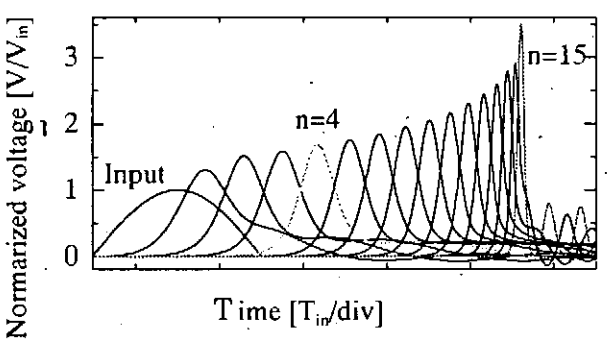

Fig.4 Pulse propagation in the Taper NLTL

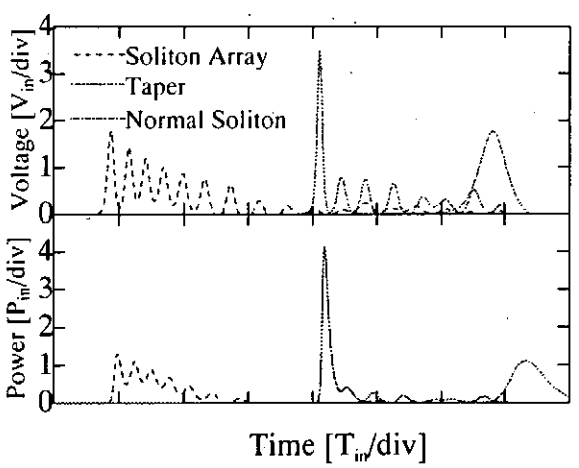

Fig.5 Comparison with normal soliton and

A tapered nonlinear transmission line(tapered NLTL), where the time constant of LC components decreases in the direction of pulse propagation with constant surge impedance, is proposed to obtain more efficient pulse compression and voltage amplification. The numerical calculation suggests that the optimum way of decreasing the circuit parameters is exponential one[3]. However, considering difficulty of obtaining the nonlinear capacitors with various C-V characteristics, we select the linear way of decreasing the parameters. We define a compression factor as $k=C_0/C_n(=L_0/L_n)$. Figure4 shows pulse propagation in the taper NLTL of L_0=5μH, C_0=27.5nF, α=4.4, k=5, N=15. After soliton formation at n=4, the pulse is compressed gradually as it propagates in the tapered NLTL.

Figure 5 shows normal soliton ($L_n=L_0$, $C_n=C_0$) and soliton array ($L_n=L_0/k$, $C_n=C_0/k$) and soliton in tapered NTLT with the same nonlinearity capacitors. The compression ratio of each curve is 2.5, 10, 10 and the voltage amplification effect is 1.8, 1.8, 3.5, respectively. The compression and amplification of input pulse are realized most effectively in the tapered NLTL.

4. Application of the fabricated $BaTiO_3$ based nonlinear ceramic disk capacitors to high-voltage nonlinear transmission line

The front edge of voltage pulse is easily sharpened in a *LC* ladder circuit with nonlinear capacitors[4]. The conventional NLTL consisted of air core coils as linear inductors and commercially available ceramic disk capacitors as nonlinear capacitors. The rise time of input voltage up to 20 kV was reduced from 1μsec to 200 nsec at the end of the NLTL[1]. For generating much shorter pulses, a few difficulties are in these NLTL. First, the nonlinearity of commercially available ceramic disk capacitors deviates from the ideal curves over the self-resonance frequency because the residual inductance spoils the characteristics of the capacitor. Second, the *C-V* curves of such capacitors are somewhat apart from the ideal one. Third, the NLTL cannot derive large current and high power to the low impedance load because of the large characteristic impedance of the NLTL. To overcome these difficulties, we have fabricated the high voltage $BaTiO_3$ based ceramic disk capacitors that show strong voltage dependence with extremely low residual inductance. With these capacitors, we can build the low impedance NLTL.

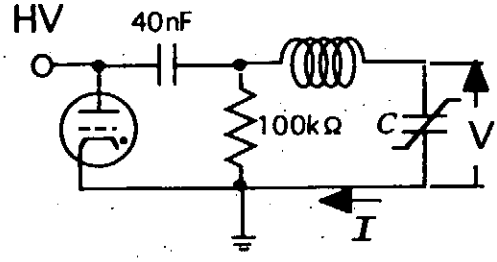

Fig.6 Test circuit for nonlinear capacitance

The ceramic capacitors were fabricated from the barium titanate powder of ~1μm grain size. The mixture was hydraulically pressed at 1 t/cm^2 into the disc of 30mm diameter. After sintering, diameter of disk was about 24 mm, thickness was about 2mm, and density was 5.1-5.4 g/cm^3. Diameter of silver electrode was 21 mm, the capacitance at zero applied voltage was about 10 nF, and relative permittivity was about 7000 at the temperature of 21℃.

The capacitance dependency on the pulsed voltage was measured in the circuit as shown in Fig.6. From the measured voltage and current waveformes of *C*, the capacitance C can be calculated as follows.

$$C = \frac{dQ}{dV} = \frac{dQ/dt}{dV/dt} = \frac{I}{dV/dt} \quad \cdots\cdots\cdots\cdots\cdots\cdots\cdots\cdots\cdots\cdots\cdots\cdots\cdots\cdots\cdots\cdots\cdots\cdots \quad (4)$$

, where Q is the charge of the capacitor. Figure 7 shows the measured voltage and current waveforms. From Fig.7 and equation (4), the measured typical normalized *C-V* response under pulsed applied voltage is shown in Fig.8. As we expected, the fabricated capacitor shows the

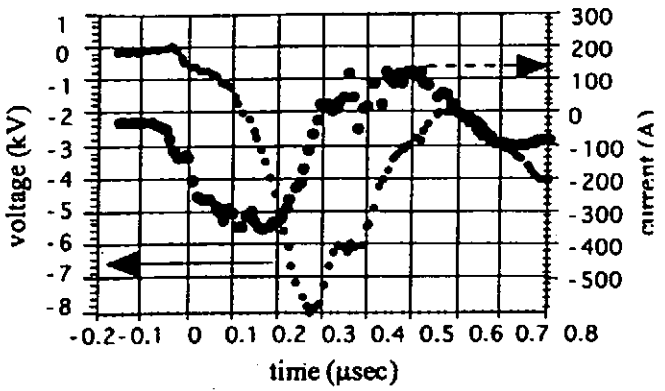

Fig.7 Voltage and current waveforms of the nonlinear capacitor.

strong dependence of voltage. The ratio of capacitance at zero applied voltage to that at the maximum voltage is 6. The withstand voltage under DC voltage was 9 kV.

Fig.9 shows the typical P-E hysteresis loop of the fabricated ceramic disk capacitor measured by the Saywer-Tower Circuit at the temperature of 21℃. The hysteresis loss is estimated to be about 40 mJ at

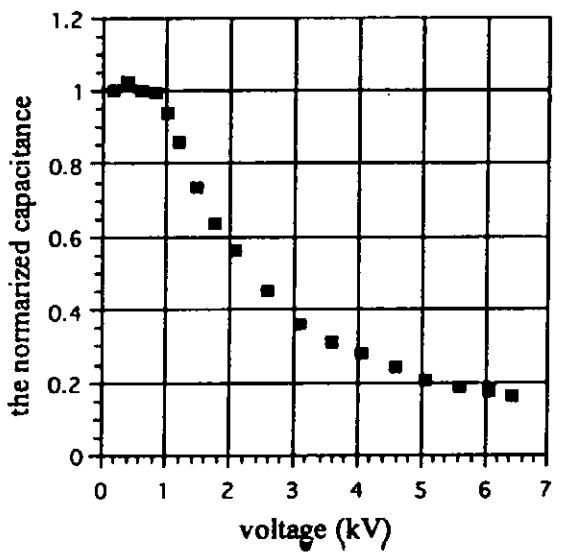

Fig.8 C-V curve of $BaTiO_3$ ceramic

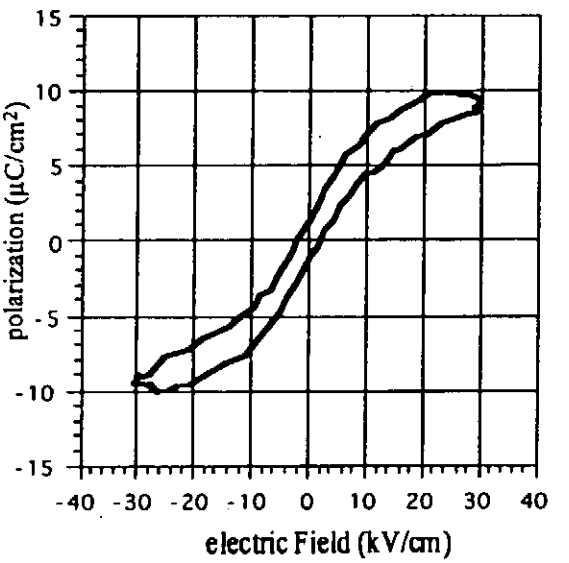

Fig.9 Pulsed P-E hysteresis loop of $BaTiO_3$

the operating voltage of ±6kV. Hysteresis loss causes the voltage attenuation and the efficiency drop in the NLTL. By the temperature control of the sintering and optimization of ingredient ratio, the loss could be reduced.

Figure 10(a) shows the frequency characteristics of the fabricated ceramic capacitor measured by an impedance gain/phase analyzer. For comparison, the data of a commercially available ceramic capacitor is shown in Fig.10(b). The distinguished difference between them is that the fabricated ceramic capacitor does not have the self-resonance point of frequency because of no lead wire. Moreover, in the variation of capacitance with frequency, the dielectric relaxation does not arise below the range of 10 MHz.

One section of the NLTL with these fabricated capacitors, we connected four ceramic capacitors in series-parallel between the two copper sheets as shown in Fig.11. The capacitance of one section without applied voltage is about 10 nF. The residual inductance L is given by equation (5) and estimated 7 nH per one section.

$$L = \mu_0 \frac{ld}{w} \quad \cdots\cdots (5)$$

, where w is the width of the copper sheet, l is the length between the sections and d is the

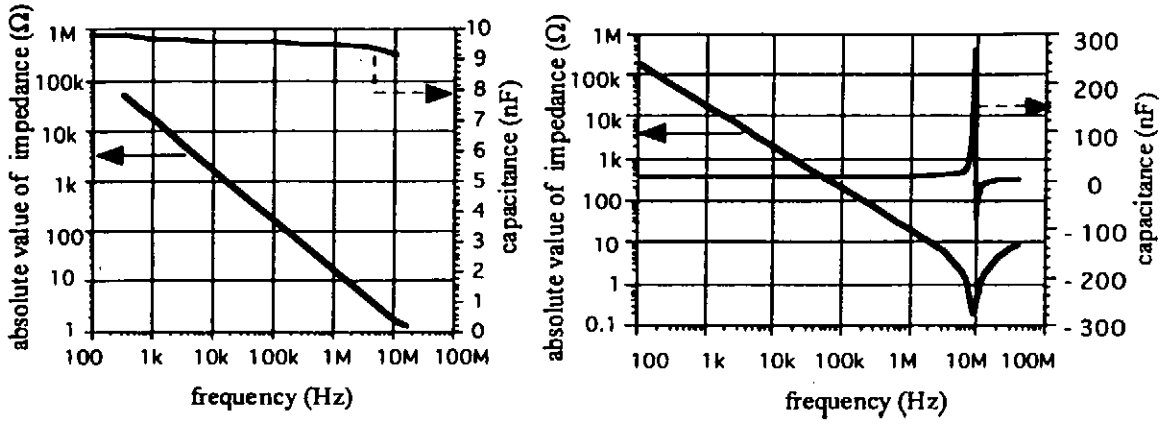

(a) Fabricated $BaTiO_3$ capacitor (b) Commercial $BaTiO_3$ capacitor

Fig.10 Frequency dependency of $BaTiO_3$ ceramic capacitors

distance between the upper and the lower copper sheets. The impedance of the NLTL is calculated as about 1.4Ω. The average capacitance C_{lh} in the range of 0~15 kV is given by equation (6)

$$C_{lh} = \frac{1}{V_h - V_l} \int_{V_l}^{V_h} C(V) dV \quad \cdots\cdots (6)$$

, where V_h is the maximum voltage, V_l is the minimum voltage and $C(V)$ is the approximate equation of capacitance via voltage shown in Fig.8.

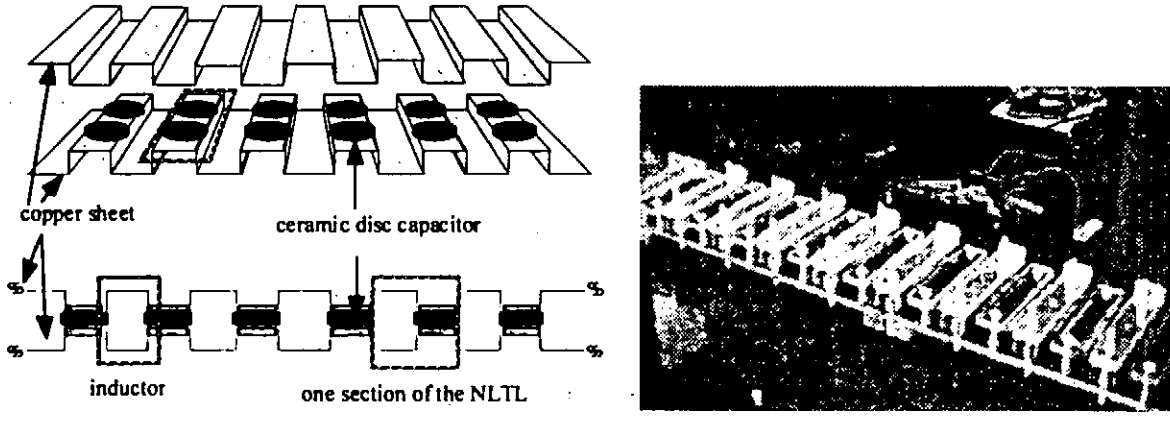

Fig.11 NLTL assembled with fabricated $BaTiO_3$ ceramic capacitors

Figure 12 shows voltage waveforms measured at input and output points of the NLTL immersed in the insulation liquid 'fluorinert' to prevent the discharge between copper sheets. The NLTL is terminated by 1.5 Ω resistor. Because the characteristic impedance of the NLTL changes with the applied voltage, the impedance does not match to the resistive load. Thus,

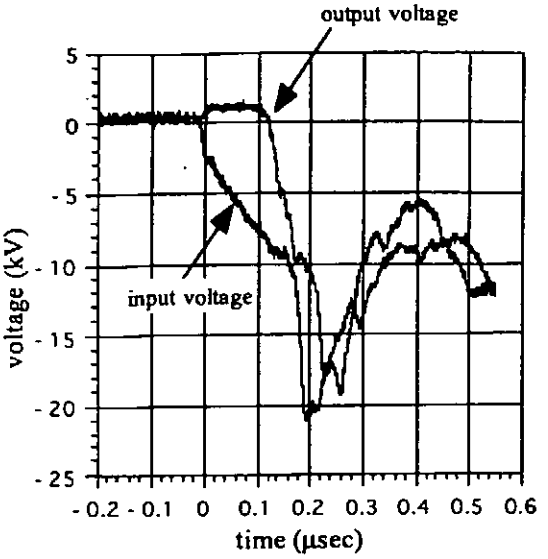

Fig.12 Input and output voltage waveforms of the NLTL

the reflected wave arises toward the input point of the NLTL. The length of the NLTL is too short to distinguish the incident wave from the reflected wave, so we cannot estimate the sharpening effect around the voltage range of 10 kV. Below 10 kV, the input rise time of 150 nsec is reduced to 60 nsec. We are now planning to increase the number of the section in the NLTL and to estimate the characteristic of the NLTL in detail.

5. Conclusion

We have developed a NLTL with specially fabricated nonlinear $BaTiO_3$ capacitors according to the design rules revealed by numerical calculations. The calculated date shows a limit of the pulse compression and the voltage amplification effects by a soliton formation. Newly proposed tapered NLTL could improve the pulse compressing efficiency of fast high voltage pulse generators. The fabricated $BaTiO_3$ based ceramic disk capacitors show the strong nonlinearity on the applied voltage. The reduction rate of the capacitance at zero applied voltage to the maximum one is about 6. The response frequency is over 10 MHz by the absence of the self-resonance frequency and the dielectric relaxation. We have applied the fabricated nonlinear ceramic capacitors to build a high voltage and low impedance NLTL. The input pulse of 150 nsec rise time and of 10kV peak voltage was sharpened to 60nsec rise time without voltage drop using newly developed NLTL.

References

1) A.Ishii, et al.: Int. Conf. on Gas Discharge and Their Applications, **2** (1995),344~347.

2) R J Baker, et al. :Meas.Sci.Technol.,**4** (1993)893~895.

3) Amir Mostofi, et al.:IEEE. Journal of quantum electronics, **33**,no.4(1997)620~628.

4) G.Branch, et al. :J.Phys D Appl.Phys.,**29**(1996)2170~2178.

Control of Radial Motion of a Gas-puff Z-pinch Plasma by an Axial Magnetic Field

Takehito Igusa,[+] Keiichi Takasugi
and Tetsu Miyamoto

Atomic Energy Research Institute, Nihon University
[+]College of Science and Technology, Nihon University

Abstract

The axial magnetic field was applied to the Ar gas-puff z-pinch plasma for the control of x-ray emission. The K-shell radiation of Ar ions was suppressed and the L-shell radiation was intensified by the axial field. The suppression of $m = 0$ mode instability was observed by using a framing camera.

I. Introduction

Hot spots of z-pinch plasmas are produced as the results of $m = 0$ mode instability, which is originated from the Rayleigh-Taylor instability on the contraction of the z-pinch column.[1] The application of axial magnetic field to z-pinch plasma have been examined to stabilize and sustain the plasma for the controled nuclear fusion research. This technique was used for pulsed high magnetic field generation[2] or creating a new magnetic configuration for plasma confinement.[3] We applied the same technique to control the x-ray radiation from z-pinch plasma through the control of plasma dynamics.

In the Ar z-pinch the x-ray occurrs mostly in K-shell (0.3–0.4 nm) and L-shell (3–4 nm) radiations of ions.[4] The use of axial magnetic field will control the extent of the maximum pinch, the temperature of the hot spots, hence the wavelength region of the x-ray emission. The suppression of K-shell radiation of Ar ions has been observed by the use of the axial magnetic field.[5,6] In this experiment we again reexamined the advantage of this technique, and investigated the radial motion of the collapsing plasma using a framing camera. The experiment is intended to clarify the role of axial magnetic field on the dynamics of the plasma and the x-ray generation.

II. Concept of Axial Field Application

After the plasma is sufficiently heated up during discharge, the pinch effect takes place, and the plasma begins to collapse. The plasma current is localized on its surface as a sheet. The externally applied axial magnetic field will be taken in the current sheet on the collapse if the conductivity of the plasma is sufficiently high (Fig. 1). If the total magnetic flux inside the current sheet is conserved,

$$B_z = B_{z0}\left(\frac{r_0}{r}\right)^2, \tag{1}$$

where B_z and B_{z0} are the axial magnetic field at the sheet radius r and r_0. The radius r_0 corresponds to the initial radius. The self magnetic field produced by the plasma current J_z is

$$B_\theta = \frac{\mu_0 J_z}{2\pi r}. \tag{2}$$

The trapped axial magnetic field B_z is weak and takes little effect on the radial motion at large radius. It increases faster than the outer field B_θ as it shrinks. The inner magnetic pressure takes important effect at smaller radius. Assuming the inner and the outer magnetic pressures are balanced (the plasma pressure is neglected), the equilibrium radius is

$$r = \frac{2\pi r_0^2 B_{z0}}{\mu_0 J_z}. \tag{3}$$

This indicates that the equilibrium radius is proportional to the initially applied axial magnetic field B_{z0}. This internal magnetic pressure will prevent overheating of the plasma due

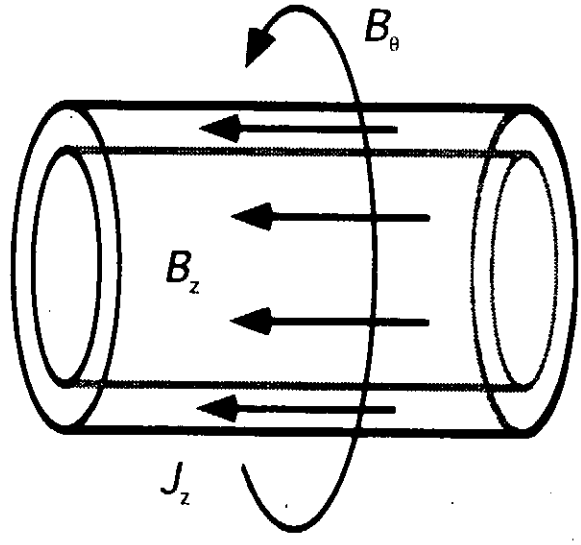

Fig. 1. Application of the axial magnetic field.

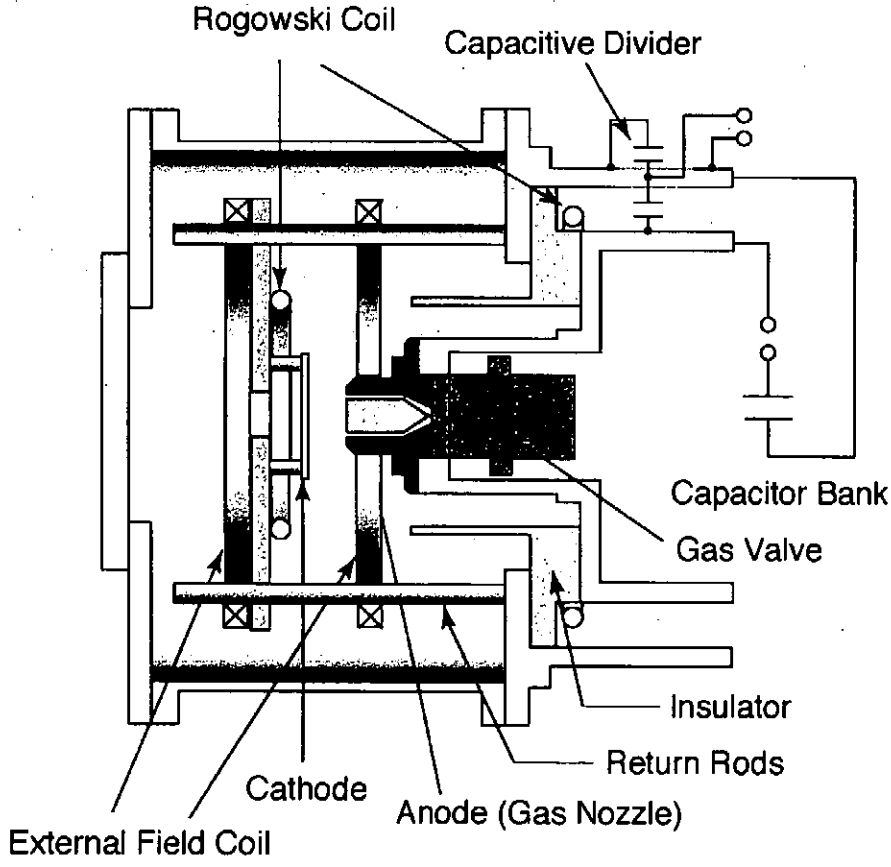

Fig. 2. Schematic view of the "SHOTGUN" z-pinch device.

to $m = 0$ mode instability. The axial magnetic field will take effect only at the maximum pinch without changing the discharge characteristics.

III. Experimental Setup

Figure 2 shows the schematic view of the gas-puff z-pinch device, "SHOTGUN". The storage capacitance is 24 μF, and the storage energy is 7.5 kJ at the charged voltage of 25 kV. The spacing of electrodes is 30 mm. Annular gas shell with the diameter of 28 mm is formed between the electrodes using a high speed gas valve. Ar gas is used in the experiment.

Axial magnetic field is produced by a pair of parallel coils placed near the electrodes. The radius and the separation of the coils are 15.9 cm and 12.4 cm, respectively, and the coil winding is 100. The coil is connected to the storage capacitor of 1.6 mF. The peak current of the coil is 13.4 A (64.6 G at the center) at 7.1 ms after the trigger with the charged voltage of 100 V. The main discharge of the plasma is adjusted to occur at the peak field. Almost uniform magnetic field distribution is formed between the electrodes.

Discharge current of the plasma is measured by a Rogowskii coil placed near the cathode. A scintillation probe (SCI) with Be 10 μm filter is used to detect hard x-ray from the pinched plasma ($E > 1$ keV). A vacuum x-ray diode (XRD) with Al photocathode is used to detect wide range of XUV to soft x-ray (20 eV $< E <$ 2 keV). The K-shell radiations of Ar ions are detected mainly by the scintillation probe, and the L-shell radiations are detected by the XRD.

A framing camera is prepared for the study of plasma motion during the collapse. An Image Intensifier Tube (Hamamatsu Photonics V3063U) is installed in the Polaroid 600SE Camera together with a set of relay lenses. The gate width of the electrical shutter is adjusted to 10 ns.

IV. Experimental Results

In Fig. 3 the typical discharge current and x-ray signals detected by the SCI and the XRD are compared for (a) without and (b) with axial magnetic field. Maximum pinch

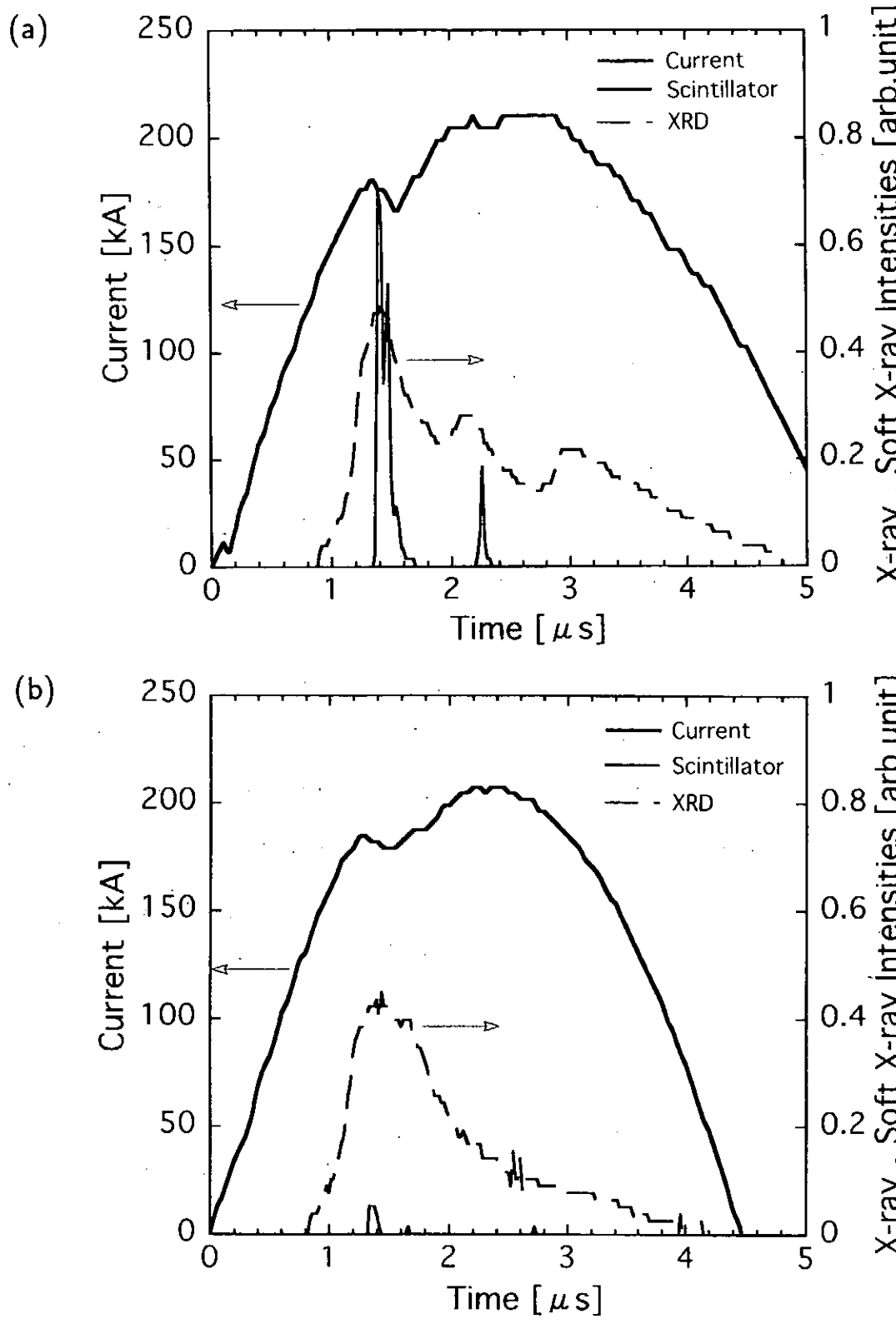

Fig. 3. Discharge current and x-ray radiation intensities (a) without and (b) with axial magnetic field (400 G).

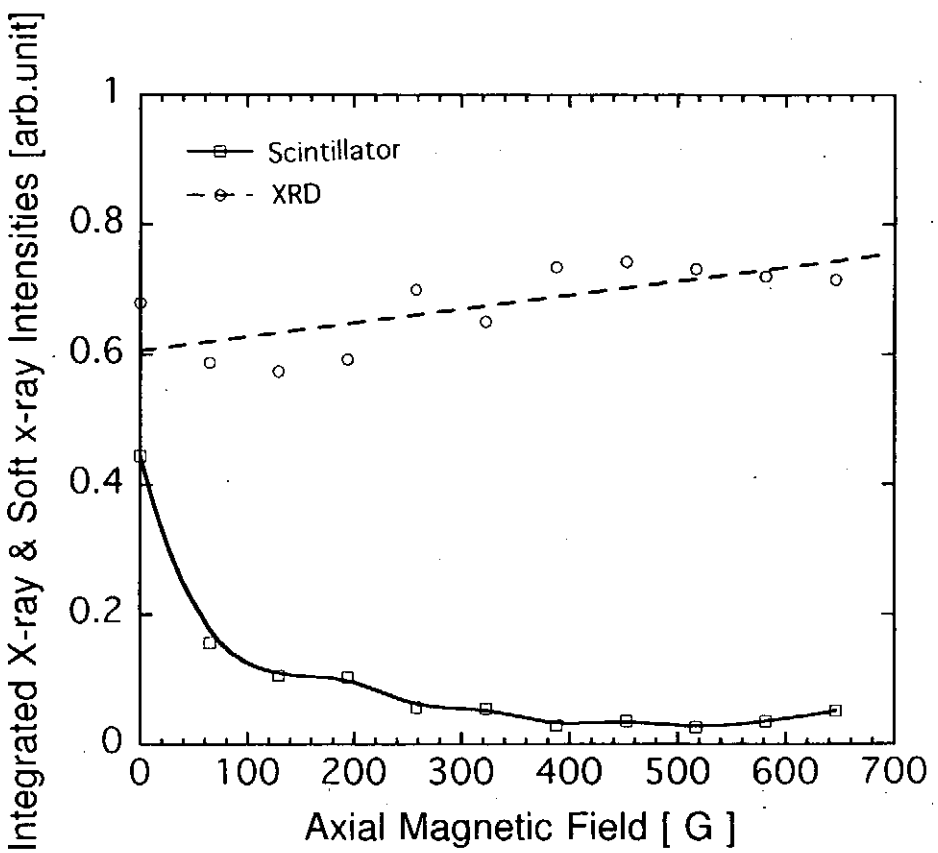

Fig. 4. Dependences of x-ray radiation intensities on the axial field.

occurrs at about 1.5 μs after the discharge starting. The plasma current is about 180 kA. Without axial magnetic field a sharp dip is formed on the current signal, which shows a sudden increase of circuit inductance due to the maximum pinch of the plasma. Pulses of both the SCI and XRD signals are observed coincident with the current dip. The first pinch is followd by one or a few more pinches. This indicates that the excess compression of the pinch column occurrs at the first pinch and the radial motion bounces. This bouncing is avoided by a small amount of axial magnetic field (60 G).

When the axial magnetic field of 400 G is applied (Fig. 3(b)), the dip of the current becomes shallow and wide. The SCI signal almost disappears. The XRD signal still exists, and the duration of the signal becomes longer than the case without the axial field.

The dependences of the SCI and XRD on the axial magnetic field intensity was investigated. Figure 4 shows the time-integrated signals of SCI and XRD plotted as a function of the axial field. The SCI signal rapidly decreases with the field and is very weak above the field of 300 G. On the other hand the XRD signal increases slightly with the field. As the peak intensity of the XRD do not change significantly, the duration of the signal increases. It is again confirmed that the life time of the pinched plasma is expanded by the axial magnetic field.

Figure 5 shows (a) a visible framing photograph at the maximum pinch and (b) an x-ray pinhole photograph taken in a shot without axial magnetic field. The visible plasma column is divided into three sections as shown in Fig. 5(a). The plasma may not be actually separated. It may be locally compressed and heated up to high temparature, and the plasma do not emit visible light. One of the hot spots in the x-ray corresponds to that position (Fig. 5(b)).

With the axial field of 200 G the hot spot disappears (Fig. 6(b)). The plasma column at the maximum pinch becomes more uniform and no separation is seen in Fig. 6(a). The equilibrium radius calculated using eq. (3) would be 0.1 mm for $J_z = 180$ kA and $B_{z0} = 200$ G. The observed plasma radius is about 1 mm. This is larger than the estimation. The main reason for this would be the increase of plasma pressure due to the adiabatic compression.

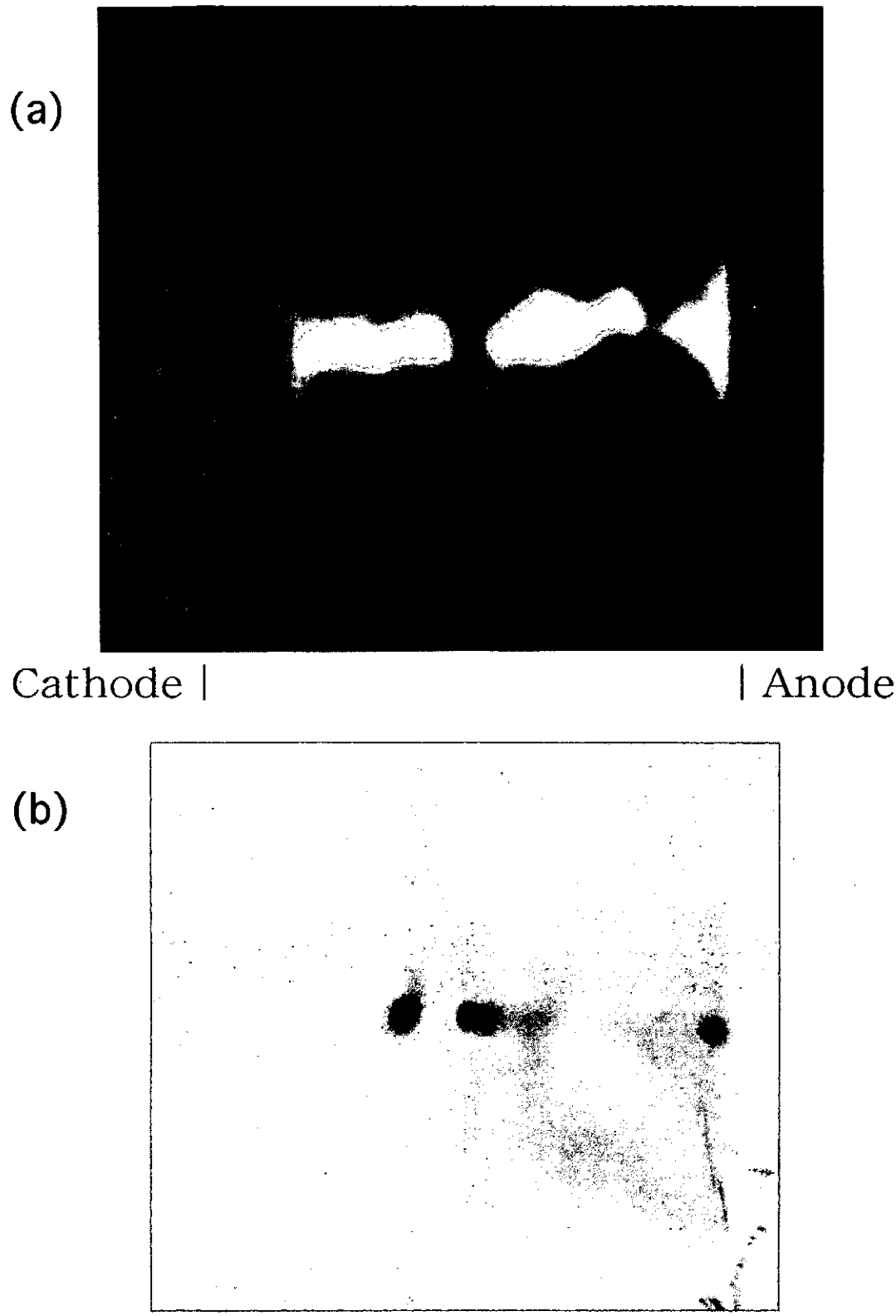

Fig. 5. (a) Visible framing and (b) x-ray pinhole phographs without axial magnetic field.

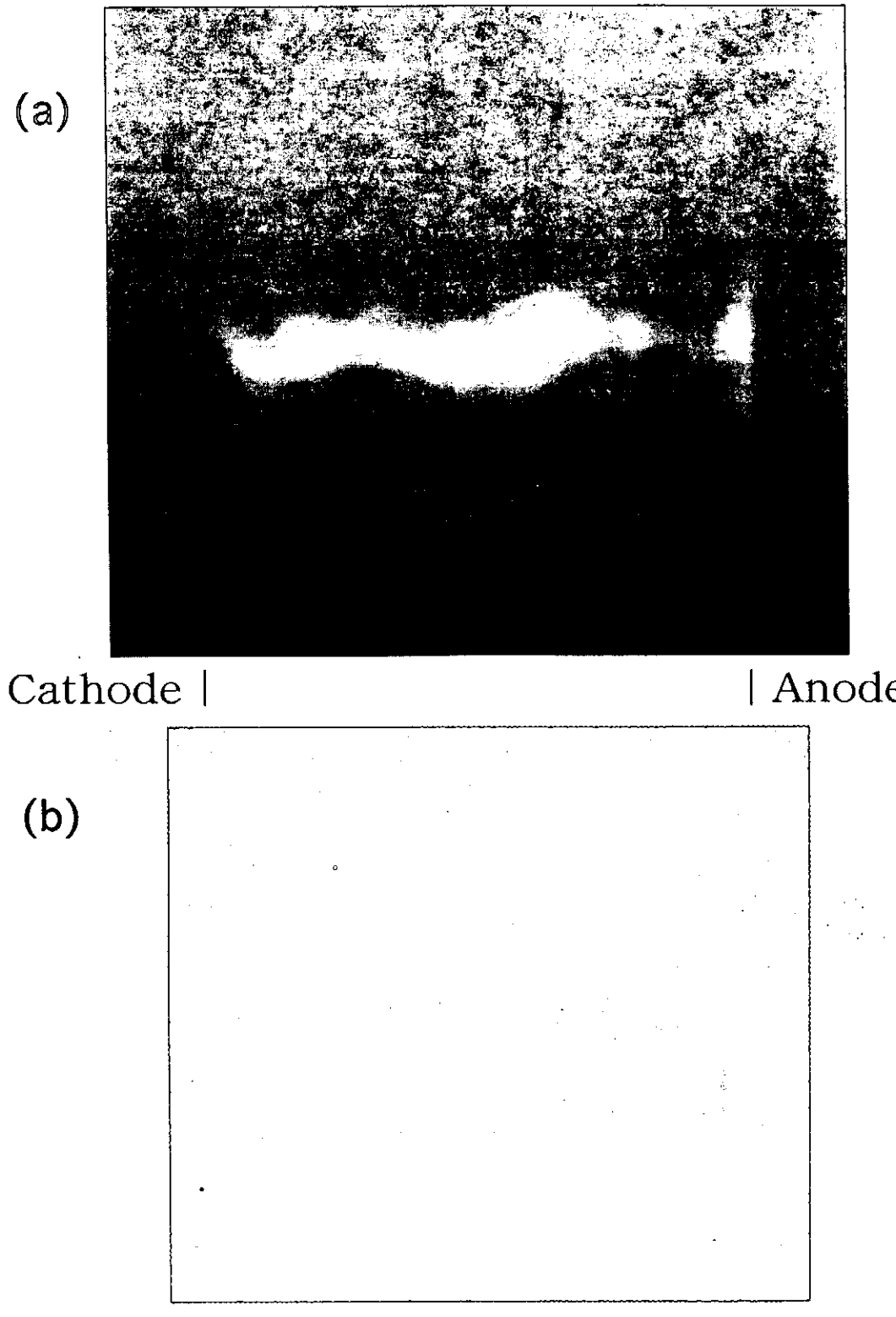

Fig. 6. (a) Visible framing and (b) x-ray pinhole phographs with axial magnetic field (200 G).

V. Summary

The axial magnetic field was applied to the gas-puff z-pinch plasma for the control of x-ray emission. The SCI signal (due to K-shell radiation of Ar ions) was suppressed and the XRD signal (mostly from L-shell radiation) was intensified by the axial field. The lifetime of the pinched plasma was extended by applying the axial magnetic field.

Visible images of the plasma column at maximum pinch was observed by a fast framing camera. The plasma is pretty unstable and is separated into several sections due to $m = 0$ mode instability without the axial field. This strong compression was suppressed by the axial field. The observed equilibrium radius of the plasma was larger than the estimation.

References

[1] K. Takasugi, T. Miyamoto, K. Moriyama and H. Suzuki: AIP Conf. Proc. **299**, 251 (1994).

[2] F.J. Wessel, F.S. Felber, N.C. Wild, H.U. Rahman, E. Ruden and A. Fisher: Appl. Phys. Lett. **48**, 1119 (1986).

[3] H.U. Rahman, P. Ney, F.J. Wessel and N. Rostoker: AIP Conf. Proc. **299**, 696 (1994).

[4] V.L. Kantsyrev, K. Takasugi, K. Tatsumi, T. Miyamoto and A.S. Shlyaptseva: Proc. 1996 Int. Conf. Plasma Physics Vol. 2, 1106 (1997).

[5] K. Tatsumi, K. Takasugi, T. Igusa and T. Miyamoto : NIFS-PROC-36, 121 (1997).

[6] K. Takasugi, T. Miyamoto, K. Tatsumi and T. Igusa: AIP Conf. Proc. **409**, 299 (1998).

Equilibrium of Z-pinch in the Magnetic Field of Return Current.

A.Muravich and T.Miyamoto
Atomic Energy Research Institute, Nihon University

Abstract.

Stationary state of Z-pinch in the presence of magnetic field of return current is studied. Equilibrium shape of plasma boundary is found numerically. Different types of return current conductors are tested from the point of view of producing of elongated plasma sheet, which is significantly more stable against instabilities of interchange mode than ordinary fiber Z-pinch.

Introduction.

Equilibrium state of most Z-pinches (for example, of ordinary fiber pinch) is circular column, but it is not the case, if there is some external magnetic field ([1], [2]). In the present paper we study equilibrium of noncircular Z-pinches that can be produced under the influence of the magnetic field of return current conductors. The purpose of this research is finding a configuration of return current conductors, that allow to produce plasma sheet, that has elongated central part with zero or negative curvature. As was shown in [1], such pinch configurations are of considerable interest from the point of view of stability properties.

The model.

Present calculations are provided for the case of fully ionized hydrogen plasma with homogeneous temperature and current density. Plasma is assumed to spread infinitely in Z-direction (accordingly, there is only Z-component of plasma current density $\vec{i} = (0,0,i)$), the boundary shape is symmetric in XZ and YZ planes. The characteristic time is much less than time of penetration of magnetic field into a metal, so we concern the return current conductors as ideal conductors. The return current conductors are also assumed to be symmetric in XZ and YZ planes, so the shapes of electrodes $r_1(x)$ and $r_2(x)$ can be expressed by one function $y=r(x)$, $(0 \le x \le l)$: $r_1(\pm x) = -r_2(\pm x) = r(x)$.

Plasma current density i and plasma temperature T are used as free parameters. Boundary of plasma $y = f(x)$ is a surface of zero plasma pressure:

$$p(x, f(x)) = 0 \qquad (1)$$

Pressure in turn determines by pressure equilibrium equation:

$$\nabla p = \vec{i} \times (\vec{B}^p + \vec{B}^r) \qquad (2)$$

where $\vec{B}^p$ is plasma magnetic field and $\vec{B}^r$ is magnetic field of return current. Full energy balance equation is:

$$\int_{-a}^{a} dx \int_{-f(x)}^{f(x)} P_{RAD} dy = \int_{-a}^{a} dx \int_{-f(x)}^{f(x)} \frac{i^2}{\sigma} dy \qquad (3)$$

where P_{RAD} is radiated power density and σ is plasma conductivity, so $P_J = i^2/\sigma$ is joule heating. The problem is self-consistent: equilibrium plasma boundary shape $y = f(x)$ (fig.1) determined by eqs.(1) and (2) must simultaneously satisfy to eq.(3). We use method of iterations. For the supposed plasma boundary shape $f_i(x)$ ($f_i(a) = f_i(-a) = 0$) we calculate return current density distribution, using condition that normal component of magnetic field B_n must vanish in the surface $y = r(x)$ of return current conductors. Magnetic field is calculated in mesh points as a sum of plasma magnetic field (B_x^p, B_y^p) and return current magnetic field (B_x^r, B_y^r). In this total magnetic field we find surface $y = f_{i+1}(x)$ that simultaneously satisfies to the eqs.(1-3). We repeat calculation procedure using $y = f_{i+1}(x)$ as new iteration for boundary shape. If the initially supposed shape $f_0(x)$ is not very distinguish from true self-consistent solution, a rather small number of iterations are needed.

We distinguish two types of return current conductors: configurations with open ends and closed ends (chambers). As an example of "open ends" type, we consider flat ($r(x) = d = const$, fig.3) and hyperbolic configurations ($r(x) = d(1 + (x/h)^2)^{1/2}$, fig.2). Different kinds of chambers (fig.4-6) are investigated as well.

Results

① Parallel flat return current conductors.

In this case it is convenient to introduce parameter $r_{PB} = (I_{PB}/(\pi i))^{1/2}$, where I_{PB} is Pease-Braginskii current of ordinary circular Z-pinch. Thus r_{PB} has univalent correspondence with i and means radius of equilibrium isolated pinch. Calculation shows that despite there are 4 free parameters in this problem (T, r_{PB}, d, l),

plasma boundary shape is critically depends only on two non-dimensional parameters: r_{PB}/d and l/d. While r_{PB}/d is much smaller than 1, $|a-r_{PB}|/r_{PB}$ and $|b-r_{PB}|/r_{PB}$ are also respectively small and shape of pinch is almost not differ from circular column. But when r_{PB}/d is increased up to order of 1, b stops growth because of influence of magnetic field of return current (in fact, b can not be larger, than $0.75d$), a in turn increase dramatically (up to order of l), so pinch cross-section becomes very distinguish from circular. Parameter l/d expresses relative elongation of conductors: $l/d=0$ means two infinitely thin wires and $l/d=\infty$ correspond to the case of two planes, which spread infinitely in x-direction. In the fig.3 calculated plasma boundary lines are shown for the different parameters r_{PB} for $l/d=2$ and $l/d=5$. One can see that with decreasing of current density, plasma shape changes from circular towards elliptic, and finally to sheet with elliptic ends. For the large l/d stable sheet solutions can be obtained for a less than $a_{\max}=l-1.5d\pm d$. The ambiguity in determination of $a_{\max}$ is caused by existence of critical minimum value of current density i_{cr} (or critical maximum value of r_{PB}/d). At this value derivatives of a, full current I, and some other plasma parameters becomes infinity, as one can see in the fig.7. So, it is rather difficult to determine values $a_{\max}=a(i_{cr})$ and $I_{\max}=I(i_{cr})$ numerically with better accuracy. If a is large enough ($a \geq 3d$), b is nearly constant about $0.75d$ for any l/d. Radius of curvature of sheet ends is also almost a constant, $r_c \approx 0.5d$. This type of solutions was predicted in [1].

② Hyperbolic return current conductors.

Hyperbolic configuration makes possible existence of plasma sheet, which has a negative boundary curvature of the central part (below negative curvature sheet) (fig.2). But in this case for the given length l, $a_{\max}$ decreases with increasing of d/h, as shown in fig.8. Namely, small d/h means that conductors are almost flat, so negative curvature can't be obtained, but maximum length of sheet is comparable with l. Conductors with large d/h has significantly curved central part and let to obtain plasma sheet with some negative curvature, but length of such a sheet can't exceed $2d$ (fig.8). Thus, equilibrium negative curvature sheet produced by this configuration of return current conductors can not be very elongated. So, we suppose that "open ends" configurations are not very effective in obtaining of elongated negative curvature plasma sheets.

③ Various kinds of closed return current conductors.

The simplest one is rectangular (fig.4). Shape of sheet, obtained for this type of chamber, is only slightly distinguished from obtained for two flat conductors. More interesting cases are the types of chambers with expanded ends (fig.5-6), because they

let possibility to obtain solutions of elongated negative curvature sheet type. Firstly we considered chambers of fig.5 type, because for this type calculation procedure is quite simple and fast. But chambers of this type have such a shortage as right angles inside of chamber (points A, B, C, D in fig.5). In this points density of return current will be large, and respectively large gradients of electromagnetic fields will occur, that can cause parasitic discharges, additional heating of walls and other undesired processes. Chambers with hyperbolic central part and elliptic ends (fig.6) has smooth walls with continuos derivative $\partial r(x)/\partial x$, so these chambers are free from mentioned above shortage and looks preferable for the experimental producing of elongated negative curvature sheets.

Discussion

Sheet pinch of negative curvature type, is more stable against MHD instabilities of interchange mode. In this case magnetic field lines has negative curvature in most part of pinch, so fast plasma boundary perturbations in the central part will be damped. But even if plasma configuration has MHD stability, it is affected by tearing mode instability.

If the time of penetration of interchange mode instability τ_i is less than time of penetration of tearing mode instability τ_t, perturbations will mainly rise from the ends of sheet. In this case, the curvature of central part will not affect on the time of penetration of perturbations. But if τ_i is not much smaller than τ_t, pinch configuration with negative curvature can be more stable, because it prevented from additional growth of instabilities of interchange mode in the central region.

Growth rate of tearing mode disturbance γ_t can be expressed in terms of "Alfven transit time" τ_a, and "magnetic field diffusion time" τ_r:

$$\gamma_t \sim \tau_a^{-2/5} \tau_r^{-3/5} \qquad (4)$$

In our case

$$\tau_a \approx \frac{a}{C_s} \qquad (5)$$

$$\tau_r \approx \frac{a^2 \mu_0}{\eta} \qquad (6),$$

where $C_s = (k_B T / M_i)^{1/2}$ is velocity of ion sound, η is a plasma resistivity and a is a width of plasma sheet. Accordingly, γ_t can be estimated as

$$\gamma_t \sim \frac{C_s^{2/5}}{a^{8/5}}\left(\frac{\eta}{\mu_0}\right)^{3/5} \qquad (7)$$

For the hydrogen plasma we have approximately

$$\gamma_t \sim 10^7 a^{-1.6} T^{-0.7} \qquad (8)$$

where a in mm, T in keV, γ_t in $\sec^{-1}$. Equation (8) shows that if we want to have $\tau_t = \gamma_t \geq 10^{-6} s$, we must satisfy condition:

$$a^{1.6} T^{0.7} \geq 10, \qquad (9)$$

or, roughly speaking, $a^2 T$ must be more, than some tens.

Thus, even if we will have high plasma temperatures about order of some keV, from eq.(9) it follows that a and accordingly distance between return current conductors d must be not less than some millimeters. Otherwise tearing mode instability perturbations will disturb the central part of sheet within some hundreds nanoseconds.

Growth rate of interchange mode γ_i from the sheet ends can be estimated as:

$$\gamma_i \approx \frac{C_s}{\sqrt{r_c s}} \qquad (10)$$

where r_c is radius of curvature, and s is pressure gradient scale-length. In our case $r_c \approx 0.5d$, $s \sim d$ (near the ends), so

$$\gamma_i^e \sim \frac{C_s}{0.7d} \approx \frac{C_s}{a} \approx 3 \times 10^8 \frac{\sqrt{T}}{a} \qquad (11)$$

It is quite naturally, that γ_i of the sheet ends is the same with ordinary fiber pinch of radius a. For instance, if $a \sim 3mm$ and $T \sim 1keV$, time of growing of interchange mode instability in the ends $\tau_i^e = (\gamma_i^e)^{-1} \sim 10ns$. Nevertheless, much longer time is needed to the penetration of such a perturbations into the central region. Firstly, even if velocity of these perturbations V_p will have maximum possible value $\sim C_s$, it will take time about $\tau_i^e b/a$ to disturb central region. But the x component of pressure gradient is very small in most part of sheet pinch, so we suppose in this region parameter $s >> d$ and accordingly growth rate of interchange mode instability $\gamma_i^c << \gamma_i^e$, so velocity of perturbations $V_p << C_s$. For this reason we estimate the time of penetration of these perturbations into the central region as $\tau_i^c >> \tau_i^e b/a$, and for mentioned above plasma sheet parameters τ_i^c can be of order of microsecond.

Conclusions

Equilibrium configurations of sheet pinch plasma were numerically tested for the different types of return current conductors. Pair of parallel flat conductors seems preferable for the obtaining sheet pinch with zero curvature of central part. Open configurations of return current conductors are not very effective for the producing of sheet pinch with negative curvature of central part, so we propose for this aim chambers with barbell-like cross section (fig.5). Under some plasma parameters the time of penetration of instabilities both interchange and tearing mode into central part of pinch can be of order of microsecond. As a next step of this work, we are preparing realization of sheet pinch experiments. In these experiments we are planning to check the theoretical considerations, and find the way of formation of homogeneous plasma sheet.

References

[1]. T.Miyamoto, "Steady state of elliptic Z-pinches", AIP Conf. Proc. 409 (1997), p.401-405.

[2]. T.Miyamoto and A.Muravich, "Elliptic Z-pinches", Proc. of 1st Asia-Pacific Int. Symp. on Basic and Appl. of Plasma Tech. (Dec.15-16, 1997, Taiwan) pp.109-112.

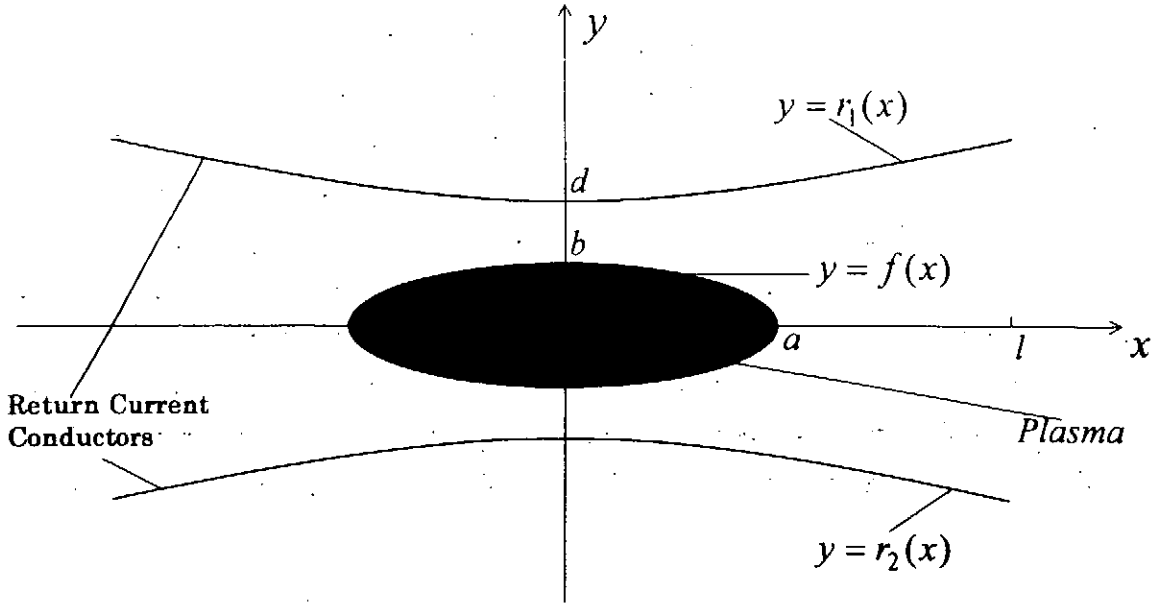

Fig.1 Schema of sheet pinch configuration.

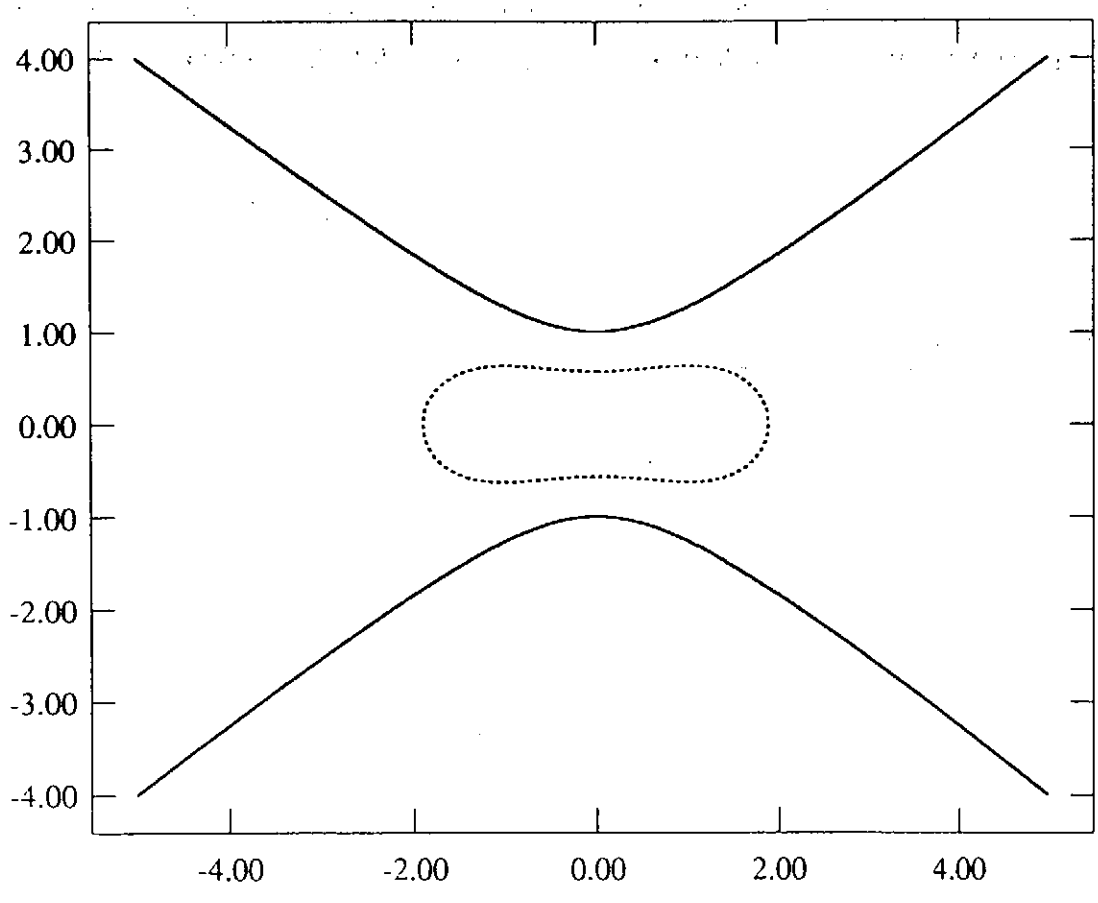

Fig.2 Hyperbolic return current conductors.

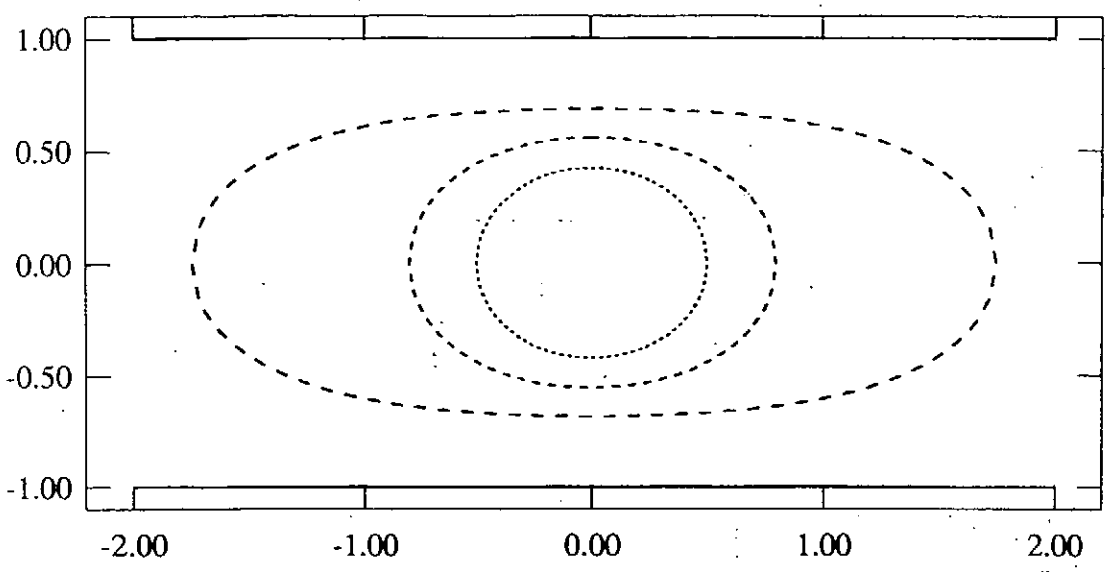

(*a*)

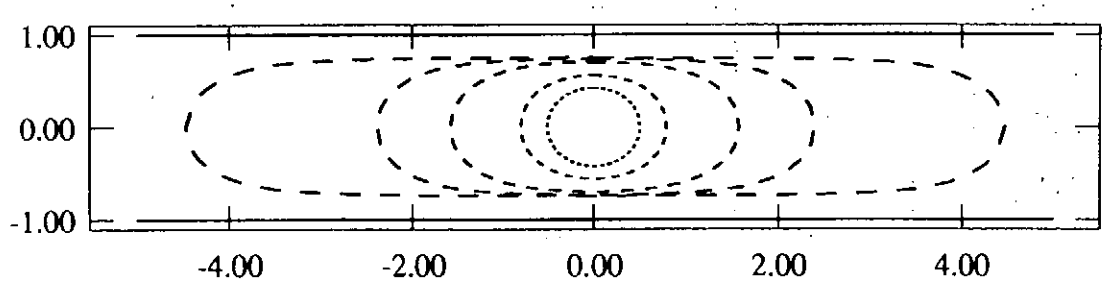

(*b*)

Fig.3 Flat return current conductors. Plasma equilibrium shapes at different values of parameter r_{PB}/d for l/d=2 (a) and l/d=5 (b).

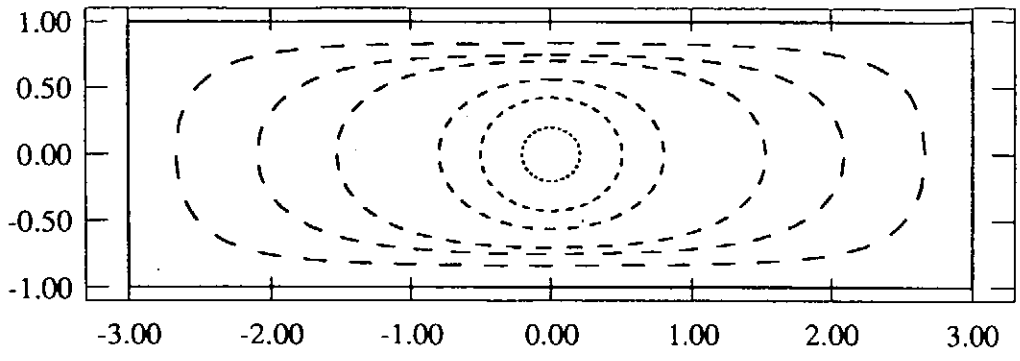

Fig.4 Rectangular return current.

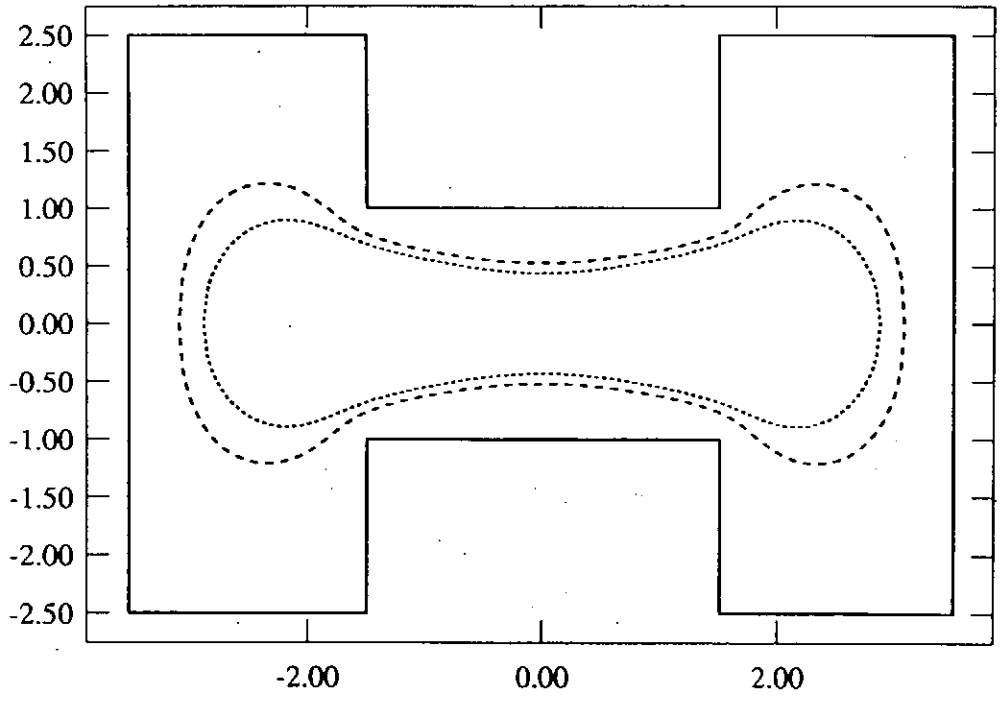

Fig.5 Rectangular return current conductors with expanded ends.

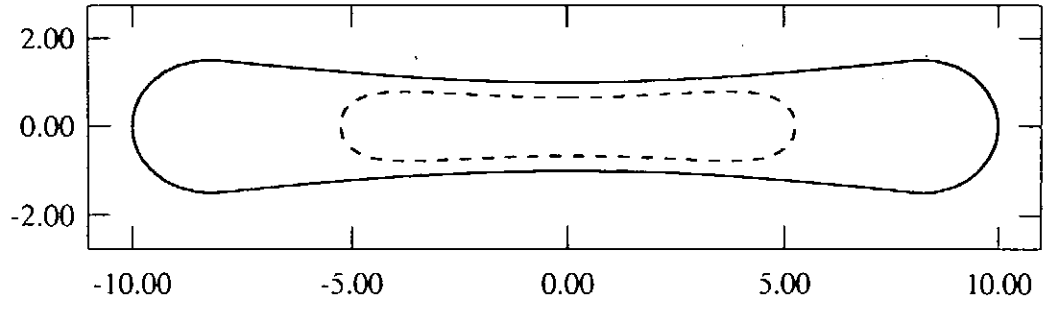

Fig.6 Return current conductors with hyperbolic central part and elliptic ends.

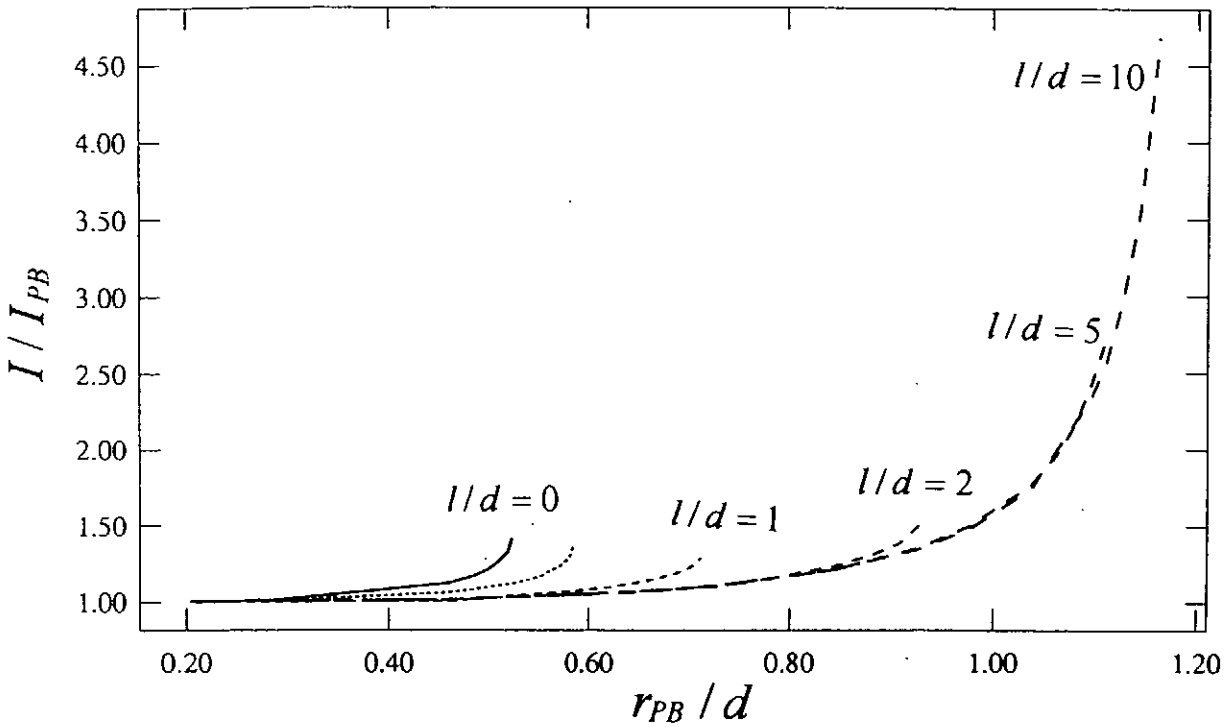

Fig.7. Normalized pinch current I/I_{PB} versus parameter r_{PB}/d for the different values of l/d.

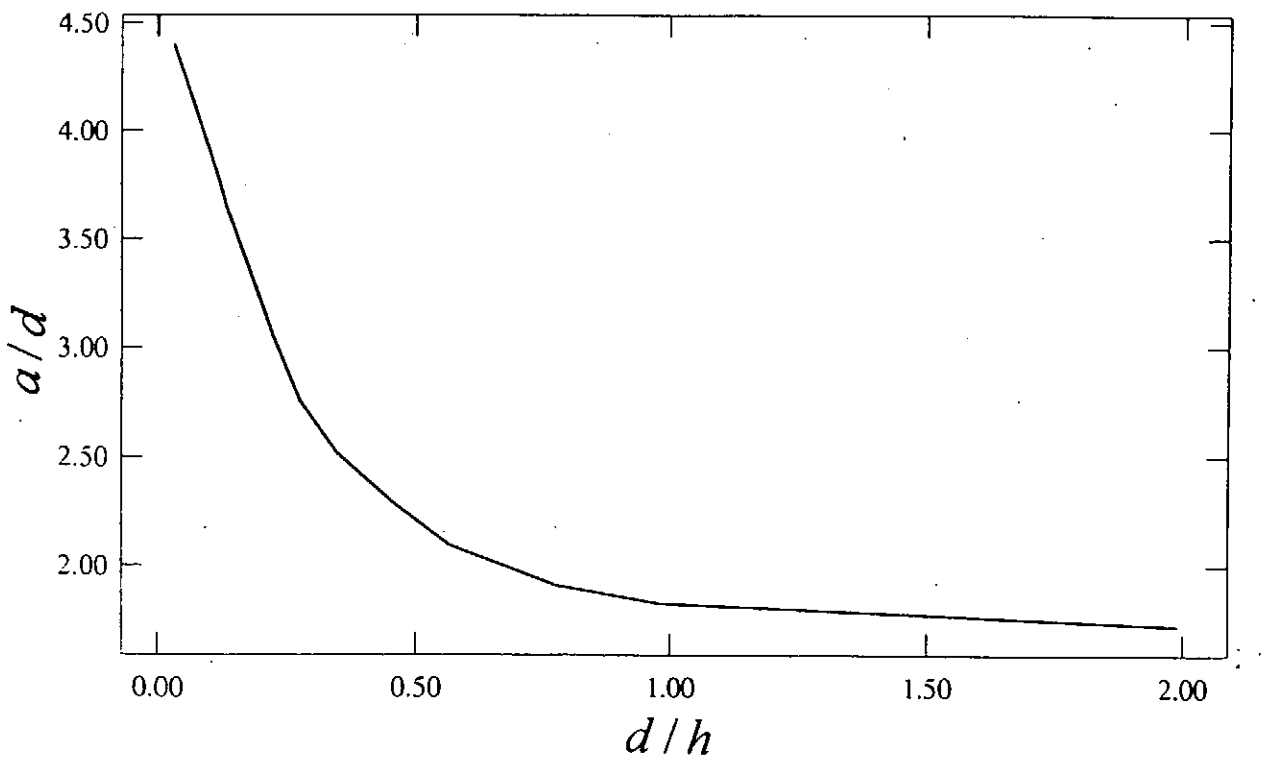

Fig.8. Maximum normalized length of plasma sheet a_{max}/d versus

SCALING OF SOFT X-RAY LASERS PUMPED BY FAST Z-DISCHARGE

Kazuhiko HORIOKA, Kaichi HATSUNE, Mitsuo NAKAJIMA, Hikaru HANAJIMA,
Takayuki AOKI*, Masao OGAWA* and Tomonao HOSOKAI**

Department of Energy Sciences, Tokyo Institute of Technology,
Nagatsuta 4259, Midori-ku Yokohama 226, Japan
* Research Laboratory for Nuclear Reactors, Tokyo Institute of Technology,
O-okayama 2-12-1, Meguro-ku, Tokyo 152, Japan
** Advanced Photon Research Center, Japan Atomic Energy Research Institute,
Tokai Ibaraki 319-11, Japan

Abstract

Based on some experimental results, the potentiality of Z-discharge plasma as a pumping source of soft X-ray laser is discussed. Z-discharges pumped by fast pulse power generator can make axi-symmetric and high energy density plasmas of large aspect ratio. With well controlled pre-ionization, it makes the rapidly imploding z-pinch plasma with good reproducibility. In contrast to laser excited scheme, the discharge pumping uses compression process for making the high energy density plasma. Thus the plasma at the final compression phase can be controlled so as to make optimum parameter and structure of plasma for pumping the laser line. In this scheme, there are a lot of "control parameters" such as the initial gas pressure, the diameter, the peak current and the rise time of drive current. A prospect for the operation at shorter wavelength is also briefly discussed.

1 Introduction

Lasings at short wavelength are rare, inefficient and unusually expensive. Until recently, it was considered that the lasing at soft-X-ray region is only possible with huge and expensive high power lasers. A few years ago, it was demonstrated that the lasing from Ne-like Ar at 46.9nm (3p-3s) is possible with a fast capillary discharge plasma[1]. In the experiment, the load gas was imploded in a thin capillary tube. The plasma was electrically heated and hydro-dynamically compressed up-to the temperature Te of $\sim$100eV and the electron density ne of $\sim 10^{19}cm^{-3}$. Then the energy density of

the core plasma was order of GPa. At about the maximum compression phase, the electrically stored energy was converted to short wavelength coherent radiation.

As compared with the laser plasma, the high density plasma made by fast discharge process has intrinsically coaxial symmetrical shape, large aspect ratio, and high implosion velocity. Moreover, the experimental apparatus is compact and inexpensive. All of these characteristics are favorable for laser operation of large energy output with low cost.

We could demonstrate that by carefully controlled initial condition and a fast discharge drive, we can make high energy density plasma with good reproducibility[2),3)]. In the same experiments, we made clear that the plasma column has sufficient margin of stability for Ne-like Ar scheme. Extending this scheme to shorter wavelength is of major concern of the present study. The possibility largely depends on whether we can compress the plasma up-to order of 100Gpa to get hotter and denser plasma.

2 Experimental Results

2-1 Dynamics of Fast Capillary Plasma

In order to investigate the dynamics of fast z-discharge, experiment was conducted using a capillary made of a polyacetal cylinder[3)]. In the experiments, care was taken to make well defined discharge condition. The prepulse was almost completely suppressed by SF_6 pre-pulse switches and a spark gap switch was eliminated from the discharge circuit. Thus the capillary was directly driven with fast rise by the LIMAY-I fast pulse power generator (3 Ω-70nsec). It drove the load current of order of 10^5A with a rise time less than a few tens of nsec.

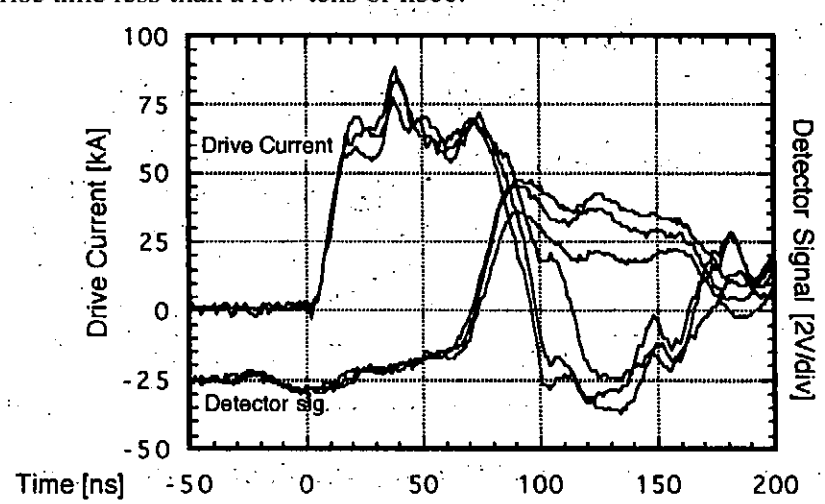

Fig.1 Typical X-ray Signals from Capillary Discharges

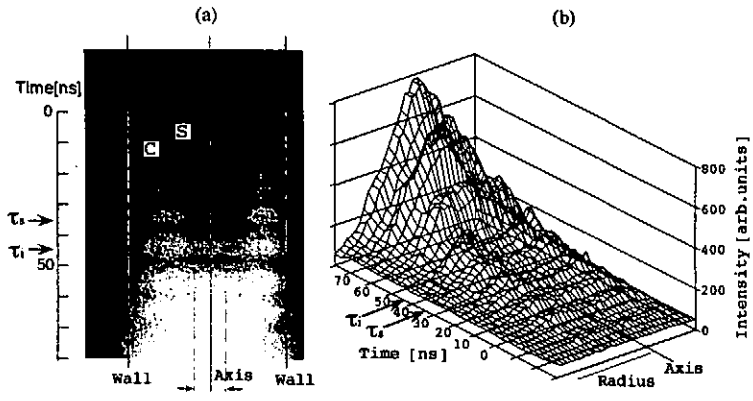

Fig.2 Streak Image (a) and Simulated Flow Diagram (b) of Implosion Process for 400Pa of Ar

The X-ray out-put from the discharge was observed with scintillation detector. Fig.1 shows the typical waveforms of the X-ray signal. The waveforms were superimposed for successive three shots. As can be seen, the reproducibility of the signal is very well.

Fig.2 shows a streak photograph of the discharge process and its flow diagram obtained by a 1-D MHD simulation code[4]. As shown in the figure, the implosion velocity is order of 10^7cm/sec and a strong shock wave is driven ahead of a current skin

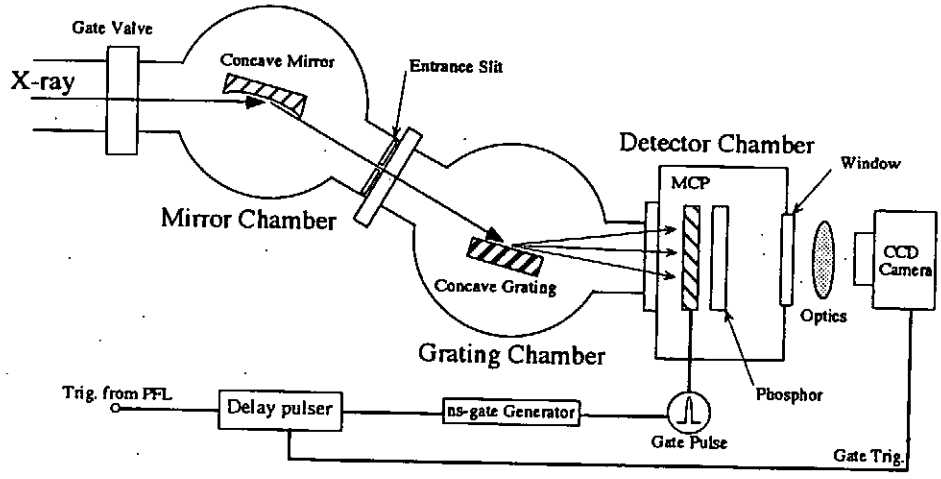

Fig.3 Schematic Diagram of Grazing Incidence Spectrometer

layer (contact surface). When the shock wave reaches the central axis, it reflects back and after that it interacts with the current layer. The shock wave, the skin layer and the interaction of them make a complex structure in the core plasma. We can also see that the behavior of the plasma column are well explained by the 1-D MHD simulation, over a wide range of discharge condition.

2-2 Spectral Measurements of Capillary Plasma

In order to correlate the plasma dynamics and the spectral emission, we constructed a flat-field grazing incidence spectrometer. A schematic diagram of the spectrometer is shown in Fig.3. The photo emission from the end of the capillary is reflected by a grazing-incidence gold-coated spherical mirror and diffracted by an aberration corrected concave grating (HITACHI-001-0437). Each chamber is evacuated to 10^{-7}torr by a turbo-molecular differential pumping system. The diffrated light is measured with a 5nsec-gated MCP (Micro Channel Plate).

Fig.4 shows a typical output spectrum of the capillary plasma obtained by the spectrometer. Here, t shows the discharge time. As has been pointed out in (2-1), the discharge plasma dynamically changes its density distribution with time. Because of the refraction effect, the light emission diverges or contracts depending on the emission region and the density distribution. Generally, working in this spectrum region requires complicated optical set-up including a pinhole for differential pumping and the grazing incidence mirror. Thus for a further analysis of the results, cares should be taken for interpretation of the spectrum output.

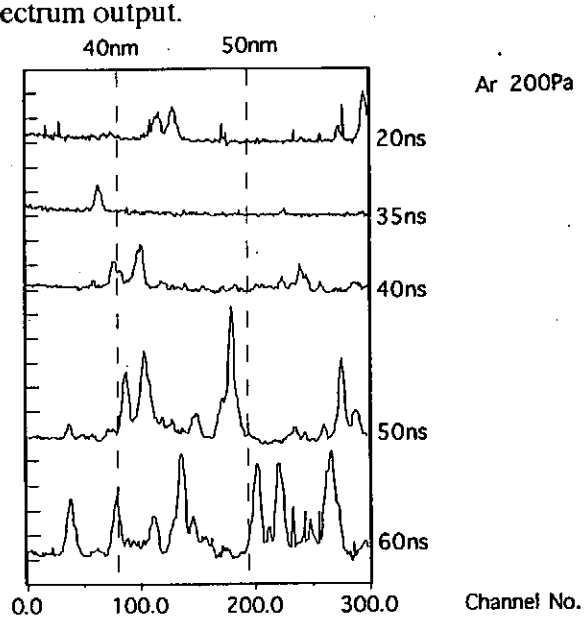

Fig.4 Typical Spectrum as a Function of Discharge Time

3 Prospect for Operation at Shorter Wavelength and Larger Output Energy

The Z-discharge plasma is confined by the self magnetic field B_θ. The most simple expression for the confinement of the plasma is derived by the Bennett relation as,

$$nkT(Z+1) \sim Iz^2/r^2 \qquad (1)$$

where, n denotes the number density, T is the temperature, Z is the charge, Iz is the current, and r is the radius of plasma column. Then for making the high energy density plasma, the radius of the plasma column should be as small as possible. On the other hand, the hydrodynamic instability grows as a function of time. The confinement time scales roughly proportional to the diameter of the plasma column. Then we should drive the thin capillary as fast as possible.

Fig.5 illustrates the operational ranges of Ne-like and Ni-like collisional excitation scheme for the soft X-ray laser [5,6,7]. In the same figure, required current for confinement of the high energy density plasma is also shown. As can be seen we need about 10^5A for the confinement of plasma for Ni-like Xe scheme. These current level is well within the operational range of conventional pulse power technology.

Generally, hydrodynamic expansion phase is isentropic and the compression phase is a dissipative process. A temperature-density diagram for the expansion or the compression phase is schematically shown in Fig.6. The hatched area in the figure denotes the final core parameter aimed at to make the lasing condition. As we can see, we need denser and hotter plasma for operation at shorter wavelength region. This means the discharge process becomes more dynamic and structure of the core plasma is more influenced by the interaction of the shock wave and the current sheet.

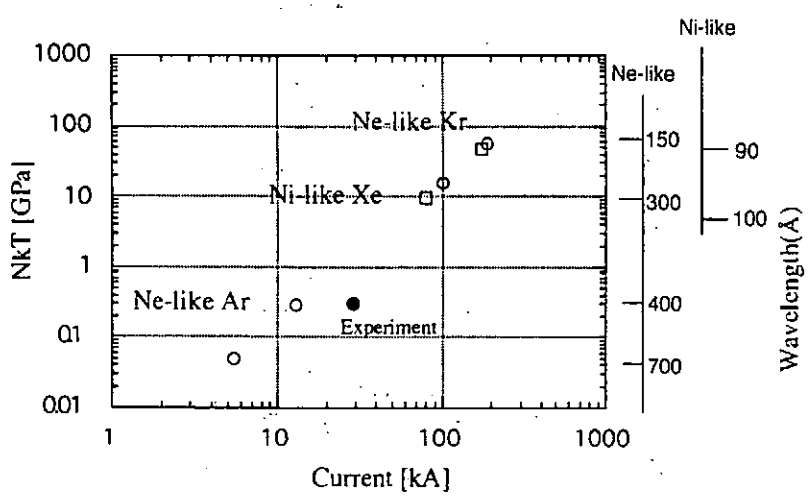

Fig.5 Operational Region of Collisionally Pumped X-ray Laser

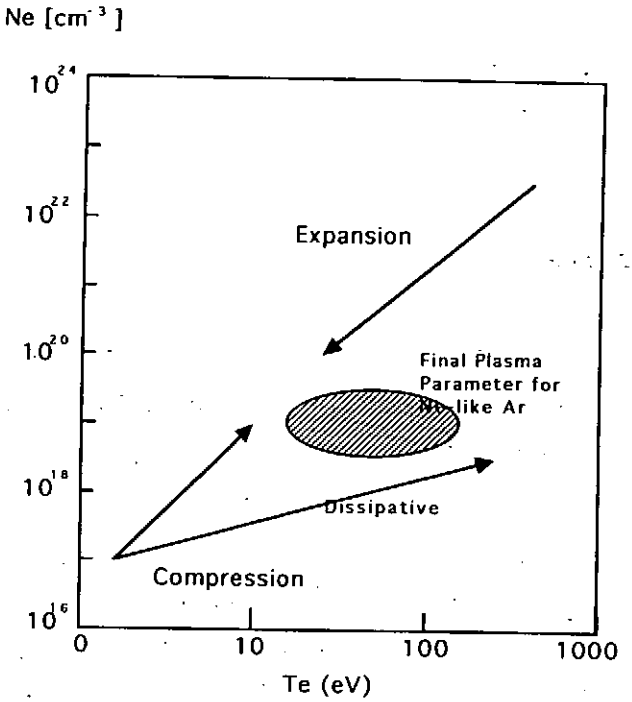

Fig.6 Schematic of Compression and Expansion Process and Operational Region of X-ray Laser in Temperature-Density Diagram

The discharge pumping scheme makes the plasma by compression from low density initial gas of order of $10^{17}cm^{-3}$ to core plasma of ne $\sim 10^{19}cm^{-3}$ and Te $\sim$100eV. A rate of implosion depends on the initial plasma density, radius and the rise time of the drive current. This means the final parameter of imploded plasma depends on the compression process. If the process is strongly dissipative, it makes high temperature and low density plasma and vice versa. In other words, with implosion scheme we can control the parameter and structure of the final core-plasma.

The population density of the upper Nu and the lower Nl laser levels of collisionally excited scheme, basically depend on the electron density ne and electron temperature Te. The spectral shape depends on ion temperature and the opacity of lower level resonance (3s-2p) line depends on the velocity of ion drift. Thus, the gain coefficient of rapidly moving plasma can be expressed as,

$$G \sim g(\lambda)(Nu - Nl) = f(ne, Te, Ti, vi) \quad (2)$$

here, $g(\lambda)$ is the line shape factor, Ti is the ion temperature and vi shows the ion velocity. Thus the gain coefficient of the Z-discharge plasma is not only functions of ne, Te and Ti, but also function of the ion drift velocity vi. At shorter wavelength region i.e., at higher density level reabsorption of radiation become more serious. Fortunately

we can expect that the dynamic Doppler shift in the radial direction reduces the optical depth at rapidly implosion scheme.

4 Concluding Remarks

The role of refraction in limiting the gain length and output energy depends on the shape of density profile and gain profiles of the plasma. The refraction effect becomes more serious for shorter wavelength region. Capillary discharges pumped by fast pulse power generator can make a long, axi-symmetric, high energy density plasma with very good reproducibility. The distribution of electron density can be controlled so as to make optimum profile for propagation of the amplified ray.

From the point view of radiation trapping, it is necessary to make a plasma column as narrow as possible. The key obstacle for such a scheme is the MHD instability. A possibility in obtaining a stable plasma is utilizing the capillary of small initial radius and shorter implosion time. When we drove the capillary of 4mm diameter and 100mm length, the implosion velocity of the plasma is measured to be order of 10^7cm/sec. The high ion velocity should be helpful for radiation cooling of 3s population (lower level) of Ne-like level.

In conclusion we can say that with proper conditioning of the fast discharge process, we may have both the high energy out-put and short wavelength laser with low cost.

References

(1) J.J.Rocca et. al., Phys. Rev. Lett., **73**, p.2192 (1995)

(2) K. Horioka, T.Hosokai, M.Nakajima, T.Aoki and M.Ogawa ; Proc. Int. Workshop on Generation and Application of Coherent X-rays, pp.359-377 (1996)

(3) T. Hosokai, M.Nakajima, T.Aoki, M.Ogawa and K.Horioka ; Jap. J. Appl. Phys, Vol.**36**, pp.2327-2335 (1997)

(4) T.Aoki, K.Horioka and M.Ogawa ; **NIFS-Proc.23**, p.124 (1995)

(5) A.V.Vinogradov and V.N.Shlyaptsev; Sov. J. Quantum Electron, **13**, No.3 p.303 (1983)

(6) V.N.Shlyaptsev et. ak., **SPIE-2012**, p.99 (1993)

(7) T.Hosokai, M.Nakajima, T.Aoki, M.Ogawa and K.Horioka; **SPIE Proc.3156**, pp.187-192 (1997) □

Study of spatial reproducibility of hot spots by using a mesh electrode in gas puff z-pinch experiment

S. Katsuki, T. Shinkai, H. Akiyama, I. V. Lisitsyn

Department of Electrical Engineering and Computer Science, Kumamoto University, Kumamoto 860

K. Murayama

Yatsushiro National College of Technology, Yatsushiro 866

Abstract

The spatial distribution of the gas injected from the anode is one of the important factors to stabilize the position of hot spots in the gas puff z-pinch plasmas, since the turbulence of the injected gas causes its position uncertain. A mesh cathode enables a laminar flow and axial symmetry of the gas. Here, two kinds of electrodes, a brass solid and a stainless mesh, are used as a cathode and the implosion process in both cases is compared. The pinch process is observed by the Schlieren method and the position of hot spots is obtained by a pinhole camera. Though the mesh cathode contributes to produce the symmetrical discharges, this does not directly lead the spatial stability of hot spots. This is because the plasma pinches twice until x-ray is radiated.

1. Introduction

Gas-puff z-pinch plasmas1)-5) have potentiality as a radiation source of soft x-ray for industrial applications such as x-ray lithography, x-ray microscopy and so on because of their high x-ray output efficiency. Especially using gas-puff z-pinch plasmas as a light source of x-ray lithography, intensity of soft x-ray and spatial reproducibility of the hot spots are important since the energy of soft x-ray radiated from z-pinch in a single shot is not enough and as the result several ten shots are needed for exposing the resists. The spatially studded hot spots mean the deviation in light source location and make the resolution of lithography worse.

The distribution of the incident gas from anode before discharge is one of significant factors for spatial stability of hot spots. Usual solid type electrodes as cathodes cause a turbulence of the flow gas around the surface, and the turbulence disturbs forming the symmetrical discharges. Therefore, the position of hot spots is uncertain. A mesh cathode enables to form a laminar flow and a symmetrical distribution of the gas. It is expected that the symmetrical discharges lead the spatial stability of the hot spots.

Here, two kinds of electrodes, a brass solid and a stainless mesh, are used as a cathode and the pinch process in both cases is compared. The pinch process is observed by a schlieren method and the position of hot spots is obtained by a pinhole camera.

2. Experimental Setup

Figure 1 shows the schematic diagram of the z-pinch device. It consists of a fast magnetic valve, two electrodes placed in a vacuum vessel evacuated to less than 10^{-4} torr, and a power source. Ar gas is injected into the z-pinch region from an anode hole with a diameter of 8 mm by operating the fast valve. The separation between the anode and cathode is 10 mm. Two kinds of cathodes shown in Fig. 2 are used. One is a solid stuff electrode with a diameter of 30 mm, which is made of brass (a). The other is a mesh electrode with a diameter of 30 mm, which is made of a stainless steel mesh with a transparency of 81% (b). The device has a coaxial configuration. The power source consists of a capacitor with capacitance of 6.4 μF and a triggered spark gap (TSG) switch. The stray inductance of circuit is approximately 210 nH. The energy stored in the capacitor is 2.9 kJ. Several hundreds μs after operating the fast valve, the TSG switch is closed. Time delay between operating of the fast valve and the TSG closing is 800 μs, which is optimized so that the x-ray output becomes large in case of using the solid cathode. The current and dI/dt are measured by a Rogowski coil and a one-turn coil, respectively. The voltage drop along the z-pinch plasmas can be obtained by the one-turn coil signals.

Figure 3 shows a schematic arrangement of the diagnostics. The light source for a Schlieren method is a 400 mJ YAG laser (Hoya-Continuum Surelite II) with a pulse duration (full width at half maximum) of 5 ns. The laser light expanded to approximately 5 cm in diameter passes through the vacuum vessel including z-pinch plasmas, and is recorded by Polaroid films placed behind an infrared filter. A pinhole camera is simply composed of a 400 μm diameter pinhole, a 3 μm thick Al filter and a x-ray film (Fuji Super HR-A). The spatial resolution of the camera is 800 μm. A time evolution of soft x-ray radiation are detected by a PIN-photo diode (Hamamatsu S1722-02) with a 3 μm thick Al filter.

3. Comparison between solid and mesh cathode in pinch process

Figure 4 shows the plasma current and set of Schlieren images taken in different discharges and in different times in case of the solid cathode. Upper and lower electrodes correspond to the anode and the cathode, respectively. The exposure time of the Schlieren images corresponds to the duration of laser pulse. Zero time in this experiment is defined as the beginning of plasma current. Numbered black bars at the current waveform correspond to the time when each Schlieren photograph was taken. Dark regions in each photograph indicate an existence of high density plasmas with $n_e > 10^{21}$ cm^{-3} or a high density gradient like a current layer. A shadow along the cathode surface in photographs ② and ③ indicates the high density gas stacked at the cathode surface. The shape of plasma column is quite complicated in pinch process. In the photograph ④, plasma column is formed like a bowl, and the outlines of the plasma gradually move inward in the

series of photographs from ⑤ to ⑦. Finally plasma strongly pinches at around 1.2 μs. Also, the appearance of oscillations in the current waveform indicates the strong pinch of plasma and soft x-ray radiation. However, the plasma column is no longer symmetrical at the moment.

Figure 5 shows the plasma current waveform and set of Schlieren photographs taken in different times in case of the mesh cathode. The plasma column is more symmetrical than that in case of the solid electrode. In this case, the plasma always pinches twice at 1.0 μs and 1.8 μs and soft x-ray radiated during the second pinch. Also the evidence of the strong pinch appears around 1.8 μs on the current waveform. Though the plasma column is symmetrical until the first pinch, it does not pinch strongly (see ④). Plasma column appears to consist of the main plasma and a gas layer surrounding the plasma. The reason why it does not pinch strongly is due to generation of discharge channels outside the column, which is caused by the induced voltage along the plasma. After the first pinch, plasma column is reformed to a larger diameter, and moves inward again. However, the plasma column is no longer symmetrical in the process of the second pinch. Plasma behaviors shown in Fig. 5 and 6 are reproducible from shot to shot.

Figure 6 shows current, x-ray signal and voltage drop along the plasma from the top, respectively. The plasma voltage V_p is obtained from the following equation,

$$V_p = V_0 - R_0 I - L_0 \frac{dI}{dt} - \frac{1}{C}\int_0^t I\,dt \qquad (1)$$

where R_0, L_0, C and V_0 are stray resistance, stray inductance, capacitance of the capacitor and initial voltage of the capacitor, respectively.

The set of waveforms explains well the series of photographs shown in Fig. 5. In the case of the solid cathode, x-ray is radiated around 1.3 μs and the current while pinching is about 100 kA. Increase in the plasma voltage occurs simultaneously. In the case of the mesh cathode, the x-ray radiation is delayed and appears at around 1.8 μs. The current while pinching is 125 kA and the intensity of x-ray radiation is higher. Increase in voltage across the plasma column around 1 μs indicates the first pinch that does not radiate x-ray and the voltage pulse around 1.8 μs implies the second pinch with the radiation.

Fig. 7 shows the dependence of the soft x-ray intensity on the current when x-ray is radiated. Solid and empty circles correspond to the solid and mesh electrode, respectively. Average intensity in the case of mesh cathode is higher than that in case of solid cathode. Plasma current while pinching is higher in the case of mesh cathode since the x-ray radiation is delayed. Intensity of x-ray radiation is dependent on magnitude of the plasma current while pinching. However, intensity of the radiation is not reproducible in both cases. Plasma current, namely during the time when x-ray is radiated, in the case of solid cathode deviates much. On the other hand, in the case of mesh cathode,

x-ray is radiated at roughly the same time and current, which indicates that x-ray is always radiated at the second pinch.

4. Observations of hot spots

Figure 8 shows a set of photographs of plasma column taken by the filtered pinhole camera. (a), (b) and (c) are in the case of using solid cathode, (d) (e) and (f) show the case of using mesh cathode. (c) and (f) are superposed over 10 shots, and the others are made in a single shot. They show the hot spots between electrodes, which radiate intense x-rays. The position of hot spots varies from shot to shot in both cases. There is no clear difference between two cathodes in spatial reproducibility of hot spots. Mesh cathode does not give a great contribution to stabilize the position of hot spots.

5. Conclusion

Application of a mesh cathode and its contribution to the spatial reproducibility of hot spot in gas-puff z-pinch experiment was described. Schlieren method is used for the observation of the plasma column. In case of using mesh cathode, symmetrical plasma column is initially formed and smoothly pinched. However, x-ray is not radiated during the first pinch. After the first pinch, the plasma column with a larger diameter is reformed and strongly pinched. Since plasma column is not symmetrical in the second pinch process, the position of hot spots is uncertain as well as in case of solid cathode configuration.

In order to improve the reproducibility of x-ray radiation with respect to a spatial stability and intensity, it is important to make a strong pinch at the first time. Current with a higher rising rate and hollow distribution of incident gas might be necessary to improve spatial reproducibility of hot spots.

References

1) J. Shiloh, A. Fisher, and N. Rostoker, Phys. Rev. Lett., 40 (1978) 515.

2) M. Badaye, R. Stempork, and R. P Gupta, Rev. Sci. Instrum. 61 (1990) 1457.

3) J. Bailey, Y. Ettinger, A. Fisher, and R. Feder, Appl. Phys. Lett. 40 (1982) 33.

4) J. Du, T. Ohata, K. Shimoda, and K. Hirano, Jpn. J. Appl. Phys. 64 (1995) 4185.

5) K. Takasugi, H. Suzuki, K. Moriyama, and T. Miyamoto, Jpn. J. Appl. Phys. 35 (1996) 4051.

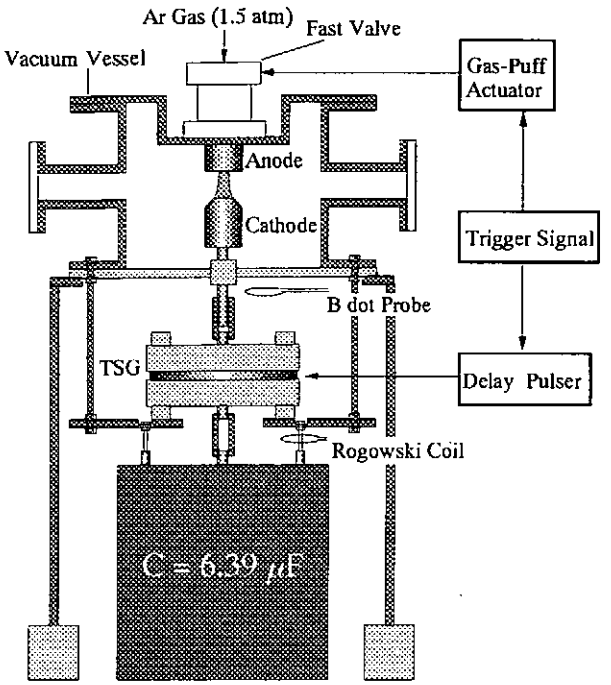

Fig. 1 Schematic diagram of experimental apparatus

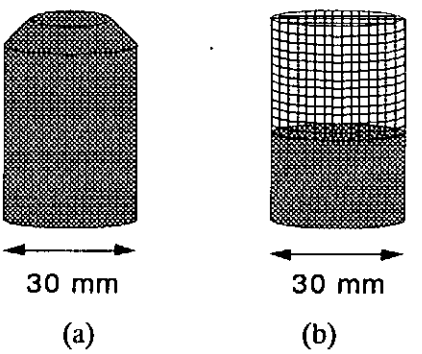

Fig. 2 Two kinds of cathode. (a) is solid cathode and (b) is mesh cathode

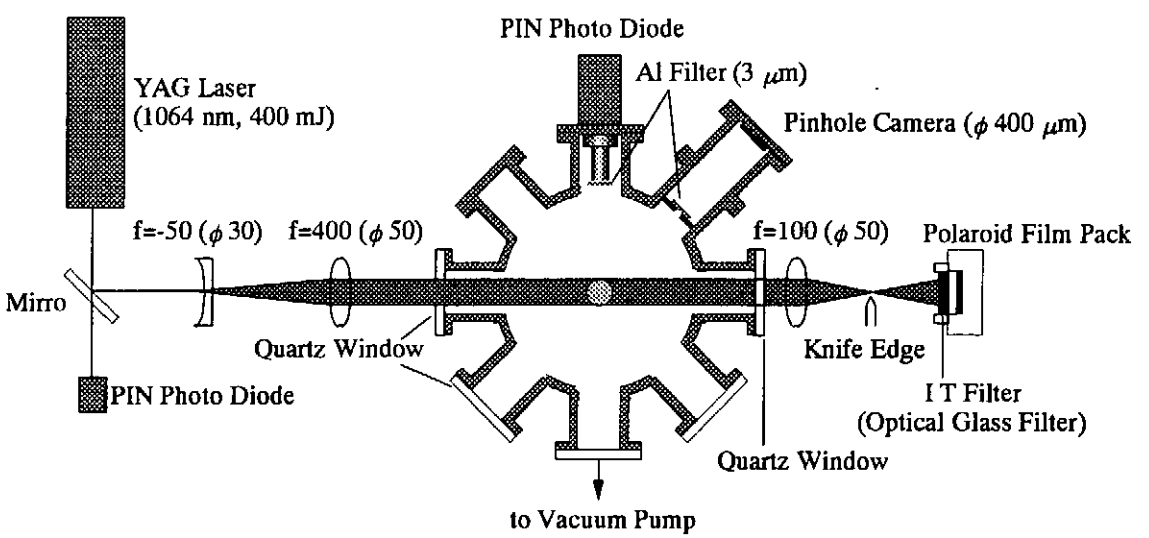

Fig. 3 Schematic arrangement of the diagnostics

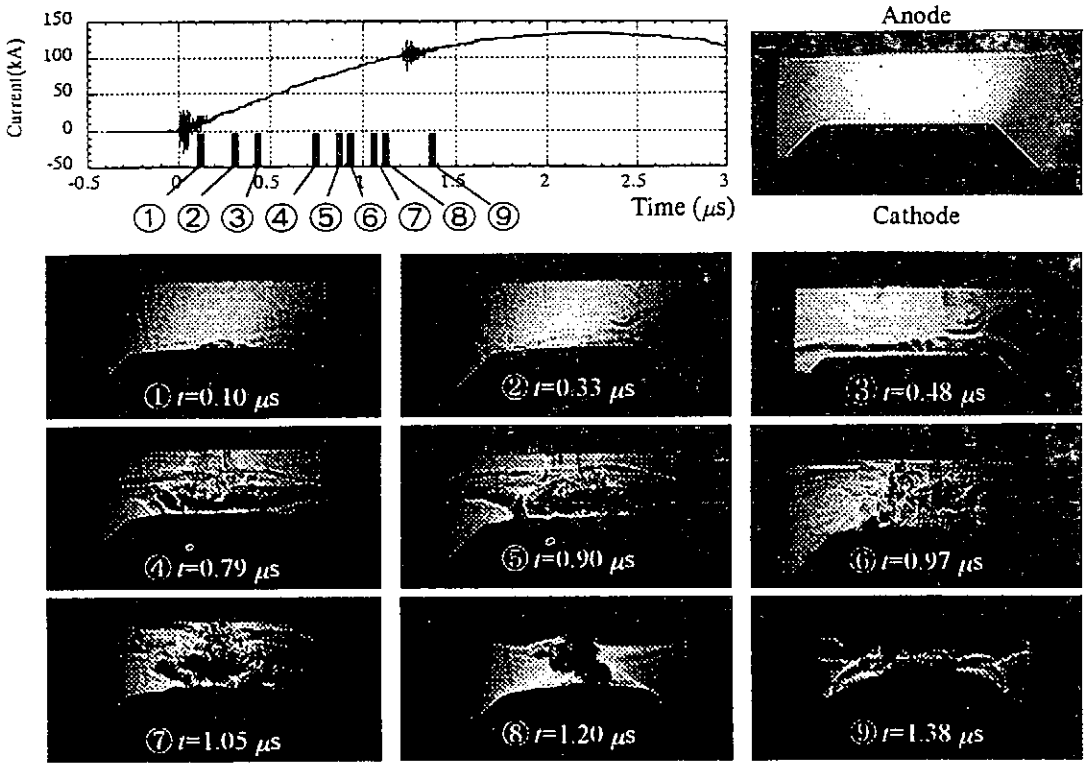

Fig. 4 Pinch process in case of the solid electrode

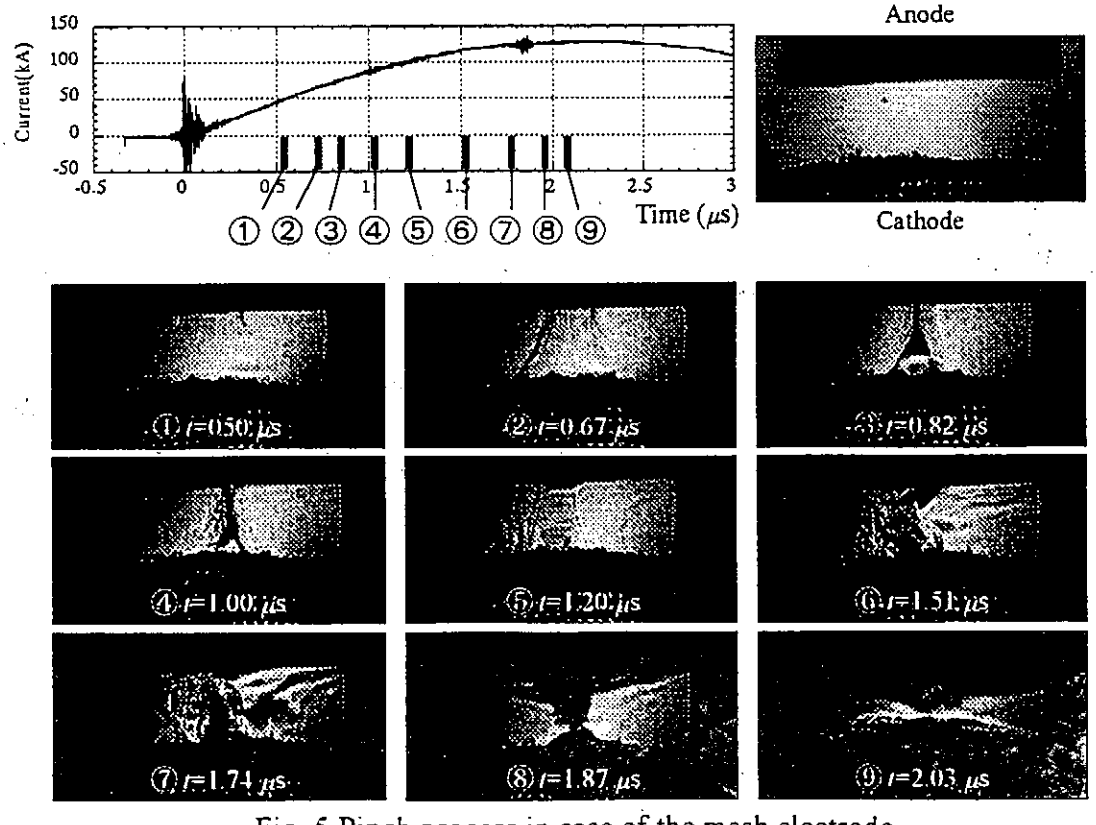

Fig. 5 Pinch process in case of the mesh electrode

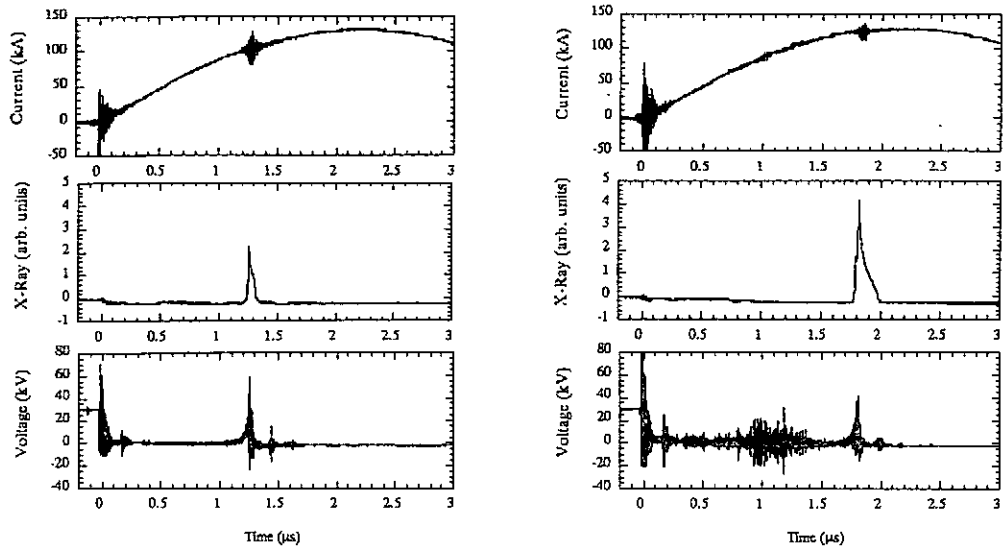

(a) solid cathode (b) mesh cathode

Fig.6 Current, soft x-ray intensity and voltage in solid and mesh cathode

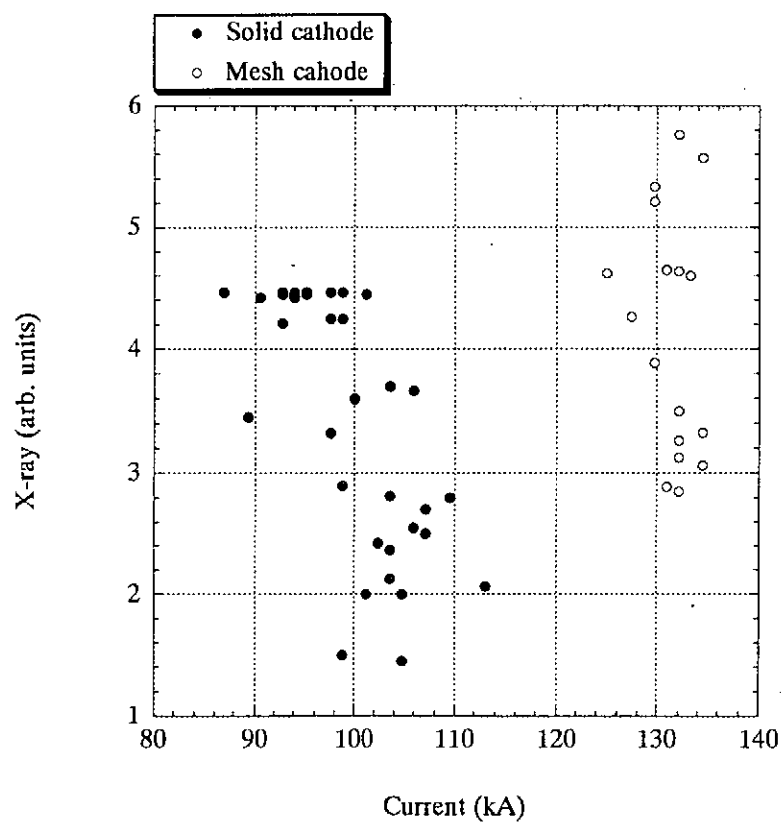

Fig. 7 Dependence of the soft x-ray intensity on the current when x-ray is radiated

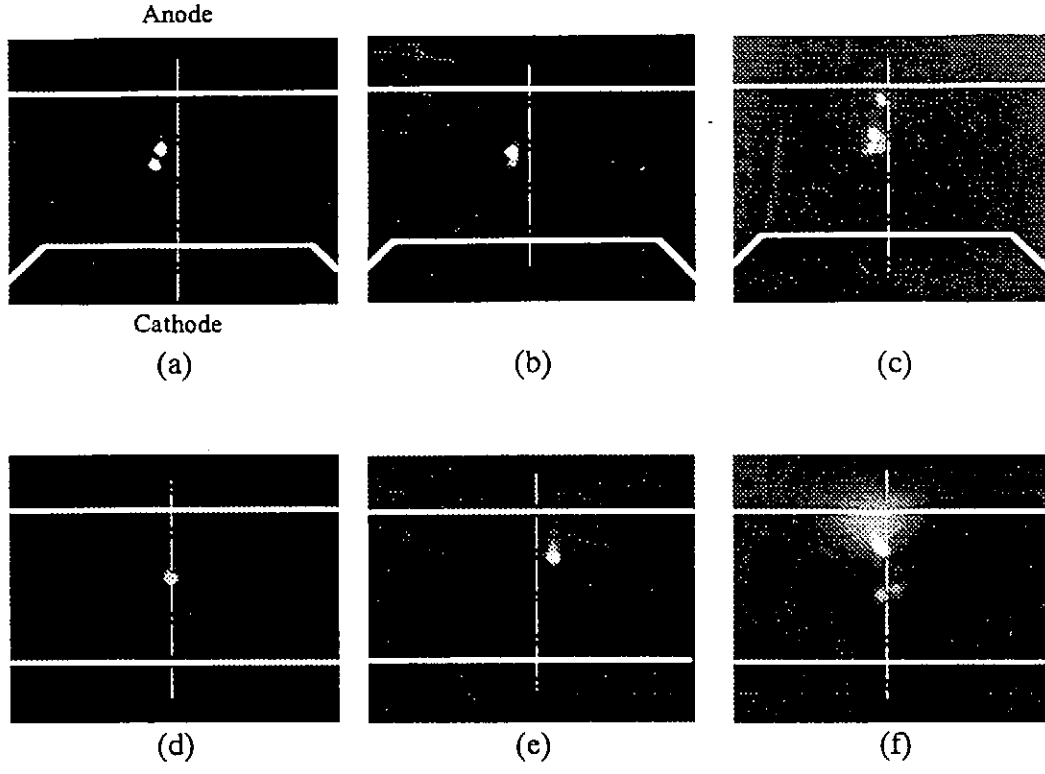

Fig. 8 Pinhole photographs of solid and mesh cathode

A novel method of acquiring high-speed images of pinched plasmas

Takeshi Yanagidaira, Yasushi Ono and Katsumi Hirano
Department of Electronic Engineering, Gunma University,
Kiryu, Gunma 376, Japan

Development of a high-speed imaging system in both visible and soft x-ray regions is described. The system can record time variation of source intensity onto digitizing oscilloscopes at a sampling rate of 2 GSamples/s. Software that processes data and reconstructs time-resolved images by inversion technique is developed. Using this system, correlation between macroscopic behavior of pinched plasma and x-ray generation is observed in 150 kJ plasma focus device with Ar gas puff.

I. Introduction

Industrial or biological applications of impulsive soft x-ray sources are expanding in fields such as x-ray lithography and x-ray microscope.[1] The plasma focus and the gas-puff z-pinch are intense sources of soft x-ray with high efficiency. It is necessary to clarify the mechanism of soft x-ray generation to control intentionally operational parameters to obtain x-ray emission appropriate for particular application.

Close relationships between the generation of soft x-ray sources and the macroscopic behavior of pinched plasma have been recognized. Theoretical considerations have been made for the x-ray generation, and several models such as beam-plasma interaction and radiative collapse have been proposed.[2, 3] However, there are few studies that deal with the mechanism of the x-ray generation on the basis of observation.

It should be useful to perform simultaneous imaging in x-ray and visible range with high-time resolution for observation of the relationship between the macroscopic behavior and the x-ray generation of pinched plasma. For the high-speed imaging in framing- or streak-mode, gated micro-channel plates or image tubes had been used. In framing-mode-observations, the available area of the phosphor screen limits number of frames. On the other hand, the field of view of the streak-mode observation is restricted to a narrow region using a slit, otherwise, streaked images of different time

and space would be overlapped on the phosphor screen. These limitation and restriction are difficult to overcome in recording single, transient phenomena using gated MCPs or image tubes. Furthermore, such devices are very expensive.

In a previous paper, we have developed a soft x-ray imaging system in which no special devices are used.[4] It records data continuously on oscilloscopes, and then, a computer translates the data into time-resolved images in framing- and streak-mode by the inversion technique.

In this paper, the development of time-resolved imaging system for observation of macroscopic behavior of plasma and x-ray generation is described. Detection system in both visible and soft x-ray ranges is developed. In the inversion, the 'maximum entropy' criterion is newly introduced for more reliable reconstruction of images. A parallel genetic algorithm is used to speed up the computation in the inversion.

II. Description of the system

A. High-speed imaging

The high-speed imaging system is composed of an arrayed soft x-ray and visible detection system and software that process data from the detection system by the inversion technique. The basic idea is to produce time-resolved images by processing the analog signals obtained by the arrayed detector. A pinhole camera can be used for determining the position of the x-ray source and its time-integrated intensity more accurately. The viewing fields of the adjacent channels in the arrayed detector are designed to overlap each other. Therefore, the system enables to make continuous detection over the whole area where the sources are generated.

At the inversion, the viewing field is divided into pixels numbered by J. The source intensity to be determined is expressed as $i(J,t)$, where t is the time. Let the quantities measured experimentally in the analog signals of the m-th channel and the pinhole image be $V_m^{(m)}(t)$ and $I^{(m)}(J)$, respectively. Determination of $i(J,t)$'s is made possible by using the least-squares method. We tentatively assume an initial value for the presumed intensity. Corresponding to the presumed intensity $i(J,t)$, the analog signals and pinhole image are calculated as

$$V_m^{(c)}(t) = \sum_J S_m(J) i(J,t)$$

and

$$I^{(c)}(J)=\sum_t i(J,t)$$

where $S_m(J)$ is the sensitivity of the m-th channel at the pixel J. We compare the calculated $V_m{}^{(m)}(t)$ and $I^{(m)}(J)$ with their measured values by taking the summation of the square of the residual, R. Therefore,

$$R^2 = w_1\sum_m\sum_t[V_m{}^{(c)}(t)-V_m{}^{(m)}(t)]^2 + w_2\sum_J[I^{(c)}(J)-I^{(m)}(J)]^2$$

where w_1 and w_2 are the coefficients for adjusting the weight of each term.

The maximum entropy criterion was introduced in order to select the best solution in cases when the number of pixels to reconstruct is greater than the number of available data points. The entropy measure in the image reconstruction is given by

$$S=-\sum_t\sum_J\left[\frac{i(J,t)}{\sum_J i(J,t)}\cdot\log\left(\frac{i(J,t)}{\sum_J i(J,t)}\Big/ i_{\text{default}}(J,t)\right)\right]$$

where $i_{\text{default}}(J,t)$ is the default intensity.[5, 6] The quantity to be minimized in finding the maximum entropy image is then

$$R^2-\lambda S$$

The maximum entropy image contains only such structure as is required to fit the data. Fine structural details will appear in the reconstruction if and only if the data demand them.[5, 6] Thus, the 'maximum entropy' criterion enables more reliable image reconstruction.

We used the genetic algorithm[7] to find a solution of the intensity $i(J,t)$. Genetic algorithms model natural processes, such as selection, crossover, and mutation of individuals. Individuals are selected for the production of offspring. All offspring are mutated with a certain probability. This cycle is performed until the optimization criteria are reached.[7] To improve the capability to bring the inversion into convergence, a 'parallel' algorithm with migration operation was adopted (Fig. 1).

Each frame in the framing mode display is obtained by multiplying the luminosity of each pixel in the pinhole image by coefficients calculated by the corresponding $i(J,t)$. Namely, the luminosity of the framing images is given as

$$i_f(\mathbf{x},T)=i_p(\mathbf{x})i[J(\mathbf{x}),T]\Big/\sum_T i[J(\mathbf{x}),T]$$

where $\mathbf{x}$ is the arbitrary location in images and $i_p(\mathbf{x})$ is the luminosity of the pinhole

image at $\mathbf{x}$. And, $J(\mathbf{x})$ is the pixel in which the position $\mathbf{x}$ is included.

On the other hand, the streak mode display is obtained by sweeping a region specified arbitrarily by introducing a 'virtual slit' after the acquisition of the data. The luminosity of the streak image is given as

$$i_s(L,T) = \sum_w i_f(\mathbf{r} + L\mathbf{e}_1 + w\mathbf{e}_2, T)$$

where $\mathbf{e}_1$ and $\mathbf{e}_2$ are unit vectors parallel to and perpendicular to the virtual slit, and $\mathbf{r}$ is the location of the virtual slit in the pinhole image. L is the position in the virtual slit, and w is the width of the virtual slit.

B. Detection system

We have previously developed an x-ray detection system which consists of a pinhole camera and a time-resolved x-ray detector with one-dimensional spatial-resolution.[4] This detector (1D x-ray detector, shown in Fig. 2) is composed of a pinhole, a scintillator plate (Nuclear Enterprises NE142), 12 slits, bundled fiber optics, and 12 optical sensor modules (Hamamatsu Photonics H5783). The pinhole camera is capable of on-line capturing of soft x-ray images and is described in a previous paper.[8] The experimental result with this system is given in chapter III B-1.

In addition to the 1D x-ray detector, we have developed a 20-channel, visible and x-ray detector with two-dimensional spatial resolution (2D visible and x-ray detector, shown in Fig. 3). It includes two linear photo diode array (International Radiation Detectors AXUV-10EL)-slits combinations, one for spatial resolution in the axial direction of the plasma focus device and the other side for spatial resolution in the radial direction. Each array has 10 sensitive elements and we assigned the half of elements to x-ray and the other half to visible light by using different filters. The center-to-center distance of the elements is 1 mm and the separation between the viewing field of each channel is 3 mm. The analog signals are led to oscilloscopes (Hewlett-Packard 54542A) and recorded at a sampling rate of 2 G-samples/s. The impulse response of the photodiode array is 1 ns.

C. Plasma focus device as a soft x-ray source

Performance of the system was examined using a soft x-ray source generated with a Mather-type plasma focus device. The inner- and outer-diameter of the coaxial electrodes are 50 mm and 100 mm. The lengths of the inner and outer electrodes are

280 mm and 230 mm, respectively. The anode (inner electrode) is hollow. The condenser bank consists of 28 x 1.56 uF capacitors. The device was operated at a bank voltage of 45 kV and an embedded H_2 gas pressure of 5.5 Torr. Additional Ar gas was puffed with a fast acting valve through the anode hole immediately before each discharge.

III. Performance of the system

A. Simulation

The spatial resolution of the 2D visible and x-ray detector was examined by simulation. As test sources, 25 point sources ware assumed one after another at random position within the viewing field, and corresponding responses of the detection system were calculated. Figure 4 shows the averaged profile of reconstructed images, which indicates the spatial resolution of about 3 mm.

Figure 5 compares the convergence using a 'simple' genetic algorithm to the 'parallel' one. The 'parallel' software can reconstruct a smoother image, and also the CPU time was reduced by 20 % compared to the 'simple' algorithm.

B. Experimental results

B-1. Time-resolved observation of soft x-ray emission from pinched plasma [4]

In the first example, as shown in Fig. 6(a)-A, two filamentary sources and several spots overlapped generated along the electrode axis. It is recognized in Fig. 6(a)-B that the lifetime of the filamentary source is less than 10 ns. In the third example, many spots that were scattered along the electrode axis were observed [Fig. 6(c)-A]. The spots had various lengths along the axis ranging from 0.2 to 1 mm. It is recognized that the spot with the shorter length has a tendency of a shorter lifetime. The x-ray emitting part in the pinched plasma initially appears at several mm (2.5 mm in this example) distant from the anode and moves with a velocity of about 10^6 m/s apart from a point, demonstrating the zipping effect. The overall duration of emission by the scattered spots was extended up to about 30 ns.

B-2. Simultaneous observation of visible and soft x-ray emission

Figure 7 shows an example of simultaneous visible and soft x-ray observation in which the viewing field set along the electrode axis of the plasma focus device. After the maximum compression shown by (1), soft x-ray spots were generated as marked in

the figure by (2) and (3) where the visible emission became feeble, which may corresponds to the decrease of plasma density caused by the necking or disruption of the pinch column. In previous experiments, extreme turbulence of plasma was detected only in disrupted region for about 10 ns by laser scattering.[9] It may be considered that x-ray was emitted from extreme turbulent plasma.

In summary, the system which we developed is sufficient to characterize pinch evolution in plasma focus with high-Z gas puff. Further development is in progress to improve the temporal and the spatial resolution.

References

1) J. S. Pearlman and J. C. Riordan; J. Vac. Sci. Technol. **19** (1981) 1190.

2) Y. J. W. Shearer; Phys. Fluids **19** (1976) 1426.

3) A. E. Robson; Phys. Fluids **B3** (1991) 1461.

4) T. Yanagidaira and K. Hirano: Rev. Sci. Instrum. **68** (1997) 3074.

5) S. F. Gull and J. Skilling: IEE Proc. **131** (1984) 646.

6) David J. Battle, Robert P. Harrison and Mark Hedley: Ieee Trans. Image Processing **6** (1997) 1139.

7) Fogel, D. B.: IEEE Trans. on neural networks, **5** (1994) 3.

8) Y. Takahama, J. Du, T. Yanagidaira and K. Hirano: Rev. Sci. Instrum. **65** (1994) 2505.

9) K. Hirano and T. Yamamoto: Phys. Fluids **31** (1988) 2710.

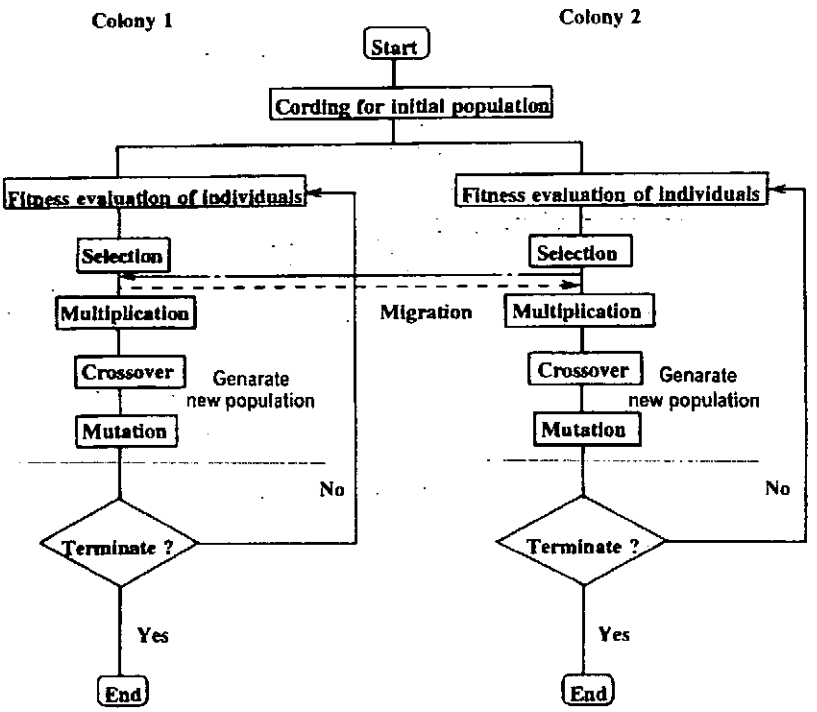

Fig. 1. Structure of parallel genetic algorithm with migration operation.

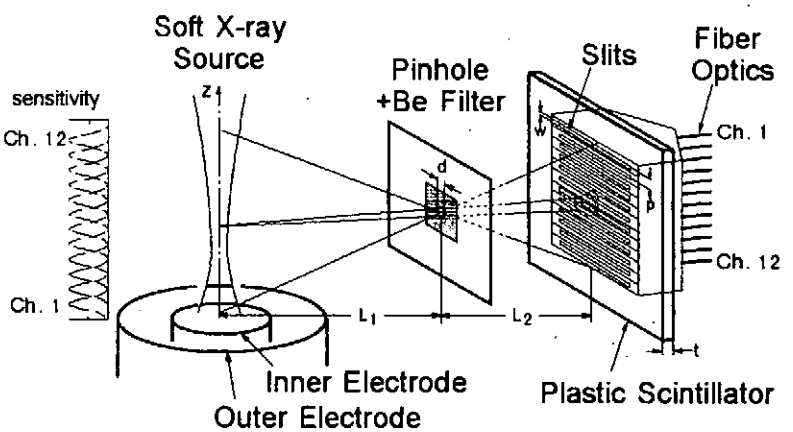

Fig. 2. 1D x-ray detector. The inset shows the viewing field of each channel.

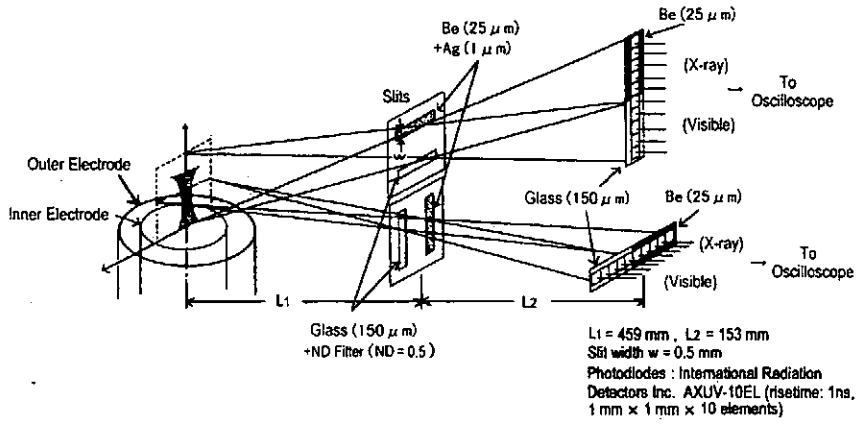

Fig. 3. 2D visible and x-ray detector.

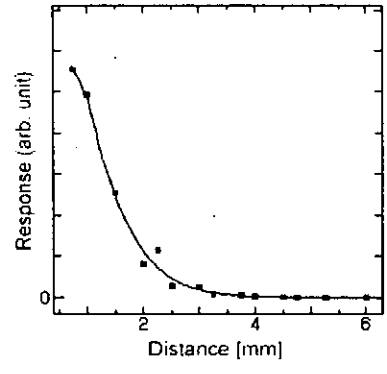

Fig. 4. Reconstruction of point sources. The spatial resolution for point sources was estimated to be 3 mm.

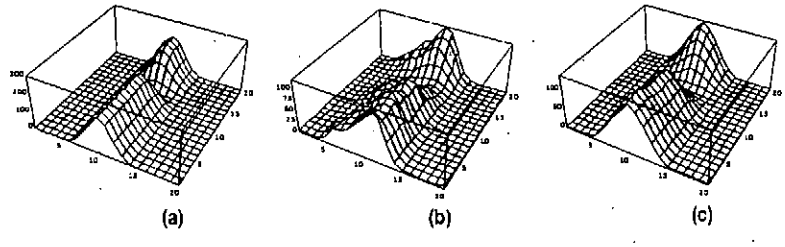

Fig. 5. Simulation of image reconstruction by genetic algorithms. (a) Assumed intensity for performance check. (b) Reconstruction by using a 'simple' genetic algorithm. (c) Reconstruction by using the 'parallel' genetic algorithm. It is clear that accuracy and smoothness in the reconstructed images is much improved by adopting the 'migration' operation.

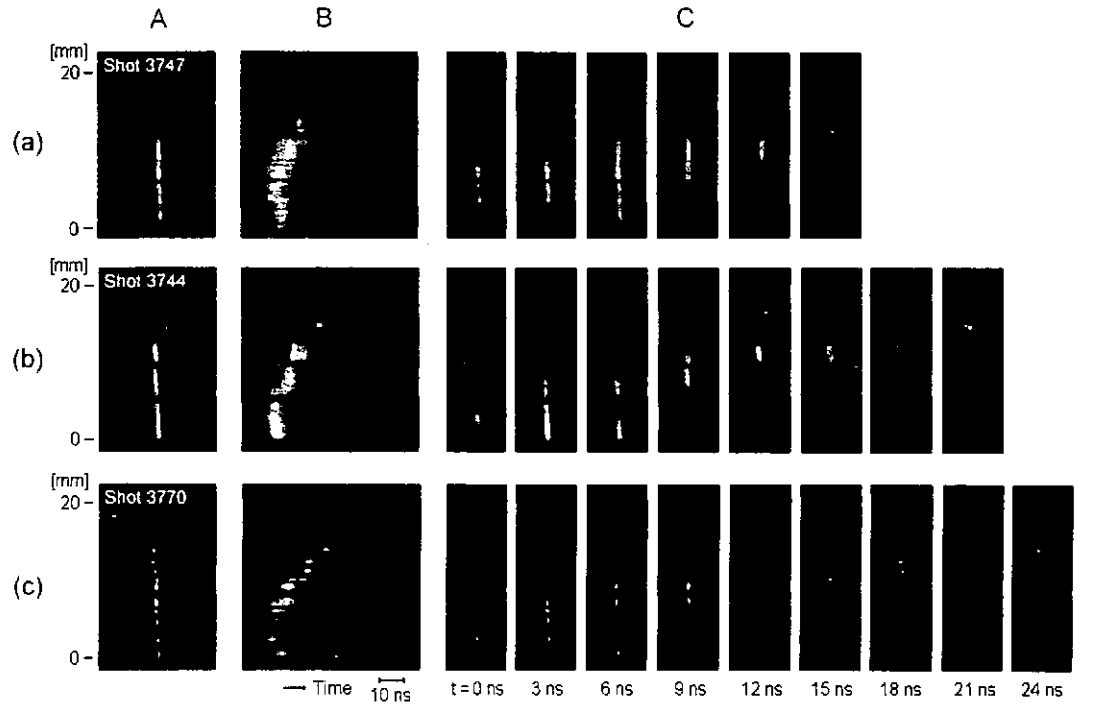

Fig. 6. Examples of the time integrated pinhole image (column A) and the time resolved streak- and framing-mode images (column B and C) of soft x-ray sources generated by plasma focus discharges with Ar gas puff.

[Rev. Sci. Instrum. **68** (1997) 3074]

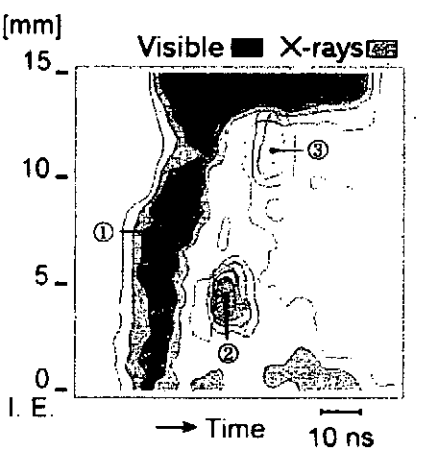

Fig. 7. An example of simultaneous imaging of plasma focus pinch with Ar gas puff in both visible and soft x-ray region. The viewing field is set parallel to the electrode axis.

Spectral analysis of soft x-ray source generated in a plasma focus with neon gas puff

T. Yamamoto, T. Yanagidaira, K. Shimoda and K. Hirano
Dept. of Electronic Engineering, Gunma University
Kiryu, Gunma 376-8515, Japan

Synopsis

Soft x-ray emitting spots (hot spots) generated in a plasma focus with a gas puff is investigated using a streak mode imaging system for the soft x-ray region and a convex Bragg spectrometer which enables to make a time resolved measurement. Using the imaging system, the typical size and the life time of the hot spots in the focused neon plasma were measured to be 1.4 mm in diameter, 13 mm in length and 5 ~ 8 ns, approximately. The FWHM of the spectral lines of NeX (12.19 Å) 1s-2p and NeIX (13.449 Å) $1s^2$-1s2p agree with the life time measured with the imaging system. It is estimated that the electron temperature of the spot is from 0.5 ~ 0.8 keV.

I. Introduction

Intense sources of soft x-rays have been required for many purposes such as x-ray microscopy, x-ray laser pumping and x-ray lithography. In the z pinch plasmas, x-ray sources which emit intense soft x-ray region are easily generated.[1,2,3] They are well known as the hot spots or the micropinches.

In the plasma focus with gas puff it is expected that the obtained electron density and temperature are higher than 10^{22} / cm^3 and from 1 ~ 2 keV, respectively.[4] The hot spots produce the soft x-rays which consist of K- and L series emission of puffed gas. However, mechanism of the soft x-ray emission in this spectral region has hardly discussed yet. To characterize the spots as the soft x-ray source, many plasma parameters such as the electron density, the electron temperature and the lifetime of the spots should be measured simultaneously. Moreover, to clarify emission mechanism, observation of correlation between the macroscopic behavior of the pinched plasma and the time evolution of the hot spots in the plasma should be carried out.

For this purpose spectroscopic investigation is extremely important. Frequently, spectroscopic investigation of the plasma has been carried out using time- and/or spatially integrated spectrometers. It is clear if we employ spatially integrated spectrometer, intensity of the spectral lines are radially averaged over the plasma column. On the other hand, when the spectral lines are recorded with a medium with time integration like a photographic film, we can not help assuming synchronization of each line emission in the way to evaluate the electron temperature and density by a spectroscopic method, for example,

In this paper. we intend to solve these problem by using an imaging spectrometer and the time resolved measurement with soft x-ray sensitive PIN diodes mounted at locations at which spectral lines appear in the spectrometer. Using these diagnostic tools we evaluate the plasma parameters such as the size, the lifetime and the time evolution of the soft x-ray emitting spots generated in the focused plasma with a neon gas puff. Correlation between the macroscopic behavior of the plasma and the line emission is also discussed.

II. Apparatus

2-1 Plasma focus facility with gas puff

A Mather type plasma focus facility was used to generate a current sheet to compress the puffed high z gases.[5] The outer electrode of the facility is a squirrel cage type. The diameter of the inner and the outer electrode were 50 and 100 mm. respectively. The lengths of them were 280 and 230 mm. The condenser bank consisted 28 x 1.56 μ F. 80 kV capacitors. The facility was operated at the bank voltage of 45 kV in this experiment.

Neon was puffed with a fast acting valve through the inner electrode immediately before each discharge. The hydrogen base pressure of 5.5 Torr. and the neon plenum pressure of 3 atm were employed. Approximately 5 cm^3 at 3 atm of neon was introduce by a operation.

The schematic diagram of the plasma focus facility and the diagnostic tools are shown in Fig. 1

2-2 Diagnostic tools

a) Imaging Bragg spectrometer

An imaging Bragg spectrometer in which an RAP(rubidium acid phutarate. 2d = 26.12 Å) convex crystal with the diameter of 12.5 mm was installed was employed. For the imaging an entrance slit of 100 μ m and 5 mm in width and length was used. The spectrometer was capable of collecting x-ray spectra in 3 ~ 20 Å region with the resolution power of > 600 and the dispersion of < 1.1 x 10^{-1} Å/mm. In this spectrometer. a pinhole image was simultaneously recorded with the spectral data on the same film. The pinhole image provided the base line to measure the wavelength. As the pinhole was installed on the slit plane. a precise identification of the wavelength was carried out. in spite of fluctuation of the x-ray source position in shot to shot. A Kodak TRI X film is employed as a recording medium.

To carry out time resolved measurement of the spectral lines. PIN diodes for the soft x-rays were mounted at the positions at which the spectral lines were formed when the photographic film was removed. In this experiment. PIN diodes were mounted to collect the line emission of NeX 12.19 Å and NeIX 13.447 Å (resonance line) +. NeIX 13.549 Å (intercombination line). Each PIN diodes accepts the spectrally analyzed images at 2.0 mm from the inner electrode face.

b) Soft x-ray imaging system

The soft x-ray imaging system used in this experiment is described in previous papers.[6,7] The system which was composed of a combination of an MCP pinhole camera and a 12-

channel arrayed detector was prepared for simultaneous observation both in streak and framing modes. In the arrayed detector the image of the soft x-ray source is formed on a plastic scintillator plate though a Be foil filter (25 μ m in thickness) and a pinhole. The optical signals from each channel are led to photomultipliertubes with a 12-channel fiber optics and recorded in oscilloscopes. Using the analog signals obtained by the arrayed detector and the pinhole image taken by the pinhole camera, the time and spatial resolved x-ray image is restructured by the inversion technique.

c) Image converter camera for the visible light

An image converter camera (Hadland Phomics IMACON 700) operating in streak mode was employed in order to observe the macroscopic behavior of the plasma. The camera viewed the region of 2.0 mm from the inner electrode face through a slit 100 μ m in width which was mounted perpendicular to the electrode axis.

d) Auxiliary tools

The soft x-ray emission was monitored with an x-ray sensitive PIN diode which was coupled with a Be foil filter of 25 μ m in thickness. The view field of the diode was limited by a collimator to observe only the plasma produced by the discharge.

III. Result and discussion

3-1 Spectroscopic observation of NeX Lyman series and NeIX $1s^2$-$1snp$ series

A typical example of a time integrated soft x-ray pinhole image taken with the MCP pinhole camera which installed in the imaging system is shown in Fig. 2 a). The x-ray sources are located along the electrode axis. The soft x-ray source is divided roughly four parts and one of them appears near the inner electrode first, then they shift along the electrode axis. A streak mode observation is displayed in Fig. 2 b). The slit in the imaging system was set up in parallel to the electrode axis. Figure 2 c) shows a typical example of the time integrated spectrogram. These were taken from a single shot. It is obvious that the spatially resolved image formed by the spectral lines shown in Fig. 2 c) agree with b) approximately.

In order to identify wavelengths in the spectrogram the spectrum on the photographic film was scanned with a scanner (EPSON FS-1200WINP). The soft x-ray intensity is displayed in a linear scale in this figure. As shown in Fig. 2 d), it is recognized that the spectral lines of $2 \leq n \leqq 6$ for the NeX Lyman series and $2 \leq n' \leqq 6$ for the NeIX $1s^2$-$1sn$p series. However, it was barely distinguished between the resonance lines, NeX $1s^2$ $^1S_0$-1s2p $^1P_1$ and the intercombination line $1s^2$ $^1S_0$-1s2p$^3P_1$. The intensity of the former is comparable to the later. This is possibly brought from a higher absorption because NeX $1s^2$ $^1S_0$-1s2p $^1P_1$ is a resonance line. The satellite lines near the resonance lines seem to be masked in continuous spectrum.

3-2. Plasma behavior and soft x-ray emission

A typical example of the plasma evolution and soft x-ray emission is shown in Fig. 3. In this figure, a) is a streak photograph taken with the image converter camera by visible light through a slit mounted at 2.0 mm from the inner electrode face and in perpendicular with the

electrode axis which is the same axial location as that of the PIN diodes mounted in the imaging spectrometer. It is recognized that the plasma is constricted toward the electrode axis and then formed a plasma column whose diameter is less than 1 mm. The column lasts for $\sim$ 20 ns after formation of the plasma column at this axial position. A faint light found around the time at which the plasma column distinguished is caused by vapor from the electrode material.

Figure 3 b) is a time integrated pinhole image which is taken through a Be foil filter (25 μm in thickness) and recorded on an MCP. On the other hand, Fig. 3 c) is a streak photograph taken with the imaging system in the same spectral band with the pinhole camera. The slit of the imaging system was set up in parallel to the electrode axis.

Comparison between Figs. 3 b) and c) makes it clear that the x-ray emitting regions (hot spots) in the pinched plasma are not generated simultaneously along the electrode axis. It is understood that the regions appeared near the inner electrode at first and shifted along the electrode axis according to the zippering effect, that is, the constriction of the plasma column shifts along the electrode axis from the location near the inner electrode. The life time of each spot is estimated to be $\sim$ 8 ns in this shot.

Figures 3 d), e) and f) show a time variation of the spectral line intensity of NeIX (13.447 A) $1s^2$-$1s2p\ {}^1P_1$ + NeIX(13.549 A)$1s^2$-$1s2p\ {}^1P_2$ and NeX(12.19 A) 1s-2p and the total soft x-rays, respectively. These signals rose almost at the same time and showed similar waveforms. However, f), the total soft x-rays continued for several hundred ns after its peak. The sharp peak in f) is caused by overlapping of the line spectra on the continuous radiation. Typically, the line spectra consisted of successive two pulses with their FWHM's of 5 $\sim$ 8 ns. The second pulse coincided with the life time of the spot which was measured by the streak photograph. On the other hand, Bayley et al. claimed they obtained $\sim$ 250 ps in their experiment with argon.[8]

Possibly the resonance lines were subjected to strong absorption by the surrounding plasma. Even if we assume 20 $\sim$ 80 % of absorption of the resonance line, we obtained 0.5 $\sim$ 0.8 keV of the electron temperature according to the intensity ratio methode by Mewe.[9]

IV. Conclusion

Using the convex Bragg spectrometer, we obtained the monochromatic images of the hot spots formed by the spectral lines of $2 \leqq n \leqq 6$ for the NeX Lyman series and $2 \leqq n' \leqq 6$ for the NeIX $1s^2$-$1sn'p$ series. It was clarified that the x-ray emitting regions (hot spots) in the pinched plasma were not generated simultaneously in the axial direction, but the region appeared near the inner electrode first and shifted along the electrode axis.

The time variation of the spectral lines of NeIX $1s^2$-$1s2p\ {}^1P_1$ + Ne $1s^2$-$1s2p\ {}^3P_1$ and NeX 1s-2p and the total soft x-rays were observed. These signals rose almost at the same time and showed a similar time variation. Typically, the line spectra consisted of successive two pulses with their width of 5 $\sim$ 8 ns. The second one coincided with the life time of the spot which was observed by the soft x-ray imaging system in streak mode. The electron density at the center of the hot spot was estimated to be 0.5 $\sim$ 0.8 keV.

References

1 N. J. Peacock. R. J. speer and M. G. Hobby: J. Phys. B 2 (1969) 798.
2 P. G. Burkalter. G. Mehhlman and D. A. Newman: Rev. Sci. Instrum. 63(1992) 5052.
3 H. Kitaoka. T. Yamamoto and K. Hirano: J. Phys. Soc. Jpn. 67 (1998) 486.
4 K. N. Koshelev. Yu. V. Sidel'nikov. G. Decker. V. Kies. M. Mälzig. P. Röwekamp. F. Rosmej. A. Schulz and H. I. Kunze: Optics and Spectroscopy: 76 (1994) 198.
5 H. Kitaoka. A. Sakurai. T. Yamamoto. K. Shimoda and K. Hirano: J. Phys. Soc. Jpn. 64 (1995) 4191.
6 T. Yanagidaira. M. Sato and K. Hirano: J. J. Appl. Phys. 35 (1996) 5862.
7 T. Yanagidaira and K. Hirano: Rev. Sci. Instrum. 68 (1997) 3074.
8 J. M. Bayley. G. Decker. W. Kies. M. Mälzig. F. Müller. P. Röwekamp and J. Westheide: J. Appl. Phys. 69 (1991) 613.
9 R. Mewe: Solar Phys. 22 (1972) 459.

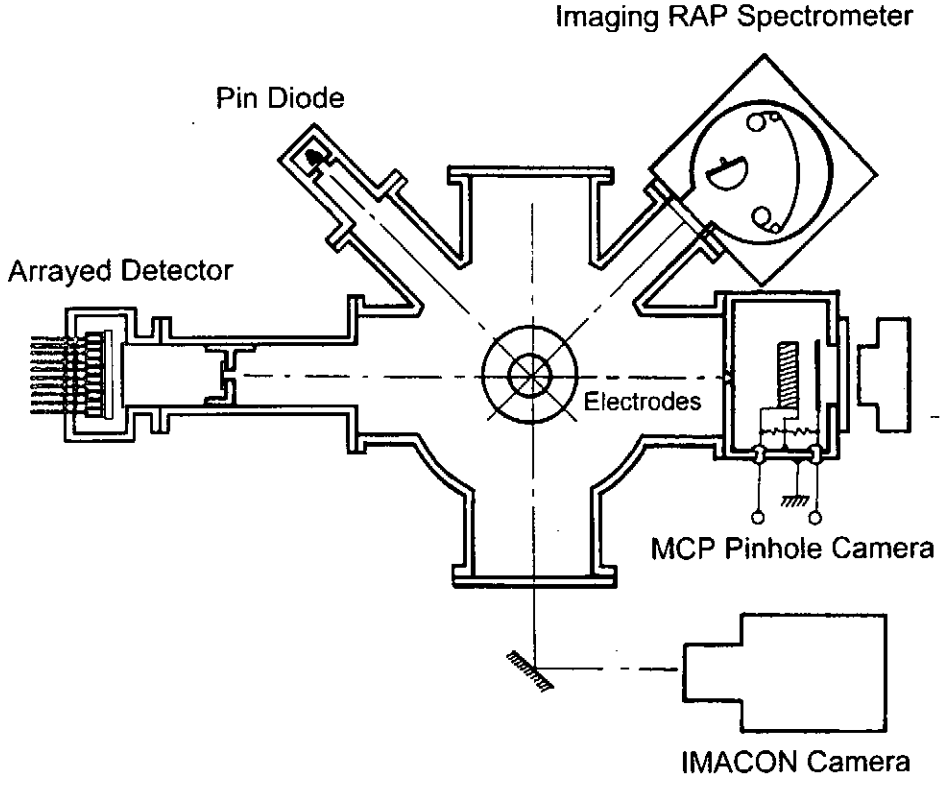

Fig. 1. Plasma focus facility and alignment of diagnostic tools.

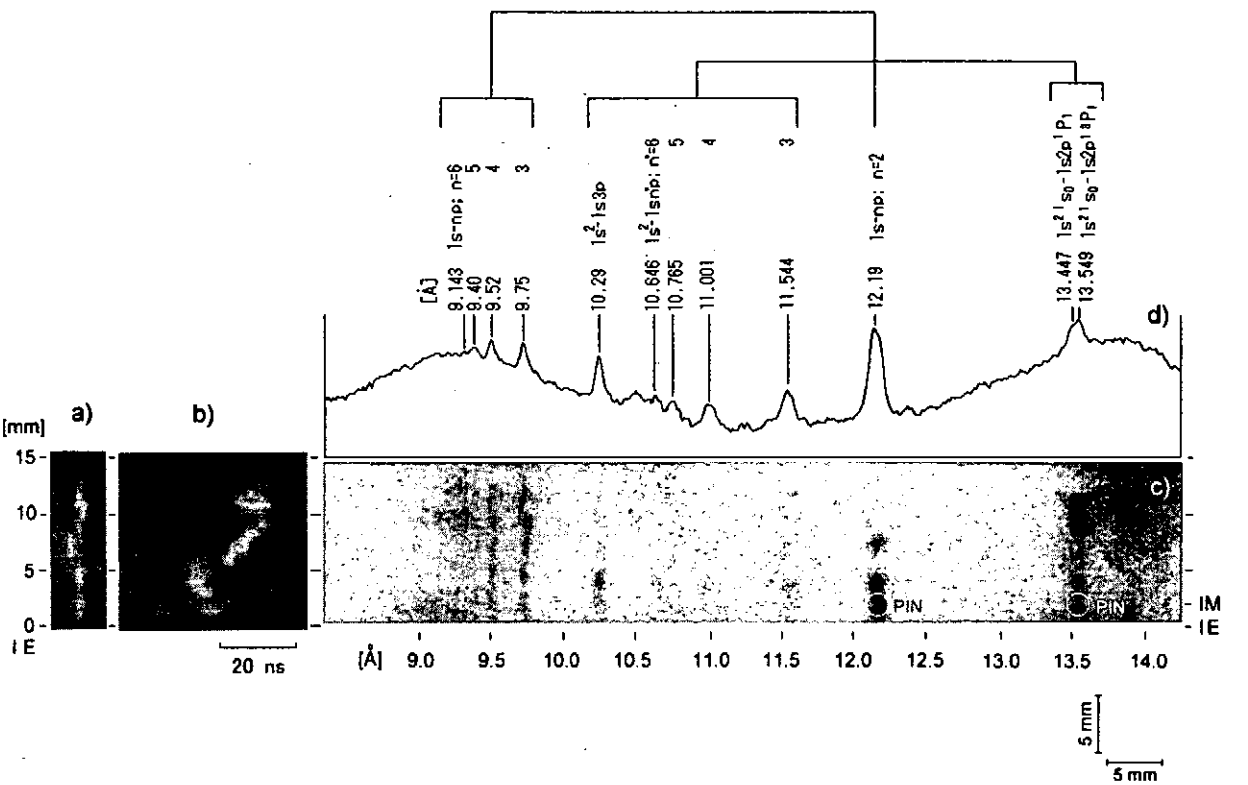

Fig. 2. Macroscopic behavior and imaging spectrogram of neon focused plasma. PIN, IM and IE indicate the locations of the PIN diode, the image converting system and the inner electrode.

a) Time integrated soft x-ray image taken with the MCP pinhole camera.

b) Streak photograph taken with the image converting system.

c) Neon spectrum of plasma focus in the NeX Lyman series and NeIX $1s^2$-$1snp$ series.

d) Neon spectrogram obtained by scanning of c). Intensity is displayed in a linear scale.

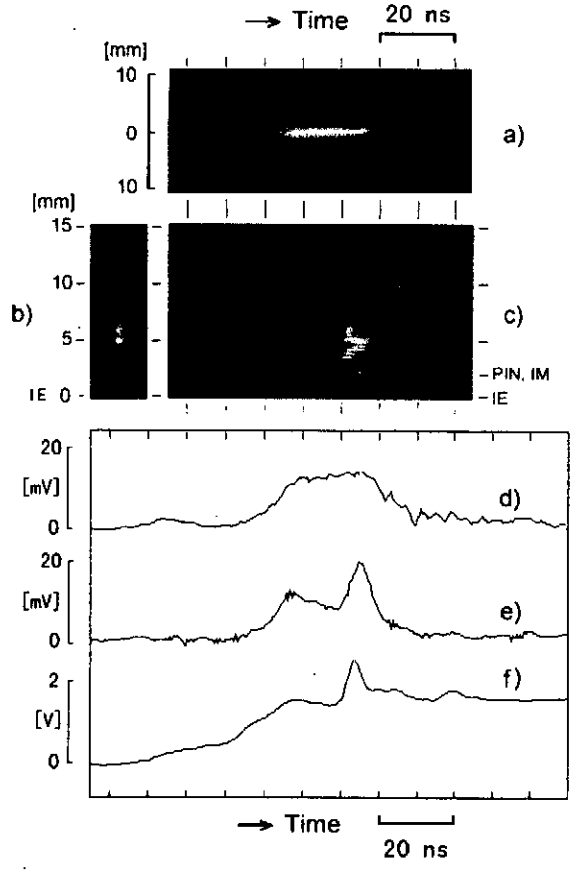

Fig. 3. Correlation between the macroscopic behavior and the soft x-ray emission of the plasma focus. PIN, IM and IE indicate the locations of the PIN diode, the image converting system and the inner electrode.

a) streak photograph taken with the image converter camera in visible light.

b) Time integrated image of the soft x-ray taken with the MCP pinhole camera.

c) Streak photograph taken with the image converting system in soft x-ray.

d) Signal of NeIX (13.449 Å) $1s^2$-1s2p $^1P_1$ + NeIX (13.547 Å) $1s^2$-1s2p $^3P_1$.

e) Signal of NeX (12.19 Å) 1s-2p.

f) Signal of the total soft x-ray intensity.

A High-speed Gated X-ray System for Time-resolved Observation of Z-pinch Plasma

B. Shan*, K. Shimoda, T.Yamamoto, T. Yanagidaira, and K. Hirano

Department of Electronic Engineering, Gunma University, Kiryu, Gunma 376, Japan

Abstract

A multiframe X-ray imaging system was developed in order to make temporally and spatially measurement of Z-pinch plasma. The system was based on a gated MCP with time resolution of ~400ps. It can take four successive frames at a time. The time interval between frames can be adjusted flexibly. The spatial resolution of the whole system was estimated to be 120μm. The output images of MCP imager were taken by a 512X480 CCD and read out at video rate of 8-bit resolution. And the phosphor current of the imager was led to oscilloscope by a circuit to make quantitative evaluation of the intensities of x-ray images. In primary test operation, we had observed the compression and split process of a plasma column in neon puff experiment in a plasma focus device.

KEYWORDS: Z-pinch, Plasma, X-ray, Gated MCP, Multiframe

1. Introduction

Z-pinches driven by multiterawatt pulse power machines produces very high power radiation bursts. It has been proposed and studied as a potential x-ray source for many applications because of its high energy conversion efficiency into the soft x-ray radiation. In gas-puff plasma experiment, high z material is admixed into hydrogen or deuterium background, resulting a series of soft x-ray emitting points known as hot spot or micropinch in which its temperature and density are much higher than other region. The soft x-ray emission mainly comes from these small region. The typical density and temperature of the hot spot have been estimated to be $10^{22}/cm^3$ and several kev. And the observed diameter and length are sub-mm and mm ranges respectively. Several models such as beam plasma interaction and radiative collapse are proposed to explain the formation of the hot spot. But the mechanism has not been understood well in spite of many studies[1,2].

The Z-pinch induces a process with very rapidly changing properties(dimensions, density, and temperature). Moreover, reproducibility is rather poor. These gives much difficulty for the measurements of the plasma parameters.

The dynamics of Z-pinch plasma can be ideally studied using time-resolved pinhole cameras based on a gated MCP framing system. It can record the plasma shape in a picosecond time scale and is capable of recording the evolution of the instabilities of the plasma with several successive frames. It is also possible to make a measurement of a high spectral-, time-, and spatial resolution simultaneously combined with spectrometer. This method is widely known in high temperature laser plasma experiments[3]. However there is still some technical difficulties for implementation of such technique to Z-pinch plasma experiment.

In this paper, we describe the design and construction of a gated MCP framing camera system. It can take four successive frames in an event with time resolution of about 400ps, and is suitable for the

* email: b. shan@usa. net
On leave from State Key Laboratory of Transient Optics Technology, Chinese Academy of Sciences

measurement of the rapid changing properties of Z-pinch plasmas. We had used this device to measure the plasma evolution in a neon puff experiment and observed the process of a plasma compression in radial direction and splitting in axial direction.

2. System design and evaluation

2.1. Working principle and system parameters

Figure 1 shows the working principle of the gated MCP camera. The camera is composed by a proximity focused MCP imager with four parallel stripline cathodes and a pulser providing gating pulses for each stripline. During experiment, the four pinholes produce four x-ray images of the plasma on each stripline. These x-ray images are converted into electron images by the Au stripline cathode. The lifetime of these electron image is of femtosecond order according to the characteristics of Au cathode, and these images can be seen as well represented the time-varied x-ray images. At the same time, high voltage gating pulses are generated by pulser and propagated along stripline with different delay. The pulses gate and multiple these electron images passing through MCP at different times. The gated electron images are then converted to optical images by phosphor screen and recorded by CCD. It can be seen that the time intervals between successive images are the time interval between the gating pulses on each image and can be adjusted by the delay of each pulse. And the exposure time of each image was mainly determined by the pulse width.

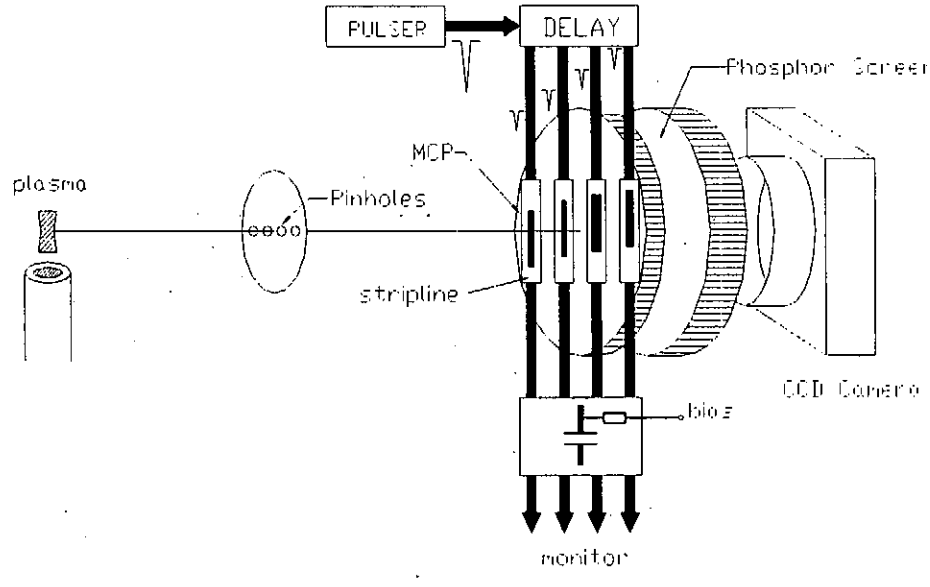

Figure 1. Working principle of gated MCP camera.

The most important parameters of the system is the exposure time, the spatial resolution and the system gain. Precise measurements of these parameters need special instrument[6,7,8]. Because of lack of corresponding measurement tools, we estimate these parameters in the experiment.

2.2. Time resolution

Because of the highly non-linear dependence of the gain on the applied voltage of MCP, the exposure time of gated MCP is shorter than the duration of the applied voltage pulse. Typical gain of MCP is,

$$G = G_0 V^{\gamma} \tag{1}$$

Here G is the gain of MCP and V the applied voltage. For the MCP we used, L/D=40 (Length/Diameter of a microchannel in MCP) and γ is ~9[4,5].

The gating pulse we used is a Gaussian voltage pulse with pulse width of about 1ns in FWHM. The waveform can be written as,

$$V(t) = V_0 e^{-4\ln 2 \left(\frac{t}{W_{pulse}}\right)^2} \tag{2}$$

where V_0 is the peak voltage and W_{pulse} is the FWHM of the pulse. When this pulse is applied to MCP, the consequent gain of MCP is,

$$G(t) = G_0 V_0^{\gamma} e^{-4\ln 2 \left(\frac{t}{W_{pulse}/\sqrt{\gamma}}\right)^2} \tag{3}$$

Equation (3) means that the FWHM of gain is $W_{pulse}/\sqrt{\gamma}$. For the W_{pulse}=1.2ns gating pulse and $\gamma = 9$ (L/D=40) MCP we used, the gating width can be concluded as,

$$W_{gain} = W_{pulse}/\sqrt{\gamma} = 1.2ns/3 \approx 400ps \tag{4}$$

It should be pointed out that equation (1) is only valid when the applied voltage changes slowly compared to the response time of the MCP. Usually the average transit time for the electrons in MCP of L/D=40 and L=0.5mm is 200-300ps[4,5,6]. So the above analysis is reasonable. If a pulse faster than the duration is applied, a time-dependent model for the MCP gain has to be employed[6,7,8].

2.3. Spatial resolution

The spatial resolution of the whole system is determined by its component of the pinhole imaging, MCP imager and CCD camera.

A. Pinhole imaging

We can calculate the spatial resolution with the geometric optics because the wavelength of x-ray is much smaller than pinhole size and the diffraction effect can be neglected.

As shown in figure 2a, the intensity of point x on image plane I(x) comes from the contribution of the pinhole shadow area from Z1 to Z2 viewed from x,

$$I(x) = C \int_{z1}^{z2} I(z)\,dz \tag{5}$$

The input function on source object plane is to be,

$$I(z) = 1 + \cos(2\pi f z) \tag{6}$$

Therefore, we can calculate the intensity distribution I(x) on the image plane. And then get the

MTF of different spatial frequency f by,

$$MTF = \frac{I_{max} - I_{min}}{I_{max} + I_{min}} \tag{7}$$

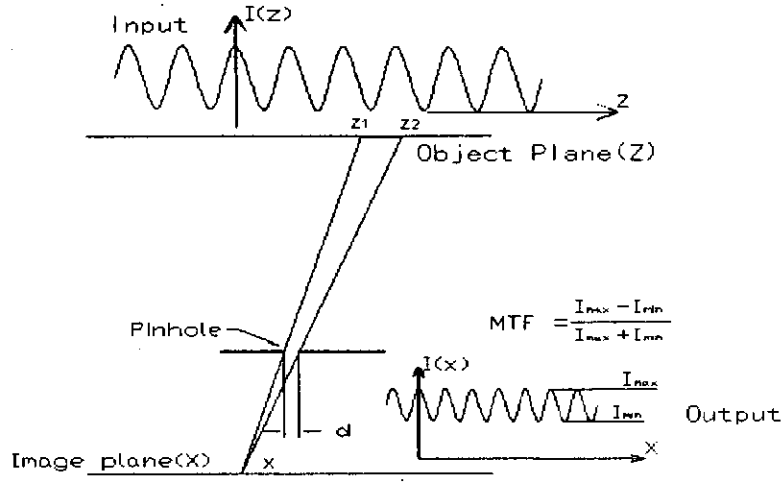

Figure 2a. Calculation of MTF of pinhole imaging

Figure 2b shows the calculated spatial resolution of 15, 25 and 50μm pinholes with 0.6X imaging magnification. The experiment setup of our system is Φ25μm pinhole with 0.6X imaging. We can see from the figure that the MTF is 10%-30% at the spatial resolution 10-12lp/mm(object plane). Compared to the MCP imager and CCD system, the spatial resolution of pinhole imaging is much better.

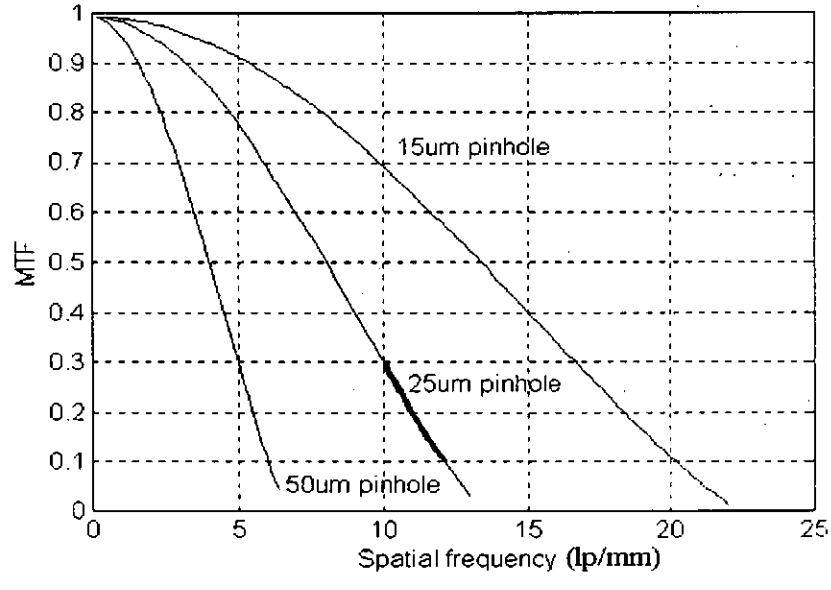

Figure 2b. Calculated imaging MTF for 15, 25, and 50μm pinhole

The above analysis is made with one-dimension pinhole. The practically used circular pinhole can be seemed to be composed of a series one-dimension pinhole with the size ranging from 0 to the

diameter of the pinhole. So the true spatial resolution of the ϕ25μm pinhole will be better than analyzed above.

B. Imager

The factor which determines the spatial resolution of the imager is the proximity focus between the output of MCP and phosphor screen. As shown in figure3, the electrons has a horizontal velocity component v_s when it comes out of the channel of MCP. And it will cause a blur in the horizontal direction while the electron flight from MCP to phosphor. That's the main reason for the limited spatial resolution of the proximity focusing.

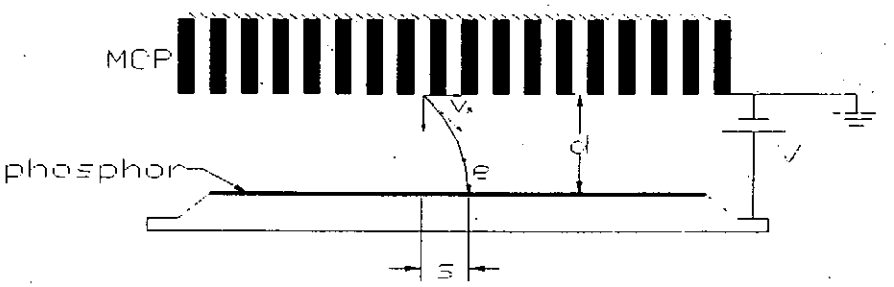

Figure 3. Dispersion of electron image at MCP/phosphor gap

It can be deduced that the horizontal displacement on phosphor screen is,

$$S = v_s \sqrt{\frac{2m}{e}\frac{d^2}{V}} \tag{8}$$

where V is the voltage across the MCP/phosphor gap. It is constrained by the breakdown voltage of the gap. Usually the distance of MCP/phosphor gap, d is chosen between 0.5 to 1mm. For the routine working in our z-pinch chamber, our camera has a configuration of d=1mm and V=2KV.

The horizontal velocity v_s of electron at the exit of MCP is only determined by the MCP itself. So we can estimate the spatial resolution of MCP/phosphor gap by other data. For the configuration in ref. 6, the spatial resolution is 25lp/mm(~20um) with d=0.5mm and V=3KV. So we can estimate the spatial resolution of our imager as,

$$R_{imager1} = \frac{\sqrt{d_1^2/V_1}}{\sqrt{d_2^2/V_2}} \times R_{imager2} = \sqrt{\frac{1^2/2000}{0.5^2/3000}} \times 20\mu m \approx 50\mu m \tag{9}$$

This value is in same order with the spatial resolution of our CCD system.

C. CCD camera

The spatial resolution of CCDs is determined by the number of pixels and the view window of CCD camera. Usually the resolution of lens is much higher than CCD.

The CCD which we employed has a pixel array of 512X480 and a view window of 27.4X25.7mm. So the spatial resolution can be estimated as the size of pixels at the phosphor screen,

$$R_{CCD} = \frac{27.4mm}{512} \approx 50\mu m \qquad (10)$$

So the spatial resolution of the whole system is determined by the imager and the CCD system. As the magnification rate of pinhole imaging is 0.6X, the resolution of whole system at plasma is about $\sqrt{\left(R_{imager}/0.6\right)^2 + \left(R_{CCD}/0.6\right)^2} \approx 120\mu m$.

2.4. System gain and Quantitatively evaluation of x-ray intensity

The CCD system we used is a normal type and coupled by a normal commercial lens to imager. It has a rather low sensitivity, so the gain of the system is critical for observing the plasma. In the system, the gain is controlled by the pinhole size, gate width and voltage across MCP/phosphor gap.

Apparently the passed energy through the pinhole is proportional to its area. On the contrary a smaller pinhole will have a better spatial resolution. Considering both the detectable energy of imager and spatial resolution, we choosed the 25um pinhole.

There is also such balance between time resolution and system gain. With the 1.2ns pulse we used, the gate width is about 400ps. It's just greater than the average transmission time of the electrons in MCP. If the pulse width is shorter than 1ns, the gain will decrease rapidly with the gate width. So it is necessary to use such a longer pulse to obtain useable gain of the system.

From equation (3), we can get the electron gain of a pulse as,

$$G_{MCP} = \int G_0 V_0^{\gamma} e^{-4\ln 2\left(\frac{t}{W_{pulse}/\sqrt{\gamma}}\right)^2}$$

$$= G_0 V_0^{\gamma} W_{pulse} \sqrt{\frac{\pi}{\gamma \ln 2}} \qquad (11)$$

With above calculated gain of MCP and the conversion efficiency of Au cathode[10], we can take measure of the phosphor current to quantitatively evaluate the x-ray sources[11].

3. Construction of the system

3.1. MCP imager

Because the gating pulses are very fast, the key technique of gated MCP imager is the transmission structure for the gating pulses. It should be ensured that the fast gating pulse can be transferred onto the MCP effectively.

The MCP, Hamamatsu F1552-01 was employed in the imager. Its diameter and thickness is 32.8mm and 0.48mm respectively, and the microchannel diameter is 12um. The width of each stripline cathode is 3mm, and its effective length is 18mm. This means even the largest size of images on MCP is limited to 18X3mm.

The stripline cathode was made by coating 1-2um Au with a mask on MCP. For 3mm stripline on MCP, the resultant transmission impedance is about 28ohms. To match the 50ohm connectors and pulse generator, an exponential stripline transformer is utilized to change the impedance from 50ohm to 28ohm at the input side of the MCP and change the impedance from 28ohm to 50ohm at the output side.

A Teflon PCB(printed Circuit Board) is used as transmission circuit of the gating pulses from connectors to MCP. The dielectric constant of the PCB is 2.65, which is almost same with that of MCP. So we simply made the same width(3mm) of the striplines on the connection end to MCP, to match the transmission impedance at the joint point. The stripline transformer is fabricated on the PCB by suitable etching. Its width was changed exponentially from the 50ohm connector side of 1.32mm to 3mm at the PCB/MCP joint.

We used a 20um gold foil for connecting striplines from PCB to MCP with a ceramics fixing ring on the MCP/PCB joint, securing the MCP and the gold foil in the imager. There is also eight adjusting screws in the fixing ring just at the eight ends of the four striplines on the MCP. The transmission characteristics can be adjusted by the screws which pressed each gold foil at the stripline end. The structure is shown in the figure 4. Eight vacuum sealed SMA microstripline connectors were welded on the flange connecting the eight ends of stripline transformer to pulser and matched circuit.

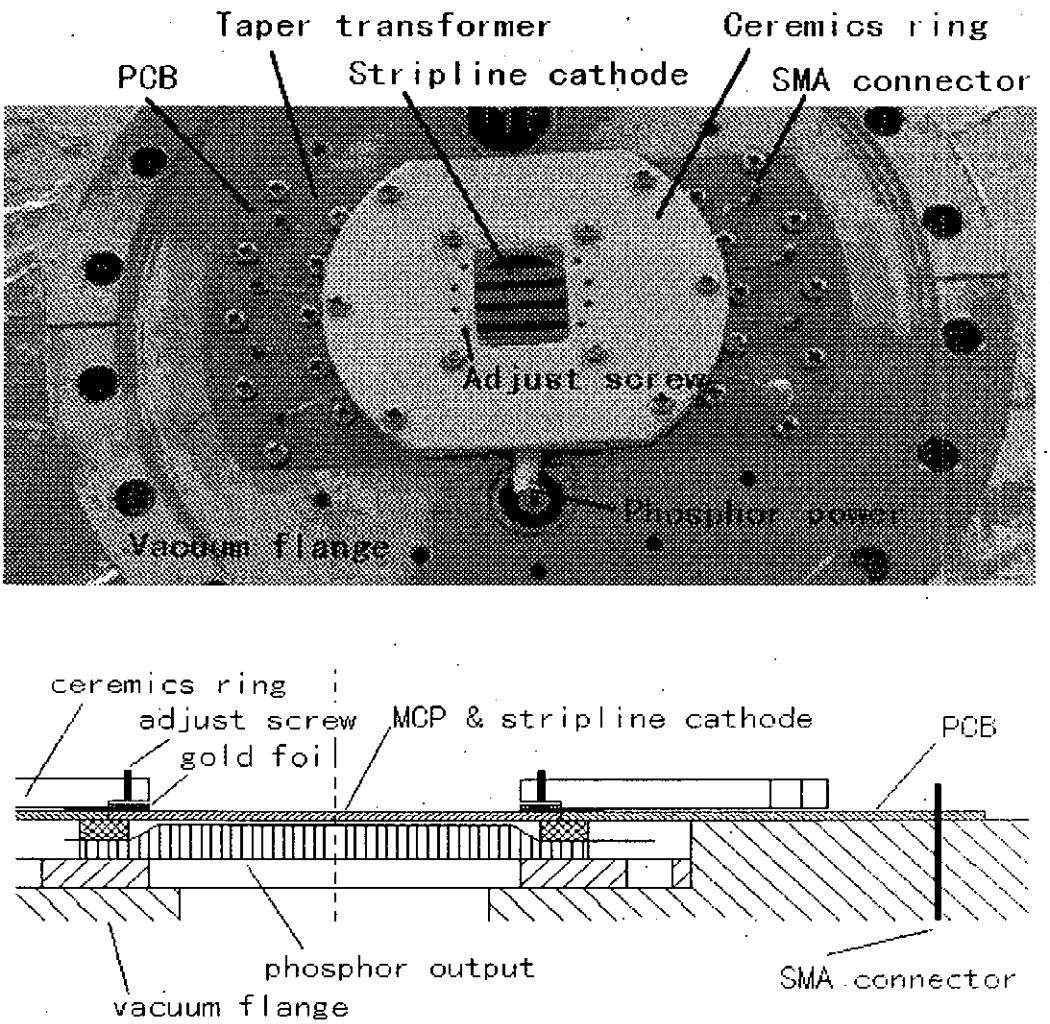

Figure 4. Structure of gated MCP imager

The phosphor screen Hamamatsu F2223 type coated with P20 phosphor was mounted behind the MCP. The effective area of the phosphor window is ϕ24. The distance between the output surface of MCP to phosphor is 1mm.

It should be pointed out that if the system gain is enough to output a clear image, the structure of the imager is capable to get time resolution of sub-100ps with 200-300ps gating pulse[6,9].

3.2. Pulser

The gating pulses were generated by a marx bank type avalanche transistor circuit and two sharpening diode circuits. The avalanche circuit is composed of trains of avalanche transistor FMMT417 aligned in CPWG transmission line type. The FMMT417 has a avalanche voltage of 320V. Seven transistors were used in one string. We first use two strings connected in marx bank type as the primary pulse generator, then the pulse from the first stage was split into two pulses to drive another two symmetrically arranged transistor strings. Then we can get two identical high voltage step pulses. The whole circuit has six strings of FMMT417 transistors all aligned in marx bank type, and each string was applied with power of -2.5kV. The output step pulse of the transistor circuit is more than 4KV into 50ohm load. With these pulses be led to the sharpening diode circuit, we can get a very narrow high voltage pulse[13].

The diode we used in the sharpening circuit is 1N5408, it undergoes a very fast TRAPATT avalanche breakdown when applied with fast step pulse[12]. We use two diode circuits driven by the two outputs of the transistor circuit. The four gating pulses were obtained by using a divider to split each of the output pulse from diode circuit. The measured gating pulse is shown in figure 5, the generated four pulses is 1.1ns FWHM and about 2.7kV amplitude into the 50ohm load. These pulses were then sent to MCP though 10 meter long cables. The pulses degraded to 1.9kV, 1.2ns in the amplitude and the width after the transmission of the 10 meter cables. If there was no loss for pulses transferred from the 50 ohm SMA connectors to the 28 ohm stripline on MCP, the voltage amplitude on MCP could be calculated as,

$$V_{MCP} = V_{input}\sqrt{\frac{28}{50}} \approx 1.42\ KV \qquad (12)$$

We estimated voltage loss of the taper transformer in the imager is 5%~10%[14]. So the amplitude of the gating pulse on MCP should be ~1.3kV.

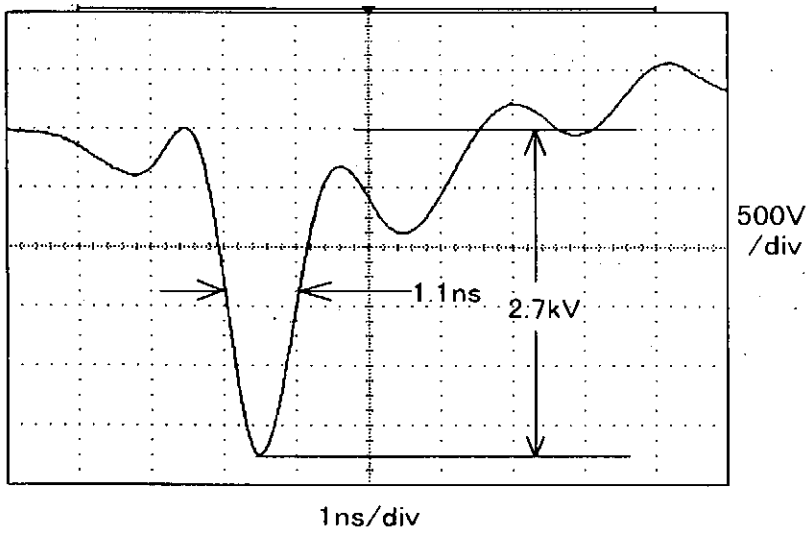

Figure 5. Generated gating pulse

The jitters between pulses to trigger are dominated by the transistor pulser. It is in several tens picosecond order and is very small compare to the jitters of the plasma onset. And the jitters between pulses will be even smaller because all the pulses come from the same circuit[9].

3.3. System structure

The layout of whole system in the z-pinch plasma experiment is shown in figure 6. The vacuum chamber for MCP is separated from the main chamber by flange with four small holes blocked with 50um Be filter. In the experiment the vacuum is better than $3X10^{-6}$Torr in the MCP chamber while the main chamber is 10^{-4}Torr. The Be filter is also used to block the visible light emitted from the source and provides an appropriate passband for the x-ray. The recorded x-rays were in the energy range of 1-2keV which is determined by the 50um Be filter and the Au photocathode. This fact is very important for the evaluation of the x-ray intensity.

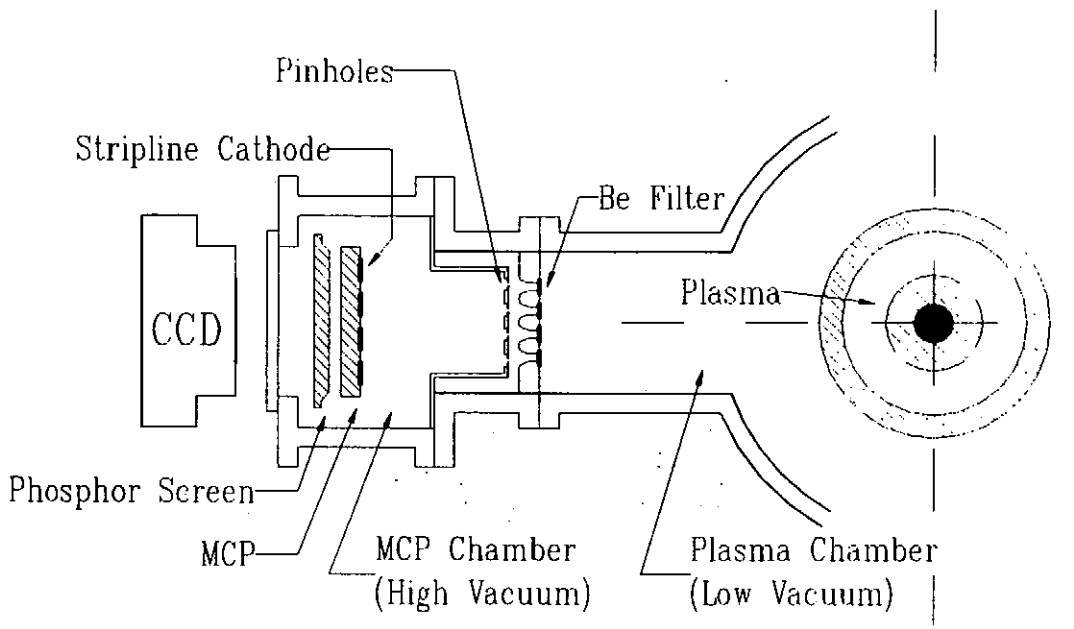

Figure 6. System structure

The phosphor screen current, which represents the flux of electrons emitted from the MCP was measured. It is possible to obtain a quantitative relationship between the intensity of the visible image and the electron number. And as discussed in 2.4, we can also get a quantitative relationship between the electron number and the incident x-ray photons. Therefore, we can evaluate the number of photos which pass through the pinhole after taking into account the response of Au photocathode and Be filter[11]. Combined with the XRD or the PIN signal, the phosphor current can be also used to resolve the time sequence of measured images with plasma onset.

The visible image on phosphor screen is recorded by a CCD camera(Sony XC-77RR) with 8 bit intensity resolution and registered in an image memory board(Photron FRM2-512).The image data can be stored in standard image file format. This system permits flexible processing of the data and its presentation in various formats. The CCD camera was operated in the mode in which the response of the CCD was proportional to the luminosity of the object. The image board was modified to be operated in a single shot mode.

The four pinholes were mounted just behind the four small holes of Be filter. And a stepping motor was used to adjust pinhole position. So we can adjust to alignment the pinhole position with plasma and striplines out of the vacuum chamber during experiment. An UV light source was installed in the imager to make in-situ examination of the imager.

4. Primary application

The system has been used to make time resolved measurement in a Mather type plasma focus device[15]. In the experiment, the discharge chamber of the plasma focus device was embedded with 5.5 torr hydrogen base and the Neon gas was puffed with a fast acting valve just before the discharge. The device was operated at bank voltage of 45kV and the discharge current was ~1MA.

Figure 7 shows the x-ray images of a typical neon puff experiment results. The time interval between two adjacent frames is 2.5ns. The shape of the plasmas changes rapidly from frame to frame.

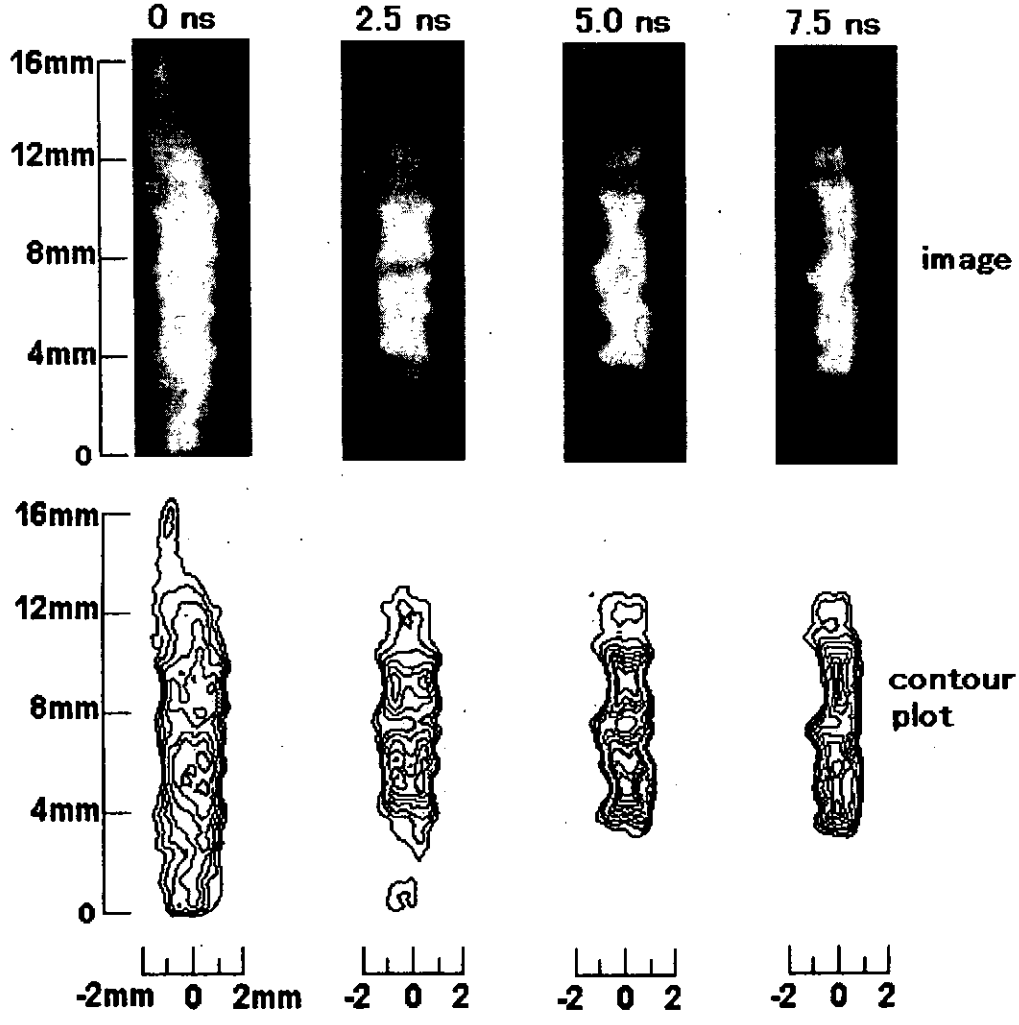

Figure 7a. Time resolved observation of compression process in pinch plasma

In figure 7a, there are two separated areas in the pinched plasma. We take the arc shape in the figure as the plasma-vacuum border to calculate the pinch speed. From Frame1 to Frame4 in duration of 7.5ns, the minimums between radius of the arc shaped plasma columns in the two parts were constricted from ~2.05 to ~0.27mm, and from ~2.22mm to~0.35mm, respectively. We can calculate from these that the radial compression speed of the plasma column in the figure is ~2.33 $X10^5$m/s, which is in same order with that by other works[2].

Figure 7b shows another results. In this figure, in Frame1 the plasma had already compressed to a very narrow area, and in the succeeded frames begin to split into two parts in axial direction. The upper part moves in the direction of gas puff, while the lower part in opposite direction. And the axial speed of the two parts were calculated to be $3.33X10^5$m/s and $2.08X10^5$m/s, respectively. These results are also in same order with that of a carbon fiber z-pinch experiments[16].

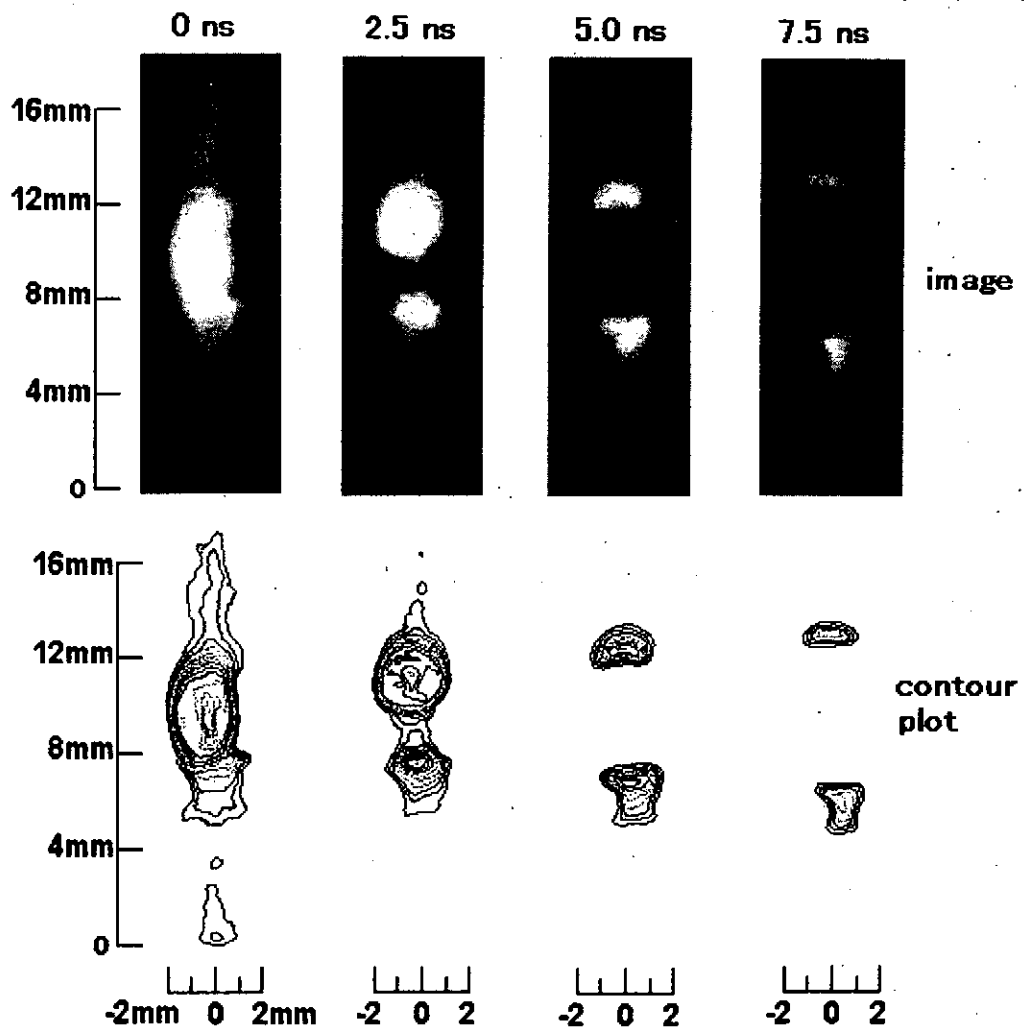

Figure 7b. Time resolved observation of splitting process in pinch plasma

5. Summary

We had constructed a time resolved pinhole system based on a gated MCP. The time resolution of the system is ~400ps and spatial resolution is ~120um. The primary test operation in a gas puff pinch plasma experiment showed that the system is capable to make time resolved research for the pinched plasma. The primary experimental results of neon puff plasma had deduced some useful information. The process of compression and splitting of the pinched plasma were observed by the system. The compression speed of the plasma column is measured to be ~$2.33X10^5$m/s and the splitting speeds in axial direction were $3.33X10^5$m/s.

Further development of the system is going on to get better time and spatial resolution. With a better CCD system, we can improve both spatial resolution and gain of the system. And the time resolution could be improved to ~100ps by shorter gating pulses if the gain of the system can be improved.

6.References

1. K. Hirano, Y. Takahama, M. Han, and T. Yanagidaira, Jpn. J. Appl. Phys., 63(10), 3657-3660(1994)
2. K. N. Koshelev, Yu. V. Sidel'nikov, G. Decker, V. Kies, M. Malzig, P. Rowekamp, F. Rozmej, A. Schulz, and H.-I. Kunze, Optics and Spectroscopy, 76(2), 198-202(1994)
3. J. A. Oertel, T. Archuleta, C.G. Peterson, F. J. Marshall, Rev. Sci. Instrum, 68(1), 789-791(1997)
4. "Characteristics and applications of microchannel plates", Hamamatsu Inc.,
5. P. M. Bell, J. D. Kilkenny, R. Hanks, O. Landen, Proc. SPIE 1346, 456-464(1990)
6. Z. Chang, B. Shan, X. Liu, J. Liu, W. Zhu, H. Yang, Y. Ren, M. Gong, Proc. SPIE Vol. 2549, p. 53-59
7. M. Katayama, M. Nakai, T. Yamanaka, Y. Izawa, and S. Nakai, Rev. Sci. Instrum., 62(1), 124-129(1990)
8. D. K.Bradley, P. M.Bell, O. L. Landen, J. D. Kilkenny, J. Oertel, Rev.Sci.Instrum., 66(1), 716-718(1995)
9. B. Shan, Z. Chang, J. Liu, X. Liu, et al. Proc. SPIE Vol. 2869, 182 - 188 (1997)
10. B. L. Henke, J. P. Knauer, and K. Premaratne, J.Appl.Phys. 52(3), 1509-1520(1981)
11. Y. Takahama, J. Du, T. Yanagidaira, and K. Hirano, Rev.Sci.Instrum., 65(8), 2505-2509(1994)
12. I. V. Grekhov and A. F. Kardo- Sysoev, Sov. Tech. Phys. Lett., 5(8), 395-396(1979)
13. T. E. McEwan and R. L. Hanks, Proc. SPIE Vol.1346, pp465-470
14. P. M. Bell, J. D. Kikenny, O. L. Landen, and R. L. Hanks, Rev.Sci.Instrum. 63(10), 5072-5074(1992)
15. T. Yamamoto, T. Yanagidaira, B. Shan, and K. Hirano, to be published
16. J. P. Chittenden, I.H. Mitchell, R. Aliaga-Rossel, J. M. Bayley, F.N. Beg, A. Lorenz, and M.G. Haines, Phys. Plasmas, 4(8), 2967-2971(1997)

A New 400 kA Pulsed Power Generator ASO-X

S. Kohno, I. V. Lisitsyn *,
S. Katsuki * and H. Akiyama *

Department of Electrical Engineering, Ariake National College of Technology, Omuta 836, Japan
*Department of Electrical and Computer Engineering, Kumamoto University, Kumamoto 860, Japan

Abstract

This autumn, new pulsed power generator using technique of an inductive voltage adder was put into operation in Kumamoto University. This machine, named "ASO-X", is an inductive energy storage pulsed power system. The maximum output voltage and current of ASO-X are 180 kV and 400 kA respectively with short circuit load with 1.33 μsec of current rise time. To sharpen the rise time of load current, plasma opening switch (POS) was applied to the output of ASO-X with 8 plasma guns as plasma source. In this system a very fast current rise rate of 3×10^{12} A/sec with over 1μsec of conduction time was achieved.

1. Introduction

Many applications of pulsed power systems require higher current and higher voltage; furthermore, the rising time of load current is important for a sort of applications, such as Z-pinch and capillary pinch. Recently a new pulsed power generator, which is called ASO-X, using technique of an inductive voltage adder[1-3] was built in our laboratory. It could supply high voltage and large current to the load. Fig.1 shows the schematic design of ASO-X generator and fig.2 shows its electrical circuit. ASO-X consists of 6 capacitors with a capacitance of 3.2 μF and 3 cores. These cores (Hitachi Metals Ltd. FINEMET FT-1H) are suitable for pulsed

power generator since they are fast enough. For multiplying output voltage, ASO-X has three stages. Each stage consists of a set of two capacitors and one core and this part is enclosed in a chamber filled by SF_6 gas. With charging voltage of 60 kV the maximum output voltage and the peak current are 180 kV and 400 kA. After charging 6 capacitors, thyratron is used to trigger three sparkgaps of ASO-X. All operation is controlled form a remote screen room.

The POS is one of the opening switches used to compress the pulse in the inductive energy storage pulsed power system[4-6]. During the conduction phase, the POS acts as a conductor and after some time interrupts the generator current rapidly.

In this paper the characteristics of new pulsed power generator ASO-X with microsecond POS are described.

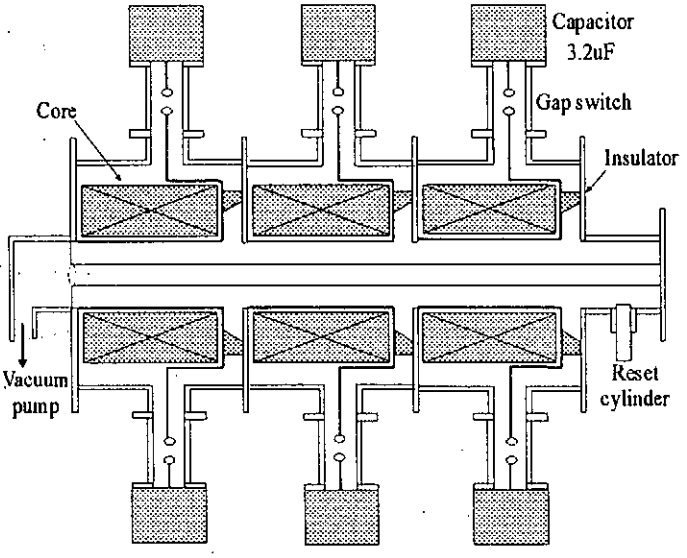

Fig.1. The configuration of ASO-X

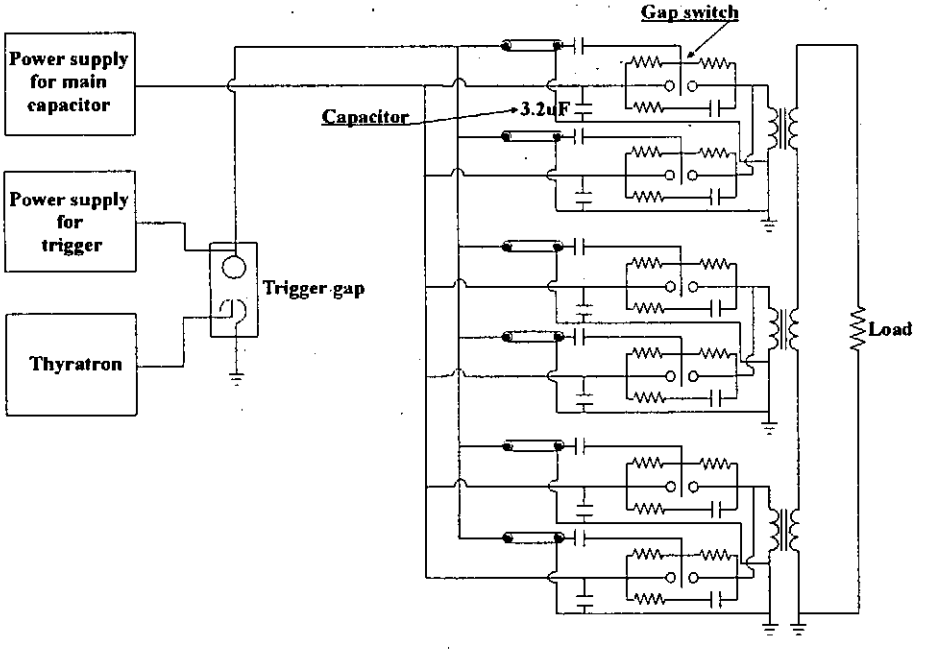

Fig.2. The equivalent circuit of ASO-X

2. Experimental Setup

To connect the POS region and the load with ASO-X, extra outer electrode and inner electrode were attached to output side of generator. Fig.3 shows the schematic diagram of the POS region. The diameters of outer electrode and inner electrode are 140 mm and 60 mm respectively. The end plate of the inner electrode is connected to outer electrode with copper plate as short load. This part is enclosed in a vacuum chamber with the residual pressure of about 10^{-4} Torr.

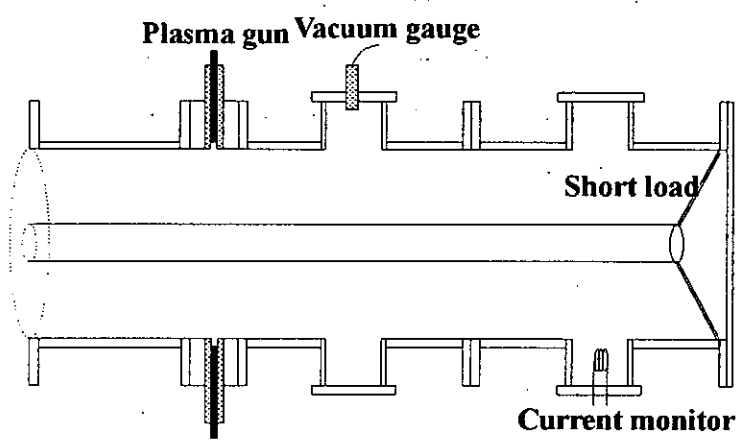

Fig.3. The scheme of POS region.

Fig.4 shows the scheme of plasma gun. To achieve uniform plasma fill density in the POS region, 8 guns were mounted in the outer electrode. The center

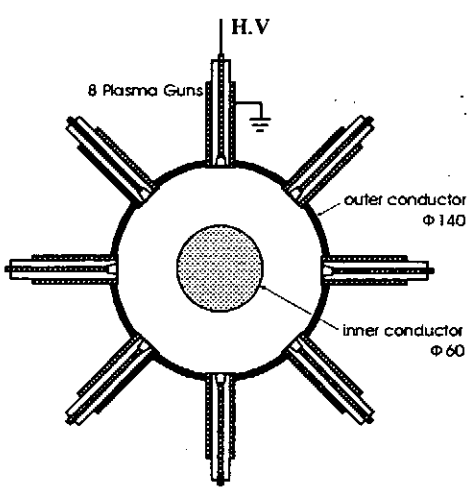

Fig.4. The scheme of plasma gun.

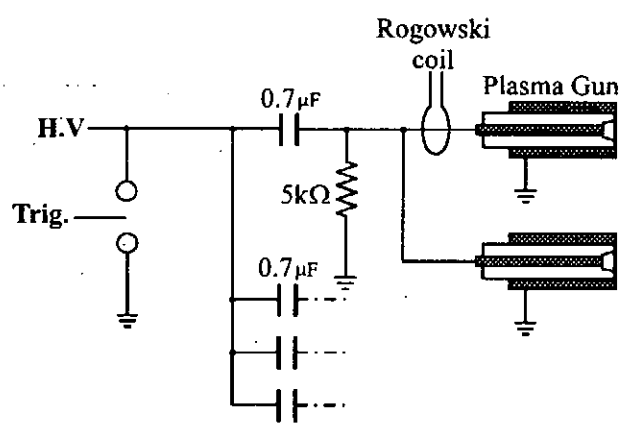

Fig.5. The circuit of plasma guns

electrode of plasma gun is a copper wire with a diameter of 2.9 mm covered with polyethylene insulator tube. Fig.5 shows the electrical circuit of plasma guns. The plasma source consists of 8 guns, 4 capacitors with a capacitance of 0.7 μF each, 4 charging resistors of 5 kΩ and one triggered spark gap (TSG). A pair of guns is driven by one capacitor. All capacitors are charged up to 25 kV and fired by the signal of external trigger producing plasma in the POS region. One of plasma gun currents is measured by a Rogowski coil.

Fig.6 shows the schematic diagram of the POS operational experiment. To control the delay time between the plasma production and the generator current flow a delay/pulse generator (Stanford Research DG535) is used. Varying the delay time, the generator current I_G is measured by a Rogowski coil located near the output of ASO-X and the load current I_L is measured by a current monitor located between the plasma guns and load. At a charging voltage of 30 kV, the generator current reached its maximum of about 150 kA in 1.4 μsec.

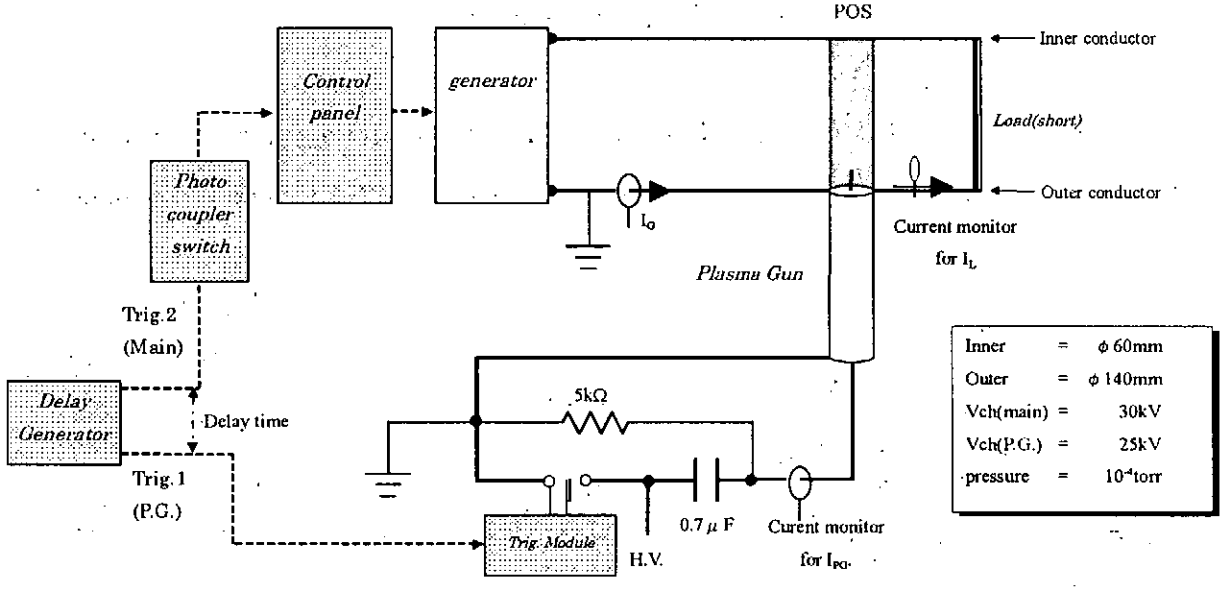

Fig.6. The schematic diagram of POS operational experiment.

3. Results and Discussion

At first, we measured the plasma ion current density from plasma gun by a biased Faraday cup. Ion current density of the distance between the muzzle of gun and faraday cup of 45 mm is shown in fig.7. The plasma flow arrives at about 1.6 μsec after firing and the peak density current takes place at 2.0 μsec and after that it does not vary so much. Fig.8 shows the dependence between distance and the peak value of plasma density. The peak plasma density at 40 mm, which corresponds to the surface of the inner electrode, is about 7×10^{13} /cm^3.

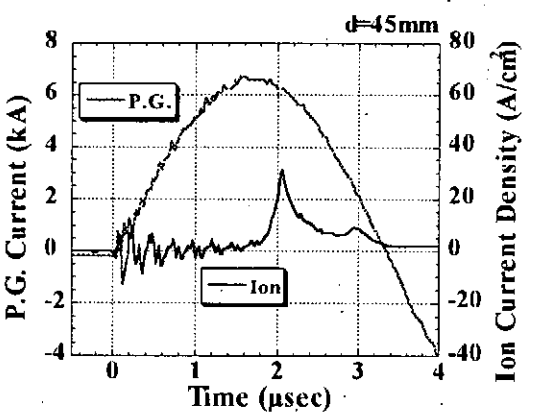

Fig.7. Ion current density(d=45mm).

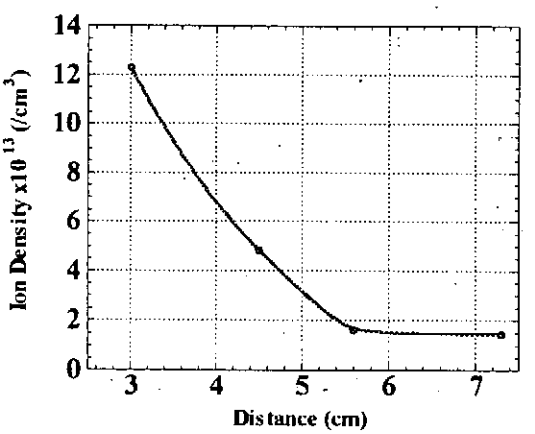

Fig.8.The dependence between Distance and the peak value of ion density.

Fig.9 shows the typical waveforms of the generator current I_G and the load current I_L in POS experiments. The delay time in figures (9.1 - 9.4) is 0.14 μsec, 1.58 μsec, 2.66 μsec and 4.68 μsec respectively. All of these I_L, except of the case of 0.14μsec, rise faster than I_G after conducting current for some hundreds ns. The plasma does not fill the switch region at 0.14 μsec yet. From this result, the fast opening of POS can be confirmed. The dependence of the delay time vs. the conduction time is shown in fig.10. The operation of POS can be seen after about 0.8 μsec of time delay and this is clearly necessary time for effective plasma to fill the POS region. The longer the delay time is, the longer the conduction time

becomes. However the long conduction time over 1.4 μsec, which corresponds to the quarter period of ASO-X current, is too long. So the preferable delay time is from 0.8 μsec to 3.8 μsec. The dependence of the delay time and dI_L/dt, which is the maximum rise rate of the load current I_L, is shown in fig.11. The fastest dI_L/dt is obtained at 2.7 μsec of delay time and its value is about 3×10^{12} A/sec. Higher and lower time delays result in lower rise rate of load current. So in this system with given parameters, the best POS operation is obtained when the delay time is about 2.7 μsec.

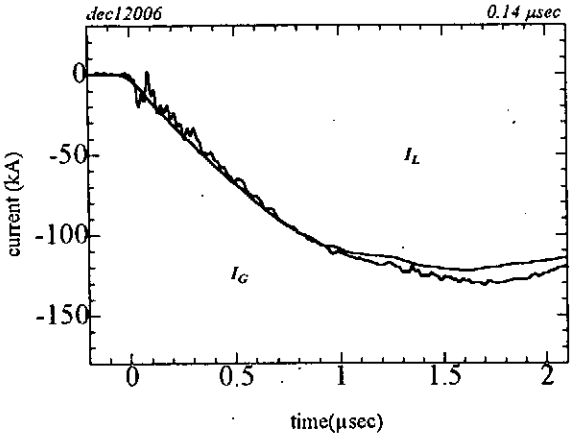

Fig.9-1. Typical waveform
(delay time = 0.14μsec)

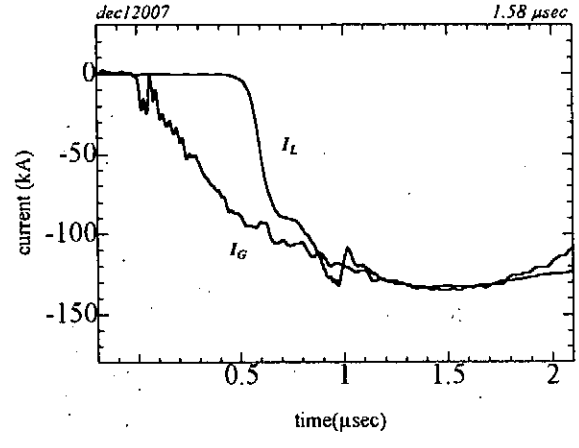

Fig.9-2. Typical waveform
(delay time = 1.58μsec)

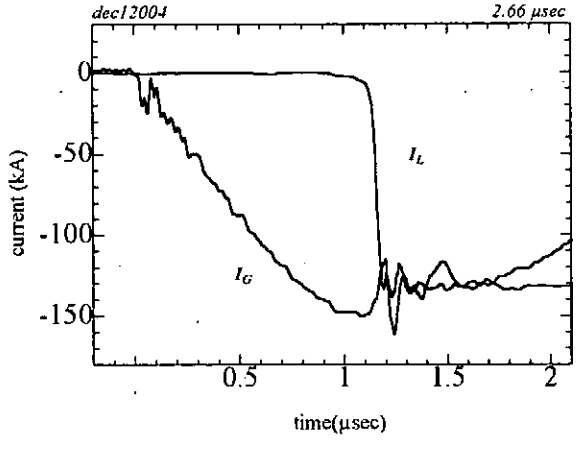

Fig.9-3. Typical waveform
(delay time = 2.66μsec)

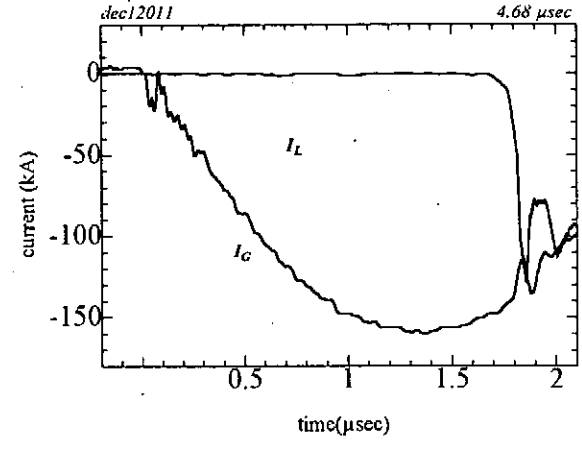

Fig.9-4. Typical waveform
(delay time = 4.68μsec)

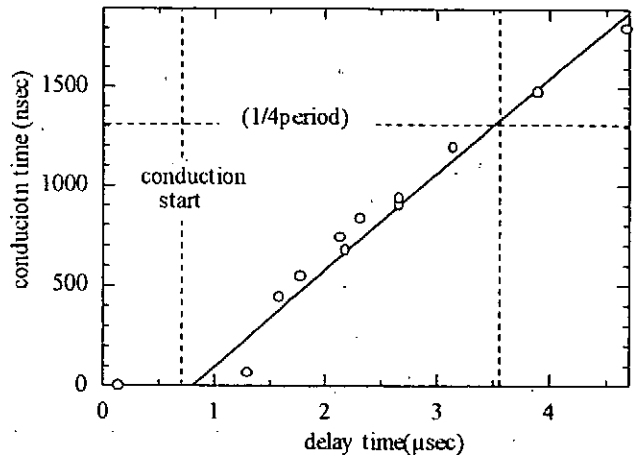

Fig.10. The dependence of the delay time and the conduction time

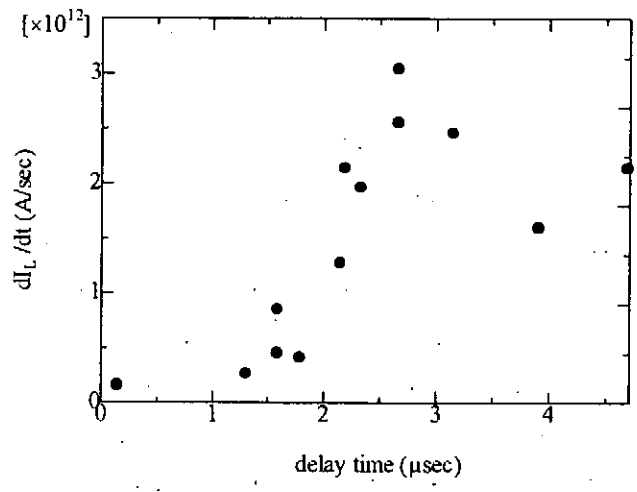

Fig.11. The dependence of the delay time and dI_L/dt

4.Refernces

[1]. W. Bauer, et al., 9th IEEE Pulsed Power Conf., pp. 431-436, 1993

[2]. M. E. Cuneo, et al., 9th IEEE Pulsed Power Conf., pp. 423-426, 1993

[3]. M. G. Mazarakis, et al., 9th IEEE Pulsed Power Conf., pp. 427-430, 1993

[4]. G. A. Mesyats, et al., IEEE Trans. Plasma Sci., Vol.PS-15, No. 6, pp. 649-653, 1987

[5]. Bruce V. Weber, et al., IEEE Trans. Plasma Sci., Vol. 19, No. 5, pp. 757-766, 1991

[6]. J. R. Goyer, et al., IEEE Trans. Plasma Sci., Vol. 22, No. 3, pp. 242-245, 1994

Characteristics of capillary plasmas in an electrothermal gun

T. Sueda, N. Nishida, S. Katsuki, I. V. Lisitsyn, H. Akiyama
Department of Electrical and Computer Engineering, Kumamoto University,
Kurokami 2-39-1, Kumamoto 860-8555, Japan

Abstract

An electrothermal gun has been studied to investigate of the physical phenomena in the initial phase of the capillary discharge. High pressure is produced momentarily and accelerates the projectile to hypervelocity as the current with short rise time is applied to the capillary. The electron density and temperature of capillary plasmas are measured for the discharge current with different rise times by spectroscopy and interferometry, and compared with results of a 0-D time dependent model in order to verify the experimental data. It is found experimentally and theoretically that the electron density and temperature for the current with short rise time tend to increase in early time.

1. Introduction

Electrothermal gun is one of electromagnetic launch devices for the final goal of accelerating projectiles to hypervelocity. The projectile is accelerated to hypervelocity by using high density and temperature plasmas, which are produced by high power pulse discharges in the capillary resulting in the high pressure in the electrothermal gun. Since the plasma pressure is very dependent on the electrical energy delivered to the capillary discharge, it is necessary to increase the energy input into the discharge in order to increase the projectile velocity. The geometry of the capillary, and the capillary material, etc. have been varied to control the input energy. [1, 2] Experiments on electrothermal guns have been conducted at various ambient pressures according to their particular applications, which are simulations for micro-meteoroid and space debris impacts, and production of extremely high pressure and temperature for the development of new materials. [1]

An electrothermal gun has been studied at Kumamoto University for investigation of the physical phenomena in an initial state of the capillary discharge. We have been changed the ambient pressure in the electrothermal gun in order to investigate the phenomena of capillary discharges and the characteristics of capillary plasmas. The initial state of the capillary discharge varies from arc discharges to surface discharges as the ambient pressure decreases. [3] At low pressure, the capillary plasma density is high during the surface discharge because wall ablation occurs on the surface of the capillary. [4] In addition, reducing the capillary diameter leads to higher kinetic energy of the projectile because the plasma resistance increases with decreasing diameter and, hence, increases the energy delivered to the capillary plasmas. It is found experimentally and theoretically that the electron density and temperature tend to increase with decreasing capillary diameter. [5]

When the current with short rise time is applied to the capillary, high pressure is rapidly produced and accelerates the projectile to the hypervelocity. The purpose in this paper is to investigate the characteristics of capillary plasmas for the discharge current with different rise times. The electron density and temperature of the capillary plasmas for the discharge current with different rise times are measured by using a spectroscopy and interferometry. The density and temperature are also calculated by a 0-D time dependent model in order to verify the experimental data for the characteristics of capillary plasmas. The experimental data are compared with the theoretical results, and then discussed in order to achieve the best operating conditions for the electrothermal gun.

2. Experimental Apparatus and Procedures

2. 1 Spectroscopic measurements

Fig. 1 shows the experimental setup for spectroscopic measurements. The power supply consists of a capacitor bank with the maximum stored energy of 80 kJ and a capacitance of 64 μF, a coil with the inductance of 3.5 μH αnd a triggered spark gap switch. The electrothermal gun usually consists of copper electrodes, a polyethylene capillary and a steel barrel, although the barrel is removed from the electrothermal gun during this experiment in order to observe the radiation from the capillary plasma. The inner diameter of the cylindrical capillary is 4 mm, and its length is equal to 30 mm. A thin copper wire with a diameter of 0.04 mm is placed in the capillary, and is connected to both electrodes. Four wire fuses with a diameter of 0.15 mm and a length of 15 cm are used as an opening switch to change the rise time of the discharge current.

The generator and load currents are measured by Rogowski coils located upstream and downstream the opening switch, respectively. The voltage across the capillary is measured by a voltage divider with 1/200 voltage division ratio. The electron density and temperature in the early phase are estimated with a Czerny-Turner 320 mm optical multichannel analyzer (OMA, Atago Bussan Co., Multiviewer Macs 320). The entrance slit width is 25 mm. The spectrum light, amplified by an image intensifier, is measured by a photodiode array with 1024 channels. The maximum wavelength window of this system is 40 nm, which limits the maximum electron density estimated from the line shape. The wavelength resolution is 0.18 nm. The light from capillary plasmas enters the OMA through a quartz optical fiber with a core diameter of 0.8 mm. The delay generator is used to control the operation time between the triggers of the spark gap switch and the OMA, which has a gate time of 200 ns.

The electron density of the capillary plasma is estimated by using Stark broadening of the H_α line, which is emitted due to the capillary wall ablation [4, 5], and the electron temperature is evaluated from the relative emission intensities of four copper lines (510.55, 515.32, 521.82, 529.25 nm).[5]

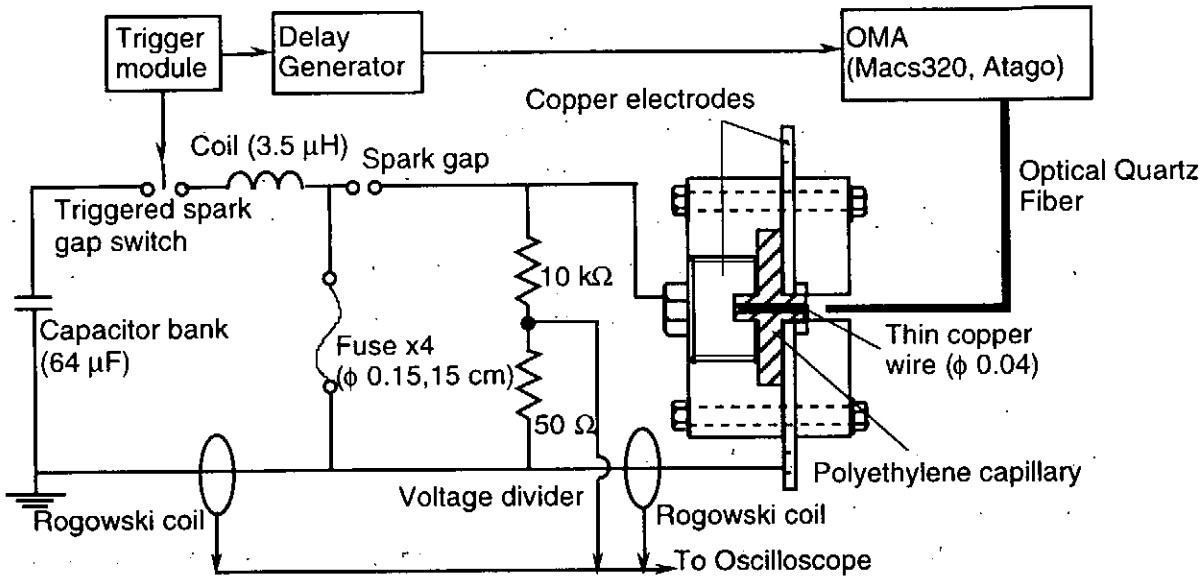

Fig. 1. Experimental setup for spectroscopic measurements.

2. 2 Interferometer measurements

Fig. 2 shows the set up of the Mach-Zehnder interferometer. The He-Ne laser beam with the maximum power of 5 mW and the diameter at $1/e^2$ power level of 0.8 mm is divided into the reference and probe beams by the first beam splitter. Both beams recombine at the second beam splitter again and are focused at the input of a quartz optical fiber using a focus lens (f = 5 cm) through the interference filter. This filter is used to avoid the plasma self luminosity. Interferometry signals are detected using Si PIN photodiode with sensitivity equal to 0.4 A/W for He-Ne laser wavelength (Hamamatsu, S5973).

The electron density of the capillary plasma is estimated by analyzing the interferometer signal [6]. The plasma produces a phase shift, $\Delta\phi$, relative to the reference beam, which is given by the following formula:

$$\Delta\phi = \frac{2\pi}{\lambda_L}\left(L - \int_0^L N_p dl\right) = \left(\frac{\pi}{\lambda_L n_c}\right)\int_0^L n_e dl, \quad (1)$$

where N_p is an index of refraction, L is a path length of the probe beam through the plasma, λ_L is a laser wavelength, and n_c is a critical electron density.

For the He-Ne laser wavelength of 632.8 nm, the line integrated plasma density is given by:

$$\int_0^L n_e dl = 5.61\times 10^{16}\,\Delta\phi, \quad (2)$$

in units of cm^{-2}. Each minimum and maximum in the fringe pattern shows the phase shift equal

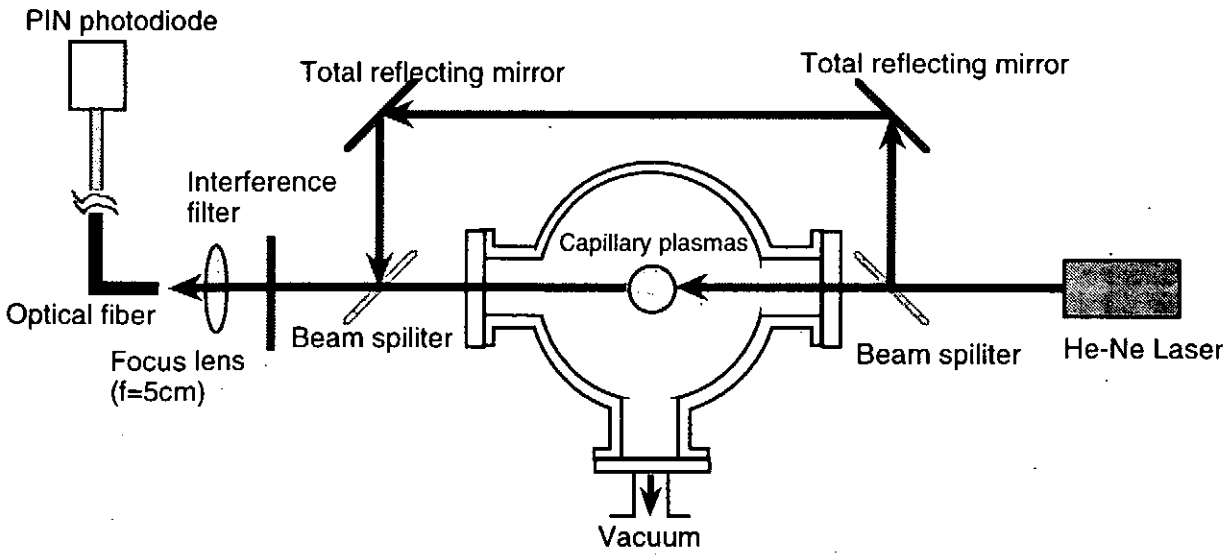

Fig. 2. Mach-Zehnder interferometer for the density measurement of capillary plasmas.

to π, that corresponds to the line integrated plasma density of 1.76×10^{17} cm^{-2}. Therefore, the density can be estimated by counting the fringes.

3. Experimental Results and Discussions

Fig. 3 shows typical waveforms of the discharge current (a), the voltage across the capillary (b), and the power input to the capillary (c) in the case of using an opening switch (dashed line) and in the conventional case (solid line). The power is calculated from measurements of the discharge current and the voltage across the capillary. The current and voltage with short rise time is applied to the capillary in the case of using of the opening switch. The maximum current with short rise time is lower than that in the conventional case, since the charging voltage of the capacitors is equal in both cases. The power supplied to the capillary in the case of using the opening switch is higher during 10 μs. Therefore, the wall ablation may violently occur in the capillary.

Fig. 4 shows typical H_α lines observed at 1.5 μs after the beginning of the discharge. The precise FWHM is measured by fitting a Lorentz profile (dashed line) to the experimental data [6], since a carbon line (C II, 657.8 nm) overlaps the H_α line. The electron density is estimated by measuring the FWHM of H_α lines.

Fig. 5 shows the typical waveforms of the discharge current and the interferometer signal. The density reaches 1.76×10^{18} cm^{-3} at 6 μs. The late attenuation of the interferometer signal is due to the decrease of fringe contrast resulting from the refraction of the laser beam through the capillary plasma and/or the decrease of the transmissivity of the laser beam because of high density.[7]

The electron densities of capillary plasmas estimated by the spectroscopic measurement(squares) and the interferometer measurement(circles) are shown in fig. 6. The density for the current with short rise time increases rapidly up to 10^{18} cm^{-3} in 2 μs. It is found

that the wall ablation violently occurs due to the increase of the heat flux from the capillary plasma. That tendency is demonstrated from results for capillary plasma simulation [5] as shown in fig. 7. The density for the current with short rise time rapidly increases.

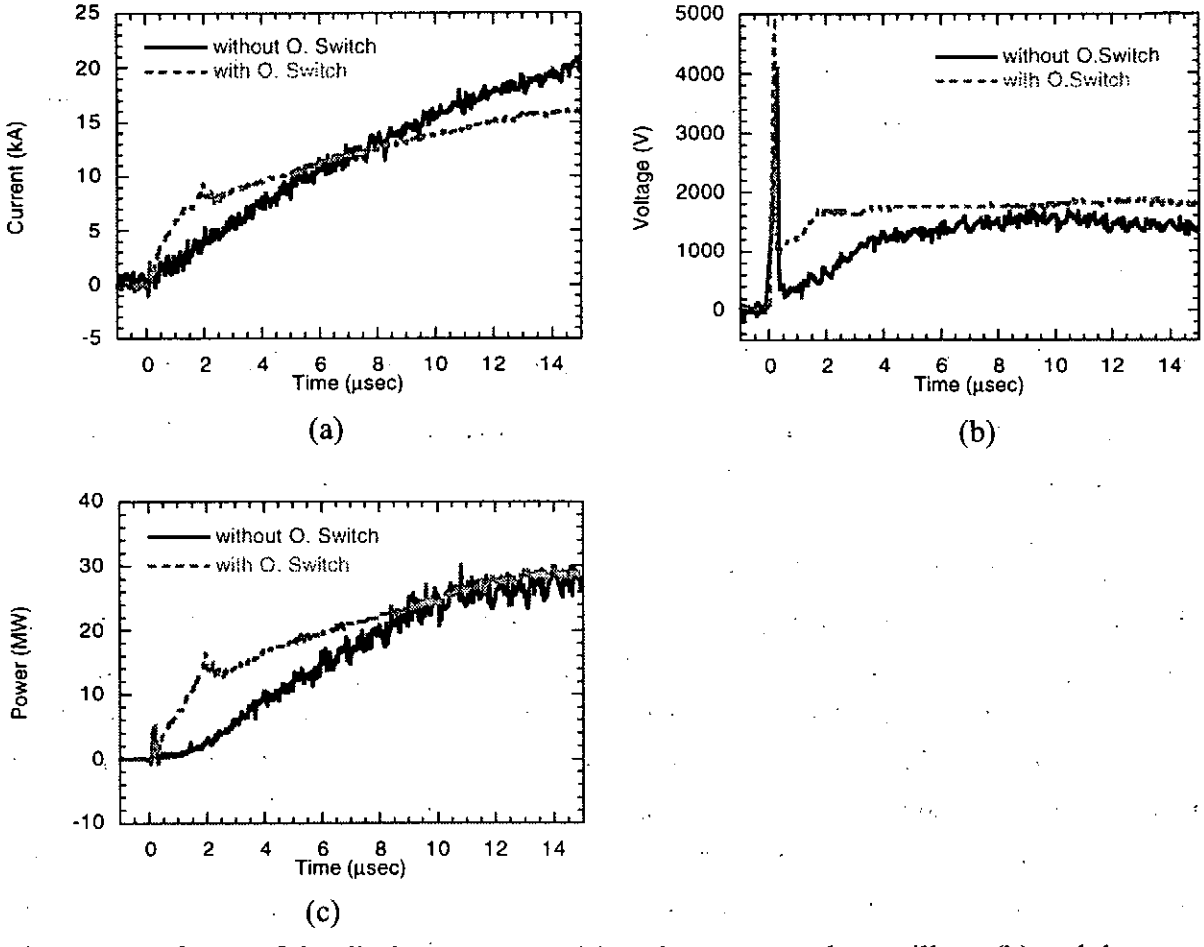

Fig. 3. Waveforms of the discharge current (a), voltage across the capillary, (b) and the power input to the capillary (c) for the current with different rise times.

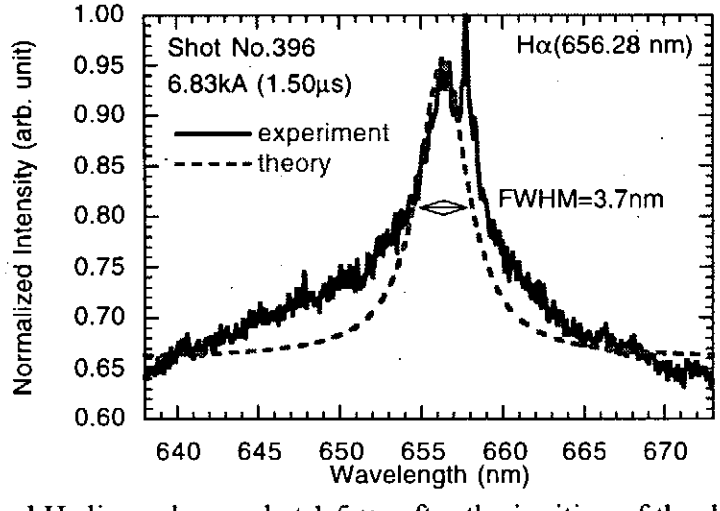

Fig. 4. Typical H_α lines observed at 1.5 μs after the ignition of the discharge.

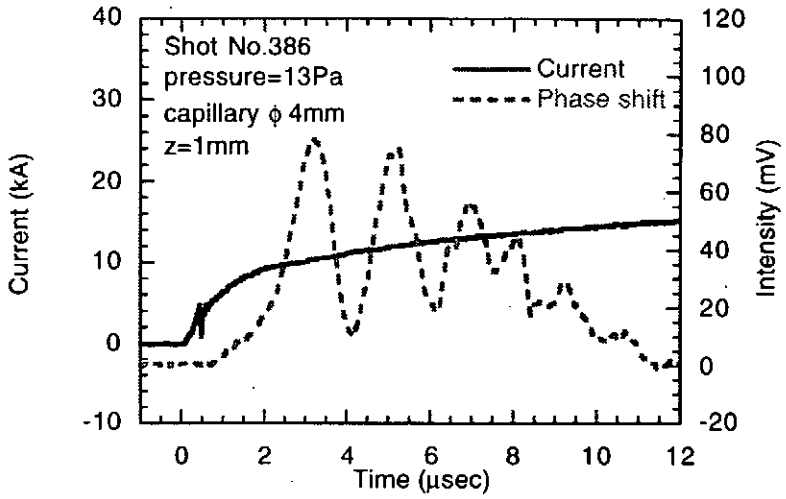

Fig. 5. Typical current and pin photodiode signal waveforms.

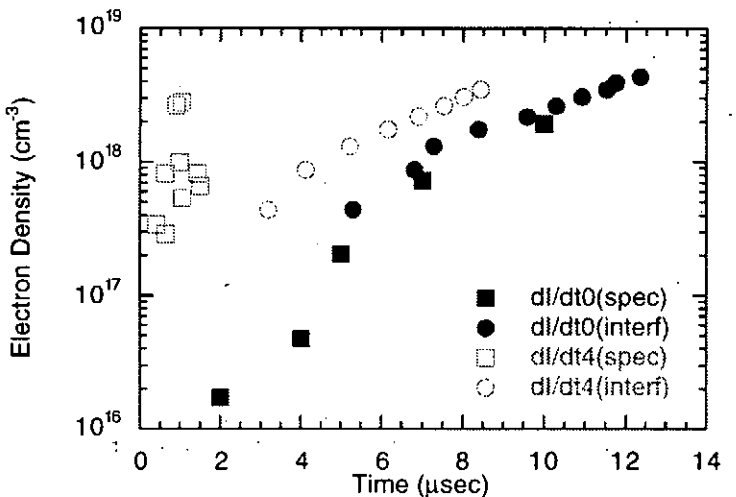

Fig. 6. Electron density of capillary plasmas estimated by the spectroscopic and the interferometer measurements for different current rise times.

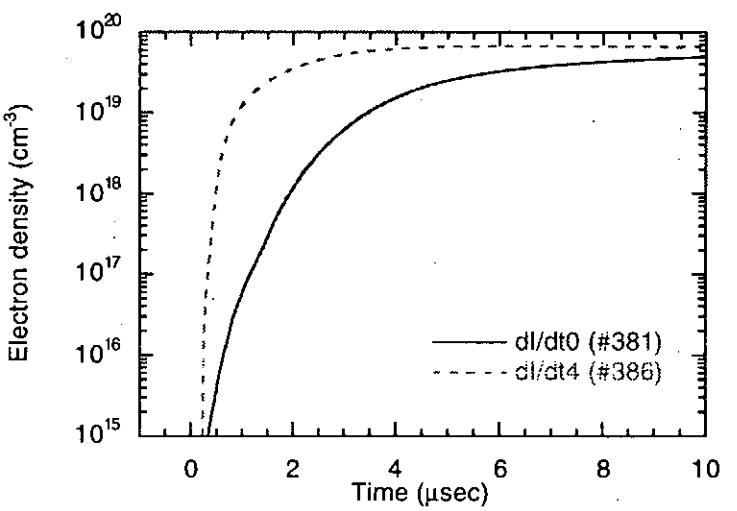

Fig. 7. Simulation result for the electron density of capillary plasmas.

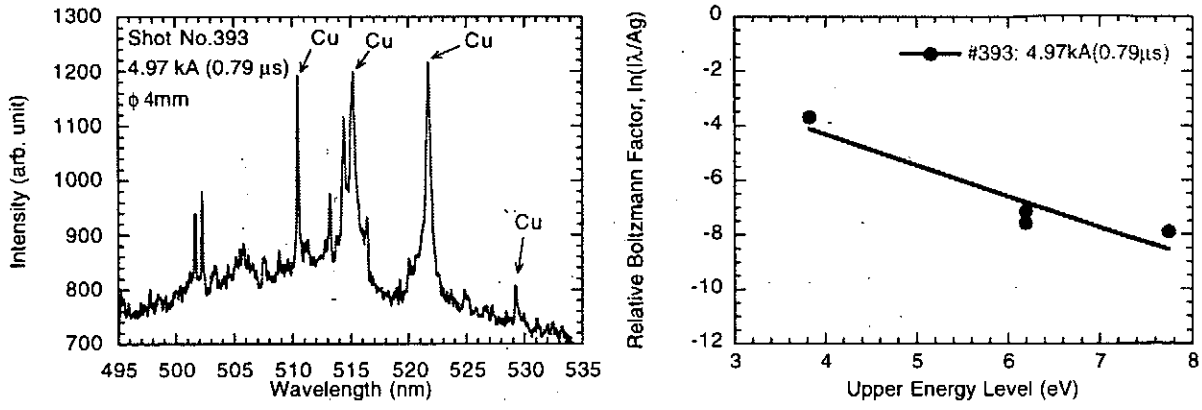

Fig. 8. Example of a copper line spectrum and the Boltzmann plot.

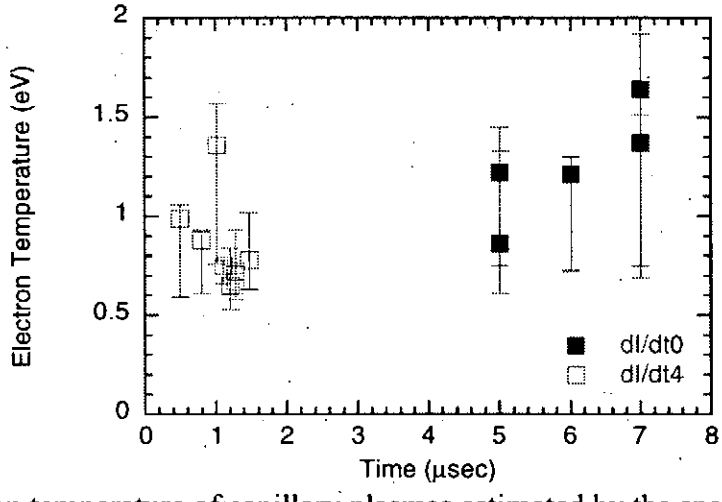

Fig. 9. Electron temperature of capillary plasmas estimated by the spectroscopic measurement for different current rise times.

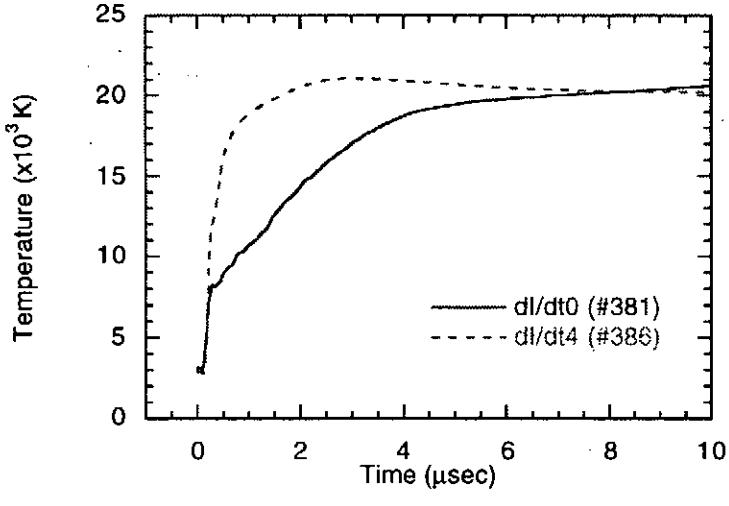

Fig. 10. Simulation result for the temperature of capillary plasmas.

Fig. 8 shows an example of the copper line spectrum for estimating the electron temperature (a) and the Boltzmann plot(b). The temperature is the reciprocal of the slope in the Boltzmann plot. The electron temperature for the discharge current with different rise times are shown in fig. 9. The temperature for the current with short rise time increases up to about 1 eV in early time. That tendency is also demonstrated as a simulation result as shown in fig. 10. The temperature dramatically increases due to the increase of input power into the capillary.

4. Conclusions

The electron density and temperature of the capillary plasma for the discharge current with different rise times are measured by spectroscopy and interferometry, and are compared with simulated results using a 0-D time dependent model in order to verify the experimental data for the characteristics of capillary plasmas. It is found experimentally and theoretically that the electron density and temperature for the current with short rise time tend to increase in early time.

REFERENCE

[1] M. Rott, "The LRT/TUM small caliber electrothermal accelerator", IEEE Trans. on Magnetics, Vol. 29, No. 1, pp. 597-602 (1993).
[2] David A. Benson, Steven N. Kempka, "Studies of confined high-pressure discharges in an electrothermal capillary", IEEE Trans. on Magnetics, Vol. 29, No. 1, pp. 544-549, (1993).
[3] T. Sueda, S. Katsuki, H. Akiyama, "Early phenomena of capillary discharges for an electrothermal gun", Appl. Phys. Lett., Vol. 68, No. 13, pp. 1766-1768 (1996).
[4] T. Sueda, S. Katsuki, H. Akiyama, "Early phenomena of capillary discharges in different ambient pressures", IEEE Trans. on Magnetics, Vol. 33, No. 1, pp. 334-339 (1997).
[5] T. Sueda, S. Katsuki, H. Akiyama, "Behavior of capillary plasmas with different diameters", Jpn. J. Appl. Phys., Vol. 36, No. 4A, pp. 2346-2350 (1997).
[6] S. Katsuki, T. Sueda, Y. Koga, H. Akiyama, K. Sato, "Spectroscopic measurements of railgun plasma armatures in an augmented railgun using a permanent magnet", IEEE Trans. on Magnetics, Vol. 33, No. 1, pp. 98-103 (1997).
[7] I. V. Lisitsyn, S. Kohno, T. Kawauchi, T. Sueda, S. Katsuki, H. Akiyama, "Interferometer measurements in pulsed plasma experiments", Jpn. J. Appl. Phys., Vol. 36, No. 11, pp. 6986-6991 (1997).

Characteristics of coaxial plasma gun as a high current pulsed ion beam source

H. Takano, T. Ishimoto, K. Masugata and K. Yatsui

Department of Electrical Engineering,

Nagaoka University of Technology,

Nagaoka, Niigata 940-21, Japan

Abstract

Characteristics of coaxial type gas puff plasma gun were studied to developed a high current pulsed ion beam source. The plasma gun was successfully operated at discharge current ≈ 20 kA and produced a high current density plasma. Ion current density of more than 100 A/cm^2 was observed on axis at 97 mm downstream from the muzzle of the plasma gun. Velocity of the plasma was evaluated from the time of flight delay and found that more than 10 km/s was obtained. From the spectroscopic measurement the plasma was found to contain N^+ and N^{++} with impurity of Cu atoms.

1. Introduction

Intense pulsed ion beam (PIB) has been actively studied since it has a wide area of applications including fusion applications or material processing.[1,2] In those applications it is very important to improve the purity of the ion beam. However, the purity of the PIB has been limited since flashover ion sources have been conventionally utilized to produce anode source plasma. That is, in the flashover ion source, plasma is produced by the surface flashover on the flashboard of dielectric material such as plastic, which contains various atoms such as hydrogen, carbon, oxygen etc. In addition, various molecules are absorbed on the surface before the operation.[3,4]

To enhance the purity of the PIB we have proposed a new type of ion source where gas puff

plasma gun [5,6] is utilized. Figure 1 shows the conceptual drawing of the ion source. In the ion source plasma is produced and accelerated in the gas-puff plasma gun. To keep vacuum in the acceleration gap discharge, gas in the plasma gun is injected by using a gas puff valve (a fast opening gas valve). After the injection of the gas, plasma gun is triggered and high current discharge is produced. Due to the strong electromagnetic force produced by the discharge current, plasma is accelerated toward the muzzle of the plasma gun. Since magnetic field is produced in the acceleration gap, plasma is stagnated and accumulated in the anode. Hence, by applying a pulsed acceleration voltage on the appropriate timing, we can obtain a high current ion beam. In the ion source, plasma is produced by the gas discharge, purity and controllability of the ion species are expected to be enhanced.

To develop the ion source we are studying the characteristics of gas puff plasma gun. In the paper the recent results of the experiment are described.

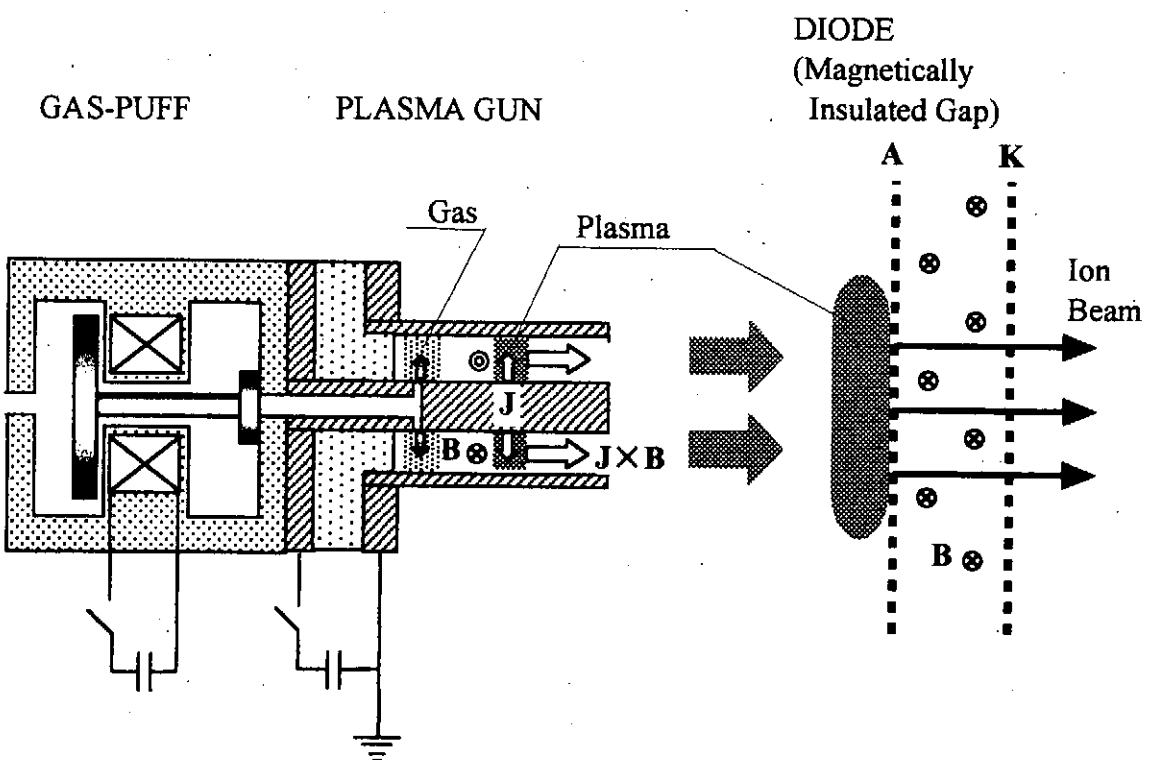

Fig.1 Conceptual drawing of the ion source

2. Experimental setup

Figure 2 shows the experimental setup of the plasma gun. The plasma gun consists of a gas puff and a coaxial electrode of the plasma gun. The gas puff consists of a pulsed magnetic coil and a metallic valve. The detailed structure of the coaxial electrode is shown in Fig. 2 (b). An outer electrode is made of brass and the inner diameter is 11 mm. An inner electrode is 150 mm long copper of diameter 6 mm. The gap length between inner and outer electrode is 2.5 mm. The inner electrode has gas nozzles of six 1.5 mm diameter holes on 50 mm downstream from the gas valve (that is 100 mm upstream from the top). In addition, to stabilize the initial discharge point an initiation electrode of thickness 1mm, width 1mm is attached on 1 mm downstream of the nozzles.

Initially the gas puff is filled with pressurized gas and the valve is closed by the filling gas pressure. By discharging the capacitor bank (C_g, 20 μF), pulsed strong magnetic field is produced in the coil, which pushes a metallic plate of the gas valve. As the results, the valve opens quickly in the time order of 100 μs. A supersonic gas flow is proceed by the fast opening of the valve and the gas is injected to the plasma gun via the nozzles.

After the injection of the gas, capacitor bank of the plasma gun (C_p, 8 μF) is triggered and produces a high current discharge between the inner and outer electrode of the plasma gun. The discharge current produces a strong magnetic field, which accelerate the discharge plasma. For the measurement of ion current density of accelerated plasma, biased charge corrector (BIC) is utilized. The BIC is placed 97 mm downstream from the muzzle of the plasma gun and bias voltage of -50 V is applied to the collector electrode of the BIC. An aperture of 0.4 mm diameter is utilized to limit the plasma current reaching to the collector.

The plasma gun is operated in the vacuum of pressure less than 10^{-4} Torr. Filling pressure of the gas puff was fixed to 2 atm in the experiment. Charging voltages of C_g and C_p were 3 kV and 10 kV, respectively. The delay time to open the valve after the start of the coil current (I_g) was evaluated to be around 110 μs [7]. The expansion time of the gas from the valve to the gas nozzle is estimated to be around 160 μs if assuming that the gas is expanding with sound velocity. Hence, the time delay of the blow out of the gas from the nozzle is expected to be around 270 μs. To adjust the delay time to trigger C_p a delay pulse generator is utilized.

(a)

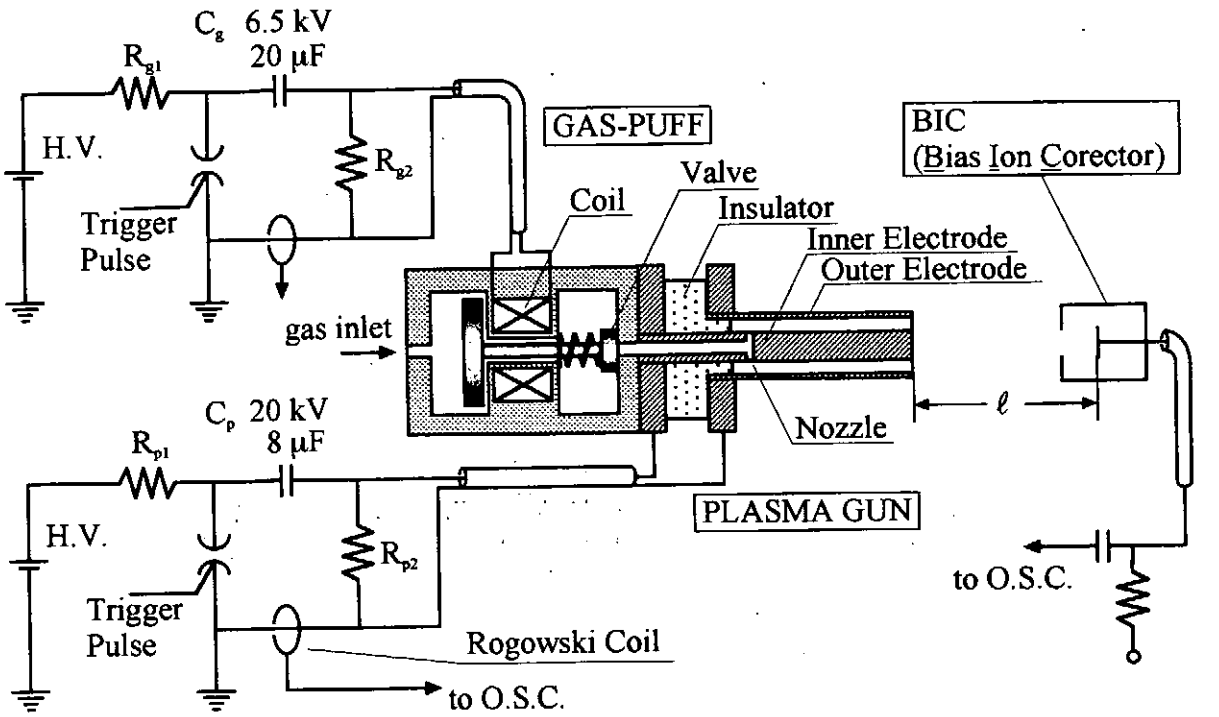

(b)

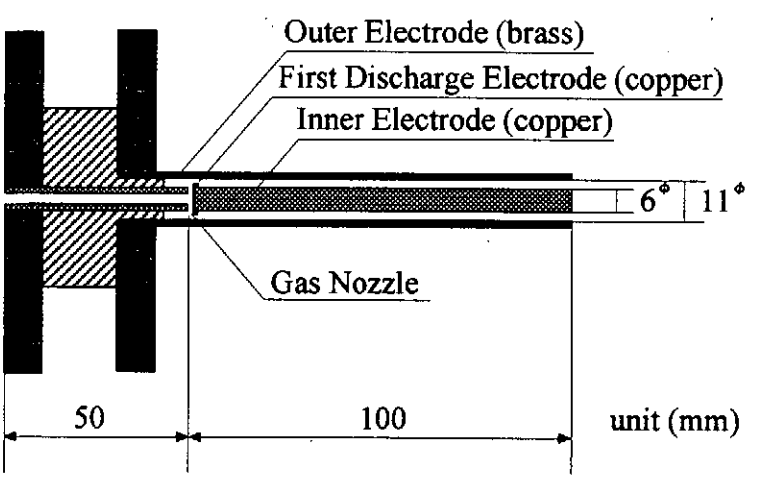

Fig.2 (a) Experimental setup.
(b) The detailed structure of the coaxial electrode.

3. Experimental results

Figure 3 shows typical waveforms of I_g and the discharge current of the plasma gun (I_p). As seen in the figure, I_g rises to open the gas puff valve at $t \approx 20$ μs and after the delay time (τ_d) of 220 μs, I_p start.

Figure 4 show the open shutter photographs of the plasma gun. The side views and the front views are shown for different delay time. As seen in the figure, plasma blows out from the plasma gun in both conditions with small expansion angle. Comparing both cases, the intensity and the uniformity of the blow out plasma is better when $\tau_d = 330$ μs.

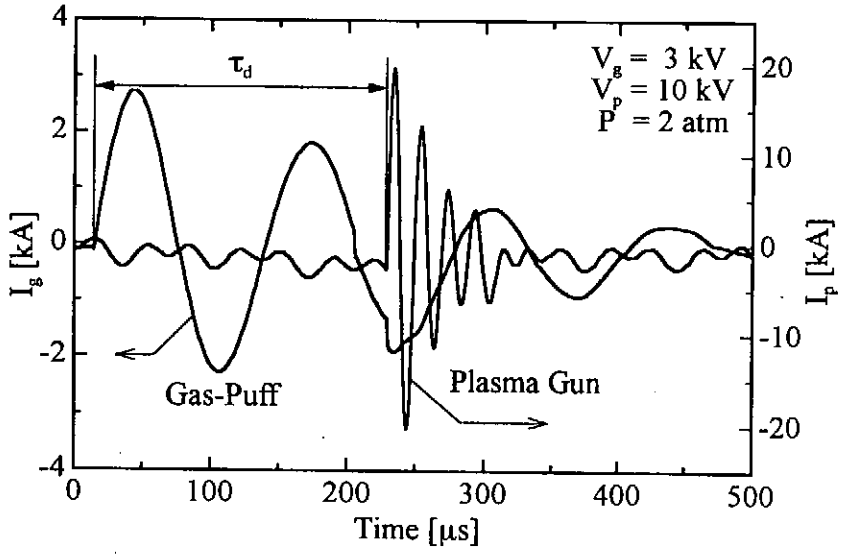

Fig.3 Typical waveforms of coil current and the discharge current of the plasma gun.

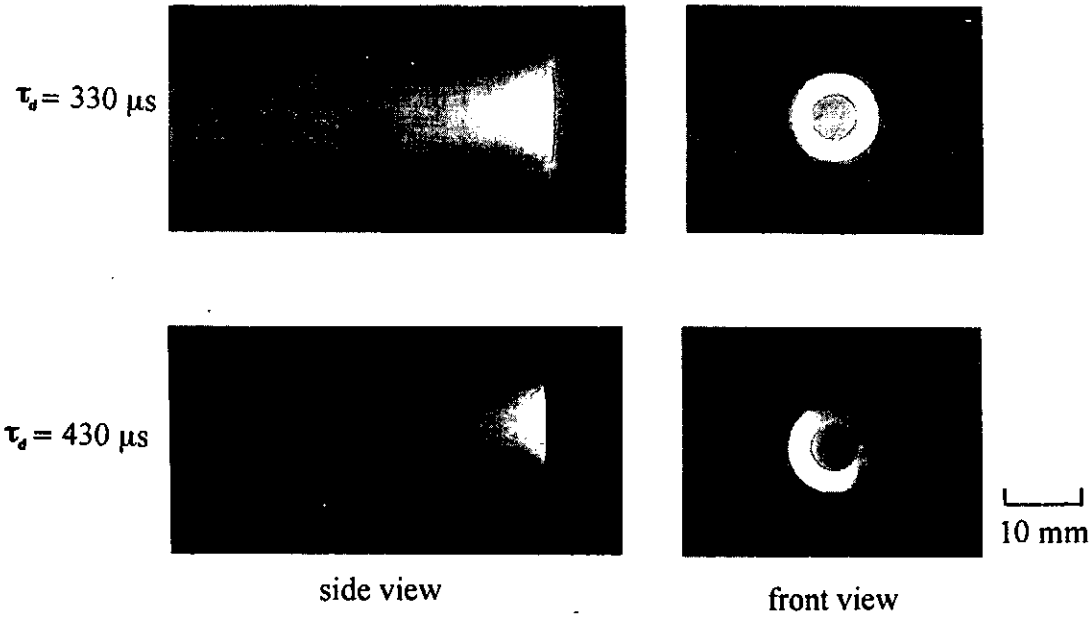

Fig.4 photograph of the plasma gun.

Figure 5 shows the typical waveforms of I_p and the ion current density (J_i) measured by BIC. I_p has a ringing waveform and the peak value of 20 kA is observed. At $t = 13$ μs after

the rise of I_p, J_i rises and have a sharp peak of peak value (J_{ip}) 180 A/cm^2 at t = 22 μs. As indicated in the figure, the delay times form the rise of I_p to the rise of J_i and to the peak of J_i are defined as t_r and t_p, respectively. From the delay times, velocities of the plasma (v_r and v_p) are estimated assuming that the plasma starts the nozzle at the timing of the rise of I_p. For example v_r for this case is calculated as follows.

$$v_r = L_f / t_r = (100\ [\text{mm}] + 97\ [\text{mm}])/13\ [\mu\text{s}] = 15.1\ [\text{km/s}] \quad (1)$$

Here L_f is the flight distance of the plasma, that is the distance from the nozzle of the plasma gun to the BIC.

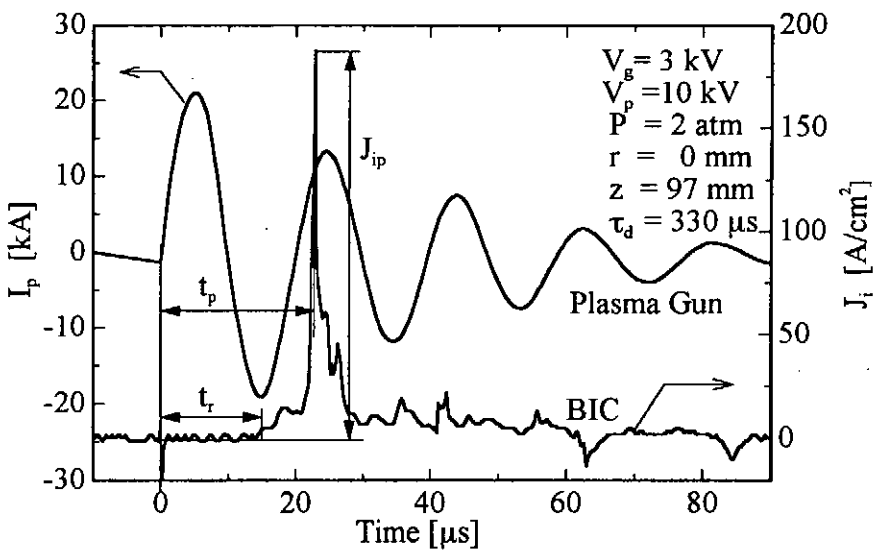

Fig.5 Typical waveforms of I_p and J_i

Figure 6 shows the dependence of v_r and v_p on τ_d. As seen in the figure, maximum velocities of $v_r \approx 25$ km/s and $v_p \approx 13$ km are obtained at $\tau_d = 230$ μs. The velocities monotonically decrease with increasing τ_d and at $\tau_d \approx 430$ μs the velocities of $v_r \approx 5$ km/s and $v_p \approx 3$ km/s are observed. The decrease of the velocities seems to be due to that the mass of the gas accelerated in the plasma gun increases with increasing τ_d since the quantity of the gas in the plasma gun increases with τ_d.

Figure 7 shows the dependence of J_{ip} on τ_d. As seen in the figure, scattering of the value of J_{ip} is very large for short τ_d. Considering that it takes about 270 μs to blow out the gas from the nozzles, the quantity of the gas in the plasma gun is not sufficient for short τ_d, hence the unstable discharge is produced. In spite of insufficient gas quantity, relatively high current density is obtained, that seems to be due to the higher degree of ionization. At τ_d =

330-360 μs reproducibility of J_{ip} is improved and J_{ip} of around 200 A/cm^2 is obtained. For τ_d > 360 μs J_{ip} steeply decreased and it is less than 10 A/cm^2 at $\tau_d \approx 430$ μs. For long τ_d, too mach quantity of the gas exist in the gun, hence the degree of ionization is extremely reduced.

From the results we see that the plasma is produced with high reproducibility when τ_d = 330-360 μs with relatively high ion current density. On the condition, $v_r \approx 13$ km/s and $v_p \approx$ 7 km/s is obtained, the velocity seems to be sufficient. Since it is more than one order of magnitude higher than the sound velocity of the gas.

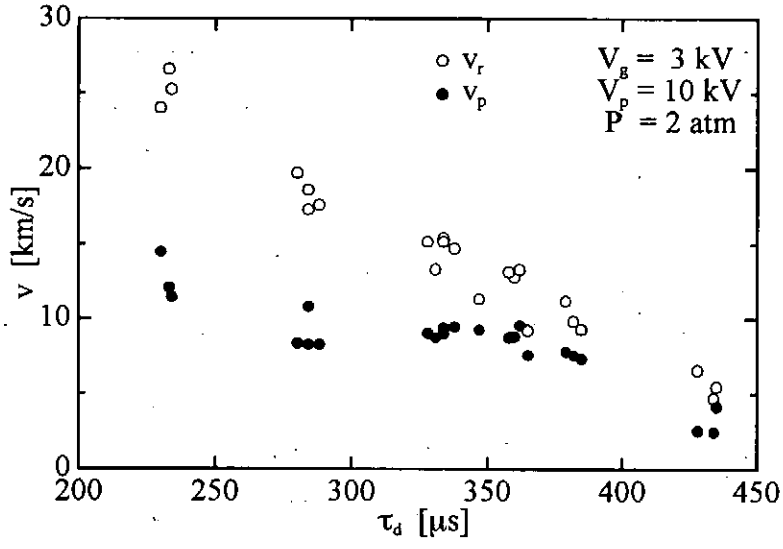

Fig.6 Dependence of v_r and v_p on τ_d.

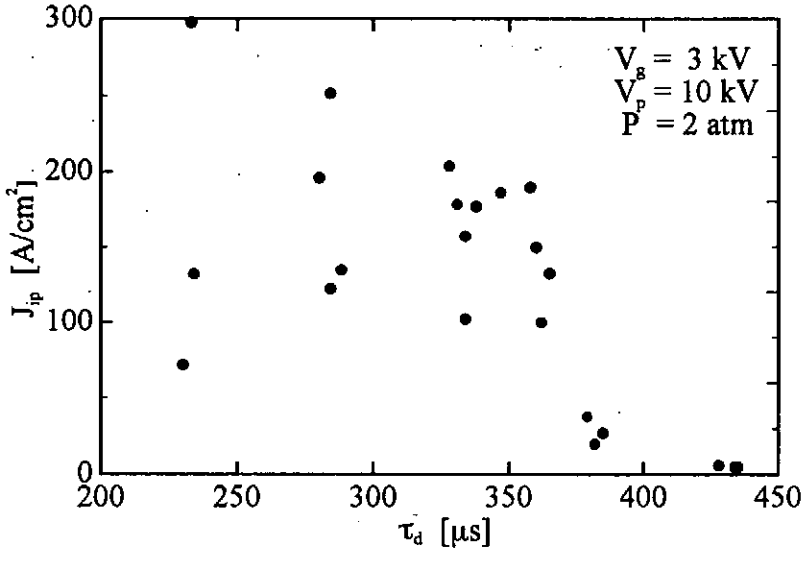

Fig.7 Dependence of J_{ip} on τ_d.

Figure 8 shows the time integrated spectrograph of the plasma observed at 10 mm downstream from the muzzle of the plasma gun. Atomic nitrogen lines of N II and N III are observed, which clearly indicate that the main component of the plasma is N^{+} and N^{++}. In addition, Cu I lines are observed, which seems to be produced by the spattering of the electrodes. The intensity of Cu I line is higher for shorter delay time. From the results we see that the concentration of the impurity atoms can be suppressed by supplying sufficient gas quantity.

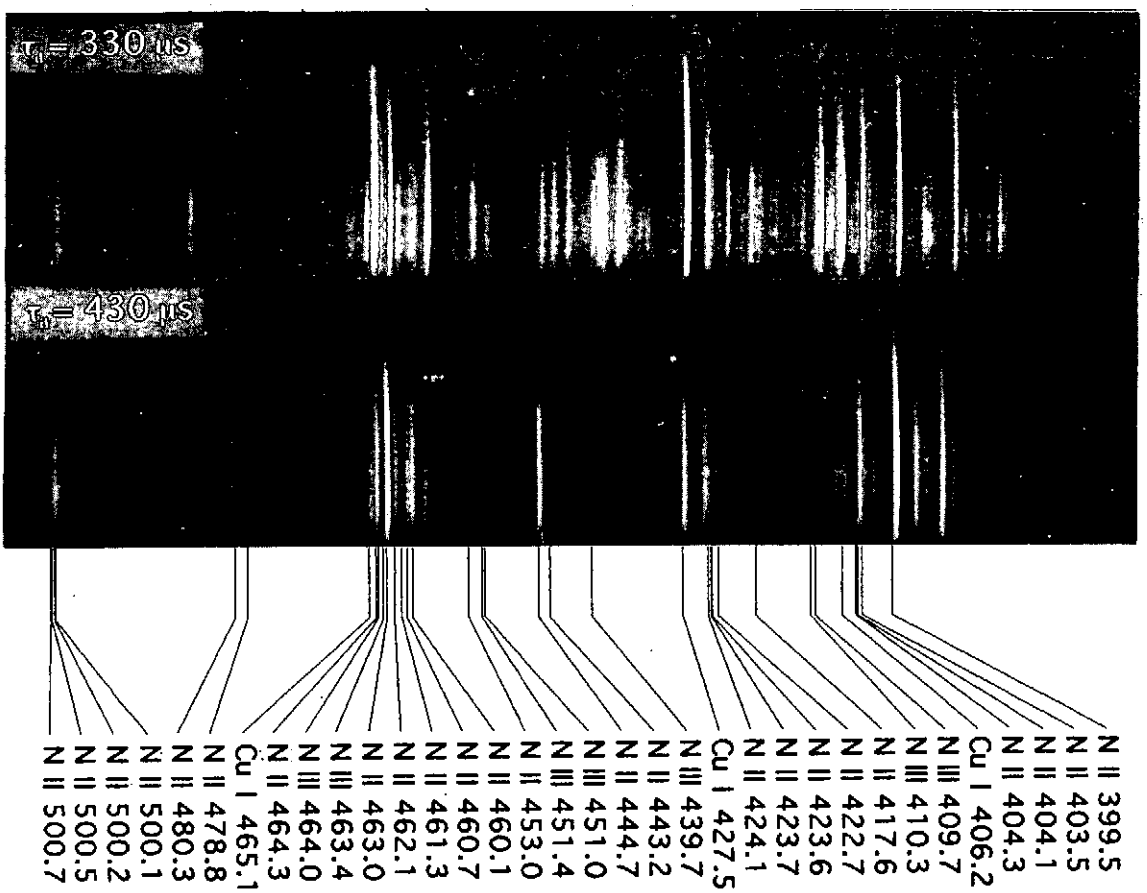

Fig.8 spectrograph of the plasma

4. Summary

The characteristics of coaxial type gas puff plasma gun was evaluated to develop a high current pulsed ion beam source. The plasma gun was successfully operated and produced a high current density plasma. The current density of more than 100 A/cm^2 was observed at 97 mm downstream from the muzzle of the plasma gun. Velocity of the plasma was

evaluated from the time of flight delay and found that more than 10 km/s was obtained. From the spectroscopic measurement the plasma was found to contain N^{+} and N^{++} with impurity of Cu atoms.

References

[1] J. A. Nation: Particle Accelerators, **10** (1979) 1.

[2] S. Humphries, Jr.: Nucl. Fusion, **20** (1980) 1549.

[3] E. Chishiro, A. Matsuyama, K. Masugata, and K. Yatsui: J. Appl. Phys., **35** (1996) 2350.

[4] E. Chishiro, K. Masugata, and K. Yatsui: Trans. IEE of Japan., **116-A** (1996) 1062 [in Japanese].

[5] J. H. Degnan, W. L. Baker, S. W. R. Warren, D. W. Price, P. Snell, R. J. Richtersand, and P. J. Turchi: J. Appl. Phys., **61** (1987) 2763.

[6] C. J. Michels, J. E. Heighway, and A. E. Johansen: AIAA J.,**4** (1966) 823.

[7] H. Takano, T. Sudou, H. Hanamoto, E. Chishiro, K. Masugata, and K. Yatsui: Proc. 6th. IEE Niigata-branch meeting, IEE of Japan, (1996) 39 [in Japanese].

Generation of Relativistic Electron Beam by Linear Induction Accelerator "ETIGO-III"

K. Ogura, Y. Oda, R. Toyoshima, Y. Sekimoto, G. Imada, W. Jiang, K. Masugata, and K. Yatsui

Laboratory of Beam Technology and Department of Electrical Engineering, Nagaoka University of Technology, Nagaoka, Niigata 940-2188

ABSTRACT

Linear induction accelerator "ETIGO-III" (8 MV, 5 kA, 30 ns) has been developed and operated for the generation of relativistic electron beam. It consists of a Marx generator, a pulse forming line, four coaxial transmission lines and four induction acceleration units. In each acceleration unit, the output voltage of 670 kV of the transmission line is coupled with three magnetic cores to induce an acceleration voltage of 2 MV to the electron beam. The electron beam is generated by the diode in the first unit and post-accelerated by the other three units, resulting in the output energy of 8MeV with the current of 4kA.

1. Introduction

Linear induction accelerator, "ETIGO-III" (8 MV, 5 kA, 30 ns), was designed for the generation of pulsed high-energy, high-current relativistic electron beam. Such an electron beam is of various applications such as in high-power microwave generation, intense X-ray generation, free electron laser studies and materials processing.

For the pulsed electron-beam generation, when the electron energy is less than 1~2 MeV, the convenient way is to generate the pulsed voltage by a pulsed power machine and then couple it to a diode gap. However, for the electron energy higher than ~ 3 MeV, due to insulation limitations, it is not practical to generate the required high voltage by the pulsed power generator and to accelerate the electron beam across a single gap. In this case, it is much better to accelerate electrons by a multi-gap system. The voltage on each gap is generated by the pulsed power generator, which is inductively coupled to the electron beam.

The pulsed power generator "ETIGO-III" is such a kind of multi-gap electron beam

accelerator, and designed to accelerate the electron beam to an energy of 8 MeV. In this paper, we report the structure and principle of "ETIGO-III", the operation parameters (including output voltage and current) of each unit, the characteristics of the guiding magnetic field, and the diagnostic results of the electron beam.

2. Linear induction accelerator "ETIGO-III" [1,2]

Figure 1 shows the schematic diagram of the "ETIGO-III". It consists of a Marx generator, a pulse forming line, four coaxial transmission lines, and four induction acceleration units.

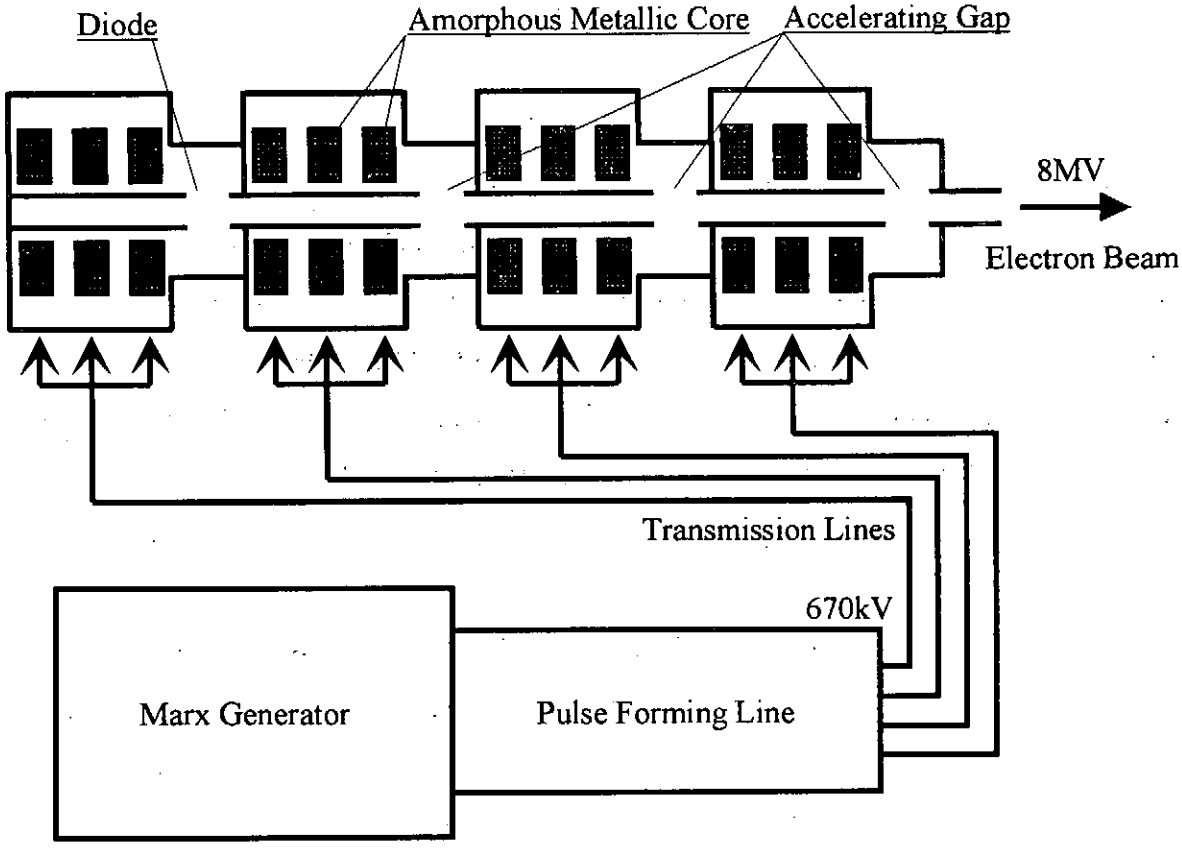

Fig. 1 Schematic diagram of induction accelerator "ETIGO-III".

The Marx generator is charged to 20 kV with the charging energy of 3 kJ. The pulse forming line converts the stored energy of the Marx generator to an output pulse with the voltage of 670 kV, current of 60 kA, and pulse width of 100 ns. The output pulse of the pulse forming line is fed, in parallel, to four induction acceleration units through the coaxial transmission lines. In each unit, three magnetic cores are installed, each of which induces a

voltage of 670 kV to the load giving rise to a voltage of ~ 2 MV across the acceleration gap. The amorphous metallic cores, having outer diameter of 656 mm, inner diameter of 264 mm, and width of 70 mm, are characterized by the following properties: ΔB (flux swing) ~ 2.1 T, and Vt ~ 0.034 Vs. An electron beam diode is located across the acceleration gap of the first unit. The electron beam extracted from the first unit is guided by an external magnetic field through the other three units so that it is post-accelerated by the three gaps giving the final electron energy of 8 MeV.

Figure 2 shows the cross-sectional view of the induction acceleration unit. Figure 3 shows the cross-sectional view of the electron-beam diode. The diode consists of a brass cathode (outer diameter 60 mm, inner diameter 50 mm) and a stainless steel anode (outer diameter 165mm, inner diameter 97 mm), with the gap length of 97 mm.

Figure 4 shows the block diagram and the electrical circuit of the external magnetic-field system. The circuit consists of the delay pulser, the pulse generators, the capacitor bank, and the magnetic coils. The trigger to the Marx generator is delayed so that the electron beam is accelerated under the peak magnetic field.

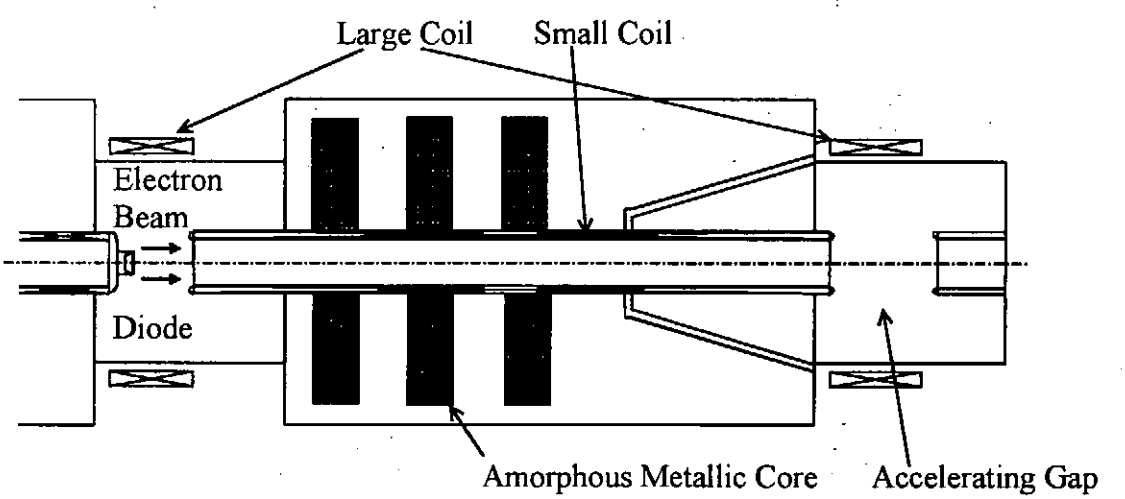

Fig. 2 Cross-sectional view of induction accelerator unit.

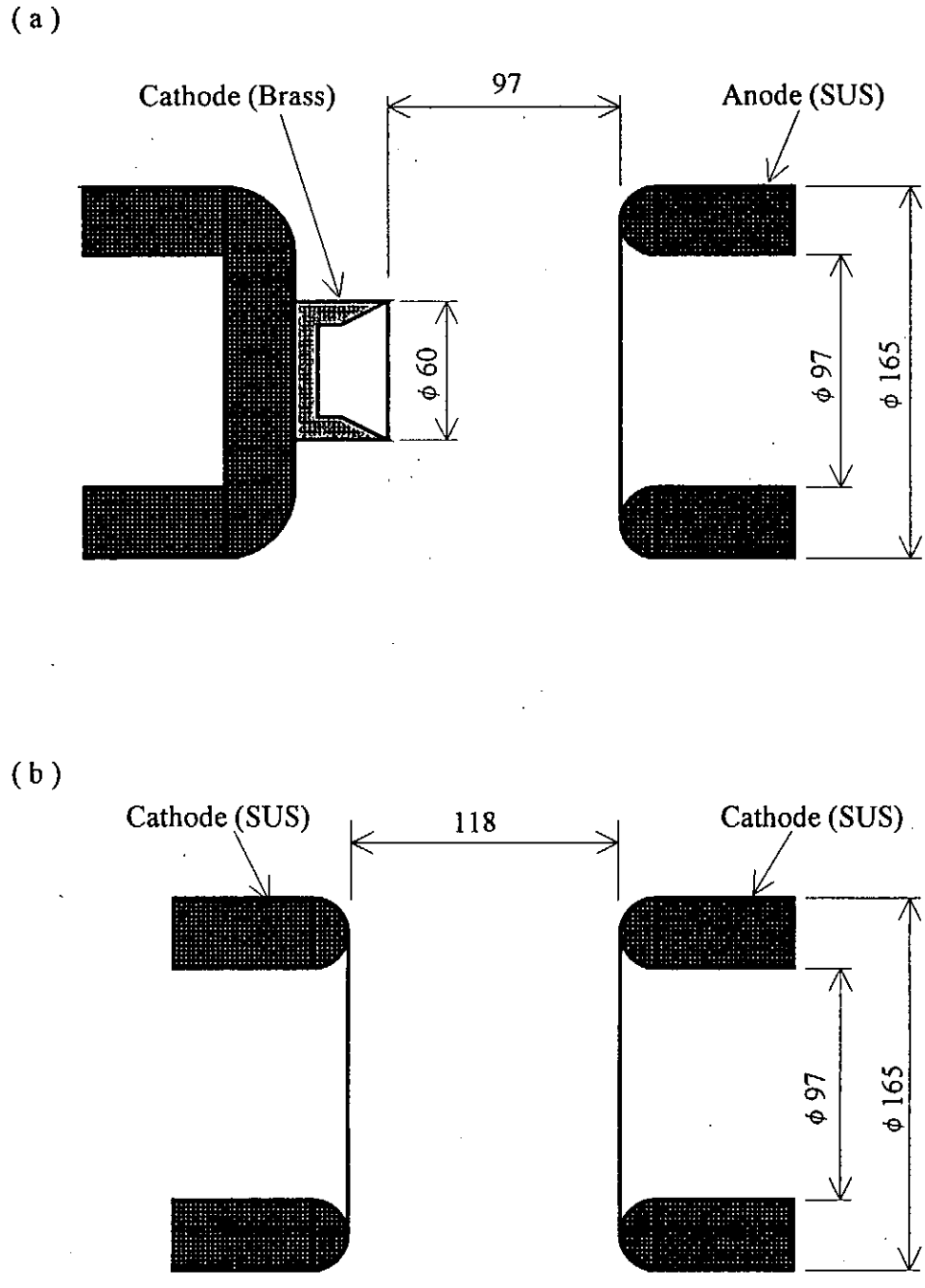

Fig. 3 Cross-sectional view of (a) electron-beam diode, and (b) acceleration gap.

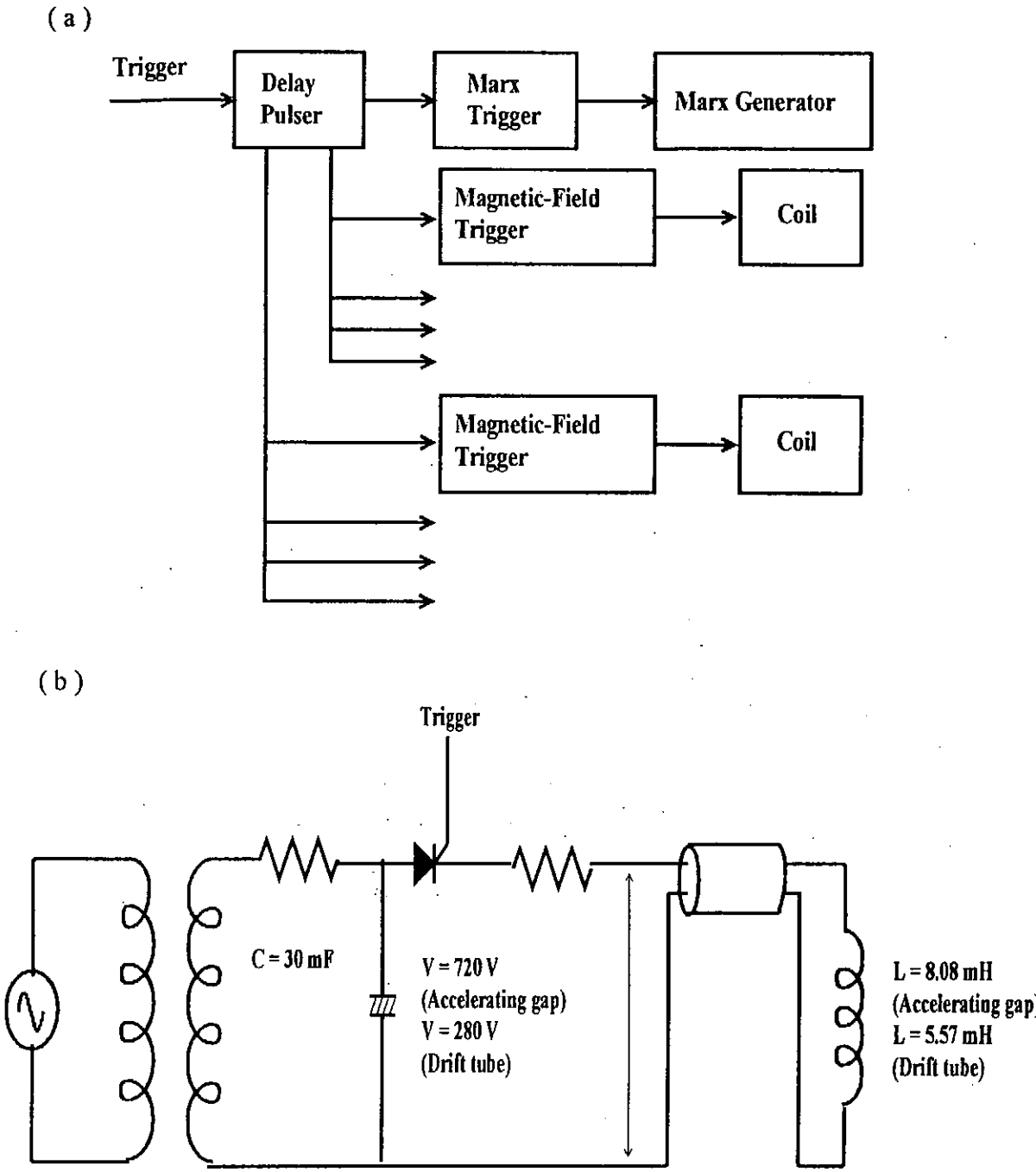

Fig 4 Block diagram and electrical circuit of external magnetic-field generation : (a) block diagram, (b) electric circuit

3. Experimental results

3.1 Magnetic field distribution

Figure 5 shows the axial distribution of the magnetic field (B) measured by a pick-up coil. The spatial resolution of the pick-up coil is ~ 5 mm. We see from Fig. 5 that the magnetic-flux density is mostly in the range of $0.13\ T < B < 0.24\ T$, which is higher than the theoretically required value of 0.1 T.

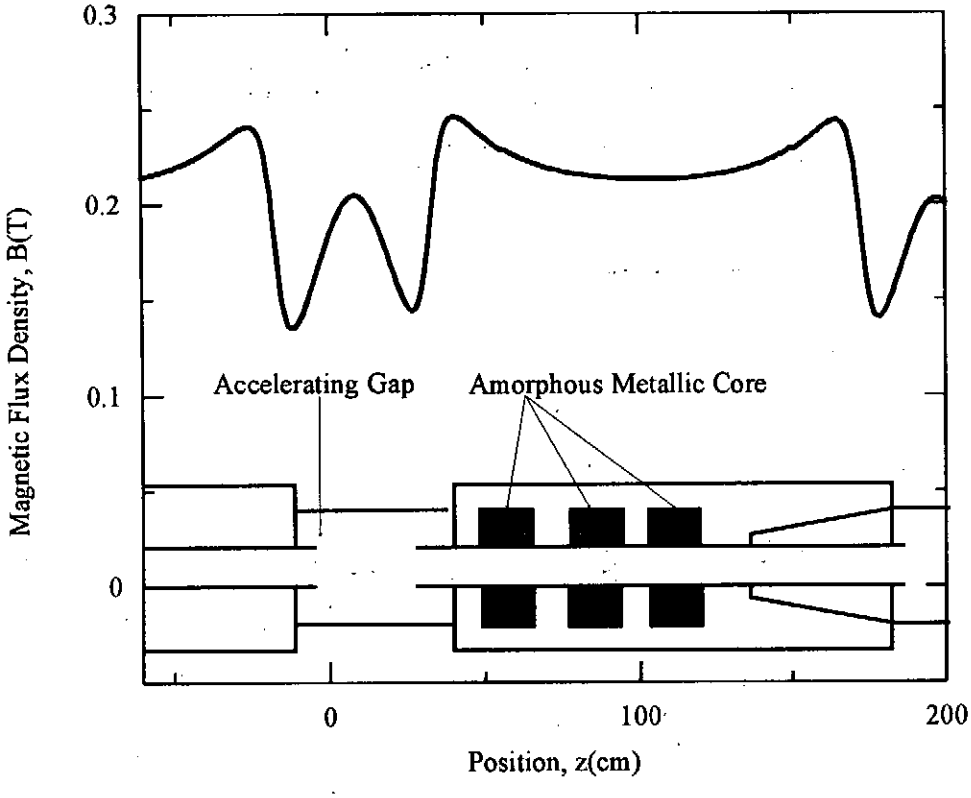

Fig. 5 Axial distribution of magnetic-flux density (B).

3.2 Electron beam generation

Figure 6 shows the typical time evolution of input voltage (V_i) and output voltage (V_d) of an acceleration unit. Here, V_i and V_d were obtained by the capacitive divider and the $CuSO_4$ resistive divider, respectively. From Fig. 5, we see that the peak value of V_d reaches ~ 2 MV at V_i ~ 700kV. The full-width at half-maximum duration of the output voltage is ~ 100ns.

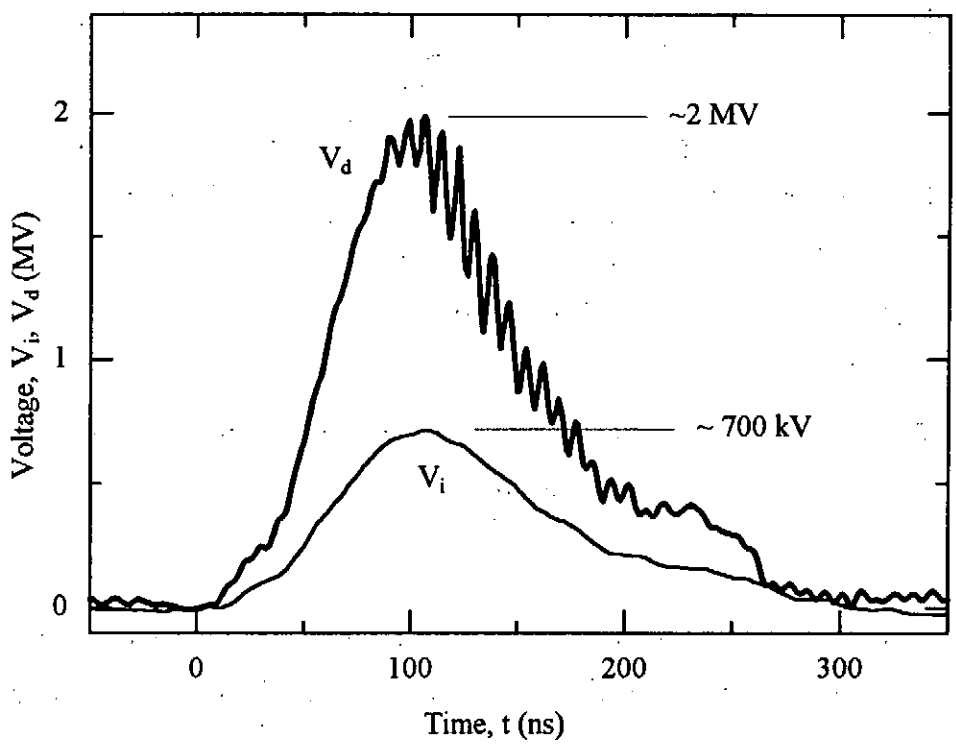

Fig. 6 Typical waveforms of input voltage (V_i) and output voltage (V_d) of induction acceleration unit.

Figure 7 shows the time evolution of diode voltage (V_d) and beam current (I_b) at the electron-beam diode. The beam current is measured by a Rogowski coil. It is seen from Fig. 6 that an electron beam with the peak current of ~ 4 kA, peak electron energy of ~ 2 MV, and time duration of ~ 50 ns is extracted from the diode.

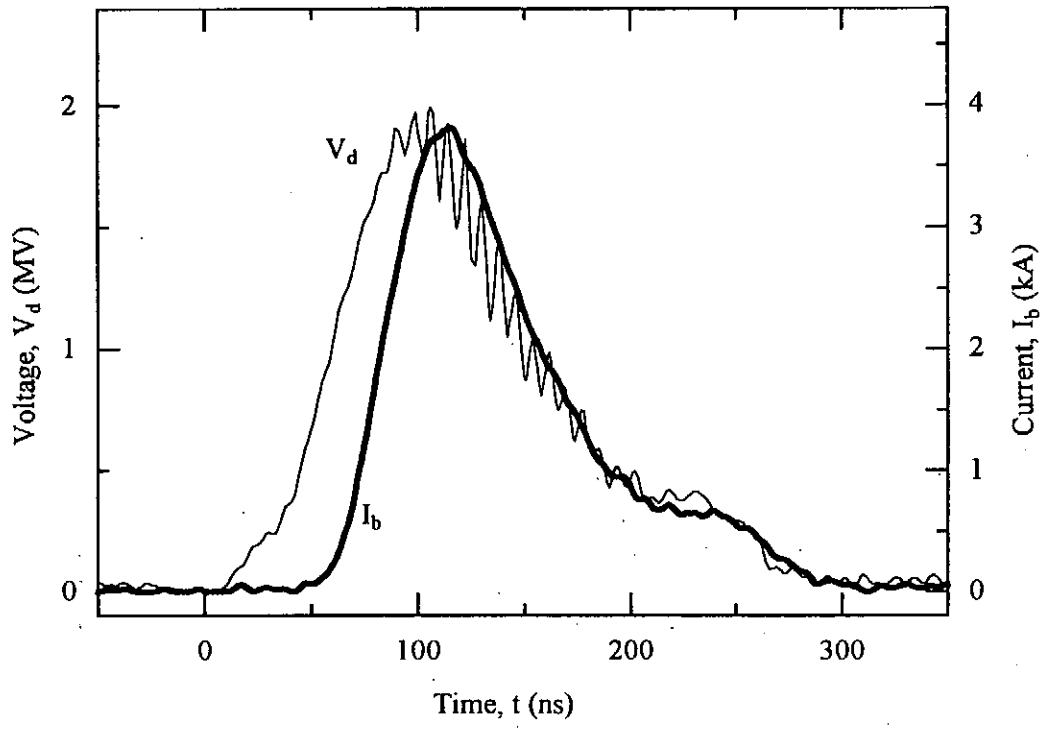

Fig. 7 Typical waveforms of diode voltage (V_d) and electron beam current (I_b) at the diode.

Figure 8 shows the electron beam damage on a Lucite plate, which is located at the downstream of the electron beam diode. It is seen that the electron beam is a hollow structure with the diameter of ~ 60 mm.

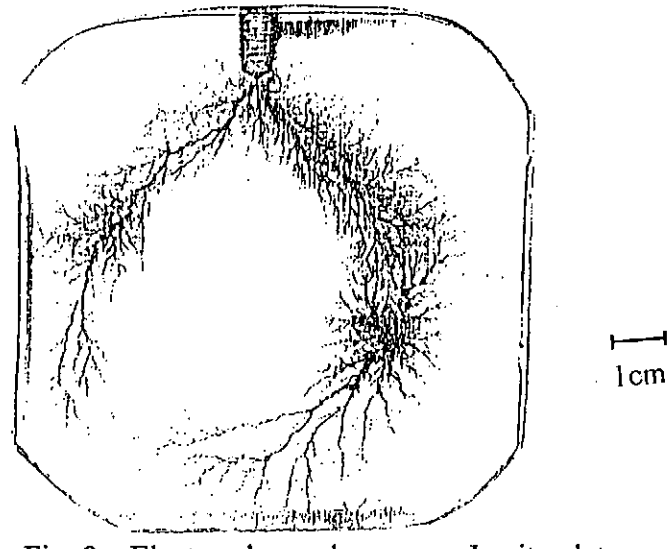

Fig. 8 Electron beam damage on Lucite plate.

3.3 Electron beam transmission and acceleration

Figure 9 shows the electron-beam current (I_b) measured at the entrance and the exit of each gap of the acceleration units.

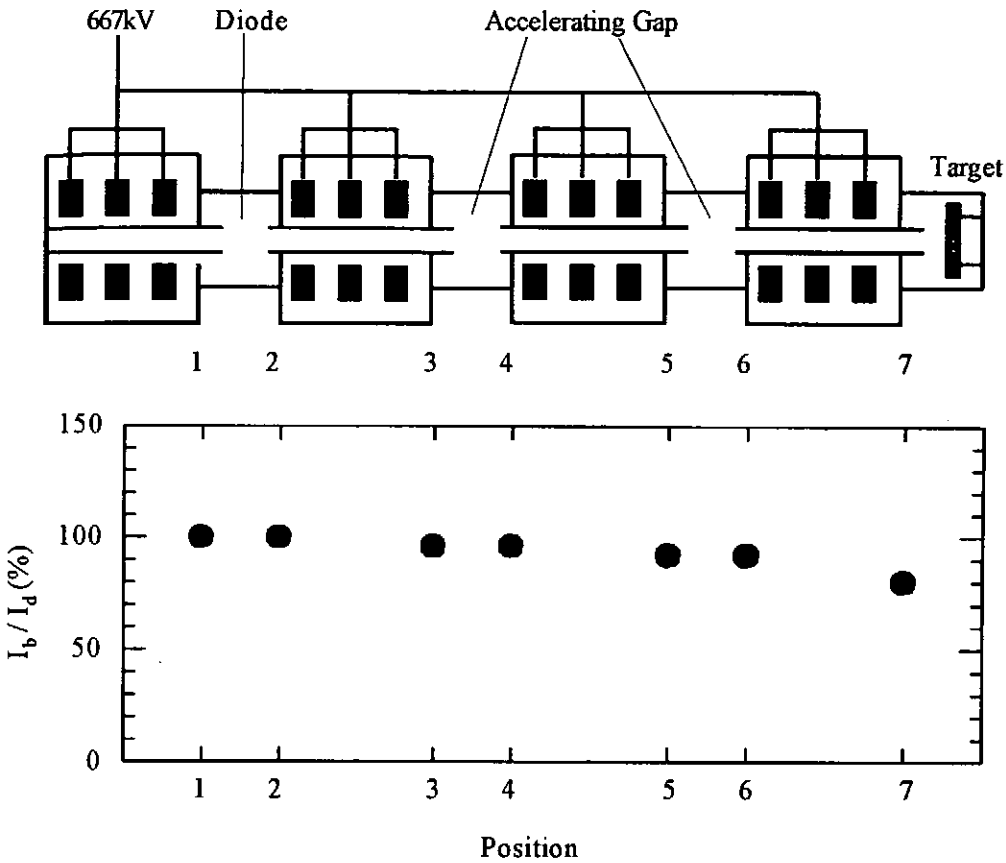

Fig. 9 Electron-beam current (I_b) obtained at entrance and exit of each acceleration gap.

Here, the current is normalized by the diode current (I_d). It is seen from Fig. 9 that ~80% of the electron-beam current generated by the diode was propagated to the target from the first to the fourth unit. This result shows that the intensity of the guiding magnetic field is large enough to prevent electrons from reaching the walls of the drift tubes.

4. Conclusions

Linear induction accelerator "ETIGO-III" has been successfully developed to generate the high-current, relativistic electron beam. From the experimental results, we have obtained the following conclusions.

1) Acceleration voltage of 2MV has been achieved at each of the four induction acceleration units.

2) Electron beam with the peak current of ~ 4 kA has been extracted from the electron beam diode located at the first acceleration unit.

3) Approximately 80% of the electron-beam current generated by the diode propagates to the fourth unit of the acceleration cell.

References

(1) K. Yatsui, W. Masuda, C. Grigoriu, K. Masugata, W. Jiang, G. Imada, K. Imanari, T. Sonegawa, and E. Chishiro : Proc. 11th Int'l Conf. High-Power Particle Beams, I, 27 (1996).

(2) K. Yatsui : Proc. 11th IEEE Int'l Pulsed Power Conf, Baltimore (1997).

Preparation of SiC and BST Thin Films by Intense, Pulsed Ion-Beam Evaporation

M. Ikarashi, K. Ohtomo, W. Jiang, K. Masugata and K. Yatsui
Laboratory of Beam Technology, Nagaoka University of Technology
Nagaoka, Niigata 940-2188

Abstract

By using an intense, pulsed ion beam evaporation (IBE) technique, we have successfully prepared thin films of SiC and (Ba, Sr)TiO_3 (BST), which are interesting materials for industrial applications. The SiC films were analyzed by scratch test, while the BST samples were analyzed by using Sawyer-Tower circuit for the measurement of dielectric constant. The diagnostic results have shown that the thin films obtained by IBE are characterized by many special properties that can not be obtained by other thin-film deposition techniques.

1. Introduction

We have succeeded in developing a new technique for thin film deposition, i.e., intense, pulsed, ion beam evaporation (IBE) [1~7]. The basic principle of IBE is shown in Fig. 1. The intense, pulsed ion beam is irradiated on the surface of a solid target. Due to very high energy density produced by the ion beam, the target material close to the surface is evaporated and ionized, resulting in high-temperature, high-density plasma. The plasma expands toward the surrounding vacuum or low-pressure area, giving rise to a plume of the evaporated target material. This expanding plasma is called the ablation plasma. If the ablation plasma reaches a substrate, some of the plume materials will be deposited on the substrate surface to prepare thin films. One of the advantages of IBE is the elimination of substrate heating.[7]

We have found that the thin films can be obtained on both the front and the back surfaces of the substrate (see Figs. 1(a) and 1(b)). In addition, the thin film obtained on the front surface, called front side IBE (FS/IBE), has very high deposition rate (~μm/shot), while that obtained on the back surface, backside IBE (BS/IBE), has very good surface quality and physical

properties.[8)]

Generally, the SiC thin films are produced by sputtering or chemical vapor deposition (CVD) techniques, where the deposition rate is considerable low (typically ~ mm/hour)[8)]. Taking the advantage of very high deposition rate of FS/IBE, we have tried to apply it on the deposition of SiC thin film.

As a capacitor material for the next-generation super-high density integrated circuit (Ba, Sr)TiO_3 (BST) material has very high dielectric constant, making it a hopeful candidate. The BST thin films have been obtained by sputtering, CVD and pulsed laser deposition (PLD). However, all these processes need considerably high temperature of the substrate. Taking the advantage of the elimination of substrate heating of IBE, we have used the BS/IBE to prepare the BST thin film.

In this paper, we report the details of the deposition and the results of the diagnostics of the thin films. All samples were analyzed by X-ray diffraction (XRD), scanning electron microscope (SEM), atomic force microscope (AFM) and Rutherford backscattering spectroscope (RBS). In addition, the SiC samples were analyzed by scratch test, while BST films were analyzed by using Sawyer-Tower circuit for the measurement of dielectric constant, respectively.

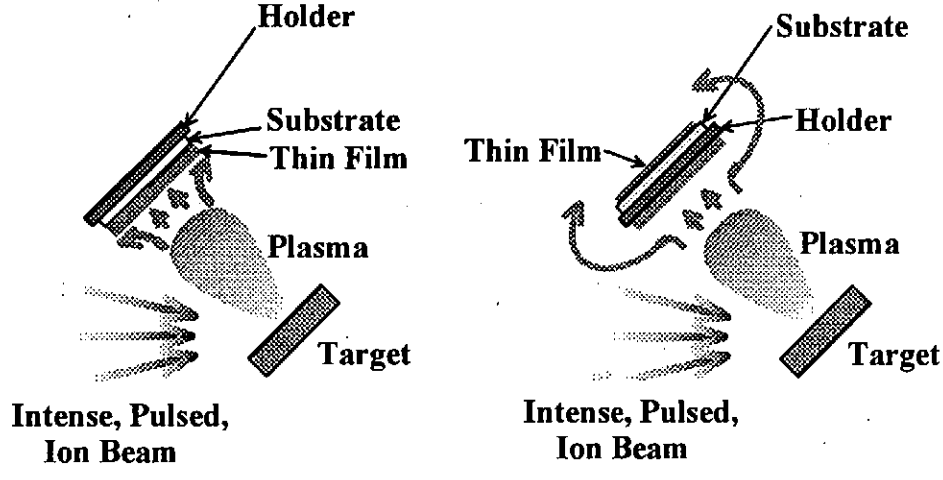

FS/IBE **BS/IBE**

(a) (b)

Fig. 1 Basic principle of IBE : (a) FS/IBE, (b) BS/IBE

2. Experimental Setup

Figure 2 shows the experimental setup. The ion beam is extracted from a magnetically insulated ion-beam diode which is driven by the pulsed power generator "ETIGO-II" [9]. The ion beam consists of 80% of proton and 20% of carbon and oxygen ions [10]. The peak ion energy is ~ 1 MeV and the pulse width is ~ 50 ns. The energy density deposited by the ion beam on the target surface is changed in the range of $34 < E_b < 67$ J/cm^2.

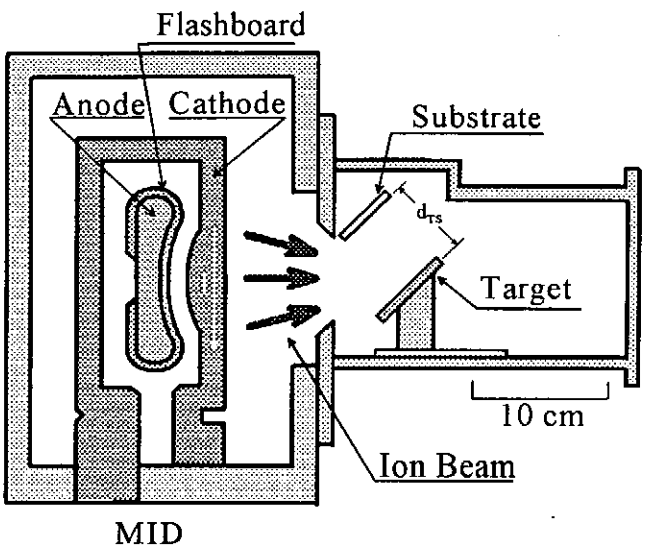

Fig. 2 Experimental setup

The FS/IBE was used for SiC thin film deposition. The target was sintered SiC (99.5% in purity) and the substrate was Si (100). The distance between the target and the substrate was d_{TS} = 40, 45, 50 mm. The deposition was carried out under the pressure of ~ 10^{-4} Torr with the substrate kept at room temperature. The samples were obtained by 1, 5, 10 of ion-beam shots.

The BS/IBE was used for BST thin film deposition. The target was sintered $(Ba_x,Sr_{x-1})TiO_3$ (x = 0, 0.5, 1.0, purity 99.9%). The substrate was a very thin aluminum layer coated on SiO_2 of 300 nm thick on Si (100) ($Al/SiO_2/Si$ (100)). The distance between the target and the substrate was d_{TS} = 40 mm. The deposition was carried out under the pressure of ~ 10^{-4} Torr with the substrate kept at room temperature. The samples were obtained by 30 shots.

3. Experimental results

3-1 SiC thin films

Figure 3 shows typical XRD patterns of SiC thin films obtained by d_{TS} = 40 mm, E_b = 67 J/cm^2 and 34 J/cm^2. Both samples were obtained after 10 shots of the ion beam. In Fig. 3, the Si (200) and Si(400) are diffraction

peaks of the substrate, while the peaks at 2θ = 35.77°, 41.62°, 60.08° clearly correspond to cubic SiC (111), (200), and (220), respectively. Therefore, it is confirmed that polycrystalline SiC appears in the thin films.

Figure 4 shows typical SEM photograph of SiC thin films. The samples were the same as those shown in Fig. 3. From Fig. 4, it is obtained that the film thickness is ~ 5μm and ~ 1.6 μm for E_b = 67 J/cm^2 and 34 J/cm^2,

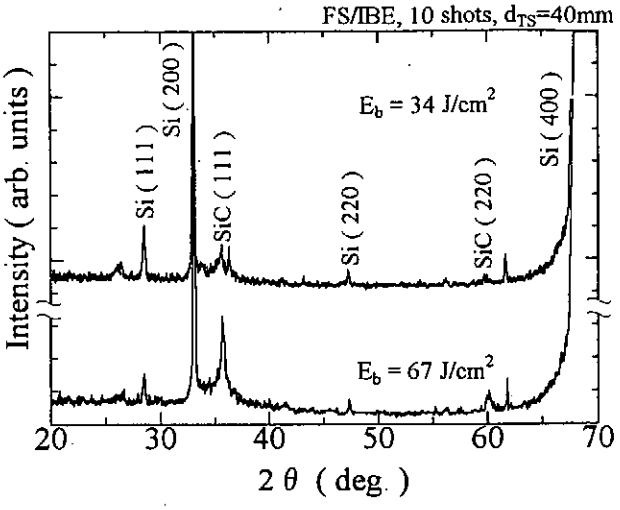

Fig. 3 Typical XRD pattern of SiC thin films

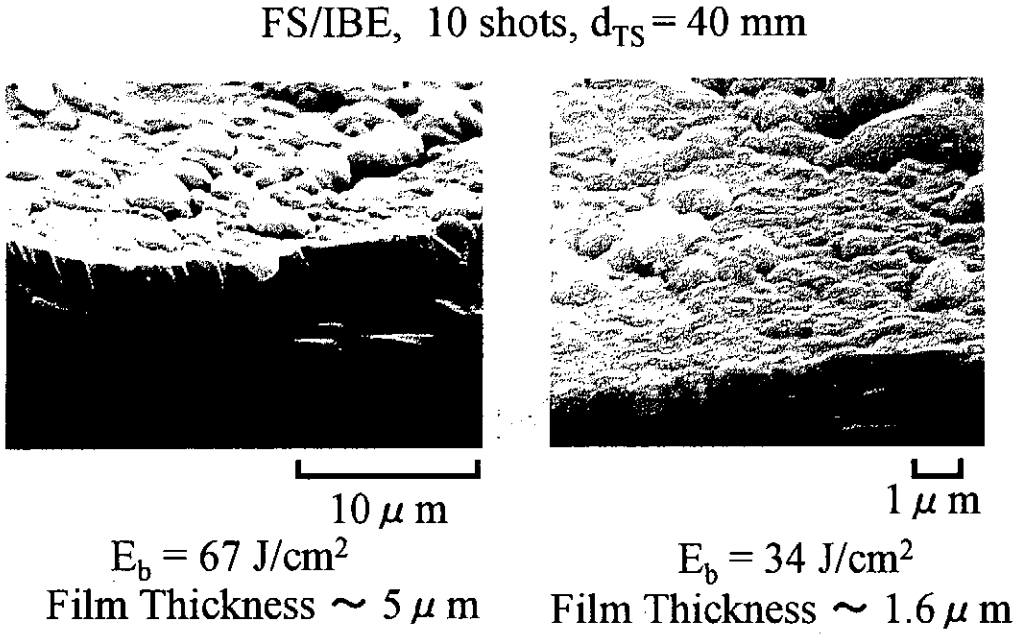

Fig.4 Typical photographs of SiC thin films

respectively. Thus, the average deposition rate is 500 nm/shot and 160 nm/shot, respectively.

Figure 5 shows the thin film thickness as a function of number of shots for E_b = 67 J/cm^2. The thickness always increases linearly with increasing number of shots.

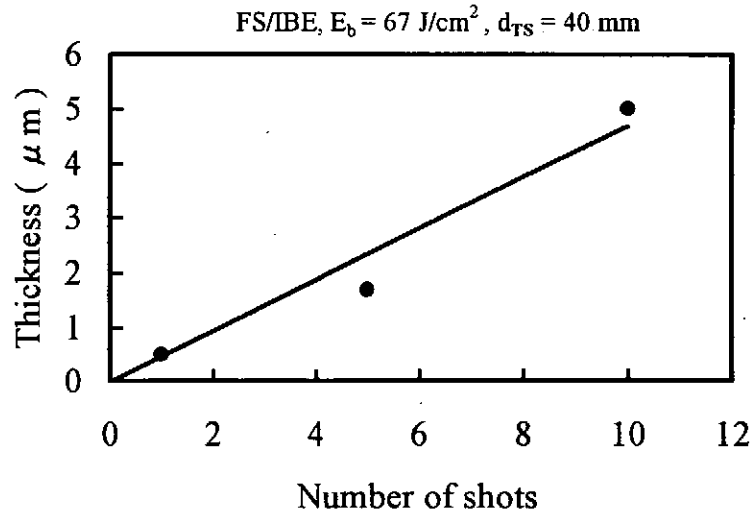

Fig. 5 Film thicknesson as a function of the number of shots.

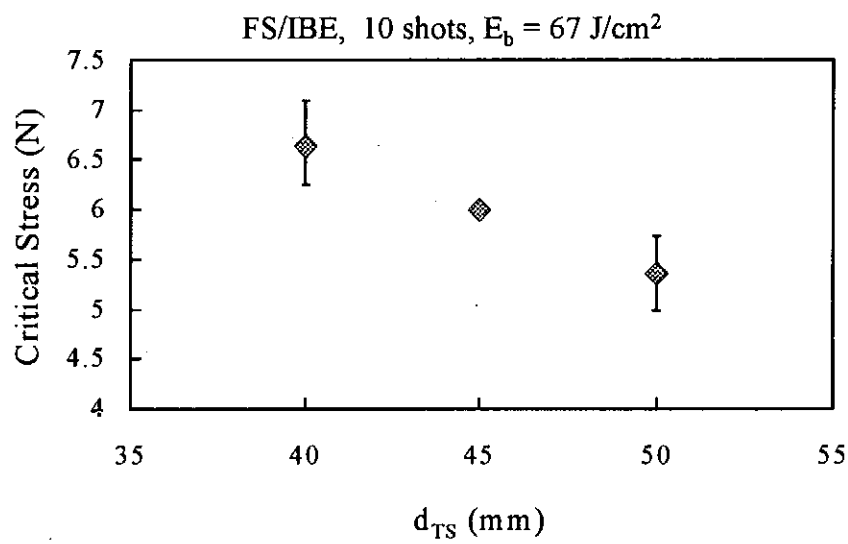

Fig.6 Critical stress of SiC thin films

Figure 6 shows results of scratch test of the SiC thin films. In Fig. 6, the critical stress represents the adhesion of the thin film on the substrate. The samples were obtained with E_b = 67 J/cm^2 by 10 shots of ion beam irradiation. From Fig.6, it is seen that the critical stress of the SiC thin film decreases with increasing d_{TS}.

3-2 BST thin films

Figure 7 shows the typical XRD results of BST thin films obtained by BS/IBE with : 30 shots, x = 0, d_{TS} = 40 mm, and E_b = 67 J/cm^2. It is found that the diffraction peaks at 2θ = 31.4°, 38.7°, 45.0°, 55.9° are those of $BaTiO_3$ (BST at x = 0)(100), (111), (200), (211), respectivity. The Si (200) and Al(111) are due to the substrate.

Figure 8 shows the typical SEM photograph of BST thin films. The sample was obtained with 30 shots, x = 1, d_{TS} = 40 mm, and E_b = 67 J/cm^2. From Figure 8, the film thickness was obtained as ~ 800 nm, giving the deposition rate of ~ 20 nm/shot.

Figure 9 shows the typical AFM photograph of the BST thin films. The sample was the same as that shown in Fig. 8. The surface mean roughness obtained from AFM measurement was ~ 4 nm.

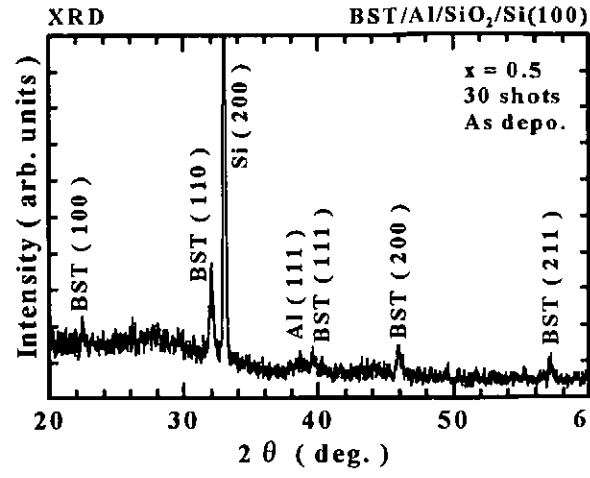

Fig. 7 Typical XRD results of BST thin films

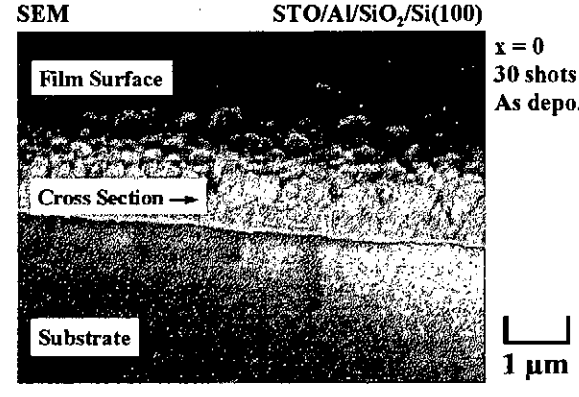

Fig. 8 Typical photograph of BST thin films

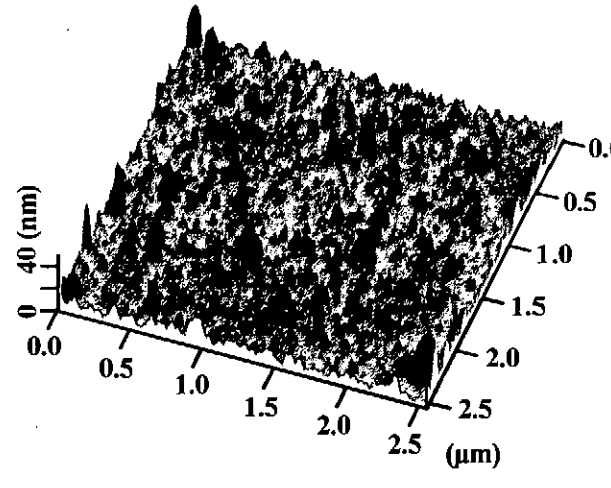

Fig. 9 Typical AFM photograph of BST thin films

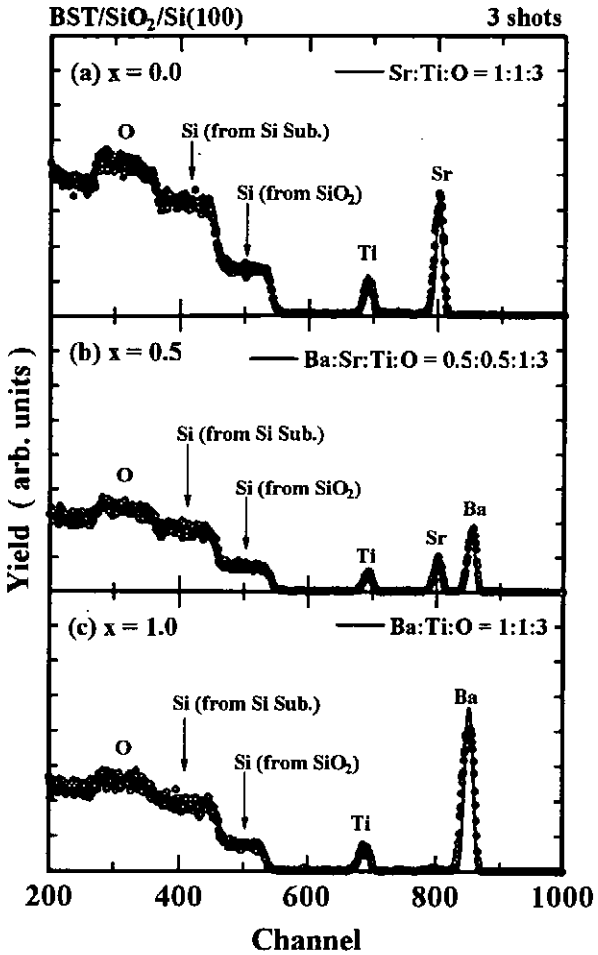

Fig. 10 RBS results of BST thin films

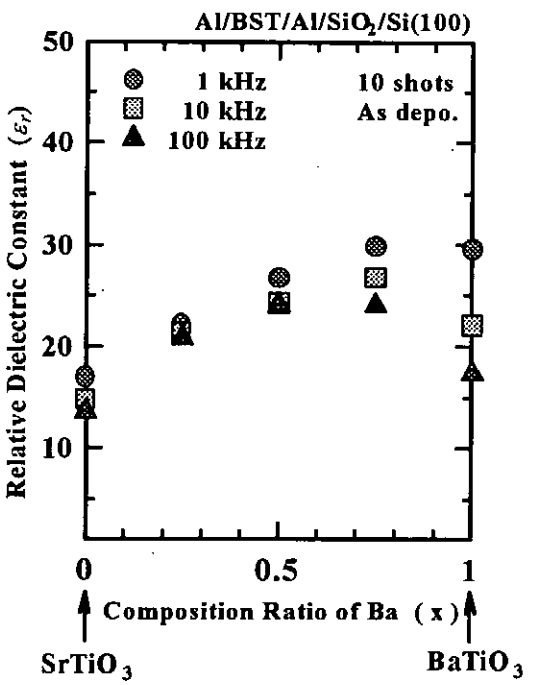

Fig.11 Relative dielectric constant as a function of x

Figure 10 shows the RBS results of BST thin films. The samples were obtained with x = 0, 0.5, and 1, 3 shots, d_{TS} = 40 mm, and E_b = 67 J/cm^2. In Fig. 10, the circles show the RBS measurement results and the dashed lines show the fitting results obtained by the conditions shown in the graph. Since the fitting condition is the same as that of the target, the good agreement between the RBS measurement and the fitting indicates that the thin film structure is the same as that of the target.

Figure 11 shows the relative dielectric constant measured by using the Sawyer-Tower circuit. The samples were obtained by the condition of x = 0, 0.25, 0.5, 0.75 and 10 shots, d_{TS} = 40 mm, and E_b = 67 J/cm^2. It is seen from Fig. 10 that, for all samples, the relative dielectric constant depends on the value of x. At 100 kHz, the relative dielectric constant has the peak in the range $0.5 < x < 0.7$.

4. Conclusion

Results of SiC thin films deposition by FS/IBE have given the following conclusions.

1) Polycrystalline β-SiC thin films were obtained on the substrate kept at room temperature.
2) Deposition rate of ~ 500 nm/shot was obtained by the ion beam energy density of E_b = 67 J/cm^2.
3) Critical stress of the film increases as the target-substrate distance is decreased.

The BS/IBE has been used for BST thin films deposition, which gives the following conclusions.

1) Polycrystalline BST thin films were obtained on the substrate kept at room temperature.
2) Deposition rate was ~ 20 nm/shot.
3) Mean roughness of the film surface was ~ 4 nm.
4) Relative dielectric constant depends on the value of x, and its peak appears in $0.5 < x < 0.7$ at the frequency of 100 kHz

References

1) Y. Shimotori, M. Yokoyama, S. Harada, K. Masugata and K. Yatsui: J. Appl. Phys. **63**, 968 (1988).
2) Y. Shimotori, M. Yokoyama, S. Harada, K. Masugata and K. Yatsui: Jpn. J. Appl. Phys. **28**, 468 (1989).
3) X. D. Kang, K. Masugata and K. Yatsui: Jpn. J. Appl. Phys. **33**, 1155 (1994).
4) X. D. Kang, K. Masugata and K. Yatsui: Jpn. J. Appl. Phys. **33**, L1041 (1994).
5) K. Yatsui, X. D. Kang, T. Sonegawa, T. Matsuoka, K. Masugata, Y. Shimotori, T. Satoh, S. Furuuchi, Y. Ohuchi, T. Takeshita and H. Yamamoto: Phys. Plasmas **1**, 1730 (1994).
6) T. Sonegawa, C. Grigoriu, K. Masugata, K. Yatsui, Y. Shimotori, S. Furuuchi and H. Yamamoto: Appl. Phys. Lett. **69**, 2193 (1996).
7) K. Yatsui, C. Grigoriu, K. Masugata, W. Jiang and T. Sonegawa: Jpn. J.

Appl. Phys. **36**, 4928 (1997).

8) S. Sohmiya and Y. Inomata: SiC Ceramics, (1988) p. 58.

9) A. Tokuchi, N. Nakamura, T. Kunimatsu, N. Ninomiya, M. Den, A. Araki, K. Masugata and K. Yatsui: *Proc. 2nd Int'l Top. Symp. Inertial Confinement Fusion Res. By High-Power Particle Beams, ed.* By K. Yatsui (Lab. of Beam Tech., Nagaoka Univ. of Tech.), (1986) p. 430.

10) Y. Shimotori, K. Aga, K. Masugata, M. Ito and K. Yatsui: Proc. Topical Meeting on Particle Beam Fusion and Its Related Problems, ed. by K.Niu, IPPJ-769 (2) 267 (1986).

Publication List of NIFS-PROC Series

NIFS-PROC-1 "*U.S.-Japan on Comparison of Theoretical and Experimental Transport in Toroidal Systems Oct. 23-27. 1989*", Mar. 1990

NIFS-PROC-2 "*Structures in Confined Plasmas –Proceedings of Workshop of US-Japan Joint Institute for Fusion Theory Program–* "; Mar. 1990

NIFS-PROC-3 "*Proceedings of the First International Toki Conference on Plasma Physics and Controlled Nuclear Fusion –Next Generation Experiments in Helical Systems– Dec. 4-7, 1989*" Mar. 1990

NIFS-PROC-4 "*Plasma Spectroscopy and Atomic Processes –Proceedings of the Workshop at Data & Planning Center in NIFS–*"; Sep. 1990

NIFS-PROC-5 "*Symposium on Development of Intensed Pulsed Particle Beams and Its Applications February 20 1990*"; Oct. 1990

NIFS-PROC-6 "*Proceedings of the Second International TOKI Conference on Plasma Physics and Controlled Nuclear Fusion , Nonlinear Phenomena in Fusion Plasmas -Theory and Computer Simulation-*"; Apr. 1991

NIFS-PROC-7 "*Proceedings of Workshop on Emissions from Heavy Current Carrying High Density Plasma and Diagnostics*"; May 1991

NIFS-PROC-8 "*Symposium on Development and Applications of Intense Pulsed Particle Beams, December 6 - 7, 1990*"; June 1991

NIFS-PROC-9 "*X-ray Radiation from Hot Dense Plasmas and Atomic Processes*"; Oct. 1991

NIFS-PROC-10 "*U.S.-Japan Workshop on "RF Heating and Current Drive in Confinement Systems Tokamaks" Nov. 18-21, 1991*, Jan. 1992

NIFS-PROC-11 "*Plasma-Based and Novel Accelerators (Proceedings of Workshop on Plasma-Based and Novel Accelerators) Nagoya, Japan, Dec. 1991*"; May 1992

NIFS-PROC-12 "*Proceedings of Japan-U.S. Workshop P-196 on High Heat Flux Components and Plasma Surface Interactions for Next Devices*"; Mar. 1993

NIFS-PROC-13 「NIFS シンポジウム
「核燃焼プラズマの研究を考える－現状と今後の取り組み方」
1992年7月15日、核融合科学研究所」1993年7月
NIFS Symposium "Toward the Research of Fusion Burning Plasmas -Present Status and Future strategy-", 1992 July 15, National Institute for Fusion Science"; July 1993 (in Japanese)

NIFS-PROC-14 "*Physics and Application of High Density Z-pinches*", July 1993

NIFS-PROC-15 岡本正雄、講義「プラズマ物理の基礎」
平成5年度 総合大学院大学1994年2月
M. Okamoto,
"Lecture Note on the Bases of Plasma Pysics"Graduate University for Advanced Studies Feb. 1994
(in Japanese)

NIFS-PROC-16 代表者 河合良信
平成5年度 核融合科学研究所共同研究
研究会報告書「プラズマ中のカオス現象」
*"Interdisciplinary Graduate School of Engineering Sciences" Report of the meeting on Chaotic Phenomena in Plasma*Apr. 1994 (in Japanese)

NIFS-PROC-17 平成5年度NIFSシンポジウム報告書
「核融合開発研究のアセスメント」平成5年11月29日-30日 於 核融合科学研究所
"Assessment of Fusion Reactor Development" Proceedings of NIFS Symposium held on November 29-30, 1993 at National Insitute for Fusion Science" Apr. 1994(in Japanese)

NIFS-PROC-18 "*Physics of High Energy Density Plasmas Produced by Pulsed Power*" June 1994

NIFS-PROC-19 K. Morita, N. Noda (Ed.),

"*Proceedings of 2nd International Workshop on Tritium Effects in Plasma Facing Components at Nagoya University, Symposion Hall, May 19-20, 1994*", Aug. 1994

NIFS-PROC-20 研究代表者 阿部 勝憲 (東北大学・工学部)
所内世話人 野田信明
平成6年度 核融合科学研究所共同研究【研究会】「金属系高熱流束材料の開発と評価」成果報告書

K. Abe and N. Noda (Eds.),
"Research and Development of Metallic Materials for Plasma Facing and High Heat Flux Components"
Nov. 1994(in Japanese)

NIFS-PROC-21 世話人:森田 健治(名大工学部)、金子 敏明(岡山理科大学理学部)
「境界プラズマと壁との相互作用に関する基礎過程の研究」研究会報告
K. Morita (Nagoya Univ.), T. Kaneko (Okayama Univ. Science)(Eds.)
"*NIFS Joint Meeting "Plasma-Divertor Interactions" and "Fundamentals of Boundary Plasma-Wall Interactions" January 6-7, 1995 National Institute for Fusion Science*" Mar. 1995 (in Japanese)

NIFS-PROC-22 代表者 河合 良信
プラズマ中のカオス現象
Y. Kawai,
"*Report of the Meeting on Chaotic Phenomena in Plasma, 1994*" Apr. 1995 (in Japanese)

NIFS-PROC-23 K. Yatsui (Ed.),
"*New Applications of Pulsed, High-Energy Density Plasmas*", June 1995

NIFS-PROC-24 T. Kuroda and M. Sasao (Eds.),
"*Proceedings of the Symposium on Negative Ion Sources and Their Applications, NIFS, Dec. 26-27, 1994*",
Aug. 1995

NIFS-PROC-25 岡本 正雄
新古典輸送概論(講義録)
M. Okamoto,
"*An Introduction to the Neoclassical Transport Theory*" (*Lecture note*), Nov. 1995 (in Japanese)

NIFS-PROC-26 Shozo Ishii (Ed.),
"*Physics, Diagnostics, and Application of Pulsed High Energy Density Plasma as an Extreme State*",
May 1996

NIFS-PROC-27 代表者 河合 良信
プラズマ中のカオスとその周辺非線形現象
Y. Kawai ,
"*Report of the Meeting on Chaotic Phenomena in Plasmas and Beyond, 1995*", Sep. 1996 (in Japanese)

NIFS-PROC-28 T..Mito (Ed.),
"*Proceedings of the Symposium on Cryogenic Systems for Large Scale Superconducting Applications*", Sep. 1996

NIFS-PROC-29 岡本 正雄
講義「核融合プラズマ物理の基礎 - I」
平成8年度 総合研究大学院大学 数物科学研究科 核融合科学専攻 1996年10月
M. Okamoto
"*Lecture Note on the Fundamentals of Fusion Plasma Physics - I" Graduate University for Advanced Studies;* Oct. 1996 (in Japanese)

NIFS-PROC-30 研究代表者 栗下 裕明(東北大学金属材料研究所)
所内世話人 加藤 雄大
平成8年度核融合科学研究所共同研究「被損傷材料の微小体積強度評価法の高度化」研究会 1996年10月 9日 於:核融合科学研究所

H. Kurishita and Y. Katoh (Eds.)
NIFS Workshop on Application of Micro-Indentation Technique to Evaluation of Mechanical Properties of Fusion Materials, Oct. 9, 1996, NIFS ; Nov. 1996 (in Japanese)

NIFS-PROC-31 岡本 正雄
講義「核融合プラズマ物理の基礎 - II」
平成8年度 総合研究大学院大学 数物科学研究科 核融合科学専攻 1997年4月
M. Okamoto
"*Lecture Note on the Fundamentals of Fusion Plasma Physics - II" Graduate University for Advanced*

Studies; Apr. 1997 (in Japanese)

NIFS-PROC-32 代表者　河合　良信
平成8年度　核融合科学研究所共同研究　研究会報告「プラズマ中のカオスとその周辺非線形現象」

Y. Kawai (Ed)
Report of the Meeting on Chaotic Phenomena in Plasmas and Beyond, 1996; Apr. 1997 (mainly in Japanese)

NIFS-PROC-33 H. Sanuki,
Studies on Wave Analysis and Electric Field in Plasmas; July 1997

NIFS-PROC-34 プラズマ対向機器・PSI・熱・粒子制御合同研究会報告
平成9年6月27日（金）9:00 ～16:20　核融合科学研究所・管理棟4F第1会議室
1997年　10月
T. Yamashina (Hokkaido University)
Plasma Facing Components, PSI and Heat/Particle Control June 27, 1997, National Institute for Fusion Science T. Yamashina (Hokkaido University) ; Oct. 1997 (in Japanese)

NIFS-PROC-35 T. Watari,
Plasma Heating and Current Drive; Oct. 1997

NIFS-PROC-36 T. Miyamoto and K. Takasugi (Eds.)
Production and Physics of High Energy Density Plasma; Production and Physics of High Energy Density Plasma; Oct. 1997

NIFS-PROC-37 (Eds.)T. Fujimoto, P. Beiersdorfer,
Proceedings of the Japan-US Workshop on Plasma Polarization Spectroscopy and The International Seminar on Plasma Polarization Spectroscopy January 26-28, 1998, Kyoto; June 1998

NIFS-PROC-38 (Eds.) Y. Tomita, Y. Nakamura and T. Hayashi,
Proceedings of the Second Asian Pacific Plasma Theory Conference APPTC '97, January 26-28, 1998, Kyoto; Aug. 1998

NIFS-PROC-39 (Ed.) K. Hirano,
Production, Diagnostics and Application of High Energy Density Plasmas; Dec. 1998